

**AFRL-SN-WP-TR-2002-1129**

**SOLID-STATE EMITTER DEVELOPMENT**

**Marc Cahay  
Punit Boolchand**



**University of Cincinnati  
Department of Electrical and Computer Engineering and Computer Science  
814 Rhodes Hall  
Cincinnati, OH 45221-0030**

**JULY 2002**

**Final Report for 19 February 1998 – 30 June 2002**

**Approved for public release; distribution is unlimited.**

**SENSORS DIRECTORATE  
AIR FORCE RESEARCH LABORATORY  
AIR FORCE MATERIEL COMMAND  
WRIGHT-PATTERSON AIR FORCE BASE, OH 45433-7318**

## NOTICE

USING GOVERNMENT DRAWINGS, SPECIFICATIONS, OR OTHER DATA INCLUDED IN THIS DOCUMENT FOR ANY PURPOSE OTHER THAN GOVERNMENT PROCUREMENT DOES NOT IN ANY WAY OBLIGATE THE U.S. GOVERNMENT. THE FACT THAT THE GOVERNMENT FORMULATED OR SUPPLIED THE DRAWINGS, SPECIFICATIONS, OR OTHER DATA DOES NOT LICENSE THE HOLDER OR ANY OTHER PERSON OR CORPORATION; OR CONVEY ANY RIGHTS OR PERMISSION TO MANUFACTURE, USE, OR SELL ANY PATENTED INVENTION THAT MAY RELATE TO THEM.

THIS REPORT HAS BEEN REVIEWED BY THE OFFICE OF PUBLIC AFFAIRS (ASC/PA) AND IS RELEASABLE TO THE NATIONAL TECHNICAL INFORMATION SERVICE (NTIS). AT NTIS, IT WILL BE AVAILABLE TO THE GENERAL PUBLIC, INCLUDING FOREIGN NATIONS.

THIS TECHNICAL REPORT HAS BEEN REVIEWED AND IS APPROVED FOR PUBLICATION.

/s/

---

JAMES A. COOK  
Project Engineer  
RF Components Branch

/s/

---

MARK C. CALCATERA, Chief  
RF Components Branch  
Aerospace Components Division

/s/

---

ROBERT T. KEMERLEY, Chief  
Aerospace Components Division  
Sensors Directorate

Do not return copies of this report unless contractual obligations or notice on a specific document require its return.

REPORT DOCUMENTATION PAGE				Form Approved OMB No. 0704-0188	
<p>The public reporting burden for this collection of information is estimated to average 1 hour per response, including the time for reviewing instructions, searching existing data sources, gathering and maintaining the data needed, and completing and reviewing the collection of information. Send comments regarding this burden estimate or any other aspect of this collection of information, including suggestions for reducing this burden, to Department of Defense, Washington Headquarters Services, Directorate for Information Operations and Reports (0704-0188), 1215 Jefferson Davis Highway, Suite 1204, Arlington, VA 22202-4302. Respondents should be aware that notwithstanding any other provision of law, no person shall be subject to any penalty for failing to comply with a collection of information if it does not display a currently valid OMB control number. <b>PLEASE DO NOT RETURN YOUR FORM TO THE ABOVE ADDRESS.</b></p>					
1. REPORT DATE (DD-MM-YY) July 2002		2. REPORT TYPE Final		3. DATES COVERED (From - To) 02/19/1998 – 06/30/2002	
4. TITLE AND SUBTITLE SOLID-STATE EMITTER DEVELOPMENT				5a. CONTRACT NUMBER F33615-98-C-1204	
				5b. GRANT NUMBER	
				5c. PROGRAM ELEMENT NUMBER 62204F	
6. AUTHOR(S) Marc Cahay Punit Boolchand				5d. PROJECT NUMBER 2002	
				5e. TASK NUMBER 02	
				5f. WORK UNIT NUMBER AU	
7. PERFORMING ORGANIZATION NAME(S) AND ADDRESS(ES)  University of Cincinnati Department of Electrical and Computer Engineering and Computer Science 814 Rhodes Hall Cincinnati, OH 45221-0030				8. PERFORMING ORGANIZATION REPORT NUMBER	
9. SPONSORING/MONITORING AGENCY NAME(S) AND ADDRESS(ES) Sensors Directorate Air Force Research Laboratory Air Force Materiel Command Wright-Patterson Air Force Base, OH 45433-7318				10. SPONSORING/MONITORING AGENCY ACRONYM(S) AFRL/SNDM	
				11. SPONSORING/MONITORING AGENCY REPORT NUMBER(S) AFRL-SN-WP-TR-2002-1129	
12. DISTRIBUTION/AVAILABILITY STATEMENT Approved for public release; distribution is unlimited.					
13. SUPPLEMENTARY NOTES Digital version is the best quality available.					
14. ABSTRACT Theoretical and experimental studies were performed to investigate the feasibility of realizing a new, voltage-activated, nonthermionic cathode proposed by Mumford and Cahay (based on W. Friz's concept). It consists of a heavily n-doped indium phosphide (InP) substrate upon which a layer of thin-film cadmium sulfide (CdS) is grown followed by a layer of lanthanum sulfide (LaS) with a metal grid atop it. Theoretically, only a low voltage (<20 volt) would need to be applied between grid and substrate to produce electron emission from the surface. Under this contract, theoretical analysis of expected self-heating, space-charge, current self-quenching and current-crowding effects was performed. Also, an attempt was made to develop growth techniques for the CdS/LaS layers needed for the structure. CdS thin films were deposited by RF magnetron sputtering and were characterized. Also, a technique was developed to synthesize bulk LaS in the form of a 2-inch-diameter target. The lowest work function measured from this material was 2.6 eV in air. Finally, LaS was grown on Si, glass, and InP by sputtering this target. These films were characterized by X-ray diffraction and X-ray photoelectron and atomic force spectroscopy. Further work will be needed to develop processing techniques for fabricating a testable emitter.					
15. SUBJECT TERMS cold cathode, nonthermionic cathode, solid-state emitter, negative electron affinity, cadmium sulfide, lanthanum sulfide, RF magnetron sputtering					
16. SECURITY CLASSIFICATION OF:			17. LIMITATION OF ABSTRACT: SAR	18. NUMBER OF PAGES 142	19a. NAME OF RESPONSIBLE PERSON (Monitor) Mark C. Calcaterra 19b. TELEPHONE NUMBER (Include Area Code) (937) 255-4831 x3380
a. REPORT Unclassified	b. ABSTRACT Unclassified	c. THIS PAGE Unclassified			

## TABLE OF CONTENTS

<u>SECTION</u>	<u>Page</u>
LIST OF FIGURES .....	vi
LIST OF TABLES .....	x
ABSTRACT .....	xi
1. Introduction .....	1
1.1 Background .....	1
1.2 Conventional Approach to NEA .....	1
1.3 Proposed New Approach to NEA .....	3
1.4 Theoretical Program .....	3
1.4.1 Earlier Work .....	6
1.4.2. Incentive for Further Theoretical Study .....	6
1.5 Experimental Program .....	8
2. A Theoretical Analysis of Self-Heating Effects in an InP/CdS/LaS Cold Cathode .....	10
2.1 Introduction .....	10
2.1 Fowler-Nordheim Emission .....	10
2.3 Inelastic scattering in CdS and LaS layers .....	11
2.4 Current Crowding Effects .....	12
2.5 Power Dissipation .....	13
2.6 Self-Heating Effects .....	16
2.7 Results .....	17
2.8 Conclusions .....	25
3. Current Self-Quenching Effects Caused by Space-Charge Effects in the Cathode to Anode Gap .....	26
3.1 Introduction .....	26
3.2 The EMC Approach .....	26
3.2.1 Calculation of Energy Distribution Function $h(E)$ .....	26
3.2.2 Effects of Shot Noise .....	29
3.2.3 Inelastic Scattering in the CdS Layer .....	31
3.3 Analytical Results .....	33
3.4 Numerical Results .....	34
3.4.1 Metal/CdS/LaS Cold Cathode .....	34
3.4.2 $n^{++}$ -InP/CdS/LaS Cold Cathode .....	41
3.5 Conclusions .....	47

## TABLE OF CONTENTS (Continued)

<u>SECTION</u>	<u>Page</u>
4. Interplay of Current Crowding And Current Self-Quenching Effects .....	51
4.1 Introduction .....	51
4.2 Model .....	51
4.3 Results .....	53
4.3.1 The $V_{bias} = 3.15$ V Case .....	55
4.3.2 The $V_{bias}$ 3.3 V Case .....	55
4.4 Conclusions .....	61
5. Growth and Characterization of Bulk LaS Samples .....	62
5.1 Introduction .....	62
5.2 Techniques for Bulk LaS Synthesis .....	62
5.2.1 The Arc Melting Process .....	62
5.2.2 The High-Temperature Vacuum Heating Process .....	64
5.3 Characterization of Bulk LaS .....	64
5.3.1 Powder XRD .....	64
5.3.2 Raman Spectroscopy .....	68
5.3.3 Work Function Measurements - Kelvin Probe Method .....	68
5.4 Conclusions .....	76
6. RF Sputtering of CdS Thin Film .....	78
6.1 Introduction .....	78
6.2 Background .....	78
6.3 Deposition Experiments .....	79
6.4 PL Characterization .....	79
6.5 RF Sputtering Deposition Parameters .....	79
6.5.1 Optimization of Substrate Preparation Method .....	83
6.5.2 Optimization of Substrate Temperature .....	83
6.5.3 Optimization of Ar Pressure .....	83
6.5.4 Optimization of RF Power .....	91
6.6 Comparison to the Previous Work in the Field .....	91
6.7 XRD Measurement Results And Discussion .....	91
6.8 Conclusion .....	101
7. Characterization of LaS Thin Films Grown on Si and InP Substrates by RF Magnetron Sputtering .....	102
7.1 Introduction .....	102
7.2 Sputtering parameters .....	102

## TABLE OF CONTENTS (Concluded)

<u>SECTION</u>	<u>Page</u>
7.3 Results .....	102
7.3.1 RF Parameters for Growth of LaS Thin Films on Si and InP Substrates ..	102
7.3.2 AFM scans .....	103
7.3.3 X-ray Photoelectron Spectroscopy (XPS) Results .....	103
7.3.4 XRD Results .....	109
7.4 Conclusions .....	117
8. Conclusions and Future Work .....	119
8.1 Conclusions .....	119
8.2 Suggestions for Future Work .....	120
8.3 List of Journal Publications, Conference Proceedings Papers, and Conference Presentations .....	120
8.4 Theses Supported By This Research Effort .....	121
9. List of References .....	122
Acronyms .....	125

## LIST OF FIGURES

<u>FIGURE</u>	<u>Page</u>
Figure 1: NEA Achieved Through Band Bending at the Surface of a Semiconductor (p-type doped) .....	2
Figure 2: Cross Section of the Proposed Cold Cathode .....	4
Figure 3: Schematic Showing the Nearly Perfect Lattice Matching Between the InP, CdS and LaS Layers .....	5
Figure 4: Schematic Representation of Conduction Band Profile Throughout the Metal (or $n^{++}$ -InP)/CdS/LaS Cold Cathode Emitter Shown in Figure 2 ....	7
Figure 5: Schematic Showing the Various Power Dissipation Mechanisms in the Cold Cathode (see Section 2.5) .....	14
Figure 6: Thermal Model of Heat Dissipation Through the InP Substrate .....	16
Figure 7: Temperature of the Active Portion of the Cathode .....	18
Figure 8: Bias Dependence of the Different Contributions to the Total Power Dissipated in the Cold Cathode .....	20
Figure 9: Bias dependence of the parameter $z$ as a function of applied bias ....	21
Figure 10: Bias Dependence of the Ballistic and Inelastic Components of the Emitted Current .....	22
Figure 11: Bias Dependence of the Emitted and Captured Current .....	23
Figure 12: Bias dependence of the power efficiency of the cold cathode .....	24
Figure 13: Modulating Action of the Electrostatic Potential Energy Profile in Front of the LaS Thin-Film as a result of the Space-Charge Effects .....	27
Figure 14: Schematic Representation of the Conduction Band Energy Profile Across the $n^{++}$ -InP/CdS/LaS Heterostructure Cold Cathode. ....	30
Figure 15: Illustration of the Effects of Inelastic Scattering in the CdS Layer. ..	32
Figure 16: Time Average of the Conduction Current Density in the Rightmost Bin of the Simulation Versus Injection Current Density, for a Cathode-to-Anode Bias of 1V .....	36
Figure 17: Time Average of the Conduction Current Density in the Rightmost Bin of the Simulation Versus Injection Current Density, for a Cathode-to-Anode Bias of 5 V .....	37
Figure 18: Plot of the Energy Density Flux of Electrons Injected Into Vacuum and Electron Beam Collected at the Anode ( $J_{FN} = 50 \text{ A/cm}^2$ and $J_A = 13 \text{ A/cm}^2$ )	38
Figure 19: Plot of the Energy Density Flux of the Electron Beam Injected Into Vacuum and Electron Beam Collected at the Anode ( $J_{FN} = 95 \text{ A/cm}^2$ and $J_A = 13 \text{ A/cm}^2$ ) .....	39
Figure 20: Plot of the Energy Flux Density of the Injected Beam for $J_{FN} = 50 \text{ A/cm}^2$ for Different Values of $\lambda_{CdS}$ .....	40

## LIST OF FIGURES (continued)

<b><u>FIGURE</u></b>	<b><u>Page</u></b>
Figure 21: Plot of the Injected and Collected Energy Density Flux for $J_{FN} = 20 \text{ A/cm}^2$ .....	42
Figure 22: Plot of the Injected and Collected Energy Density Flux for $J_{FN} = 40 \text{ A/cm}^2$ .....	43
Figure 23: Plot of the Injected and Collected Energy Density Flux for $J_{FN} = 90 \text{ A/cm}^2$ .....	44
Figure 24: Plot of the Injected and Collected Energy Density Flux for $J_{FN} = 50 \text{ A/cm}^2$ .....	45
Figure 25: Bias Dependence of the Conduction Band Energy Profile Across the $n^{++}$ -InP/CdS/LaS Heterostructure .....	46
Figure 26: Plot of the Energy Density Flux of the Electron Beam Injected into Vacuum as a Function of the Injection Current Density .....	48
Figure 27: Time Average of the Conduction Current Density (5 V) .....	49
Figure 28: Time Average of the Conduction Current Density (10 V) .....	50
Figure 29: (a) Energy Band Diagram across the Metal/CdS/LaS Cold Cathode; (b) Lateral Potential Drop Between the two Metal Fingers used to Bias the Cathode .....	52
Figure 30: Ratio $\eta$ of the Anode to Emission Current Densities Showing the Onset of Current Self-Quenching at Large Value of $J_{em}$ .....	54
Figure 31: Lateral Potential Variation of the Potential Drop across the LaS Windows of Various Widths .....	56
Figure 32: Lateral Variation of $J_A$ for Different Window Widths .....	57
Figure 33: Lateral Variation of $\eta_{tot}$ for Different Window Widths .....	58
Figure 34: $\eta_{tot}$ Variation across the Emission Window .....	59
Figure 35: $J_A$ variation for $V_{bias} = 3.3 \text{ V}$ .....	60
Figure 36: Phase Diagram of LaS .....	63
Figure 37: Typical Heating Cycle Used During Growth of Rare-Earth Samples Using the High-Temperature Furnace From Thermal Technologies, Inc. ....	65
Figure 38: Optical Micrograph Showing a Large Crystallite (Gold Platelet) of the Cubic LaS With a Staircase-Like Growth Pattern .....	66
Figure 39: Comparison of XRD Scans of LaS Sample Produced (a) Right After the Arc Melting Process Step-1 and (b) After Step-2, Carbon Reduction (See Section 5.2) .....	69
Figure 40: Comparison of XRD Scans of LaS Sample Produced (a) Right After the Arc Melting Process Step-1 and (b) After Step-2, Carbon Reduction (See Section 5.2) .....	70



## LIST OF FIGURES (continued)

<b><u>FIGURE</u></b>	<b><u>Page</u></b>
Figure 41: LaS Sample Synthesized in the Thermal Technologies, Inc. High-Temperature Furnace (a) Right After Heating at 1800 °C for 2 Hours (b) Mixing the Previous Sample, Pelletizing and then Heating again at 1800 °C for 2 Hours .....	71
Figure 42: Raman Spectra of LaS Processed Using the two Step Arc-Melting Method .....	72
Figure 43: Electronic Energy Level Diagram for two Different Metals Separated by Distance $d$ (a) Before Electrical Contact, (b) After Contact, and (c) After Inclusion of Backing Potential $V_b$ .....	74
Figure 44: (a) Circuit Diagram of the Tip Amplifier, and (b) Simplified Diagram of the First Stage Amplifier Where the I/V Converter is Represented by its Input Resistance $R_{in}$ .....	75
Figure 45: Schematic Diagram Showing the Variation of Peak-To-Peak Output Signal, $V_{ptp}$ With the Backing Potential $V_b$ .....	77
Figure 46: Planar Magnetron Sputtering .....	80
Figure 47: RF Sputtering Facility .....	80
Figure 48: Typical PL Spectrum of CdS samples (Top) and Two-Peak Fit (Bottom) .....	81
Figure 49: PL Spectrum Of High Purity CdS Crystallite .....	82
Figure 50: XRD Determining a H-phase crystal .....	82
Figure 51: Surface of InP Wafer is Damaged After Chemical Etching Using the Method 1 of Cleaning Described in the Text .....	84
Figure 52: PL Spectrum for Samples Prepared by Three Different Substrate Preparation Methods .....	85
Figure 53: Three Kinds of Surface Preparation Methods are Compared .....	86
Figure 54: Comparison of the PL Spectrum for Samples With Different Substrate Temperatures .....	87
Figure 55: PL Spectrum Analysis Showing that the Samples With Substrate Temperature in the Range of 150 °C to 200 °C Have the Best Quality .....	88
Figure 56: Illustration of the PL Peak Shift to Low Energy Side at Low Ar Pressure .....	89
Figure 57: The Ar Pressure Plays an Important Role in Sputtering .....	90
Figure 58: Similarity of PL Spectra for Samples Deposited at Different RF Power .....	92
Figure 59: Effects on Peak Center and Width of Changing the RF Power From 6 W to 15 W .....	93
Figure 60: XRD Scan Showing Hexagonal CdS Modification .....	96

## LIST OF FIGURES (concluded)

<b><u>FIGURE</u></b>	<b><u>Page</u></b>
Figure 61: Higher Resolution Scan in 40 to 60 Degree Range .....	97
Figure 62: XRD Scan From the Back Side of CdS#22 .....	98
Figure 63: All Peaks From CdS#22 Are Identifiable as Either Due to the InP Substrate or Reflection From H-CdS .....	99
Figure 64: XRD Scan of CdS#22 .....	100
Figure 65: Example of AFM of LaS Samples Deposited on a Si Substrate .....	104
Figure 66: Example of AFM over a Smaller Region (Shown in the Inset) of a LaS Thin Film Deposited on a Si Substrate .....	105
Figure 67: AFM Image of a LaS Thin Film Deposited on a InP .....	106
Figure 68: Zoom on a 1umx1um Region of a LaS/InP Film .....	107
Figure 69: AFM Scan on a Portion Between two Stripes of the LaS/InP Thin Film Shown in Figure 67 .....	108
Figure 70: XPS Analysis of The Fifth LaS/InP Sample Shown in Table 10 ....	110
Figure 71: Schematic Representation of Occurrence of (311) Bragg Peak in the Thin Film XRD .....	111
Figure 72: Thin Film X-ray Spectra of Different Runs Made on Bare p-type InP Wafer .....	113
Figure 73: Thin-Film X-ray Spectra of LaS on p-InP at a Grazing Angle of 0.5 Degree .....	114
Figure 74: Thin-Film X-ray Spectra of LaS on p-InP at a Grazing Angle of 1.0 Degree .....	115
Figure 75: Thin Film X-ray Spectra of LaS on Si Wafer by RF Sputtering .....	116
Figure 76: Thin Film X-ray Spectra of LaS on Si Wafer by E-Beam Evaporation	118

## LIST OF TABLES

<u>TABLE</u>	<u>Page</u>
Table 1: Material Parameters of Some Sulfides of Rare-Earth Metals .....	3
Table 2: Material Parameters of the Cold Cathode .....	17
Table 3: Physical Parameters of the Cold Cathode .....	19
Table 4: Parameters of the Simulated Metal/CdS/LaS Cathode .....	34
Table 5: Material Parameters of the $n^{++}$ /CdS/LaS Cold Cathode .....	41
Table 6: Physical Parameters of the Cold Cathode .....	53
Table 7: XRD Line Shape Analysis .....	68
Table 8: XRD Peaks And Corresponding Miller Indices From CdS And InP Bulk Samples .....	94
Table 9: Description Of Samples For XRD Measurement .....	95
Table 10: InP/LaS XPS Measurements Indicating the Percentage of La and S in the Grown Thin Films .....	109
Table 11: FWHM And The Angle At Which X-ray Peak Occurs For A p-InP Wafer Having (100) Orientation .....	112
Table 12: FWHM And 2 theta from the Thin Film X-ray Spectra of Different RF Sputtered LaS Samples on p-InP Substrates .....	117

## Abstract

Under this contract, the University of Cincinnati (UC) investigated the feasibility of fabricating an operating a newly proposed, cold cathode consisting of a layered structure of either a metal or a heavily-donor-doped indium phosphide ( $n^{++}$  InP) substrate, a cadmium sulfide (CdS) intermediate layer, and a lanthanum sulfide (LaS) surface layer. In the proposed design, room-temperature electron emission from the surface into vacuum would be activated by applying a positive voltage ( $< 20$  volts) to the LaS relative to the substrate. A metal grid deposited on the LaS surface would be used to apply the voltage. Key features of electron transport in this heterostructure are (1) Fowler-Nordheim field-emission current injection at the InP/CdS interface, (2) near-to-ballistic transport across a thin CdS layer, and (3) a negative electron affinity energy profile created at the surface due to the LaS work function being less than half the CdS bandgap at non-thermionic temperatures.

In Section 1, some background on previous cold cathode concepts and a description of the theory involved with the  $n^{++} - \text{InP}/\text{CdS}/\text{LaS}$  solid-state emitter proposed by Mumford and Cahay in 1996 is presented. Under this contract, UC performed theoretical analyses of self-heating effects, space-charge effects on the regime of current self-quenching, and the interplay of current crowding with current self-quenching for variations of the proposed emitter design.

In Section 2, the various power dissipation mechanisms in the cathode are described along with their effect on operating temperature. For the designs analyzed, significant current crowding was found to occur at a lesser bias than the value where self-heating could no longer be neglected. At the maximum bias at which current crowding effects can be tolerated, emission current density reaches several hundred  $\text{A}/\text{cm}^2$ . However, the ballistic fraction of the beam emitted is found to be dominant only if the CdS thickness is less than  $150 \text{ \AA}$ . In order of decreasing importance, the leading contributions to power dissipation in the cathode were found to be (1) the shadowing effect of the emitter fingers used to apply the voltage bias, (2) electron trapping in the LaS, and (3) inelastic scattering in the CdS layer. For the designs analyzed, overall power efficiency was around 20 percent and decreases with applied bias. Higher power efficiency is attainable by reducing the width of the biasing metal fingers, but their thickness would need to be increased as well to avoid substantial voltage drop along the fingers.

In Section 3, an analysis of anode current self-quenching due to space-charge effects is described. An ensemble Monte-Carlo approach was used. Inelastic scattering and ballistic transport in the CdS layer were considered respectively in the metal and InP substrate cases. In both cases, the energy spread of the electrons collected at the anode was substantially narrower than for the electrons as they were emitted from the cathode. This is due to beam modulation caused by oscillations in the electrostatic potential in front of the cathode. When inelastic scattering in the CdS layer is included, the transition to the regime of current self-quenching is more gradual compared to that of ballistic transport through the CdS layer.

In Section 4, the interplay of current crowding and self-quenching is described. When space-charge effects are neglected, anode current decreases monotonically from the edges of the emission

window toward the center as a result of the finite conductivity of the LaS. When a solution containing both current self-quenching and current crowding is derived, the anode current density across the emission window is not monotonic. Moving from the edge of the window toward the center, the anode current density increases to a maximum before dropping again for the metal substrate case.

UC also performed experimental studies in an attempt to fabricate an InP/CdS/LaS emitter. In Section 5, a sesquisulfide technique that was developed to synthesize bulk LaS was described. The lattice constant of the material synthesized was 5.8679Å. The lowest work function measured (using a Kelvin probe) was 2.6 eV. The bulk LaS work concluded with the synthesis of two, 2-inch diameter, 1/8-inch thick, LaS samples to be used as targets for RF (radio frequency) magnetron sputtering.

In Section 6, the work to develop a sputtering technique to deposit thin-film of CdS is described. CdS samples deposited under a variety of sputtering conditions were characterized and optimum conditions identified. Unfortunately, the material deposited appears to be in the hexagonal crystal form; not the cubic form needed for the emitter design. It is expected, though, that growing CdS of lesser thickness than was attempted under this contract has a good chance of yielding CdS in cubic form. This needs to be attempted in any follow-on work.

In Section 7, the work to deposit thin-film LaS is described. The RF parameters which produce thin-film LaS with close to stoichiometric ratio were identified. LaS was sputtered on silicon, glass and InP substrates. The samples produced were characterized by X-ray diffraction (XRD), X-ray photoelectron spectroscopy (XPS) and atomic force microscopy (AFM). When the contract ended, the fabrication techniques for deposition of CdS and LaS were not yet sufficiently developed to attempt fabrication of a prototype emitter structure. UC hopes to continue this work in the future using other sources of funding. In particular, UC wishes to explore deposition of LaS by thermal evaporation using a newly acquired Revap-3000 unit and eventually attempt deposition of CdS followed by LaS *in situ* (i.e., without breaking the vacuum). If CdS/LaS layers can be successfully deposited with the required thickness and material properties, then UC will attempt to fabricate prototype emitters and test them.

# 1. Introduction

## 1.1 Background

In the past decade, there has been renewed interest in cold cathode emitters for applications in a variety of electronic devices, including microwave tube amplifiers, pressure sensors, thin panel displays, and high-temperature, radiation tolerant sensors, among others [1, 2]. Introduction of such electron emitters operating without the need for heating, would permit an unprecedented compactness and weight reduction in device and equipment design. Non-thermionic electron emission is very desirable for keeping the statistical energy distribution of emitted electrons as narrow as possible, minimizing thermal drift of device characteristics, and avoiding accelerated thermal aging or destruction by mechanical stress and fatigue. Cold cathodes exhibit a narrower electron energy distribution than conventional thermionic cathodes and are therefore expected to offer several advantages, such as reduced noise, improved electron beam focusing, imaging, and beam discharge lag in camera tubes. To keep the emitter temperature moderate, emitters must be built on thin epitaxial films (using vertical layering) so as to have short heat paths allowing excellent heat sinking.

Over the last 30 years, a large number of cold and photo cathodes using a wide variety of semiconductor materials have been proposed based on the concept of negative electron affinity (NEA). NEA can be achieved through bandgap engineering of semiconductor materials by coating the surface of a wide bandgap semiconductor with a low work function material such that the surface vacuum barrier is brought below the bulk conduction band edge [3], as shown in Figure 1. A localized bending of the conduction band will occur near the surface of the material to equalize the Fermi level in the bulk with the surface state energy level. For the two cases where the semiconductor used is intrinsic or p-doped, the work function,  $\phi_M$ , of the metallic coating must obey  $\phi_M < 0.5E_G$  or  $\phi_M < E_G$ , respectively ( $E_G$  = bandgap energy) for electrons excited into the conduction band to have a favorable chance of escaping the solid into vacuum.

When the surface of the semiconductor is covered with a low work function material,  $\phi_M$ , the vacuum level outside the semiconductor can end up below the minimum of the conduction band in the bulk. This leads to an effective NEA, i.e.,  $\chi_{eff} < 0$ .

## 1.2 Conventional Approach to NEA

For an electron emitter to be useful in practical applications, it should be capable of delivering uniform current densities over operational lifetimes of on the order of  $10^5$  hours ( $\sim 10$  years). To satisfy this requirement, the structural and chemical composition of the cathodes must be stable. This rules out the use of alkali metal films on emitter surfaces to lower the work function [3]. For example, cesiated semiconductor surface technology has evolved over the years to realize NEA photoemitters made by coating the surface of a wide variety of III-V semiconductors. However, cesium suffers from poor stability due to its willingness to release bonding electrons. Cesium melts at 28.5 °C and has a high vapor-pressure ( $10^{-3}$  torr at 100 °C). Cesium, when placed in an evacuated enclosure, eventually migrates everywhere. It spreads to surfaces where electron emission is not desired and can make insulating surfaces undesirably conductive. It also spreads to interelectrode spaces where it will provide a relatively easy path for gaseous conduction and electrical arcs.

Typically, the operating lifetime of cathodes using cesiated surfaces is good as long as the tube is not subjected to excessive cathode currents from high-level usage. Otherwise, the emitted electrons from the cathode are accelerated and, depending on the accelerating voltage and cathode current density, there can be an electron scrubbing effect on the anode, resulting in positive ions being liberated and accelerated back onto the NEA surface and a continuous increase in the cathode work function. A cathode degradation which occurs under high current operating conditions is electron-stimulated desorption of the Cs + O activation layer. In general, III-V NEA surfaces are not stable in ultrahigh vacuum (UHV). At 300K, Cs will slowly desorb from the surface in UHV at a rate dependent, in part, on the partial pressure of Cs within the vacuum system. Adding Cs will restore a fraction of the original emission characteristics. A small quantum yield can still give rise to a large current if excited by the light of a laser. However, excessive light intensity may lead to the destruction of the activation layer by light-induced desorption.

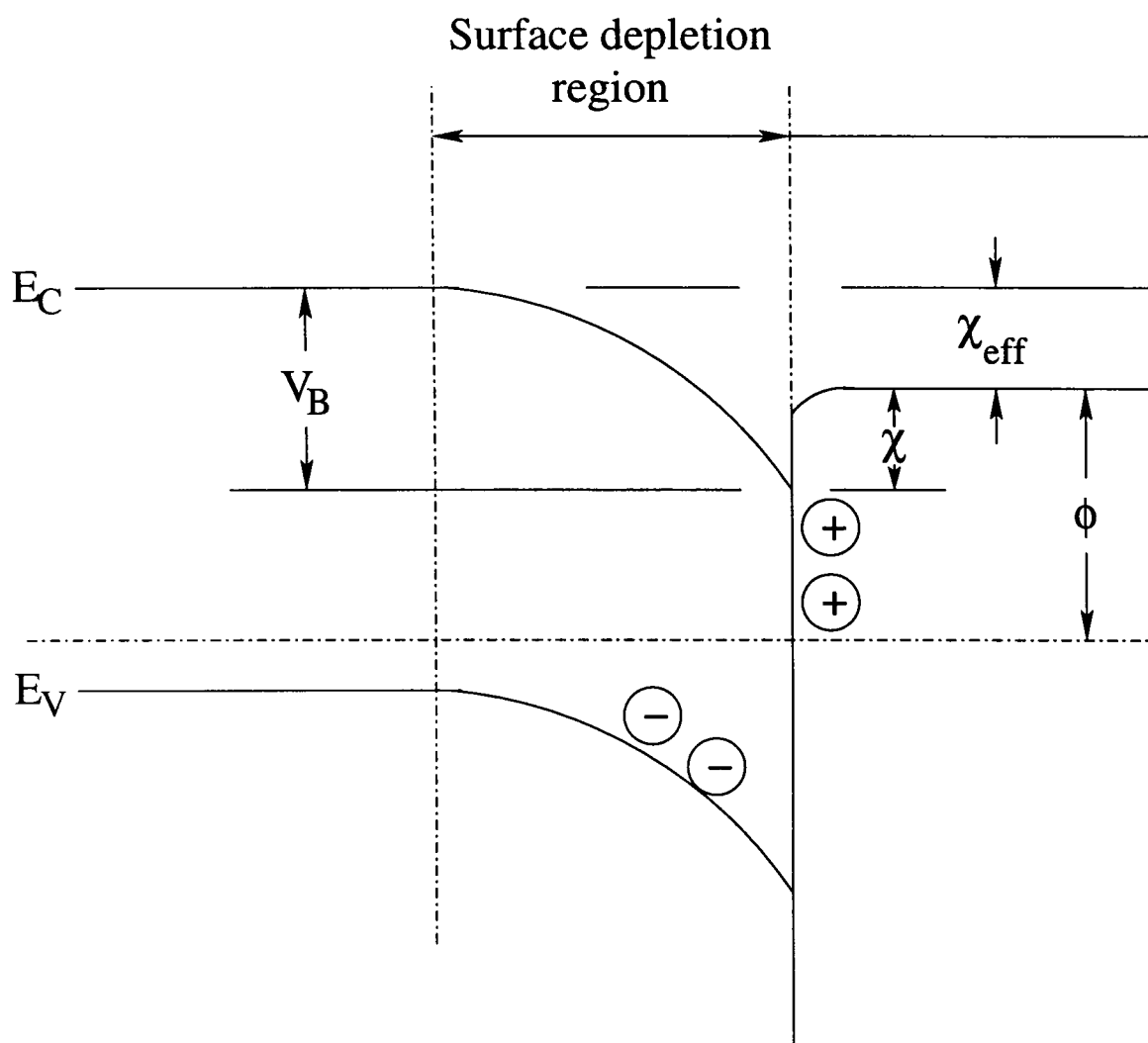


Figure 1: NEA Achieved Through Band Bending at the Surface of a Semiconductor (p-type doped)

This effect must be counteracted by continuous cesiation during operation of the source.

### 1.3 Proposed New Approach to NEA

In 1996, P.D. Mumford and M. Cahay proposed and theoretically analyzed the operation of a new material combination for a wide bandgap semiconductor-based electron emitter (i.e., a "solid-state emitter") [4, 5, 6]. It would use a sulfide of a rare-earth element, such as lanthanum, as a more stable NEA-creating layer on top of a layer of a II-VI semiconductor, such as CdS. A voltage bias to the surface layer relative to a metallic substrate would inject electrons into the conduction band of the CdS (a wide bandgap semiconductor) and out pass the NEA energy profile into vacuum. This material combination was based on suggestions by W. Friz who made the initial search of the literature for innovative materials to make the voltage-activated, solid-state emitter concept work<sup>1</sup>. These materials do not suffer from all of the limitations of cesiated surfaces. Some of the material properties of rare-earth element sulfides in their cubic form are listed in Table 1. The work function at room temperature of these compounds, when extrapolated from high-temperature measurements, are quite small [7]. Therefore, it is expected that these materials could be used to reach NEA when deposited on p-type doped semiconductors. For instance, LaS has a lattice constant  $5.854\text{\AA}$  very close to the lattice constant of InP  $5.8688\text{\AA}$ , and NdS has a lattice constant  $5.69\text{\AA}$ , very close to the lattice constant of GaAs  $5.6533\text{\AA}$ . Since the room temperature work function of LaS (1.14 eV) and NdS (1.36 eV) [8] are respectively below the bandgap of InP (1.35 eV) and GaAs (1.41 eV), NEA could therefore theoretically be attained from the InP/LaS and GaAs/NdS combinations by heavily p-type doping the semiconductors.

**Table 1: Material Parameters of Some Sulfides of Rare-Earth Metals**

	ErS	YbS	NdS	GdS	PrS	CeS	LaS	EuS	SmS
Lattice constant	5.424	5.466	5.69	5.74	5.747	5.778	5.854	5.968	5.970
Work function (300 K)			1.36		1.26	1.05	1.14		
Melting point ( $^{\circ}\text{C}$ )		2060	2200		2230	2450	2200		1870
Electrical resistivity ( $\mu\Omega$ )			242		240	170	25		

Two other important features of the fcc cubic form of the rare-earth compounds listed in Table 1 are the fairly large melting temperatures (about  $2000^{\circ}\text{C}$ ) and their fairly good electrical resistivity (about  $100\mu\Omega - \text{cm}$ ). It is, therefore, expected that thin films of these compounds used to promote semiconductor surfaces to NEA should be stable and should not suffer from current crowding effects which would lead to nonuniformity in the emitted current into vacuum.

### 1.4 Theoretical Program

Research on cold cathodes based on a NEA concept has been conducted in the laboratory of Dr. Cahay over the last 6 years. As a Ph.D. student of Dr. Cahay, Phil Mumford, proposed and analyzed a new cold cathode design shown in Figure 2. It consists of (1) an  $n^{++}$  doped InP, or a metal (aluminum or gold) which acts as a supplier of electrons, (2) an undoped wide bandgap semiconductor CdS ( $E_g = 2.42\text{eV}$ ), and (3) a thin semimetallic film of LaS having a low work function (1.14 eV). The CdS/LaS interface gives us an NEA of 60 meV. The metal (or InP) supplies electrons at a sufficient rate into the CdS conduction band, which then travel through CdS either ballistically or inelastically. The semimetallic film facilitates the coherent transport (tunneling) of electrons from the semiconductor conduction band into vacuum. The choice of InP as a substrate is particularly attractive since the lattice constant of InP ( $5.86\text{\AA}$ ) closely matches the lattice constant of the zincblende cubic CdS ( $5.83\text{\AA}$ ). The choice of LaS semimetallic thin film grown on nominally undoped CdS is quite appropriate since the lattice constant of CdS ( $5.83\text{\AA}$ ) is very close to the lattice constant of LaS ( $5.85\text{\AA}$ ) in its cubic crystalline form (see Figure 3).

<sup>1</sup>W. Friz, "The Veiled Work Function Emitter Concept," Final Report, Task 9, contract F33615-90-C-1405, June 1992 and Technical Memo dated 21 June 1994, Task ELM-6 (containing table of suggested monosulfides)



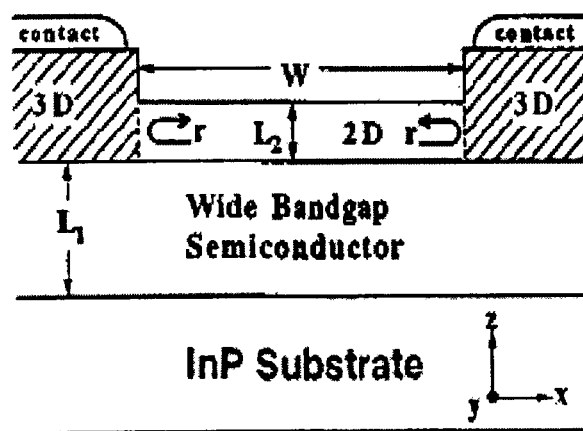
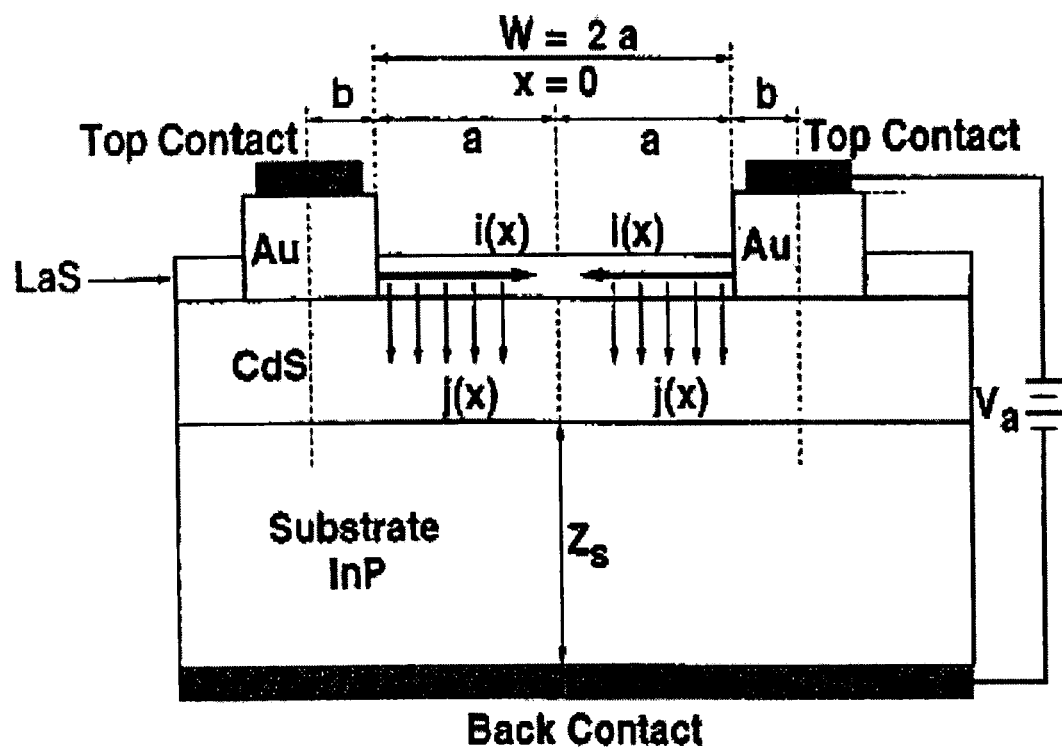


Figure 2: Cross Section of the Proposed Cold Cathode

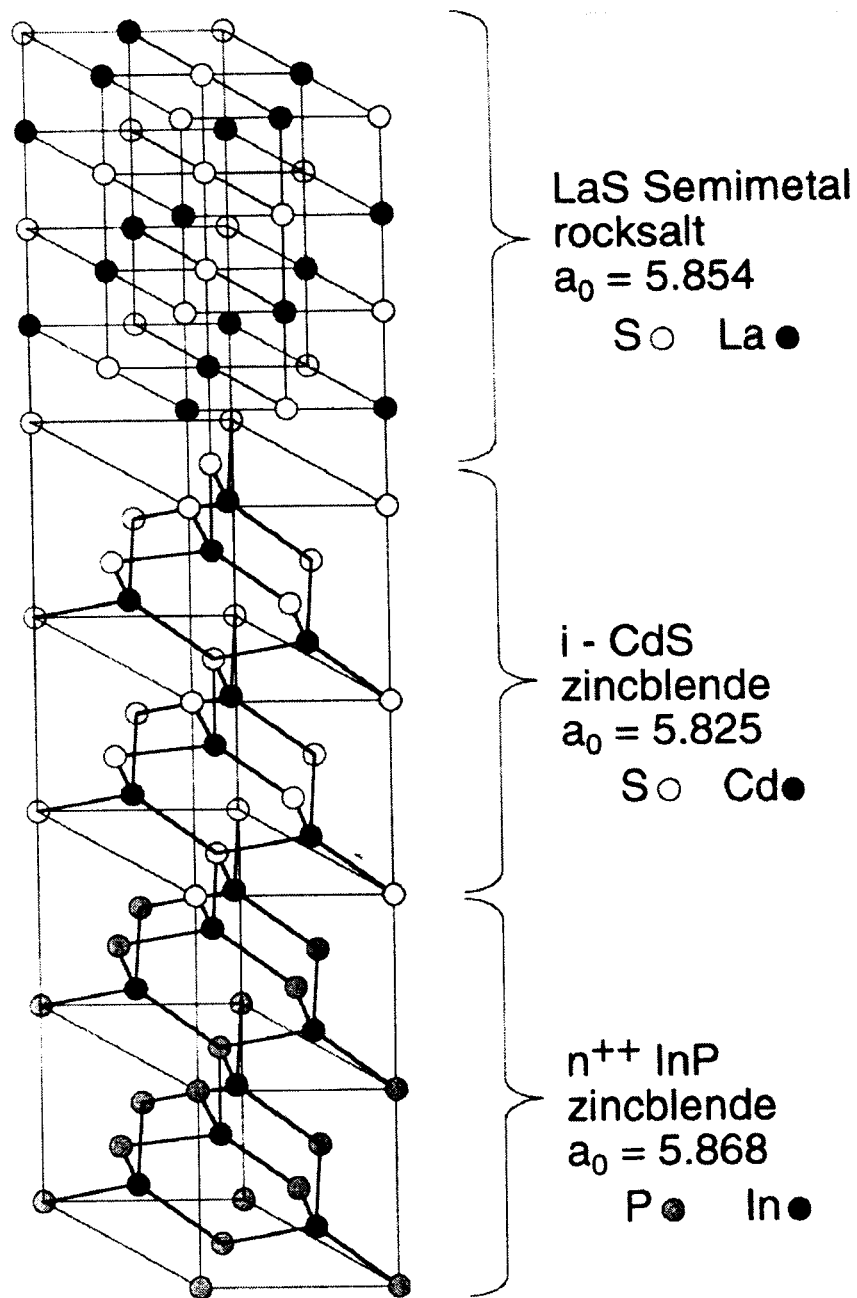


Figure 3: Schematic Showing the Nearly Perfect Lattice Matching Between the InP, CdS and LaS Layers

To facilitate electron emission into vacuum, an array of gold (Au) fingers is defined on the surface of the LaS thin film to bias the structure. There are openings in the grid structure to expose the semimetallic thin film which forms the active emission area of the cold cathode. The bias is applied between the InP substrate and the Au metal grid with emission occurring from the exposed LaS surface. If the applied voltage is equal to or larger than the semiconductor bandgap energy while the quotient of applied voltage over semiconductor thickness approaches  $0.1 \text{ eV/\AA}$ , then electrons tunnel into the conduction band and ascend during their travel across the semiconductor film to levels of increasing energy. Figure 4 shows the conduction band profile throughout the cold cathode emitter. The injection of electrons into vacuum at the CdS/LaS interface is effective as long as the semimetallic film is very thin and has a work function low enough so that its vacuum edge is located energetically below the conduction band edge of the semiconductor.

#### 1.4.1 Earlier Work

Previous to this contract, Mumford and Cahay performed a theoretical study the dynamic work function shift and current crowding effects in the LaS thin film due to the capture of electrons [4, 5]. Under forward bias operation, electrons captured in the low work function material cause an effective reduction in the semimetallic film work function with an accompanying substantial increase of the emission current. The dynamical work function shift of the LaS increases with an increase in injected current [4]. It is sensitive to the quality of the interface between the two-dimensional semimetallic layer and the three-dimensional contacts. The LaS work function shift can approach the LaS work function even for the case of a leaky interface between the thin semimetallic layer and the three-dimensional contact regions. The dynamic shift is found to be comparable to the work function of LaS for a smaller value of the applied bias in the case of silver (Ag) contact compared to Au contacts, because of the lower barrier at the Ag/CdS interface (barrier height is 0.78 and 0.56 eV for Au and Ag contacts, respectively). Mumford and Cahay also calculated the lateral potential drop across the emission window of a cold cathode with rectangular geometry. They described its current crowding effects on the emitted current density profile [5]. They found that larger current densities can be reached by reducing the emitter window width and that current crowding effects can be neglected in emitter windows with width less than  $100 \mu\text{m}$  if the emitted current density is kept under  $10 \text{ A/cm}^2$ .

Mumford and Cahay's analysis also determined the expected magnitude of space-charge effects in the cathode to anode gap region by using an ensemble Monte Carlo description of electron transport [6]. Assuming ballistic transport across the CdS and LaS layers, they modeled the transport of electrons between the LaS surface and the anode contact taking into account the energy distribution of carriers due to Fowler-Nordheim injection in the active portion of the cold cathode. The effects of space charge were studied for the cases where the CdS layer was 300 or  $75 \text{ \AA}$  CdS thick while the cathode to anode gap was  $15 \mu\text{m}$  for both. For the  $75 \text{ \AA}$  CdS layer case, there were drastic variations in the electrostatic potential within the air gap. At high injection current density, space-charge effects led to current self-quenching, and the anode current is much smaller than the Fowler-Nordheim injected current. The limiting value of the measured average anode current density was found to be much larger than the Child-Langmuir limit [9, 10].

One of the goals of this contracted effort was to refine the modeling efforts on the InP/CdS/LaS cathode by focusing on self-heating effects due to the finite conductivity of the substrate. We also wanted to study in more detail the interplay of current crowding and current self-quenching effects on the lateral distribution of the current density emitted into vacuum.

#### 1.4.2. Incentive for Further Theoretical Study

The earlier treatments described above neglected self-heating effects in the cold cathode of Figure 2 due to the finite conductivity of the substrate. Self-heating effects are very important for this cathode due to the temperature dependence of the LaS work function ( $\phi_{LaS}$ ), which increases at a rate of  $2 \text{ meV/K}^2$ . The NEA of undoped CdS with LaS is about 60 meV (since half the bandgap of CdS = 1.21 eV and  $\phi_{LaS} = 1.14 \text{ eV}$  at room temperature). So, for a 30

<sup>2</sup>The room temperature work function for LaS and NdS was calculated by extrapolating from values measured at high temperatures by Fomenko [8]

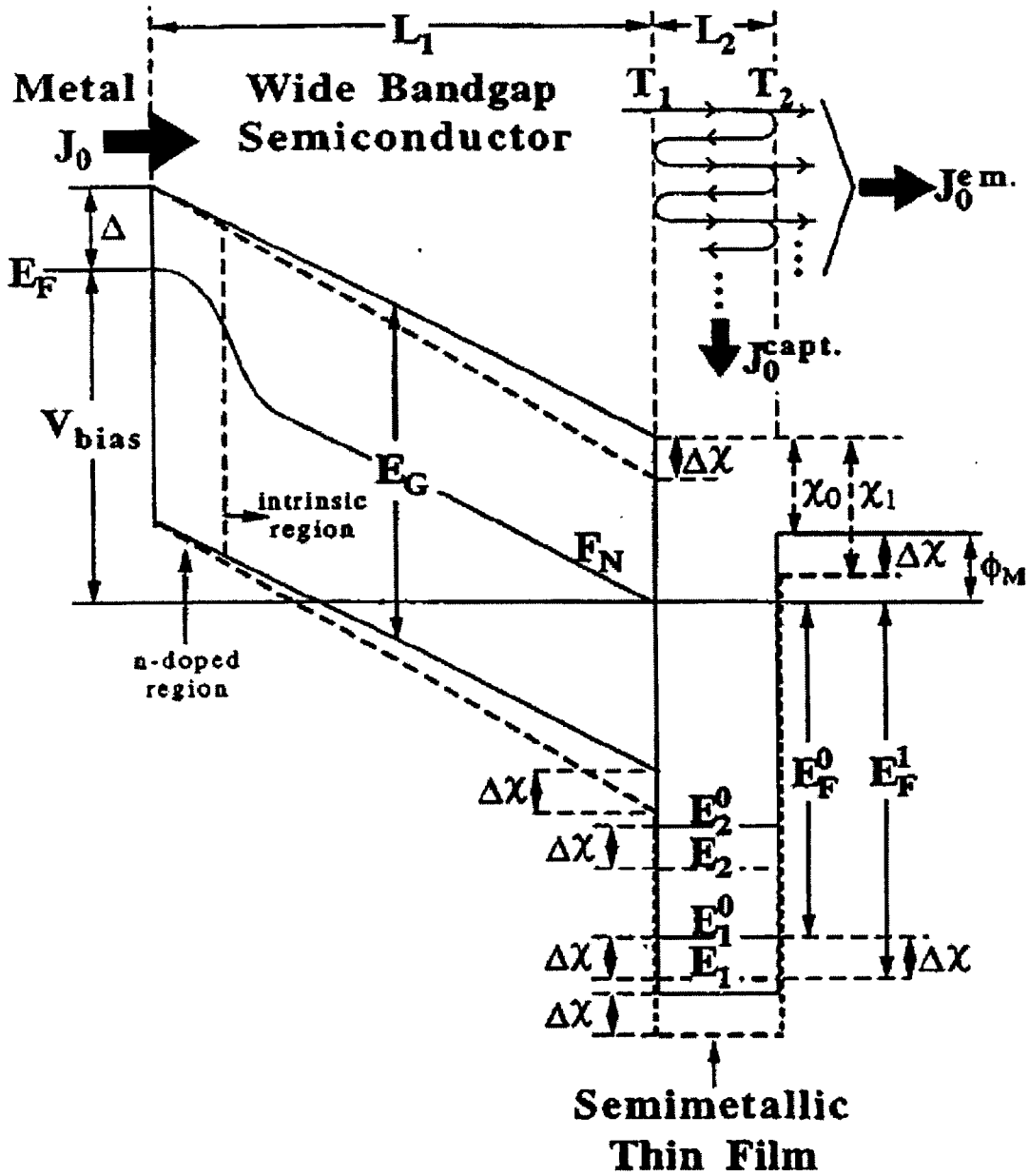


Figure 4: Schematic Representation of Conduction Band Profile Throughout the Metal (or  $n^{++}$ -InP)/CdS/LaS Cold Cathode Emitter Shown in Figure 2.

K increase in temperature above room temperature, NEA would be lost and the emission current drastically reduced. Therefore, the cathode must be designed and operated so that self-heating effects will not raise the temperature of the device above 330 K. In section 2, we analyze the importance of self-heating effects in a InP/CdS/LaS cold cathode. We identify the mechanisms leading to power dissipation in the cathode with an emission window of rectangular geometry, including the effects of inelastic scattering in the CdS and LaS layers, which are modeled using a temperature dependent mean-free path approach. The analysis includes the effects of current crowding in the emission window due to the finite resistivity of the LaS layer. The cathode parameters that minimize current crowding and self-heating effects in the cathode are determined.

As discussed earlier, Mumford and Cahay have shown that an important feature of electron transport through the cathode to anode gap is that electrons are injected into the gap with a velocity much in excess of the velocity of electrons emitted from thermionic cathodes [5]. The resulting high current density in the vacuum region causes space-charge effects that lead to current self-quenching and the anode conduction current is therefore much smaller than the Fowler-Nordheim injected current [6]. Also, the limiting value of the average anode current density is much larger than the Child-Langmuir limit when a zero electron velocity was assumed. The current modulation due to the electrostatic potential hump in front of the cathode is sometimes accompanied by high frequency (several tens of GHz) fluctuation in the minimum of the electrostatic potential in the air gap [6]. These oscillations lead to large oscillations in the anode current. The modulation of the beam current is quite substantial, leading to an energy spread at the anode with a full width at half maximum of only a few  $k_B T$ . This is important for practical applications such as flat panel displays or traveling wave tubes which require electron beams that are as monoenergetic as possible [1]. To understand better the importance of the average energy and energy spread of the beam injected into vacuum, we refined our Ensemble Monte Carlo analysis code to study the regime of inelastic scattering in the CdS layer for a metal/CdS/LaS structure and the regime of ballistic transport in CdS for a  $n^{++}$ InP/CdS/LaS structure, the results of which are described in section 3. We have compared our self-quenched anode current density to an analytical treatment of the current self-quenching regime based on a hydrodynamic description of electron transport derived by Kolinsky and Schamel [11, 12].

Due to the finite conductivity of the semimetallic thin film, the captured electrons flow toward the emitter contacts, leading to DC current crowding, as originally investigated by Mumford and Cahay [5]. For a cold cathode with a rectangular emission window, DC current crowding leads to emitted current which decreases symmetrically and monotonically from the edges of the emission window towards the center [5]. If emission current is large enough, space-charge effects may become appreciable in the vacuum region between semimetallic thin film and anode. This leads to current self-quenching effects where the potential energy hump in front of the cathode reflects part of the emitted electron beam toward the cathode. The part of the beam reflected as the result of space-charge will increase the amount of charge collected by the semimetallic thin film, hence influencing the amount of current crowding. This can lead to a non monotonic lateral distribution of the anode current density, depending on the width of the emission window. This interplay between DC current crowding and self-quenching effects is described in section 4.

## 1.5 Experimental Program

Over the last few years, Dr. Cahay and Dr. Boolchand have received funding from the Air Force and the National Science Foundation to initiate an experimental program on the use of rare-earth monosulfides as potential candidates to reach NEA using various III-V and II-VI semiconductor surfaces [9, 10]. First, to build the cold cathode device shown in Figure 2, a high purity cubic LaS must be grown in bulk form and its work function measured. Then, thin films of LaS need to be RF sputtered onto an InP/CdS substrate. H. Tang, a former student of Dr. Boolchand, has successfully demonstrated a way of growing bulk LaS samples [13]. He has also successfully grown CdS thin films on InP substrates by RF magnetron sputtering. A Ph.D. student, Y. Modukuru, has developed new methods of growing the LaS bulk material using an arc melting process and a high temperature vacuum furnace from Thermal Technologies, Inc. (Santa Rosa, CA). LaS bulk samples have been characterized by X-ray diffraction and Raman spectroscopy. Enough bulk LaS was processed to make a 2-inch diameter target about 1/8-inch thick to be used in RF magnetron sputtering experiments. In this work, we tuned the critical parameters (Argon pressure, RF power, substrate temperature, and source to target separation) which control the LaS thin-film deposition on various

substrates. To the best of our knowledge, this work is the first to report the successful growth of thin film LaS with a cubic phase on silicon (Si) and InP substrates. The thin films were characterized by XRD, Raman spectroscopy, and XPS. Our experimental work has set the stage for the complete growth of the InP/CdS/LaS cold cathode shown in Figure 2.

## 2. A Theoretical Analysis of Self-Heating Effects in an InP/CdS/LaS Cold Cathode

### 2.1 Introduction

In this Section, we extend the work of Mumford and Cahay [4] to theoretically analyze the expected self-heating effects in an InP/CdS/LaS cold cathode. The mechanisms responsible for power dissipation in a cathode with an emission window of rectangular geometry are identified. These include the effect of inelastic scattering in the CdS and LaS layers. This is modeled using a temperature-dependent mean-free path approach. The analysis includes the effect of current crowding in the emission window due to the finite resistivity of the LaS layer. We determine the cathode parameters which minimize the current crowding and self-heating effects in the cathode. The relative contribution of the ballistic and inelastic portions of the electron current emitted into vacuum is also calculated.

#### 2.1 Fowler-Nordheim Emission

The tunneling of electrons from the  $n^{++}$  InP into CdS is modeled as Fowler-Nordheim (FN) tunneling, which has a current density,  $J_0$ , given as follows [14]

$$J_0 = F J_{FN}, \quad (1)$$

where

$$J_{FN} = C_1 (E^2 / \Delta) e^{-C_2 \Delta^{3/2} / E}. \quad (2)$$

Here  $C_1$  and  $C_2$  are fitting parameters dependent on the semiconductor used (CdS in this case),  $F$  is the Murphy-Good function [14] given as:

$$F = \frac{\pi \beta k_B T}{\sin(\pi \beta k_B T)}, \quad (3)$$

where  $\beta$  is given as:

$$\beta = \frac{2\sqrt{2m\Delta}}{E q \hbar}. \quad (4)$$

Here  $\Delta$  is the barrier height at the InP/CdS junction,  $E$  is the value of the electric field in the CdS,  $m$  and  $q$  are the electron mass and charge,  $k_B$  is the Boltzmann's constant, and  $T$  is the temperature of the cathode. As shown by Good and Muller [14], Equation (1) is valid only if the following condition for  $\beta$  is satisfied:

$$\beta < \frac{1}{k_B T} - \frac{1}{\Delta}. \quad (5)$$

If this last relation is not fulfilled, thermionic emission dominates current injection across the interface. Since  $\beta$  is inversely proportional to the electric field, Equation (1) is valid only above some threshold voltage.

The self-heating effect is very important for this cathode since the LaS work function ( $\phi_{LaS}$ ) increases with temperature at a rate of 2 meV/K [8]. The NEA of undoped CdS with LaS is about - 60 meV at room temperature. For an increase in temperature of 30 K, the NEA is eliminated and the emission current is drastically reduced. Therefore, we must design and operate the cathode so that the self-heating effect will not raise the device temperature above 330 K. Since the tail of the energy distribution of electrons injected from the InP substrate extends only a few  $k_B T$  above the Fermi level while the InP/CdS barrier height,  $\Delta$ , is  $\sim 0.2$  eV [15], we expect thermionic emission from the InP layer will not be effective if the device temperature is below 330 K<sup>3, 4</sup>.

<sup>3</sup>There are conflicting reports of the electron affinity value for CdS. It is known to vary with surface orientation and material phase. Here, we use the value of 4.2 eV reported by Madelung. [16]

<sup>4</sup>For the case of a InP/CdS interface, there are no reports of the value of conduction band discontinuity,  $\Delta E_c$ , between the two materials, to the best of our knowledge. We, therefore, assumed that  $\Delta E_c$  is given by Anderson's rule, as follows  $\Delta E_c = |\chi(InP) - \chi(CdS)|$ . Here,  $\chi$  is the electron affinity of CdS (4.2 eV) and InP (4.4 eV), so  $\Delta E_c = 0.2$  eV.

In that case, Equation (1) can be applied to include the temperature dependence of the FN tunneling current. Since the cathode will be designed to work at a temperature below 330 K, we neglect in our model the temperature dependence of other physical parameters, such as effective mass and bandgap of the different materials. Since the bandgap of InP and CdS both shrink with temperature, we assume that this will not affect the barrier height,  $\Delta$ , at the interface over the limited range of temperature (300-330 K) considered here.

Equation (2) gives the temperature dependence of the current density emitted from a metal surface into vacuum when the barrier at the metal/vacuum interface can be approximated as having a triangular shape. Equation (1) for  $J_{FN}$  is actually well suited for field emission from metals at low temperature. As discussed by Jensen [17, 18], it is less satisfactory for field emission from semiconductors because the original FN derivation does not correctly include the energy distribution in the semiconductor. In a semiconductor, the energy distribution can be quite close to the maximum of the potential barrier, especially at high fields and when the image force potential is included. In our case, the situation is even more complicated since the field emission is not into vacuum but into an undoped CdS layer. Rather than trying to rederive an exact FN expression for that case which includes all the refinements discussed above, we adopt Equation (1) as a suitable fit to the actual FN tunneling current. As mentioned previously,  $C_1$  and  $C_2$  are fitting parameters we have introduced in the FN equation. Since no experimental results are available for the proposed structure, we choose some ad hoc values for  $C_1$  and  $C_2$  with the correct order of magnitude ( $C_1 = 1.5 \text{ times } 10^{-6} \text{ A/V}$  and  $C_2 = 6.9 \text{ times } 10^7 (V^{1/2} \text{ cm})^{-1}$ ). The parameter  $\beta$  in Equation (4) will be estimated while using the mass of the tunneling electron, i.e.  $m = 0.1 m_0$  for electrons in the  $\Gamma$  valley of the CdS layer, where  $m_0$  is the free electron mass.

### 2.3 Inelastic scattering in CdS and LaS layers

We model the effects of inelastic scattering in CdS and LaS layers using a mean free path concept. The electrons traversing the CdS layer without suffering any collision are called ballistic electrons. In the CdS layer, we can estimate the fraction of non ballistic electrons by introducing a mean-free path for inelastic collisions  $\lambda_{CdS}$ . With this definition, the ballistic component of current at a location  $z$  in the CdS layer is given by

$$J_z^b = J_0 e^{-z/\lambda_{CdS}}, \quad (6)$$

where  $J_0$  is given by Equation (1). The mean-free path  $\lambda_{CdS}$  of electrons in CdS is assumed to be independent of the applied bias across the CdS layer. The point  $z = 0$  corresponds to the InP/CdS interface. Under steady-state conditions and in the absence of recombination processes, the total current at any point  $z$  must be conserved. The inelastic component of the current, therefore, is given as

$$J_z^{in} = J_0 (1 - e^{-z/\lambda_{CdS}}). \quad (7)$$

Inelastic scattering in CdS results in power dissipation in this layer, which is calculated in detail in Section 2.5. The temperature dependence of the mean-free path is approximated as [19]

$$\lambda(T)/\lambda(300K) = 300/T, \quad (8)$$

where  $T$  is the operating temperature (in Kelvin) of the cathode.

The ballistic and inelastic portions of the beam will hit the CdS/LaS interface at two different energy levels. The ballistic beam will have an energy roughly equal to the Fermi level in the InP contact because the energy distribution of the FN injected beam is fairly narrow. To find the average energy of the inelastic portion, a sophisticated model for the carrier transport in the CdS should be developed. Instead we assume that the average energy of the inelastic beam is halfway between the Fermi level in the InP layer and the bottom of the conduction band in the CdS layer at the CdS/LaS interface.

Because of the finite probabilities for the injected current to be transmitted across the CdS/LaS and LaS/vacuum interfaces (see Figure 4), the contributions to the total emitted current must be calculated as the sum of the contributions resulting from the multiple reflections of electrons in the LaS layer. The total emitted current will have two



components originating from the ballistic and inelastic currents reaching the CdS/LaS interface. Taking into account the multiple reflections in the LaS layer, the fraction of the ballistic beam escaping into vacuum is given by

$$J_{em}^b = J^b(L_1)T_1(E_{av})x[T_2(E_{av} - \hbar\omega_o) + (1 - T_1(E_{av} - 2\hbar\omega_o)) \\ (1 - T_2(E_{av} - \hbar\omega_o))T_2(E_{av} - 3\hbar\omega_o)x^2 + (1 - T_1(E_{av} - 2\hbar\omega_o)) \\ (1 - T_1(E_{av} - 4\hbar\omega_o))(1 - T_2(E_{av} - \hbar\omega_o))(1 - T_2(E_{av} - 3\hbar\omega_o)) \\ T_2(E_{av} - 5\hbar\omega_o)x^4 + \dots], \quad (9)$$

where  $T_1$  and  $T_2$  are the transmission coefficients at the CdS/LaS and LaS/vacuum interfaces. Their energy dependence can be calculated using a step potential model [20] for the CdS/LaS and LaS/vacuum while including the difference in effective masses across the interface.

In Equation (9),  $x = e^{-L_2/\lambda_{LaS}}$  ( $< 1$ ) and takes into account the attenuation of the current as a result of inelastic scattering in the LaS quantum well and (assumed) subsequent trapping of the electrons by the quantum well;  $\lambda_{LaS}$  is the collisional mean-free path in the semimetallic layer, and  $L_2$  is the thickness of the semimetallic layer. Furthermore,  $E_{av}$  is the average energy of the ballistic beam while crossing the CdS/LaS for the first time. It is approximated as the energy difference between the Fermi energy level in the InP substrate and the bottom of the conduction band in LaS. Also,  $\hbar\omega_o$  is the energy of the transverse optical phonon mode in LaS. This mode is assumed to be the leading inelastic scattering mechanism in the LaS quantum well. In writing Equation (9), we assumed that only one optical phonon is lost at each crossing of the LaS thin film. Note that the progressive terms in Equation (9) contributing to  $J_{em}^b$  decrease in amplitude due to the increasing number of terms in the  $x$  factor as electrons suffer multiple reflections in the LaS quantum well.

An expression similar to Equation (9) can be written for the fraction of the emitted current into vacuum due to the inelastic portion of the emission current arriving at the CdS/LaS interface. This is achieved by substituting  $J^b(L_1)$  with  $J^{in}(L_1)$  and making  $E_{av}$  the average energy of electrons reaching the CdS/LaS interface after suffering inelastic scattering in the CdS layer. For simplicity, this  $E_{av}$  is approximated as half the energy difference between the Fermi level in the InP substrate and the bottom of the conduction band in the CdS at the CdS/LaS interface.

## 2.4 Current Crowding Effects

As discussed in Section 1, some fraction of the FN current crossing the CdS layer is captured by the LaS thin film. This captured current density  $J_{capt}$  can be obtained as the difference between the FN current density and the emitted current density calculated in Section 2.3. Because of the finite resistivity of the LaS thin film, there is a possibility for current crowding between any two fingers in the extraction grid configuration of the cold cathode (see Figure 2). This current crowding is accompanied by a lateral electric potential variation across the LaS emission window. The electric potential relative to the substrate,  $V(x)$ , is a function of the lateral position,  $x$ , along the window, where  $x = 0$  is at the center of the window. This potential is given by

$$V(x) = V_{bias} - \int_x^a i(\xi) \frac{\rho_S}{L_2} d\xi. \quad (10)$$

Here,  $\rho_S$  and  $L_2$  are the resistivity and thickness of the LaS layer and  $V_{bias}$  is the voltage applied across the emitter fingers and the back of the substrate;  $i(\xi)$  is the current per unit width flowing laterally in the LaS to the right of position  $x$  and is given by

$$i(\xi) = \int_0^\xi J_{capt}(x) dx. \quad (11)$$

Previously [4], Mumford and Cahay have shown that the captured current density can be well approximated by the following analytical expression

$$J_{capt}(x) = J_{0,c} e^{\alpha_c V(x)}, \quad (12)$$

where  $J_{0,c}$  and  $\alpha_c$  are fitting parameters. This allows us to derive the following differential equation for the lateral

variation of the electric potential in the LaS thin film:

$$\frac{d^2V}{dx^2} = \frac{\rho_S}{L_2} J_{0,c} e^{\alpha_c V(x)}. \quad (13)$$

This equation must be solved subject to the following boundary conditions

$$V(x=a) = V_{bias}, \quad (14)$$

and

$$\frac{dV}{dx} = 0, \quad (15)$$

at  $x=0$  as required by symmetry. The solution to the differential equation is

$$V(x) = V_{bias} - (2/\alpha_c) \ln\left(\frac{\cos(x/\Lambda)}{\cos(a/\Lambda)}\right), \quad (16)$$

where  $\Lambda$  is a specified constant whose value is determined below. This solution can be proven by substituting Equation (16) for  $V(x)$  on both sides of Equation (13). It can be shown that the resulting equation is true only if  $\Lambda$  is solution of the following transcendental equation:

$$z^2 \sec^2 z = \frac{\beta^2 a^2}{2}, \quad (17)$$

where  $z = a/\Lambda$  and

$$\beta^2 = \frac{\rho_S \alpha_c}{L_2} J_{capt}(a). \quad (18)$$

Thus,  $\Lambda$  is determined by Equations (17) and (18). Since Equation (16) also solves the boundary condition Equations (14) and (15), it is a complete solution. From Equations (12) and (16), we find the captured current density to be

$$J_{capt}(x) = J_{capt}(a) \frac{\cos^2 z}{\cos^2(x/\Lambda)}. \quad (19)$$

The ratio  $J_{capt}(0)/J_{capt}(a)$  is an important value characterizing the amount of current crowding. Since,

$$J_{capt}(0)/J_{capt}(a) = \cos^2 z, \quad (20)$$

the closer the value of  $z$  is to zero, the less prominent is the effect of current crowding in a given structure. In the numerical simulations, we chose to keep  $z$  under 0.3 to minimize the effect of current crowding. For  $z = 0.3$ ,  $J_{capt}(0)/J_{capt}(a) = 0.91$ , and for larger  $z$  the effect of current crowding becomes too important and the emission current density is not uniform over the window. To minimize the effect of current crowding in a given cathode, it should be designed in such a way that  $z$  is lower than 0.3.

## 2.5 Power Dissipation

If we assume ballistic transport in CdS, there are four contributions to power dissipation in the cold cathode (see Figure 5): (1) the power  $P_1$  released when the electrons are captured in the LaS, (2) the power  $P_2$  due to Joule heating because of the lateral current flow in the LaS, (3) the power  $P_3$  dissipated when electron current moves from the LaS thin-film region to the wider LaS region to the top Au contacts, and (4) the power dissipation  $P_4$  due to the blocking effect of the wide Au fingers needed to dc bias the cold cathode. These power dissipation mechanisms in a metal/CdS/LaS cold cathode have been studied earlier by Mumford and Cahay [4]. Hereafter, we add the effect of inelastic scattering in the CdS layer, which amounts to an additional power  $P_5$  in the total power dissipation (see Figure 5).

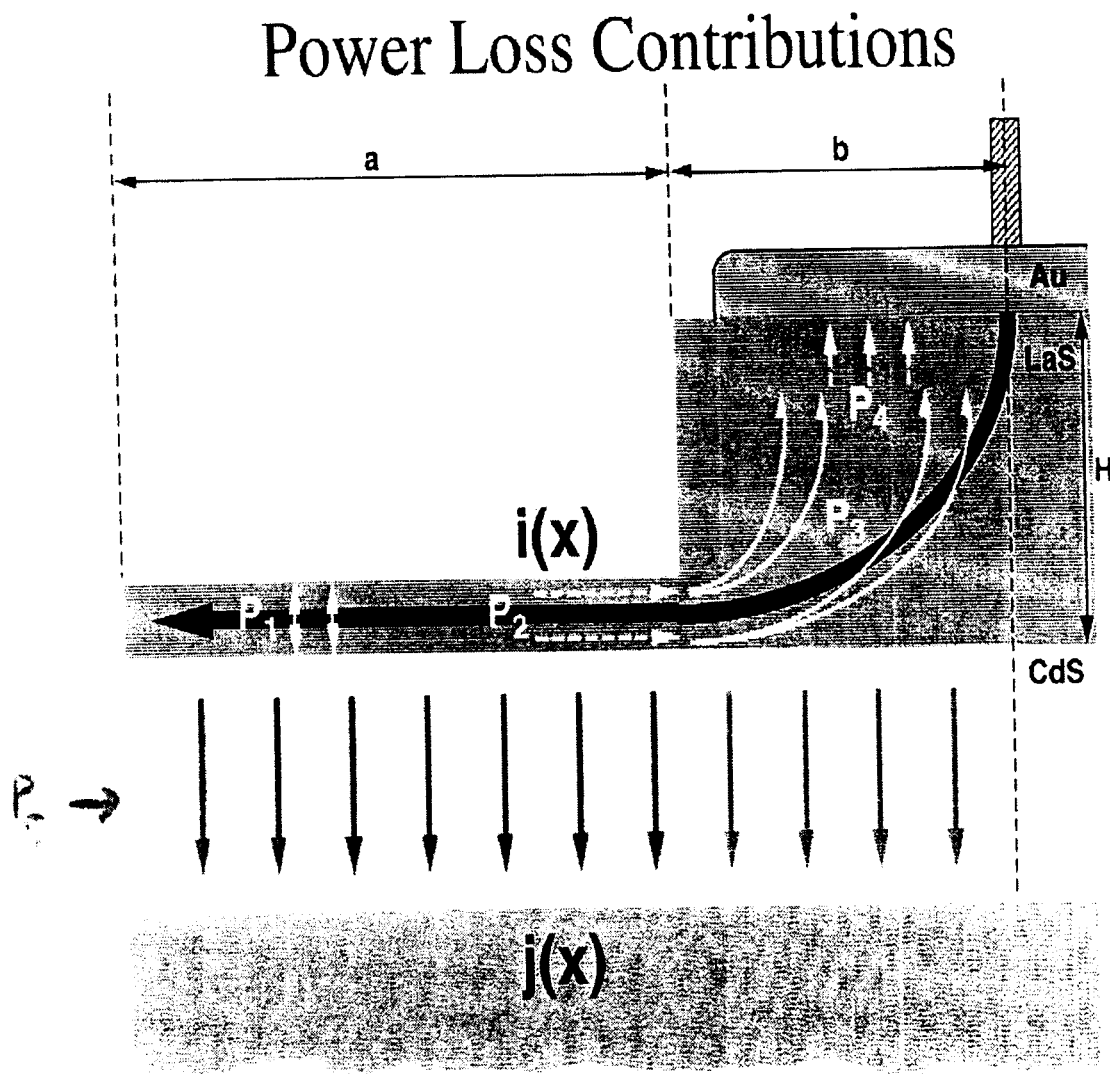


Figure 5: Schematic Showing the Various Power Dissipation Mechanisms in the Cold Cathode (see Section 2.5)

The power  $P_1$  released due to the trapping of electrons in LaS is given as [5]

$$P_1 = V_{bias} I \frac{\tan z}{z} \cos^2 z + \frac{2I}{\alpha_c} \left(1 - \frac{\tan z}{z}\right) \cos^2 z, \quad (21)$$

where  $I = 2aLJ_{capt}(a)$  is the total current captured when current crowding effects are negligible. The power dissipation  $P_2$  due to Joule heating as electrons move in LaS toward the contacts is given by [5]

$$P_2 = \frac{2I}{\alpha_c} \left(\frac{\tan z}{z} - 1\right) \cos^2 z. \quad (22)$$

The third contribution  $P_3$  is due to the excess carriers moving from the LaS to the top contact of Au fingers is given by [5]

$$P_3 = \frac{R_c}{2} I^2 \left(\frac{\sin z}{z}\right)^2 \cos^2 z, \quad (23)$$

where  $R_c$  is the resistance of LaS between the edge of the LaS thin film and the top Au layer and is estimated as [21]

$$R_c = \rho_{Au} \frac{H}{L_2 L} \frac{\ln k}{k-1}, \quad (24)$$

where  $k = H/L_2$  and  $H$  is the height of the thick Au region. The power dissipated in the thick portion of Au is given as [5]

$$P_4 = 2Lb J_0(V_{bias}) V_{bias}, \quad (25)$$

where  $b$  is the half-width of the emitter fingers. The fifth contribution to the total power dissipated comes from the inelastic scattering in the CdS. From Equation (7), at a location  $z$  the differential current density loss is given as

$$dJ_z = -\frac{1}{\lambda_{CdS}} J_0 e^{-\frac{z}{\lambda_{CdS}}} dz. \quad (26)$$

Here we make the simplifying assumption that only one scattering event takes place for each electron in the CdS layer. Then the electron kinetic energy released to the lattice within the range  $[z, z+dz]$  can be shown to be equal to

$$dE = p \left(\frac{z}{L_1}\right) V_{bias}, \quad (27)$$

where  $L_1$  is the width of the CdS layer and  $p$  is given by

$$p = 1 + \frac{\Delta}{V_{bias}} - \left(\frac{1}{2} \frac{E_G}{V_{bias}} - \frac{\Delta\chi}{V_{bias}}\right), \quad (28)$$

where  $E_G$  is the energy gap of CdS and  $\Delta\chi$  is the dynamic work function shift due to the trapping of electrons in the LaS. From the above equations, the power dissipated in the CdS layer due to inelastic scattering is found to be

$$P_5 = 2p(a+b)LJ_0V_{bias}\left(1 - \left(1 + \frac{L_1}{\lambda_{CdS}}\right)e^{-L_1/\lambda_{CdS}}\right). \quad (29)$$

In deriving Equation (29) we neglected the variation of the electrostatic potential in the transverse direction. Since the potential across the CdS layer should actually be less in the middle of the emission window compared to its value at the edges as a result of current crowding, Equation (29) gives an upper estimate of the power  $P_5$ . Hence, it will lead to an upper estimate of the temperature rise in the cathode.

The total power dissipated is the sum of the five power expressions derived above, and the power efficiency can then be calculated as

$$\eta_P = \frac{P_{input} - P_{diss}}{P_{input}}, \quad (30)$$

where  $P_{input}$  is the power delivered by the battery used for biasing the cathode.

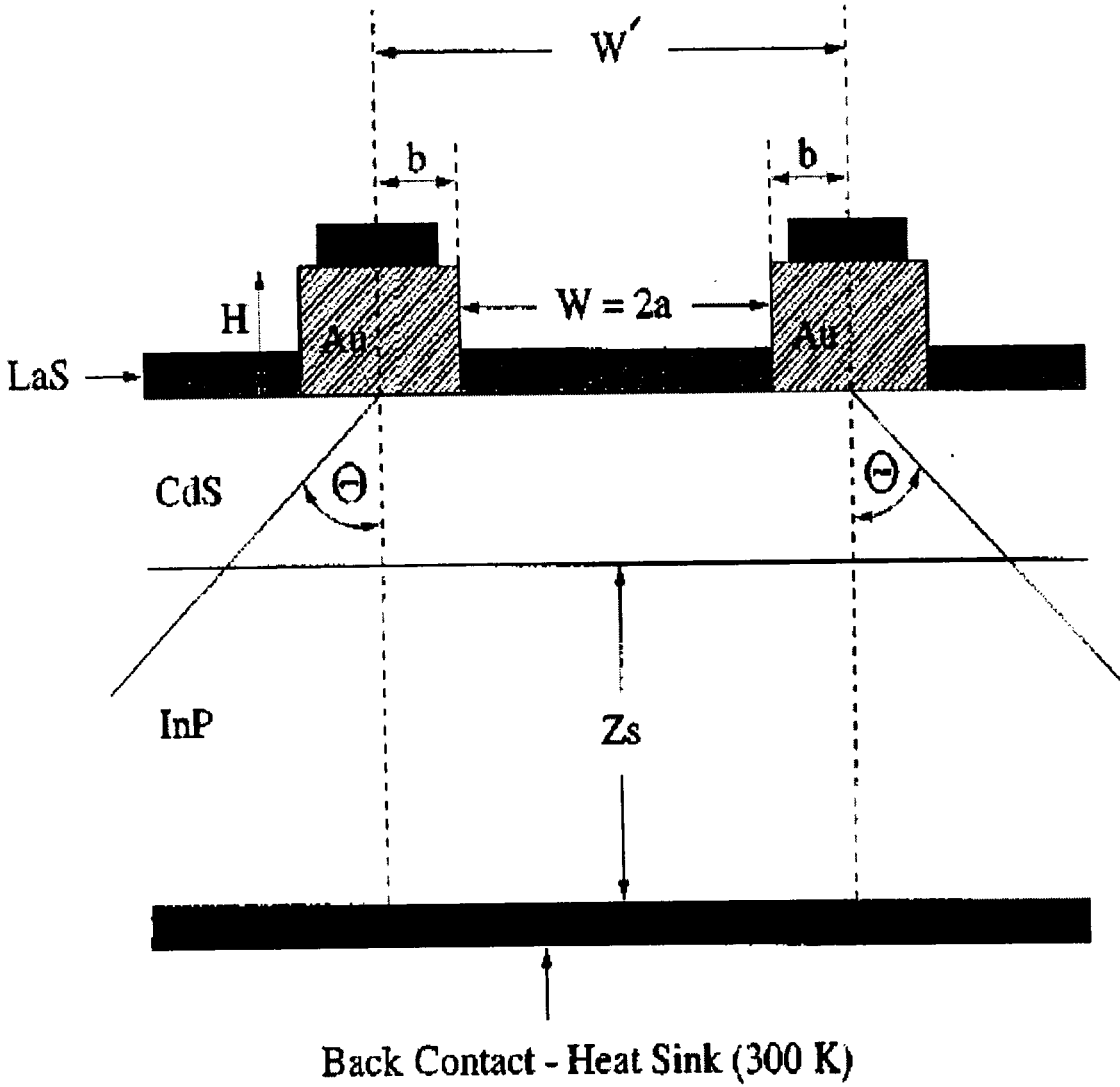


Figure 6: Thermal Model of Heat Dissipation Through the InP Substrate

## 2.6 Self-Heating Effects

We assume that the active area of the cathode, i.e., the CdS and LaS layers, are heat sources, and that the InP substrate is a perfect heat sink (held at room temperature). The total power dissipated in the active area is assumed to be removed by heat conduction through the InP substrate. As can be seen in Figure 6, the active area of the cathode (CdS and LaS layers) is assumed to be operating at a spatially constant temperature  $T$ . The thickness  $Z_s$  of the InP is much larger than indicated in the figure. The back of the substrate acts as a perfect heat sink at room temperature. Since the active portion of the cathode is much thinner than the InP substrate, it is necessary to consider the effect of heat spreading laterally in the substrate. Hereafter, we assume that the temperature of the CdS layer will be the same as the LaS top layer.

We model the thermal conductivity of the InP substrate as

$$\kappa(T) = \kappa_0(T/T_0)^{-b}, \quad (31)$$

where  $\kappa_0$  is the thermal conductivity at  $T_0$  (300K),  $\kappa_0 = 0.74 \text{ W/Kcm}$  is the room temperature thermal conductivity

of InP and  $b = 1.45$ . As shown in Figure 6, we assume that the heat is dissipated over an effective area

$$A(z) = (L + 2z \tan \Theta)(W' + 2z \tan \Theta), \quad (32)$$

where  $L$  and  $W'$  are the length and width ( $W' = 2(a+b)$ ) of the emission window, and  $\Theta$  is the heat spreading angle, which is taken to be equal to  $45^\circ$  for simplicity. Starting with Fick's law and making use of a Kirchoff transformation [22] to take into account the temperature dependence of the thermal conductivity of the InP substrate given by Equation (31) it can be shown that the active area of the cold cathode will be operating at a temperature given by

$$T - T_0 = R_{th} P_{diss}, \quad (33)$$

where  $R_{th}$  is the thermal resistance of the InP substrate and  $P_{diss}$  is the total power dissipated per emission window. By using Equations (31) and (33) and by applying the Kirchoff transformation [22], the cathode temperature is found to be

$$T = \left[ \frac{1}{T_0^{b-1}} - (b-1) \frac{R_{th,0} P_{diss}}{T_0^b} \right]^{\frac{-1}{(b-1)}}, \quad (34)$$

where  $T_0$  is the ambient temperature (300 K) and  $R_{th,0}$  is given by

$$R_{th,0} = \frac{1}{2\kappa_0 \tan \Theta (L - W')} \ln \left[ \left( \frac{W' + 2z_s \tan \Theta}{L + 2z_s \tan \Theta} \right) \frac{L}{W'} \right] \quad (35)$$

where  $Z_s$  is the InP substrate thickness.

The system of Equations (1) through (35) must be solved self-consistently. First, we assume room temperature operation of the cathode and calculate the FN emission current as a function of the applied bias. Over a limited range of bias, the captured current density is then approximated by the exponential fit in Equation (12) and Equation (17) is solved for the parameter  $z$  describing the effects of current crowding. Next, the five contributions to the power dissipated in the cathode are determined and an upgraded bias dependence of the temperature in the device is derived from Equation (33). This new bias dependence of the device temperature is used to recalculate the FN emitted current and the procedure is carried on until it converges.

## 2.7 Results

The device parameters for which simulations are done are given in Tables 2 and 3. The simulations are run for two different CdS thicknesses (150 and 300 Å) and for two different values of electron mean-free path in the CdS (300 and 500 Å).

**Table 2: Material Parameters of the Cold Cathode**

Material	InP	i-CdS	LaS
Lattice constant (Å)	5.8688	5.83	5.85
Work function (eV)	4.4	4.2	1.14
Bandgap (eV)	1.35	2.5	
# of free electrons ( $10^{22} \text{cm}^{-3}$ )	$n^{++}$	—	1.99
Electron mass ( $m_0$ )	0.08	0.14	1.0
Electron mobility ( $\text{cm}^2 \text{V}^{-1} \text{s}^{-1}$ )		400.0	
Thermal conductivity @ 300K (W/cmK)		0.05..1	0.17
Electrical resistivity (273K) ( $\mu\Omega \text{cm}$ )			25.0
Melting temperature (K)			2500

Figure 7 shows the temperature in the intrinsic portion of the cathode as a function of the applied bias across the CdS layer. In this figure,  $T_{max}$  is the maximum temperature at which the cold cathode can be operated without

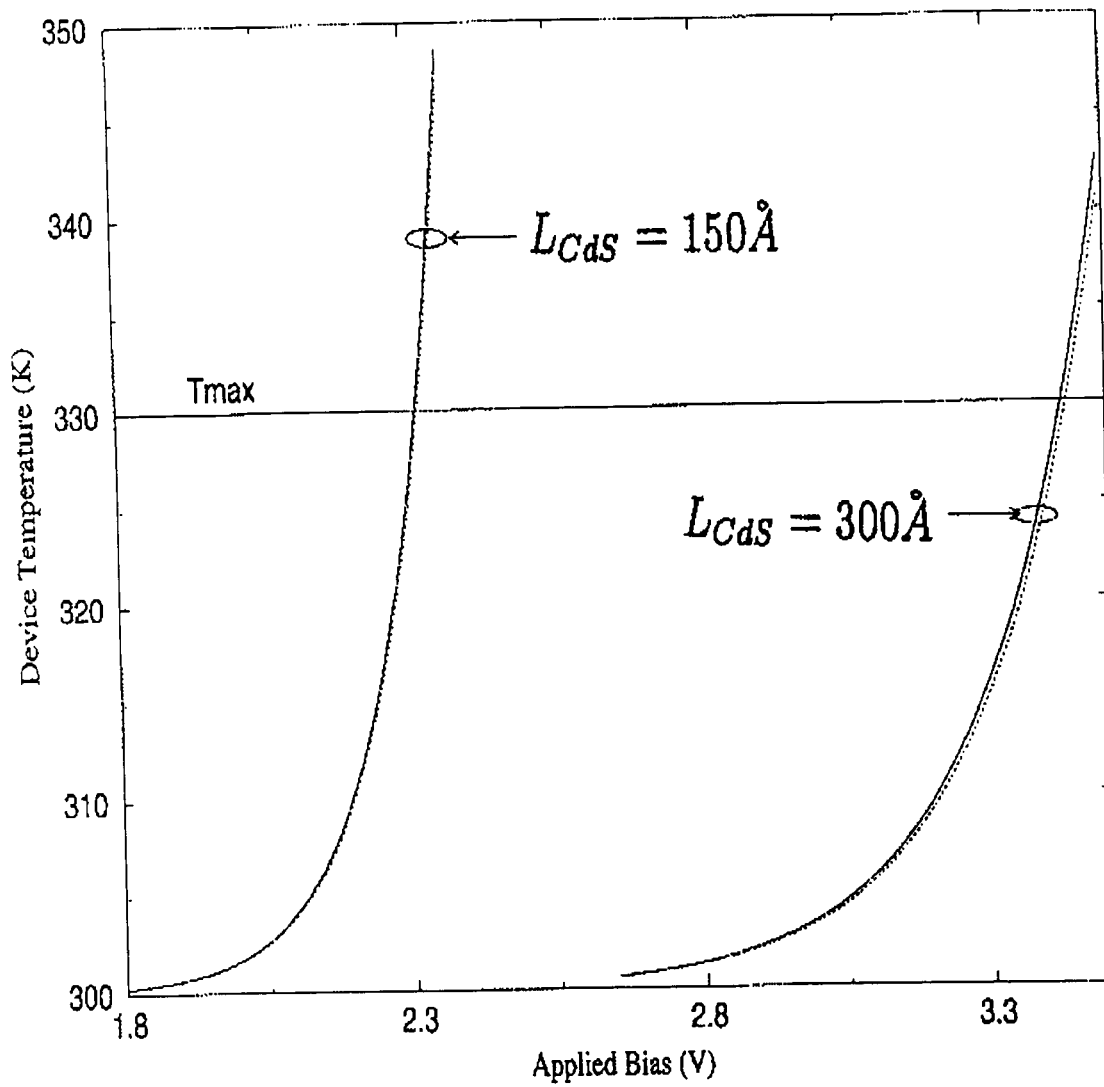


Figure 7: Temperature of the Active Portion of the Cathode

losing the benefit of NEA at the CdS/LaS interface. The curves on the left and right correspond to a CdS layer width equal to 150 and 300 Å, respectively. The full and dashed lines are the results obtained for  $\lambda_{CdS}$  equal to 300 and 500 Å, respectively. Only a few iterations in the numerical procedure described above are needed (5 or 6) to obtain the converged bias dependence of the cathode temperature displayed in Figure 7.

**Table 3: Physical Parameters of the Cold Cathode**

Thickness of CdS	150(300) Å
Emission window length	100 $\mu\text{m}$
Emission window width	20 $\mu\text{m}$
Thickness of LaS	24.6 Å
Thickness of Au fingers	5000 Å
Thickness of InP substrate	100 $\mu\text{m}$
Electron mean-free path in CdS	300(500) Å
Electron mean-free path in LaS	300 Å

For a cathode with a smaller CdS layer width, the temperature of the cathode rises at a lower applied bias since the FN injection current is larger at a smaller bias. For a fixed CdS layer width, the temperature of the cathode is larger at a given bias when  $\lambda_{CdS}$  is shorter. This results from the increased power dissipation in the CdS layer when  $\lambda_{CdS}$  is reduced from 500 to 300 Å. The horizontal line at 330 K is the temperature at which the LaS work function has increased to a point where NEA, due to the CdS/LaS combination, is lost. These results indicate that, to avoid self-heating effects in the cathode, the applied bias should be kept under 2.3 V or 3.4 V for a cathode with a CdS thickness of 150 or 300 Å, respectively. These biasing limits are not too sensitive to the value of  $\lambda_{CdS}$  because the power dissipation due to inelastic scattering in the CdS layer is not the leading self-heating mechanism, as discussed next.

Figure 8 shows the relative importance of the power dissipation mechanisms for the cold cathode with  $L_{CdS}$  equal to 150 or 300 Å (Contributions  $P_2$  and  $P_3$  are not shown because they are negligible. They coincide with the horizontal axis). Curves on the left and right correspond to a cathode with CdS thickness of 150 and 300 Å, respectively. Full and dashed lines correspond to an assumed CdS elastic mean-free path of 300 or 500 Å, respectively. It can be inferred from the figure that the power dissipation due to the shadowing effect of the biasing Au fingers,  $P_4$ , is the leading source of self-heating in the cathode, followed next in degree by power dissipation due to carrier trapping by the LaS thin film,  $P_1$ . Following this in degree is the power dissipation due to the inelastic scattering in the CdS layer,  $P_5$ . The two power dissipation mechanisms due to the lateral flow of carriers in the LaS thin film and due to the carrier flow from the LaS thin-film to the top contacts to the emitter biasing fingers are found to be negligible compared to the other terms. The curves representing the bias dependence of these two last contributions,  $P_2$  and  $P_3$ , coincide with the horizontal axis in Figure 8. For the cathodes analyzed here, our simulations indicate that the effect of current crowding will be more detrimental to the proper operation of the cathode than self-heating effects. Indeed, current crowding occurs at a lesser bias value than that at which the NEA advantage is lost as a result of self-heating effects.

Figure 9 shows the bias dependence of the parameter  $z$  for the two cathodes analyzed above. The curves on the left and right correspond to a cathode with CdS thickness equal to 150 or 300 Å, respectively. Full and dashed lines correspond to an assumed CdS elastic mean-free path equal to 300 or 500 Å, respectively. As discussed before,  $z = 0.3$  represents the threshold above which current crowding effects can no longer be neglected. The applied bias across the CdS layer should therefore be kept under  $V_1 = 2.02$  V and  $V_2 = 3.22$  V for a cathode with a CdS thickness equal to 150 or 300 Å, respectively.

Figure 10 shows the bias dependence of the ballistic and inelastic portions of the beam to be emitted into vacuum for the two cathodes with different CdS thickness. The curves on the left and right correspond to a cathode with CdS thickness equal to 150 or 300 Å, respectively. The full and dashed lines represent the results for  $\lambda_{CdS}$  equal to 300 or 500 Å. The fractions of the beam crossing the LaS quantum well into vacuum after reaching the CdS/LaS interface via ballistic or inelastic transport through the CdS layers, are labelled "ballistic" and "inelastic", respectively. For a cathode with  $L_{CdS} = 150$  Å, the ballistic fraction of the beam is close to 80 % at low bias and decreases at higher bias. This is a consequence of the self-heating effects in the cathode. According to Equation (8), the temperature rise in the cathode leads to a shorter mean-free path in the CdS layer. This causes the ballistic beam reaching the CdS/LaS interface to be diminished, according to Equation (6). For a CdS thickness of 300 Å, the



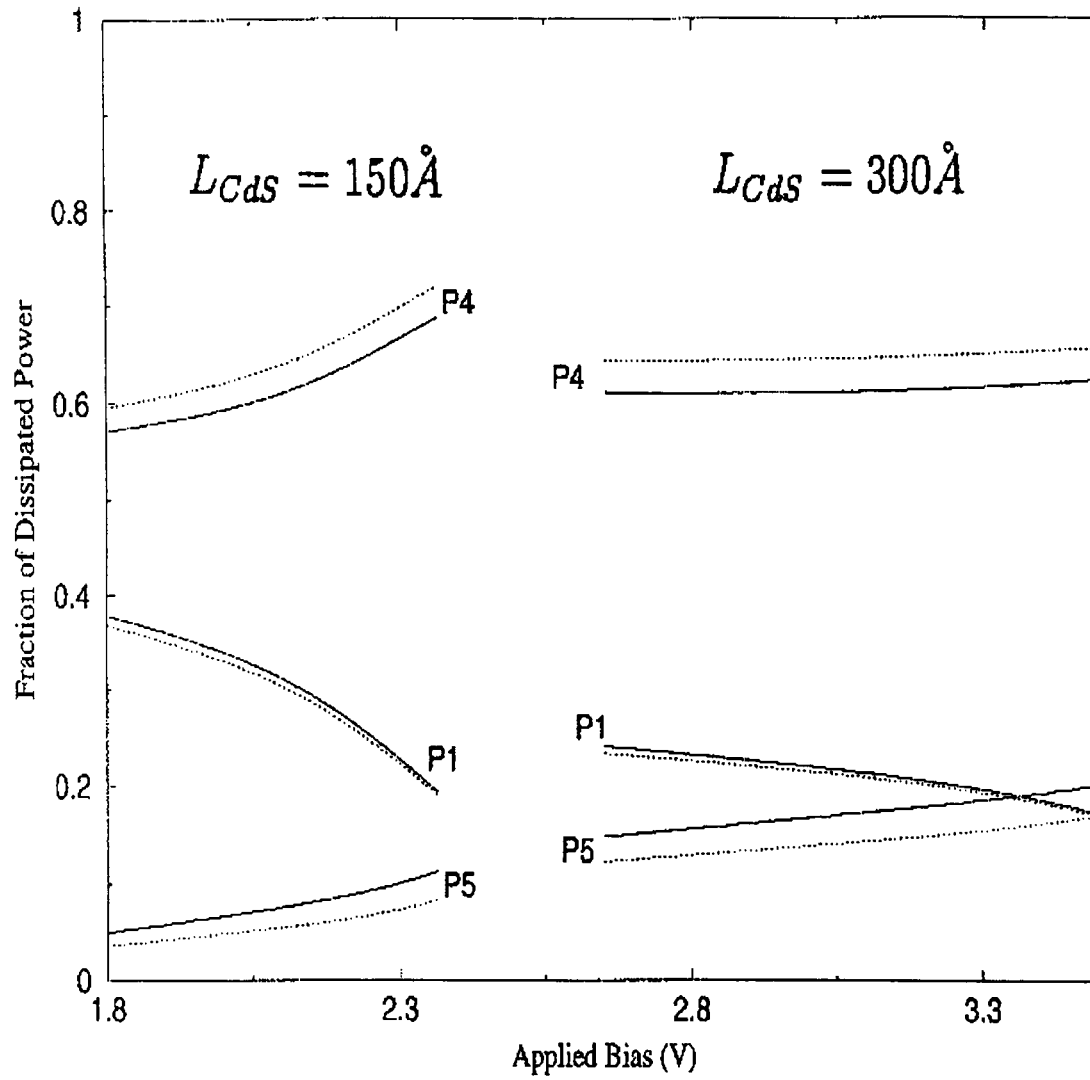


Figure 8: Bias Dependence of the Different Contributions to the Total Power Dissipated in the Cold Cathode

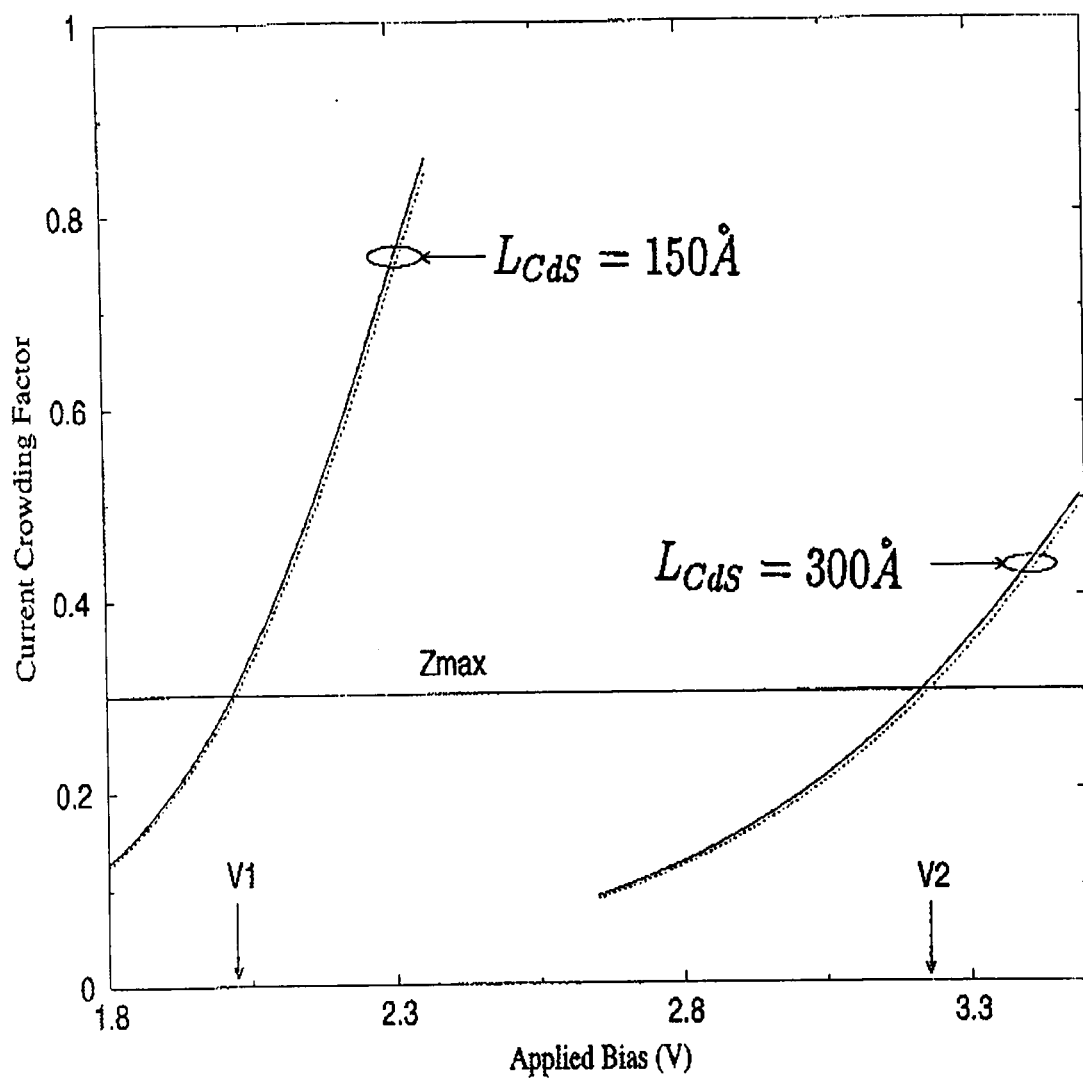


Figure 9: Bias dependence of the parameter  $z$  as a function of applied bias

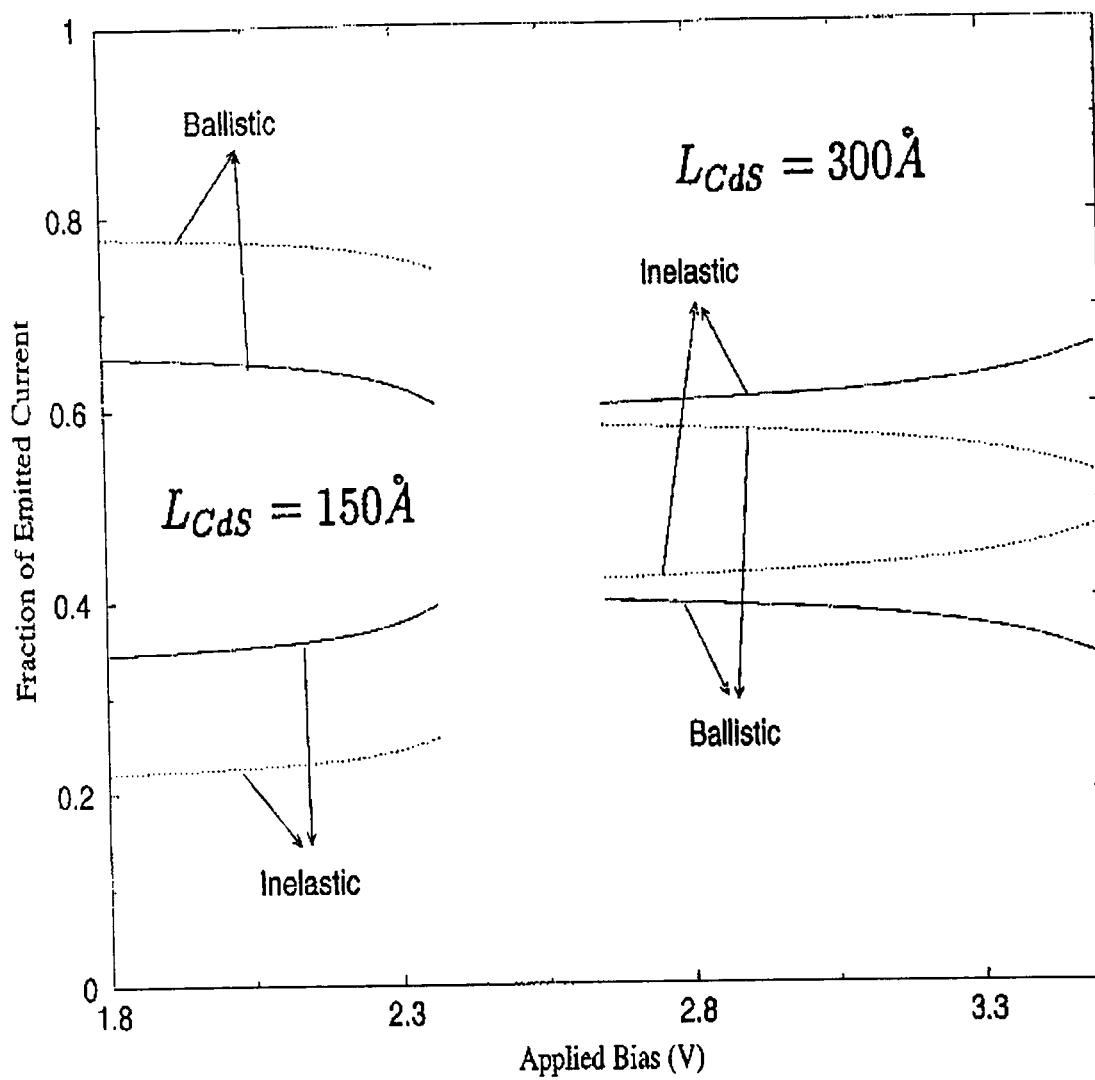


Figure 10: Bias Dependence of the Ballistic and Inelastic Components of the Emitted Current

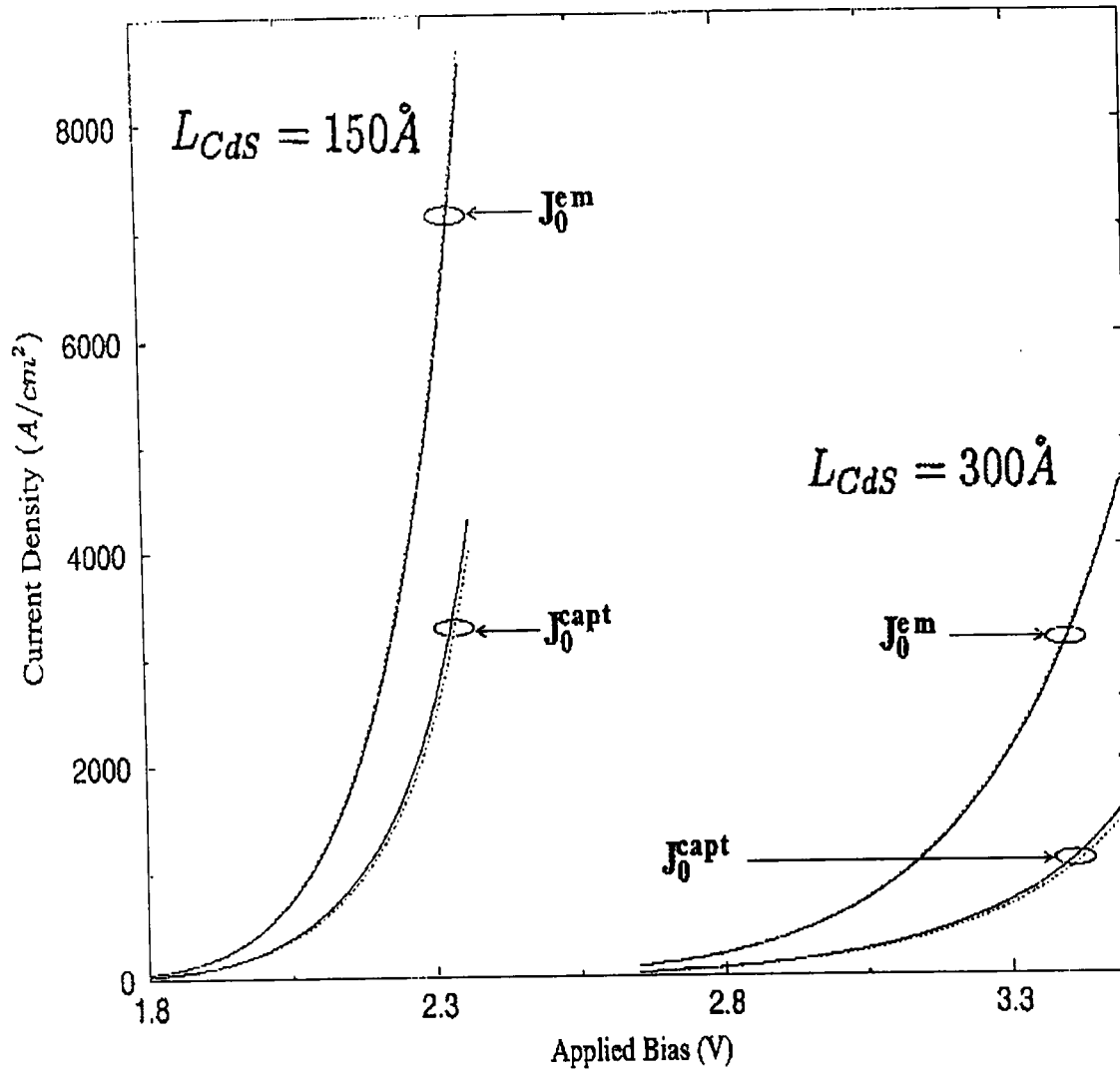


Figure 11: Bias Dependence of the Emitted and Captured Current

ballistic fraction of the beam is much less. In the right curves in Figure 10, the ballistic and inelastic fractions of the emitted current are nearly equal at a bias of 3.4 V for the  $\lambda_{CdS} = 500 \text{ Å}$  case. This is of practical importance if the cathode is to be used as a source, either for flat panel display or a microwave tube, since electron focusing is made easier for monoenergetic beams. Our theory predicts that the CdS thickness should be kept to  $\sim 150 \text{ Å}$  or below to enhance the ballistic component of the beam.

Figure 11 shows the emitted and captured current as a function of applied bias. The curves on left and right correspond to a cathode CdS thickness equal to 150 or 300 Å, respectively. Full and dashed lines correspond to an assumed elastic mean-free path equal to 300 or 500 Å, respectively. At the biasing limits at which current crowding can no longer be neglected ( $V_1$  and  $V_2$  in Figure 9), the emitted current density is found to be about 560 and 1550  $A/cm^2$  for the cathode with a 150 or 300 Å CdS layer, respectively. At the same biases, the captured current density is about 280 and 500  $A/cm^2$ , respectively.

Finally, Figure 12 shows the power efficiency of the cathode as a function of the applied bias. The curves on the left and right correspond to a cathode with CdS thickness equal to 150 and 300 Å, respectively. Full and dashed lines correspond to an assumed CdS elastic mean-free path equal to 300 or 500 Å, respectively. The total power

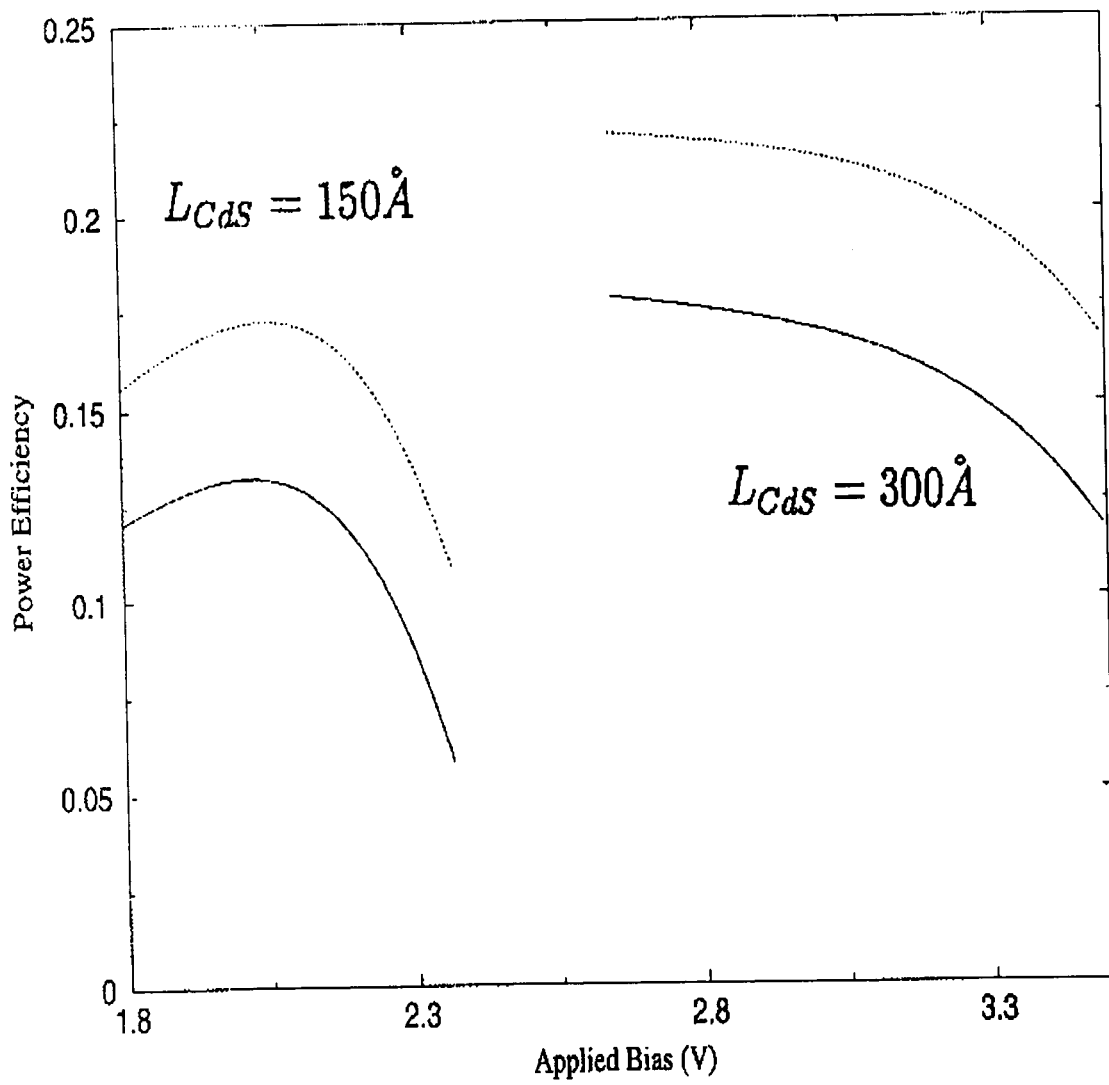


Figure 12: Bias dependence of the power efficiency of the cold cathode

dissipated in the device was found to be 131 mW or 26 mW when calculated at  $V_{bias} = V_1 = 2.02$  V or  $V_2 = 3.22$  V for a cathode with a CdS thickness equal to 150 or 300 Å, respectively. The power efficiency of the cathode can also be calculated. It is defined as the ratio of the difference between the input power and dissipated power in the cathode over the input power. For the range of bias over which current crowding can be neglected, the power efficiency reaches a maximum of 17.5 percent or 22 percent for a cathode with a 150 or 300 Å CdS layer, respectively. The power efficiency decreases with applied bias as a result of current crowding decreases even more if the self-heating effects become important. When  $L_{CdS} = 150$  Å, the power efficiency of the cathode is found to peak at  $V_{bias} = 2.05$  V. One way to increase the power efficiency would be to reduce the width of the Au emitter fingers. This would reduce the contribution of the power dissipation term due to the shadowing effect of the Au fingers. However, the width of the biasing fingers cannot be reduced too drastically since it would increase the voltage drop along the emitter fingers. To prevent this voltage drop, the height of the Au contacts should be increased as their width is reduced.

## 2.8 Conclusions

An analytical model of the effects of power dissipation on the operating temperature of a InP/CdS/LaS cold cathode was derived. The model includes the effect of current crowding and the finite thermal conductivity of the InP substrate. We included the temperature dependence of the major physical mechanisms controlling self-heating effects in the cathode. These include: (1) the temperature dependence of the FN tunneling current at the InP/CdS interface, (2) the temperature variation of the electron mean-free paths in the CdS and LaS layers, (3) the temperature variation of the thermal conductivity in the InP substrate, and (4) the increase (at a rate of 2 meV/K) of the LaS work function.

The last mechanism has a drastic influence on the emitted current since, for cathodes operating at a temperature above 330 K, the NEA advantage is lost. In determining the cathode parameters to minimize self-heating effects, the temperature variation of the other material parameters (bandgap of the InP and CdS layers, effective masses, and resistivity of the LaS semimetallic thin film) was assumed to be negligible over the temperature range of 300-330 K.

For the cold cathodes analyzed here, the current crowding effect was found to occur at a lesser bias value than that at which self-heating effects can no longer be neglected. At the maximum bias at which current crowding effects can be tolerated, the emission current density is found to be several  $10^2 A/cm^2$ . However, the ballistic fraction of the beam emitted into vacuum is dominant only if the CdS thickness is kept under 150 Å.

In order of decreasing importance, the leading contributions to power dissipation in the cathode were found to be (1) the power dissipation due to the shadowing effect of the emitter fingers used to bias the device, (2) the power dissipation due to the trapping of electrons by the LaS thin film, and (3) the power released as a result of inelastic scattering in the CdS layer. For the cathode analyzed here, the overall power efficiency of the cathode was found to be around 20 percent and to decrease with applied bias as a result of current crowding and self-heating effects. Higher power efficiency is possible by reducing the width of the biasing emitter fingers. However, the height of the fingers would have to be increased as well to avoid a substantial voltage drop along the fingers. The results of this chapter were published in reference [23].

### 3. Current Self-Quenching Effects Caused by Space-Charge Effects in the Cathode to Anode Gap

#### 3.1 Introduction

For the cold cathode discussed in Section 1, Mumford and Cahay have shown that an important feature of transport in the vacuum gap between cathode and anode is that electrons are injected into the gap with a finite velocity much in excess of the thermal velocity of thermionic cathodes [6]. At high injection current density, space-charge effects in the vacuum gap typically lead to current self-quenching and the anode conduction current is much smaller than the FN injected current [6]. Due to the space charge in the gap, a potential energy maximum appears in the gap near the LaS region. This potential energy maximum leads to a modulation of the injected electron distribution. A diagram of the electric potential energy profile in the cathode to anode gap is given in Figure 13. The energy distribution,  $h(E)$ , of the electrons injected into vacuum is shown in this figure for the cases of ballistic transport (solid line) and inelastic scattering (dashed line) in the CdS. Only the electrons having energies above the potential energy hump will reach the anode, and the rest will be reflected back into the LaS and hence get absorbed. As a result of the narrow velocity range of injected electrons, the measured average anode current density is found to be much larger than the Child-Langmuir limit which is expected for a Maxwell-Boltzmann distribution of injected carriers as in thermionic cathodes. The modulation of the electrostatic potential hump in front of the cathode is sometimes accompanied by high frequency (several tens of GHz) fluctuation in the minimum of the electric potential in the air gap. These oscillations can lead to large oscillations in the anode current. The modulation of the beam is quite substantial, leading to an energy spread at the anode with a full width at half maximum of only a few  $k_B T$ . This is important for practical applications such as flat panel displays or traveling wave tubes which require electron beams that are as monoenergetic as possible [1].

To understand better the importance of the average energy and energy spread of the beam, we have refined the Ensemble Monte-Carlo (EMC) analysis code of Mumford and Cahay to study the regime of inelastic scattering in the CdS for a metal/CdS/LaS structure and the regime of ballistic transport in CdS for a  $n^{++}$ -InP/CdS/LaS structure.

#### 3.2 The EMC Approach

In the EMC simulations, we assume room temperature operation for the cold cathode. Since the range of current densities is kept near  $100A/cm^2$  in the simulations, we neglect the dynamic work function shift in the LaS thin film as analyzed by Mumford and Cahay [4]. The inelastic transport through the CdS layer is taken into consideration. P. Mumford has studied the space charge effects for ballistic transport through the CdS layer for a metal/CdS/LaS structure. We modified his code to simulate a metal/CdS/LaS structure taking into consideration the inelastic transport through CdS. Furthermore, we repeated the EMC simulations for the case of a  $n^{++}$ -InP/CdS/LaS cathode assuming ballistic transport through the CdS layer.

##### 3.2.1 Calculation of Energy Distribution Function $h(E)$

A flux method is used to calculate the energy distribution of the injected electrons into the CdS following FN tunneling injection at the metal( $n^{++}$ -InP)/CdS interface (Figure 13). The FN emission current  $J_{FN}$  is given as

$$J_{FN} = e \int_0^{+\infty} h(E) dE, \quad (36)$$

where  $h(E)$  is the energy distribution function of emitted electrons and  $E$  is the total energy of the electron. We must first derive the  $h(E)$  function. We will use different approaches for the cases of the metal/CdS/LaS and  $n^{++}$ -InP/CdS/LaS cold cathodes. In the former case, the energy profile is obtained analytically, whereas in the latter case the computer program **SEQUAL** is used <sup>5</sup>

**The Metal/CdS/LaS Cathode Case:** We assume ballistic transport through the CdS and LaS regions and perfect transmission through the CdS/LaS and LaS/vacuum interfaces. The  $h(E)$  function is then used as an initial electron

---

<sup>5</sup>SEQUAL (Semiconductor Electrostatics by QUantum AnaLysis) is released by Purdue University.

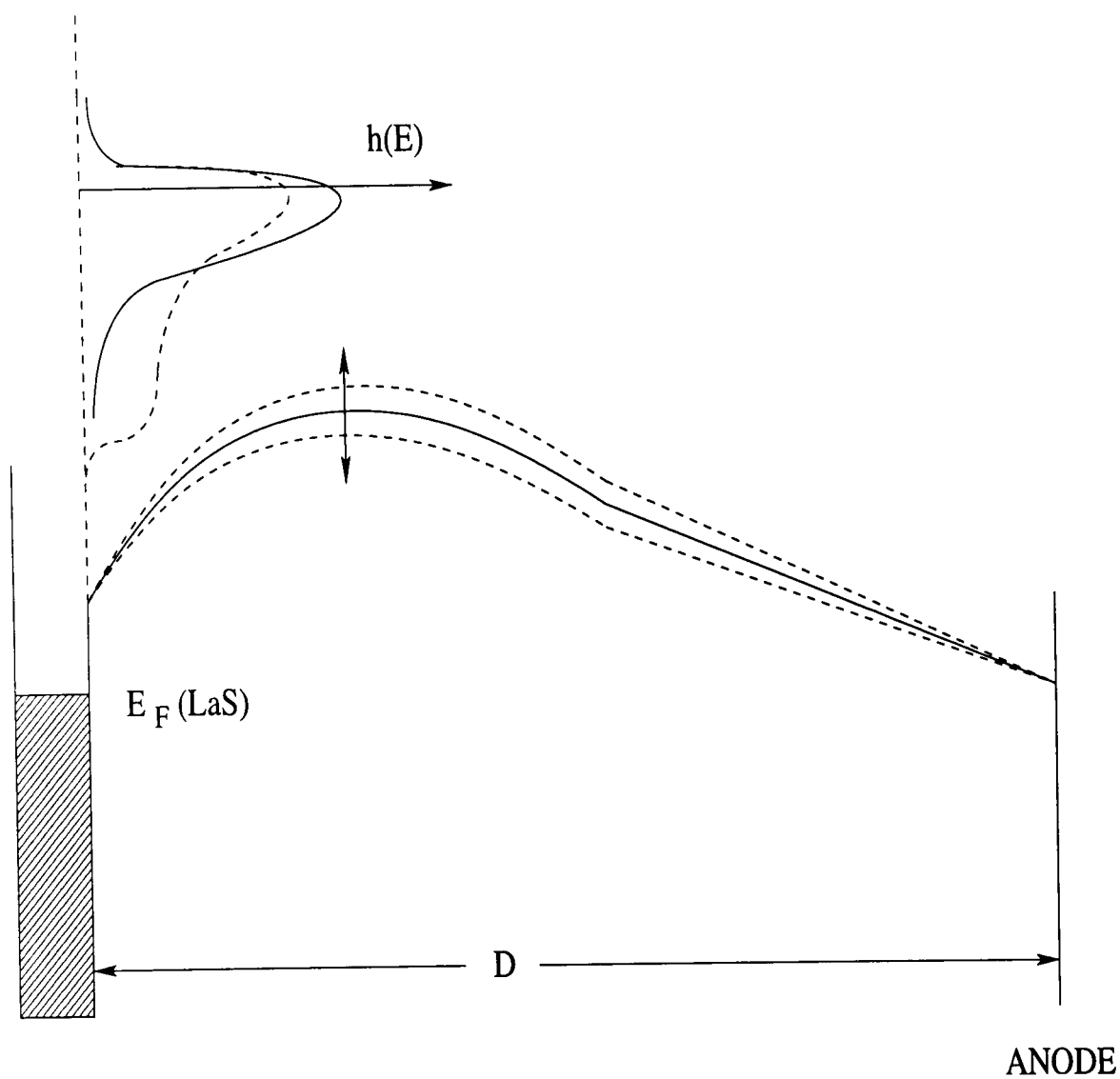


Figure 13: Modulating Action of the Electrostatic Potential Energy Profile in Front of the LaS Thin-Film as a Result of the Space-Charge Effects



energy distribution to simulate electron injection into the space-charge region between LaS thin film and anode. If we consider inelastic transport through the CdS, a new  $h(E)$  must be generated from this flux after scattering events take place. In the case of ballistic transport through the CdS layer, the FN injection current is given by [14, 24]:

$$J_{FN} = \frac{4\pi me}{h^3} \int_0^{+\infty} \int_0^E dE_x f(E) D(E_x), \quad (37)$$

where  $f(E)$  is the Fermi distribution function,  $D(E_x)$  is the transmission coefficient for an electron with normal energy  $E_x$  at the metal/CdS interface  $h$  is Planck's constant, and  $m$  is the electron mass. Including the classical image charge potential at the metal/CdS interface, the transmission coefficient  $D(E_x)$  can be calculated in the WKB approximation as

$$D(E_x) = \exp\left(-c + \frac{E_x - E_F}{d}\right), \quad (38)$$

where  $E_F$  is the Fermi energy in the metallic contact. This expression is valid for energy around the Fermi energy of the metallic contact. As shown by Good and Muller, the parameters  $c$  and  $d$  are given by [14]

$$c = \frac{2\pi\sqrt{2m\Delta^3}}{3heF} \nu(y_0), \quad (39)$$

and

$$d = \frac{heF}{4\pi\sqrt{2m\Delta}} \frac{1}{t^2(y_0)}, \quad (40)$$

where  $F$  is the electric field in the CdS layer,  $\Delta$  is the energy barrier height at the metal/CdS interface before including the Schottky effect. The functions  $\nu(y)$  and  $t^2(y)$  have been tabulated by Good and Muller where  $y$  is given as

$$y = \frac{\sqrt{e^3} F}{V_0 - E_x}. \quad (41)$$

The quantity  $y_0$  is the value of the  $y$  calculated for  $E_x = E_F$ .  $V_0$  is the sum of  $\Delta$  and  $E_F$ . The energy distribution,  $h(E)$ , is then found using Equations (36) and (37).

$$h(E) = \frac{4\pi md}{h^3} \exp\left(-c + \frac{E_x - E_F}{d}\right) f(E). \quad (42)$$

This equation is valid only for the case of field emission from a flat metallic surface into vacuum, whereas in our case, the emission is taking place from the metal to the CdS material. In our case, a more accurate calculation of the emission current density should include the difference in the effective masses across the metal/CdS interface, but we expect the resulting energy distribution for emitted electrons to be qualitatively similar to Equation (42) with the same field dependence for  $c$  and  $d$ . According to Good and Muller, this equation is only valid if the following conditions are satisfied:

$$y < 1, \quad (43)$$

and

$$d > k_B T. \quad (44)$$

Equations (43) and (44) can be rewritten as

$$\sqrt{e^3} F < \Delta, \quad (45)$$

or

$$3.79 \times 10^{-4} \sqrt{F} / \Delta < 1, \quad (46)$$

where  $F$  and  $\Delta$  are expressed in  $Vcm^{-1}$  and  $eV$ , respectively. For  $0 < y < 1$ ,  $t^2(y)$  is roughly equal to 1.1 [14], therefore, Equation (46) can be rewritten as

$$\frac{9.76 \times 10^{-9}}{\sqrt{1.1\phi}} > k_B T, \quad (47)$$

where  $F$  and  $\phi$  are expressed in  $V\text{cm}^{-1}$  and  $eV$ , respectively.

**The  $n^{++}$ -InP/CdS/LaS Cathode Case:** The  $h(E)$  function is determined using the program **SEQUAL**. The input to this program is the conduction band energy profile in the InP/CdS/LaS structure, which is determined as a function of the applied bias between the  $n^{++}$  - InP substrate and the LaS layer using the following assumptions: (1) we use the zero current approximation (ZECA) and neglect the space-charge effects in the  $i$  - CdS layer <sup>6</sup>, (2) we assume that the LaS semimetallic thin film is an equipotential, and (3) we assume that the InP substrate is heavily doped ( $5 \times 10^{18} \text{cm}^{-3}$ ). The latter approximation leads to calculated Fermi level of 0.128 eV above the bottom of the conduction band in the  $n^{++}$ -InP substrate. This is about  $5k_B T$  at room temperature. In this case, the band bending in the InP layer is found using the following approximation for the electron density of the highly degenerate electron gas [15]:

$$n(x) = \frac{8\pi}{3} \left( \frac{2mk_B T}{h^2} \right)^{3/2} \xi^{3/2} \left( 1 + \frac{0.2}{\xi} + \frac{\pi^2}{12\xi^2} \right) \quad (48)$$

where  $\xi = \frac{E_F - E_c(x)}{k_B T}$ . In Equation (48),  $E_F$  is the Fermi level in the InP substrate,  $k_B$  is Boltzmann's constant,  $m$  is the InP conduction band effective mass in the  $\Gamma$ -valley,  $h$  is Planck's constant,  $T$  is the temperature, and  $E_c(x)$  is the conduction band energy profile. Figure 14 shows the conduction band energy profile across the  $n^{++}$ -InP/CdS/LaS structure.

Once the injected energy distribution,  $h(E)$ , has been found as a function of the applied bias across the CdS layer, the electron transport between the LaS thin film and the anode is modeled by an EMC description. The reason for choosing an EMC approach is to be able to account for dynamical space-charge effects as well as random fluctuations linked to the effects of shot noise in the metallic contact. To include the shot noise effects, we need to estimate (1) the number of electrons emitted in each time interval, (2) the times at which the electrons are emitted, and (3) the initial velocities of the electrons.

First the emitted current density is determined as a function of applied bias across the CdS layer for a specific set of cathode parameters. Then the bias dependence is calculated for parameters  $y_0$  and  $d$  is calculated to check the range of applied bias over which Equations (46) and (47). The energy spectrum of the injected carriers is then determined and normalized using Equation (42). Next, the EMC simulation of electron transport through the gap between the LaS thin film and the anode is run as follows: (1) time is divided in small intervals of 50 fs value after which the conduction band energy profile between cathode and anode is upgraded through a solution of Poisson's equation. The boundary conditions of Poisson's equation are the fixed values of the potential applied at the cathode surface and the anode; (2) electrons reflected back to the cathode as a result of the conduction band maximum encountered in the gap are automatically removed from the simulation. Similarly, electrons encountering the surface of the anode are also assumed to be absorbed and therefore removed from the simulation.

### 3.2.2 Effects of Shot Noise

Electrons escape from the cathode randomly in time and with a distribution of velocities. The aggregate of emitted electrons leads to current fluctuations due to the random emission times and velocity fluctuations. As a result, the number of electrons in any small range of energies within the distribution also fluctuates. Hereafter, we assume random emission, i.e., the emission of every electron is completely independent of every other electron emission. We include these shot noise effects in our simulations by assuming that the number of electrons emitted per unit time are given by a Poisson distribution and their corresponding emission energies is given by the energy distribution density  $h(E)$  determined previously. A set of random numbers are generated which simulate the cathode emission and which possess all the statistical features of shot noise. The average number of electrons emitted in a time interval  $\Delta T$  is  $n_{av}$ . This number is computed for a given emission current and emission window area. The

<sup>6</sup>This approximation has been used in the theoretical analysis of field emission from semiconductor tips. See reference [17] for instance. A more rigorous treatment would require an appropriate calculation of the image force potential at the InP/CdS interface along the line of described in reference [25]

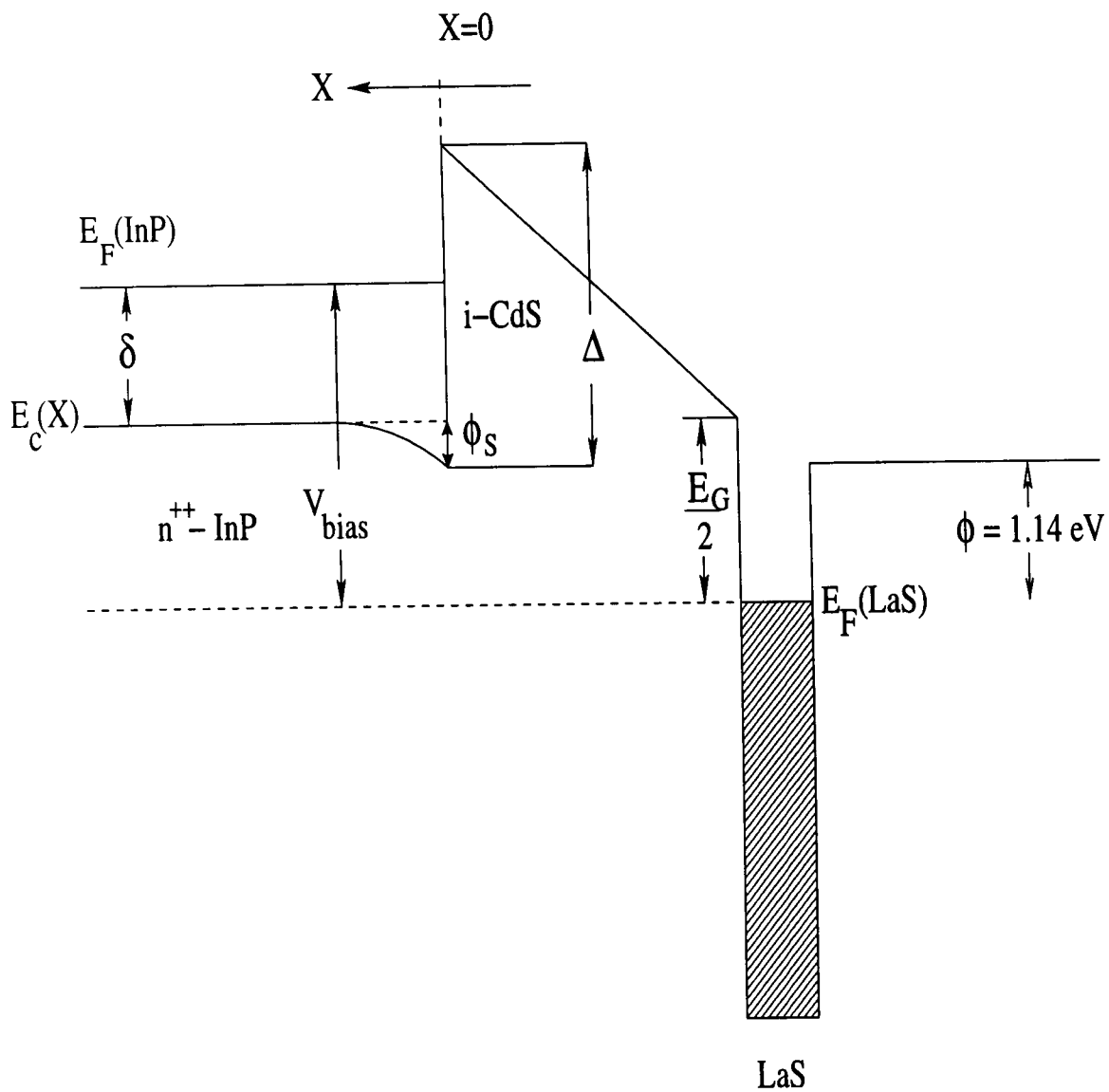


Figure 14: Schematic Representation of the Conduction Band Energy Profile Across the  $n^{++}\text{-InP/CdS/LaS}$  Heterostructure Cold Cathode.

probability that  $s$  electrons will be emitted in this time interval follows the Poisson distribution

$$f(s) = \frac{e^{-n} n^s}{s!}, \quad (49)$$

where  $s = n_{av} \Delta T$ . The cumulative sum of this distribution,  $F(s) = \sum f(s)$ , is the probability that  $s$  or fewer electrons are emitted in a time interval  $\Delta T$ . Typically,  $n_{av} = 500$  in our numerical simulations.

To determine the number of electrons emitted in a time interval  $[t_1, t_1 + \Delta T]$ , we generate a random number  $\alpha_1$  and compare it with the values of cumulative distribution function  $F(s)$ . If  $\alpha_1$  is such that

$$F(m-1) < \alpha_1 < F(m), \quad (50)$$

then the number of electrons emitted is  $m$ .

For the randomness in time, we generate additional random numbers. If the random numbers are  $\beta_1, \beta_2, \dots$ , the exact times at which electrons are emitted are  $t_1 + \beta_1 \Delta T, t_1 + \beta_2 \Delta T, \dots$ , respectively. In the actual computation, instead of taking the electrons emitted at times  $t_1 + \beta_i \Delta T$  ( $i = 1, 2, \dots$ ), we assume for simplicity that all electrons are emitted at the same time but at a varying small distance in front of the cathode. The  $i_{th}$  electron is assumed to be emitted at time  $t_1$  but at a distance  $x_i = \beta_i \Delta T v_i$  where  $v_i$  is the initial velocity of the  $i_{th}$  electron. The error involved in this approximation is negligible if  $\Delta T$  is chosen sufficiently small. The initial velocity  $v_i$  is determined using a rejection technique starting with the energy distribution density  $h(E)$ . We assume the velocity components in the direction perpendicular to the direction of current flow as zero. This approximation is reasonable because, from Equation (38), we can see that electrons with a longitudinal energy much below the Fermi level only have a very small transmission probability through the metal/CdS barrier.

### 3.2.3 Inelastic Scattering in the CdS Layer

The effect of space charge in the vacuum gap for ballistic transport of electrons through the CdS layer was studied by Mumford and Cahay [6]. Here we extend the model to include the effects of inelastic scattering in the CdS layer using a mean free path concept.

Referring to Figure 15, at location  $z$  in the CdS layer, the ballistic component of the current is approximated as

$$J_z^b = J_{FN} e^{-z/\lambda_{CdS}}, \quad (51)$$

where  $J_{FN}$  is the FN current injected into the CdS and  $\lambda_{CdS}$  is the mean-free path in the CdS layer. For simplicity the mean-free path in CdS is assumed to be independent of the applied bias across the CdS layer. The metal/CdS interface is located at  $z = 0$ . The differential current density loss at  $z$  under steady-state conditions and in the absence of recombination processes is given by

$$dJ_z^b = -\frac{1}{\lambda_{CdS}} J_{FN} e^{-z/\lambda_{CdS}} dz. \quad (52)$$

Assuming that electrons make at most one collision on their travel through the CdS layer, the kinetic energy released by electrons suffering an inelastic collision within the range  $(z, z + dz)$  can be calculated by using the law of congruent triangles:

$$\frac{\Delta + eV_{bias} - 0.5E_G}{\Delta E + \Delta} = \frac{L_{CdS}}{z}, \quad (53)$$

where  $z$  is the location where the electron loses its energy,  $e$  is the charge of the electron,  $\Delta$  is the height of the barrier at the metal/CdS interface, and  $V_{bias}$  is the applied potential across the CdS layer. Rearranging Equation (53), we obtain

$$\Delta E = eV_{bias} pz/L_{CdS} - \Delta, \quad (54)$$

where

$$p = 1 + \frac{\Delta - 0.5E_G}{eV_{bias}}. \quad (55)$$

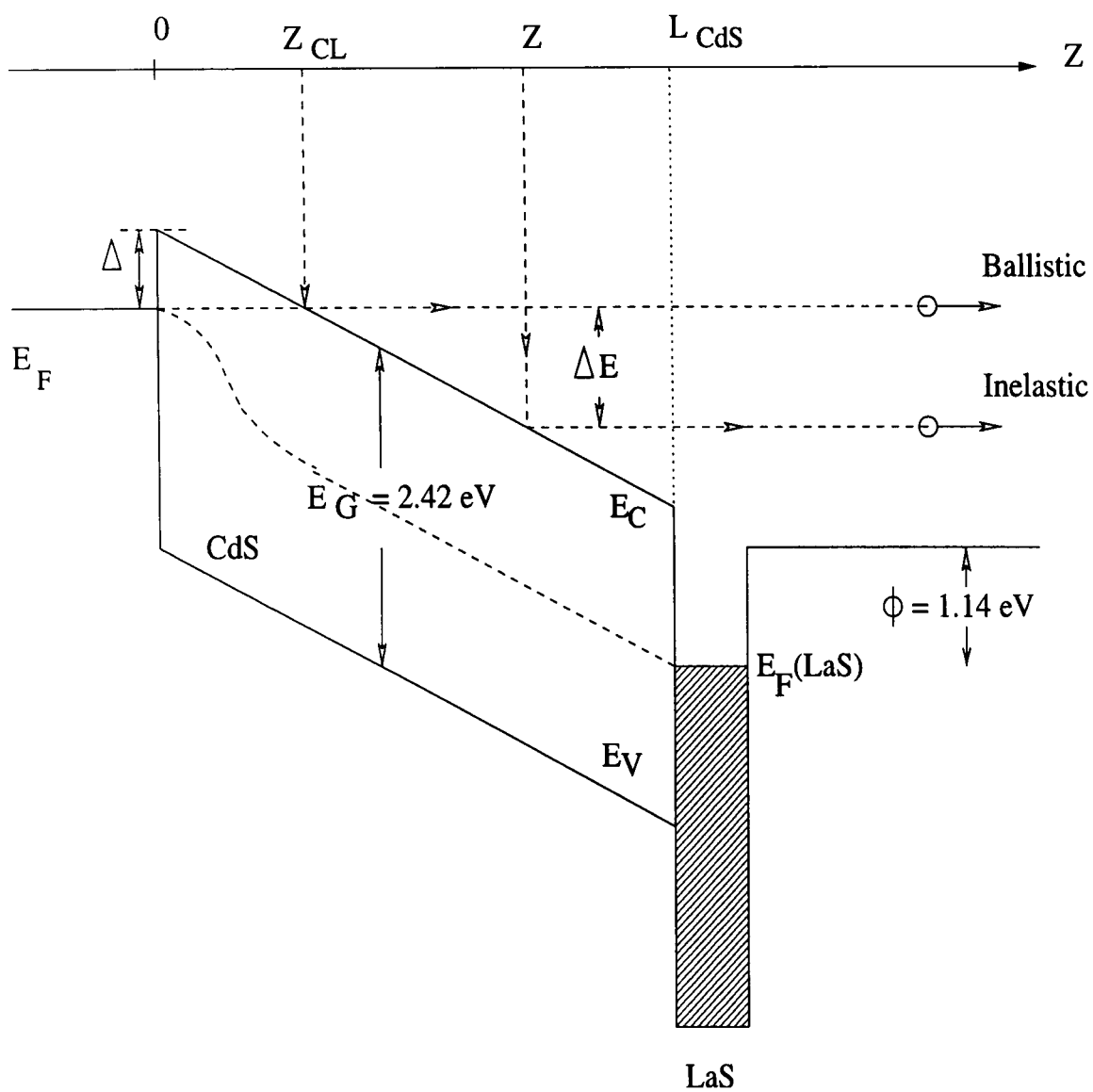


Figure 15: Illustration of the Effects of Inelastic Scattering in the CdS Layer.

We assume that the transmission coefficients through the CdS/LaS and LaS/vacuum interfaces are both equal to unity. The energy distribution of the electron beam injected into vacuum is then determined as follows. The electrons injected into CdS are randomly selected according to the energy distribution  $h(E)$  describing FN injection across that interface (see Equation (42)). Then, the probability that electron will suffer inelastic scattering in the CdS layer is selected using a rejection technique. Each electron injected into CdS from the metal is allowed to suffer inelastic scattering by generating a uniform random number  $r$  in the  $[0, 1]$  interval and checking if

$$z = -\lambda_{cds} \log \tau \quad (56)$$

is below  $L_{cds}$ . Inelastic scattering is allowed only if  $z$  is larger than the classical turning point  $z_{cl}$  shown in Figure 15. This is a simplifying assumption which amounts to neglecting inelastic processes during the tunneling process under the triangular barrier shown in Figure 15.

We assume that an electron only suffers one collision in the CdS layer which brings it down to the bottom of the conduction band in the CdS layer, after which the electron moves ballistically toward the CdS/LaS interface. According to this model, the beam injected into vacuum has a ballistic component which has a fairly narrow energy range, and a long distribution tail extending toward low energy (whose intensity increases as the mean-free path in the CdS layer is decreased).

### 3.3 Analytical Results

In our numerical simulations, we compare the EMC values for the anode current in the current self-quenching regime to the results predicted from the well-known Child-Langmuir result [9, 10]. The latter is strictly valid for thermionic cathodes with a planar geometry. For an cathode to anode gap separation  $D$  and gap voltage  $V_{gap}$ , the maximum electron current density allowed for time-independent flow solution is given by [9, 10]

$$J_{CL} = \frac{4\epsilon_0}{9D^2} \sqrt{\frac{2e}{m}} V_{gap}^{3/2}, \quad (57)$$

where  $e$  and  $m$  are, respectively, the charge and mass of the free electron, and  $\epsilon_0$  is the free space permittivity.  $J_{CL}$  is also called the limiting current density or critical current density. In the current self-quenching regime, an anode current in excess of the Child-Langmuir limit is expected since the latter is based on the assumption of zero electron emission velocity, which is not the case for the cold cathode considered here as illustrated below.

A thorough extension of the Child-Langmuir theory for planar diodes for the case of electron beam injection with finite velocity  $v_{inj}$  was recently developed by Kolinsky and Schamel [11, 12]. Using a Lagrangian integral formalism, they showed that the threshold for the injection current at which current-self quenching occurs is given by

$$J_{Th} = F(X) J_{CL}, \quad (58)$$

where

$$F(X) = \left( \frac{X + \sqrt{1+X}}{X} \right)^3. \quad (59)$$

Here,  $X = eV_{gap}/0.5m_0v_{inj}^2$  ( $V_{gap}$  being the voltage across the gap),  $m_0$  is the free electron mass, and  $v_{inj}$  is the velocity of the electrons injected into vacuum. We calculate  $v_{inj}$  by equation  $0.5 m_0 v_{inj}^2$  with  $E_{peak}$ , where  $E_{peak}$  is the peak location of the energy distribution,  $h(E)$ , of injected carriers.

In this formalism, the collected anode  $J_A$  that possess the threshold current density is given by

$$J_A = \eta J_{FN}, \quad (60)$$

where  $\eta$  is the transmitted fraction of the injected current  $J_{FN}$ . The coefficient  $\eta$  is given by

$$\eta = \frac{2v}{1+v}, \quad (61)$$

where

$$v = \frac{(2V + 1)^{\frac{3}{2}}}{(\frac{1}{X^*} - 1)^2}, \quad (62)$$

and

$$V = \frac{qV_{bias}}{m_e v_{inj}^2}. \quad (63)$$

Furthermore, the following quantities have been introduced

$$X^* = \frac{6}{(3 + \sqrt{d_1} \pm \sqrt{2c_1 - c_2 - c_3 - 54 \frac{(C+9\beta^2)}{\sqrt{d_1}}})}, \quad (64)$$

$$d_1 = c_1 + c_2 + c_3, \quad (65)$$

where

$$c_1 = -6f + 9, \quad (66)$$

$$c_2 = 9b^{1/3}, \quad (67)$$

$$c_3 = f^2 b^{-1/3}, \quad (68)$$

$$b = a_1 + \frac{2}{3}\sqrt{a_2}, \quad (69)$$

$$a_1 = \frac{1}{27}f^3 + 18C\beta^2, \quad (70)$$

$$a_2 = 3f\beta^2(f^3 + 243C\beta^2), \quad (71)$$

$$f = C + 1 - 9\beta^2, \quad (72)$$

$$C = (2V + 1)^{3/2}, \quad (73)$$

and

$$\beta = \sqrt{\frac{q^2 n_o}{\epsilon_o m_e}} \frac{D}{v_{inj}}. \quad (74)$$

### 3.4 Numerical Results

**3.4.1 Metal/CdS/LaS Cold Cathode:** The parameters of the cathode we simulated is given in Table 4.

**Table 4: Parameters of the Simulated Metal/CdS/LaS Cathode**

Material	Au	i-CdS	LaS
Thickness ( $\text{\AA}$ )	optional	75.0	24.6
Lattice Constant ( $\text{\AA}$ )	4.04	5.83	5.85
Workfunction (eV)	4.3	4.2	1.14
Bandgap (eV)		2.5	
Free Electron Density ( $10^{22} \text{cm}^{-3}$ )	(5.86)	—	1.99
Electron Effective Mass ( $m_0$ )	1.0	0.14	1.0

In all simulations, the spacing between the cathode and anode is set equal to  $15 \mu\text{m}$  and the CdS thickness is set to  $75 \text{\AA}$ . We consider a cold cathode with a Au/CdS interface for which  $\Delta$  is equal to  $0.78 \text{ eV}$  [26]. The simulation domain is divided into 300 bins of  $500 \text{\AA}$  each. This is the length traveled by an electron with a velocity of  $10^8 \text{ cm/s}$  over a period of 50 fs, the time interval at which we upgrade the Poisson solver. To make the EMC

simulator more efficient, the bin size was selected so electrons could not cross several bins between solutions of the Poisson solver. To calculate the steady-state value of the anode current, the EMC simulations are run for 20,000 time steps (1 ns total). As shown in Figure 15 of reference [6], when current self-quenching occurs, the anode current can contain an AC component of large frequency (several tens of GHz) equal to the modulation frequency of the electrostatic potential maximum in front of the cathode. In this case, the anode current and the energy spread of the electrons collected at the anode are calculated while averaging over many oscillations of the AC signal (the average is carried over the final 1,000 and 500 time steps of the EMC simulations to calculate the average anode current and distribution of collected carriers, respectively).

Figures 16 and 17 summarize the onset of current self-quenching for a bias between cathode and anode equal to 1 and 5 V, respectively. In these figures, the curves labeled with the value of  $\lambda$  are the results of our EMC simulator for different values of the inelastic mean-free path in the CdS layer. The curve labeled "Ballistic" corresponds to an infinite mean-free path in the CdS layer (ballistic transport). The bottom dashed line is the Child-Langmuir result ( $J_{CL}$ ). For  $V_{gap} = 1$  V and 5 V, Equation (57) gives  $J_{CL}$  equal to 1 A/cm<sup>2</sup> and 11 A/cm<sup>2</sup>, respectively. The curve labeled "Analytical" is the result of the Lagrangian integral formalism described in references [11, 12] based on the assumption of injection into vacuum at a finite velocity. In that case, we use the velocity corresponding to the maximum of the energy density flux  $h(E)$  of the electron beam injected into vacuum. This velocity varies with the bias across the CdS layer. The top dashed curves in the figures are the extended Child-Langmuir results (Equation (60)) in the Lagrangian formalism.

As seen in Figures 16 and 17, the prediction for the threshold to the current self-quenching regime (i.e., when  $J_A < J_{FN}$ ) is quite accurately predicted by Equation (60) in the assumption of ballistic transport through the CdS layer. In this case, the EMC results for the current collected at the anode are larger than predicted in the Lagrangian integral formalism [11, 12]. This point will be addressed in detail below. When inelastic processes are included using an electron mean-free path approach, the transition to the regime of current self-quenching is more gradual as the mean-free path decreases. Furthermore, past the threshold, the anode current is larger than in the ballistic case.

**Ballistic Regime:** To understand why the EMC  $J_a$  results are larger than the analytical results, we plot in Figures 18 and 19 the energy flux distribution of the injected electrons and electrons collected at the anode for two different values of the injected current density  $J_{FN}$  (for the case of  $V_{gap} = 1$  V). In the first of these graphs, the  $J_{FN}$  value corresponds to a biasing point right after the threshold for self-quenching is reached. In the second graph, the value is well into the self-quenching regime.

In both graphs, the energy distribution is the energy distribution of carriers collected over a period corresponding to the last 500 time steps (25 ps) of the EMC simulations. The areas under the curves are proportional to the injected current ( $J_{FN}$ ) and average anode current ( $J_A$ ) collected at the anode. For the energy flux density collected at the anode, the distribution has been shifted down in energy by an amount equal to  $eV_{gap}$  (with  $V_{gap} = 1$  V) to stress the modulation action of the electric potential in front of the cathode, the zero of energy being the vacuum level right outside the LaS thin film. In the figures we show with vertical arrows the minimum and maximum values of the electrostatic potential energy hump in the gap. These values are above the location of the maxima of the energy flux density of the injected beam. Both graphs indicate that a substantial fraction of the beam is crossing the gap with energy above the maximum of the electrostatic potential energy. This explains why the EMC results predict a larger value of the anode current than the analytical treatment which assumes injection of the carriers at an energy corresponding to the peak of the injected distribution. From Figures 18 and 19, we note that some electrons are collected at the anode with a kinetic energy below the minimum value of the electrostatic potential in front of the cathode. This is due to the time dependence of the electrostatic potential in the gap allowing the total energy of some electrons to decrease while crossing the gap. Simultaneously, some electrons can gain energy while crossing the gap which explains why the upper tail of the energy flux collected at the anode is larger than the upper tail of the injected distribution.





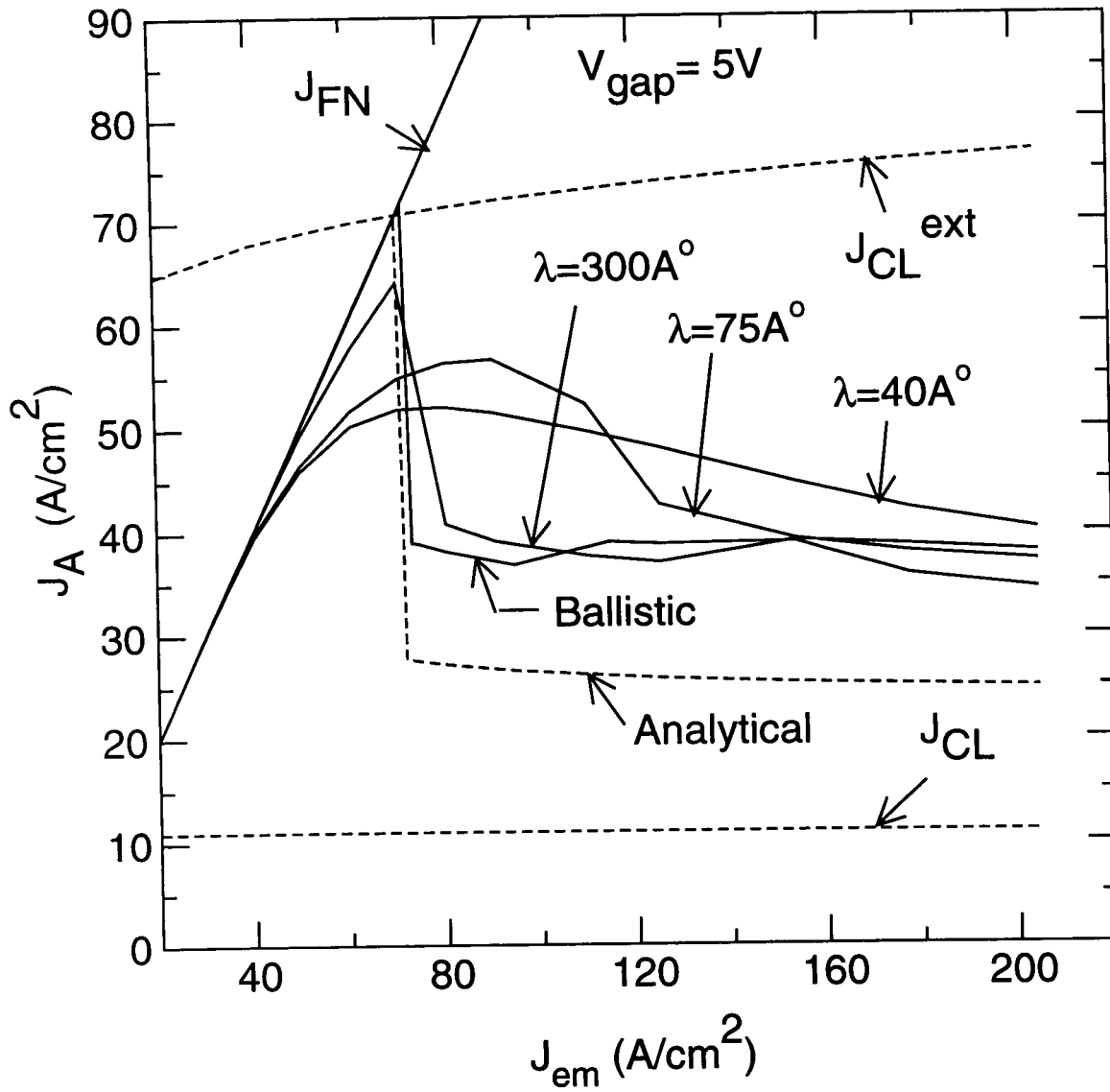


Figure 17: Time Average of the Conduction Current Density in the Rightmost Bin of the Simulation Versus Injection Current Density, for a Cathode-to-Anode Bias of 5 V.

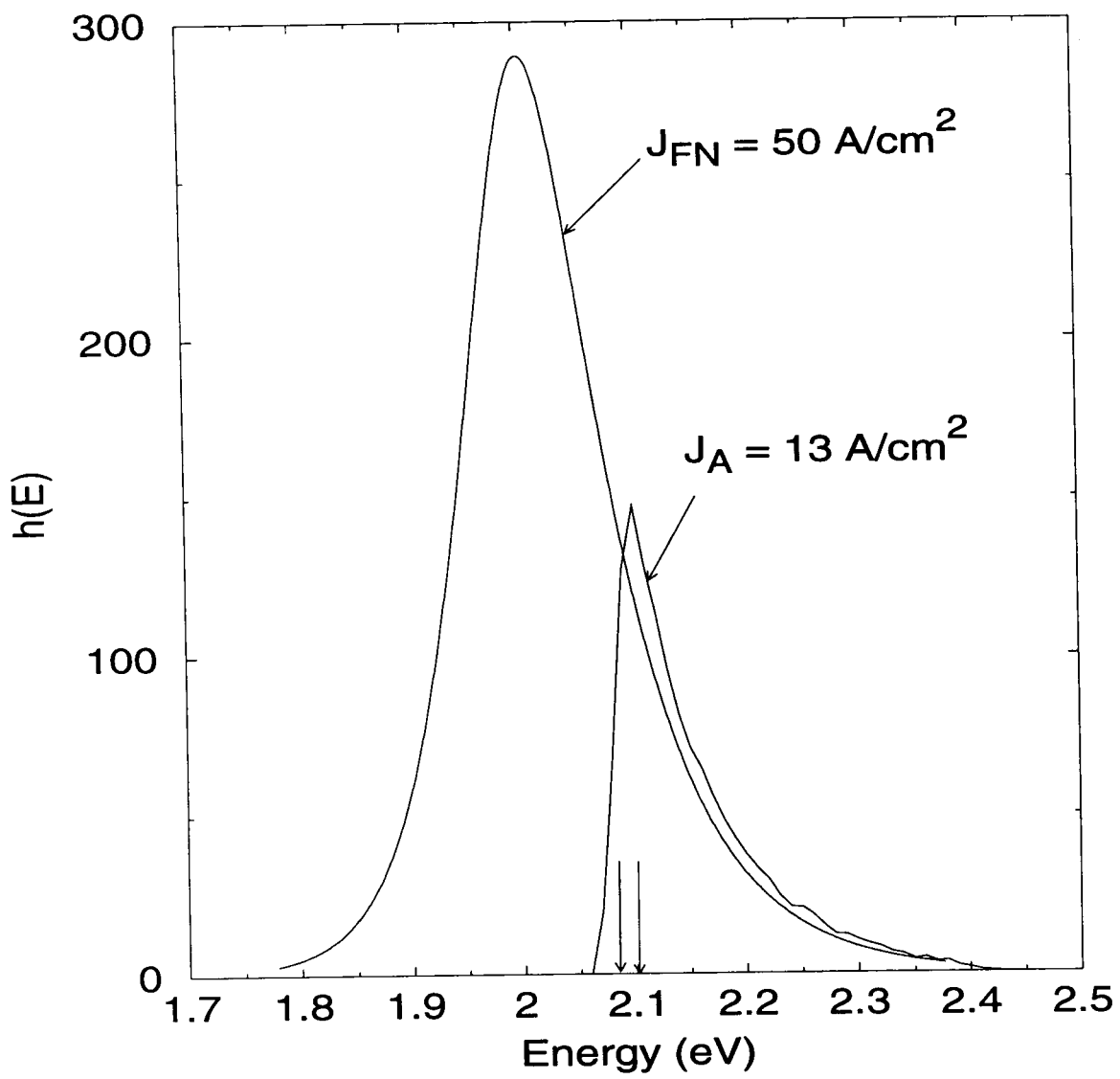


Figure 18: Plot of the Energy Density Flux of Electrons Injected Into Vacuum and Electron Beam Collected at the Anode ( $J_{FN} = 50 \text{ A/cm}^2$  and  $J_A = 13 \text{ A/cm}^2$ ).

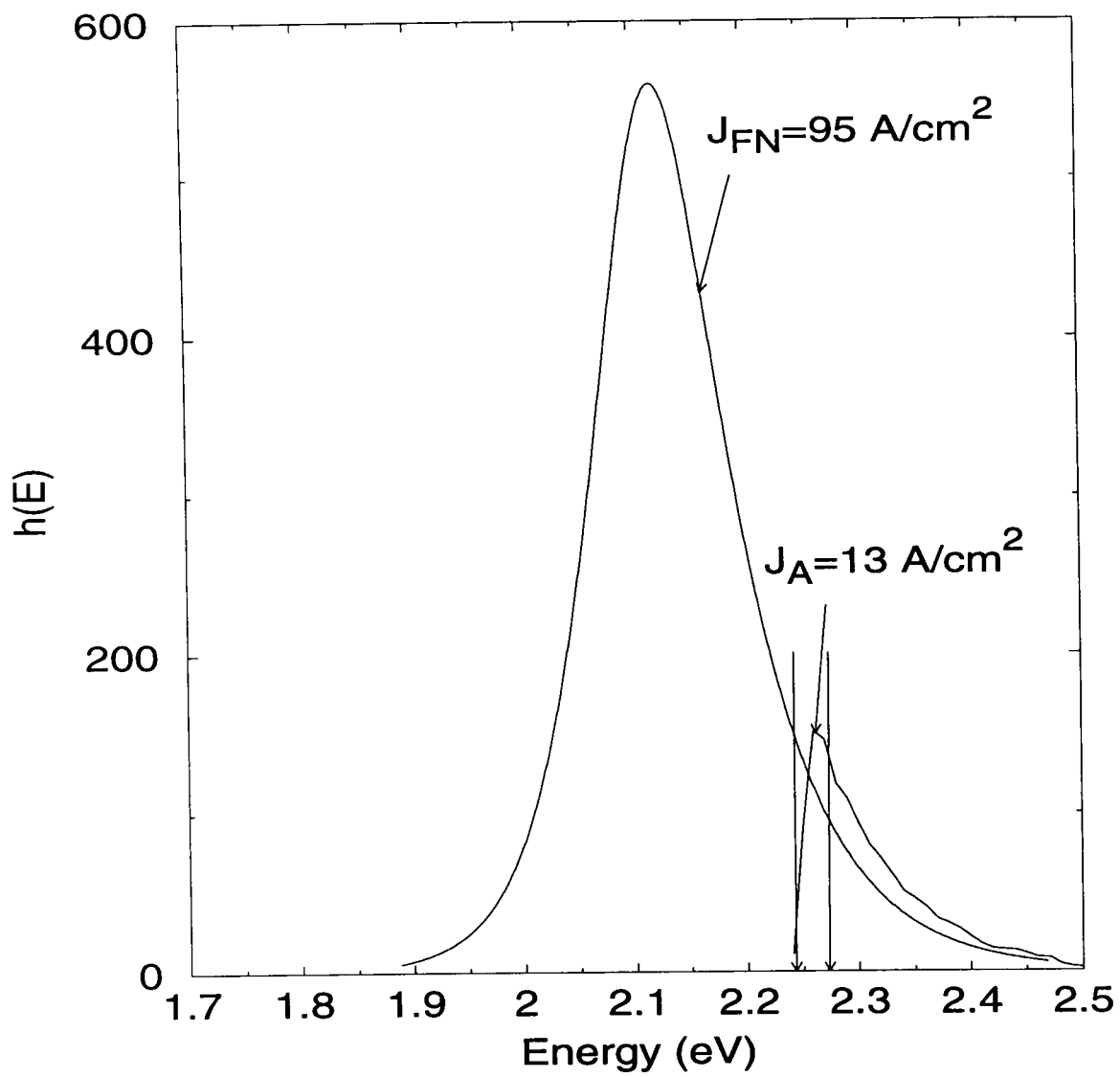


Figure 19: Plot of the Energy Density Flux of the Electron Beam Injected Into Vacuum and Electron Beam Collected at the Anode ( $J_{FN} = 95 \text{ A/cm}^2$  and  $J_A = 13 \text{ A/cm}^2$ ).

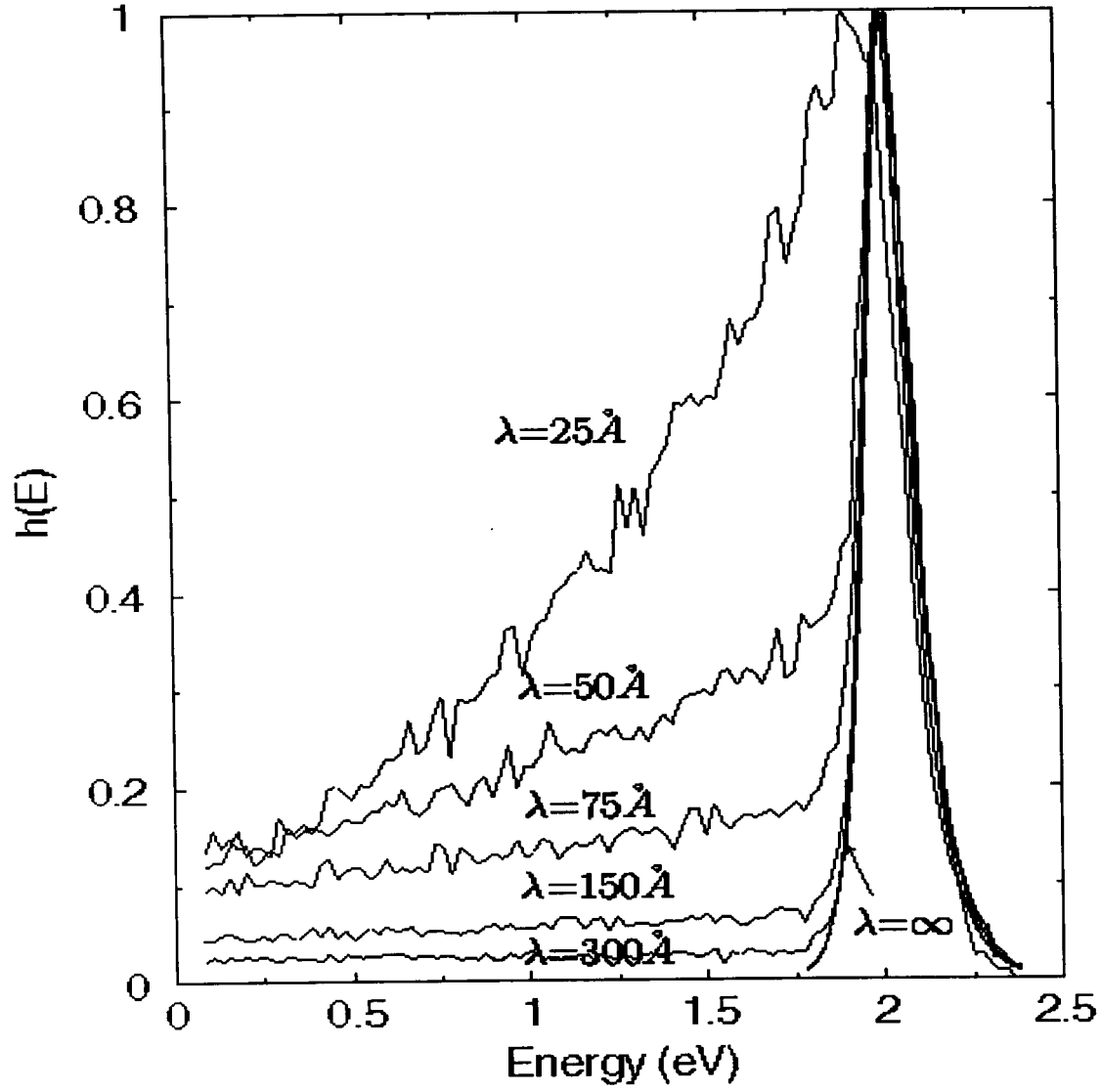


Figure 20: Plot of the Energy Flux Density of the Injected Beam for  $J_{FN} = 50 \text{ A/cm}^2$  for Different Values of  $\lambda_{CDS}$ .

**Effects of Inelastic Scattering:** Figure 20 shows the effects of inelastic scattering in the CdS layer on the energy distribution of the injected carriers for different values of the electron mean-free path  $\lambda_{CdS}$ . The different curves in Figure 20 represent the energy flux density corresponding to an injection current  $J_{FN} = 50 \text{ A/cm}^2$  for different  $\lambda_{CdS}$ . Because we neglect the effects of recombination in the CdS layer, the areas under each curve is the same (the zero of energy is the vacuum level right outside the LaS thin film). The expected larger contribution to the tail of the distribution at lower energy for shorter mean free in the CdS layer is also seen. The abrupt cut of the tail at low energy corresponds to electrons located at the minimum of the conduction band in the CdS layer at the CdS/LaS interface. As a result of the tail at low energy in the presence of inelastic scattering, we expect the chopping action of the electrostatic potential in front of the cathode to be effective at a lower value of the injected current density  $J_{FN}$ . This explains why the effects of current self-quenching occurs at a lower values of  $J_{FN}$  in both Figures 16 and 17, compared to the threshold observed in the assumption of ballistic transport. For a given bias across the gap, the current self-quenching regime also appears at lower value of the injected current density for a larger electron mean-free path in the CdS layer since the tail of the inelastic portion of the injected beam extends to lower energy.

Since the energy distribution of the injected carriers is more spread out in energy in the presence of inelastic scattering in the CdS layer, we expect the modulating action of the electrostatic potential to be more gradual as the injected current density increases leading to a smoother transition to the regime of current self-quenching. The transition is increasingly smoother as the mean free path gets shorter and shorter, as shown in Figures 16 and 17.

Figures 21 through 24 show the gradual modulating action of the electric potential in the gap on the energy flux density collected at the anode. The graphs are for the cases of three different injected current density values.  $V_{gap} = 1 \text{ V}$  and  $\lambda_{CdS} = 75 \text{ \AA}$  are assumed here. A similar trend was observed for the case of  $V_{gap} = 5 \text{ V}$ . In these figures we also show the energy flux density of the injected beam. Figure 16 shows that the anode current is roughly constant for injected current densities in excess to  $50 \text{ A/cm}^2$ . Figures 21 and 24, however, indicate that the energy spread of the beam collected at the anode is getting increasingly narrower when the cathode is operated further into the current self-quenching regime (larger  $J_{FN}$ ). This would be the favored mode of operation of the cathode for applications requiring a electron beam as narrow as possible as in traveling wave tubes. Figure 24 shows that the full width at half maximum of the beam is about  $100 \text{ meV}$ , which is about  $4 k_B T$  at room temperature.

**3.4.2  $n^{++}$ -InP/CdS/LaS Cold Cathode:** We consider a specific cathode with the parameters listed in Table 5. In all simulations, the cathode to anode spacing is set to 15 microns, and the CdS thickness is set to  $150 \text{ \AA}$ . The simulation domain is divided into 300 bins of  $500 \text{ \AA}$  each. This is the length traveled by an electron with a velocity of  $10^8 \text{ cm/s}$  over a period of 50 femtoseconds, the time interval at which we upgrade the Poisson solver. To make the EMC simulator more efficient, the bin size was selected so that electrons could not cross several bins between solutions of the Poisson solver. To calculate the steady-state value of the anode current, the EMC simulations are run for 20,000 time steps (1 ns).

**Table 5: Material Parameters of the  $n^{++}$ /CdS/LaS Cold Cathode**

Material	<i>Au</i>	<i>i – CdS</i>	<i>LaS</i>
Lattice Thickness ( $\text{\AA}$ )	optional	75.0	24.6
Lattice Constant ( $\text{\AA}$ )	4.04	5.83	5.85
Work function (eV)	4.3	4.2	1.14
Bandgap (eV)		2.5	
# of free electrons ( $10^{22} \text{ cm}^{-3}$ )	(5.86)	—	1.99
Electron Effective Mass ( $m_0$ )	1.0	0.14	1.0

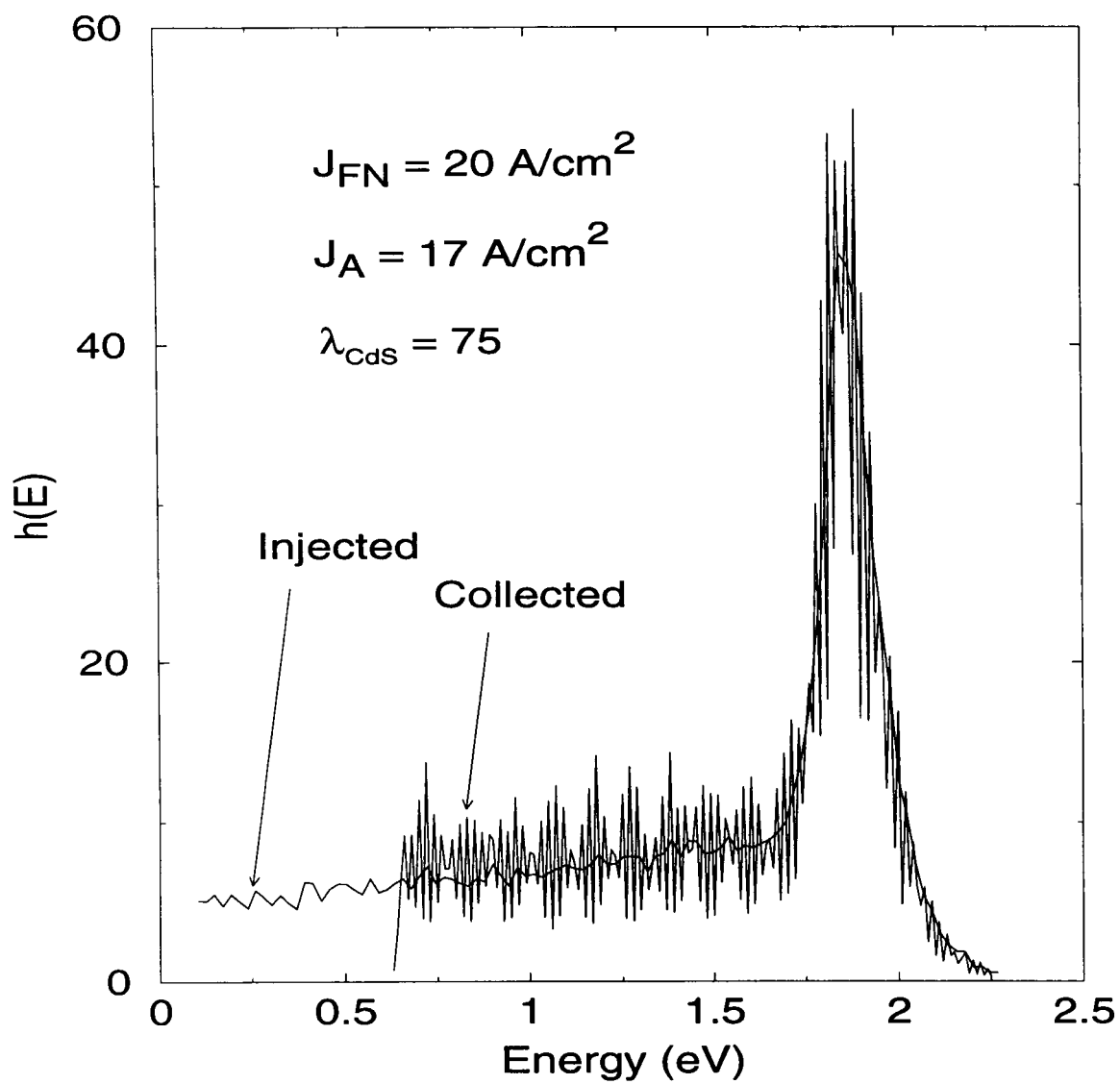


Figure 21: Plot of the Injected and Collected Energy Density Flux for  $J_{FN} = 20 \text{ A/cm}^2$

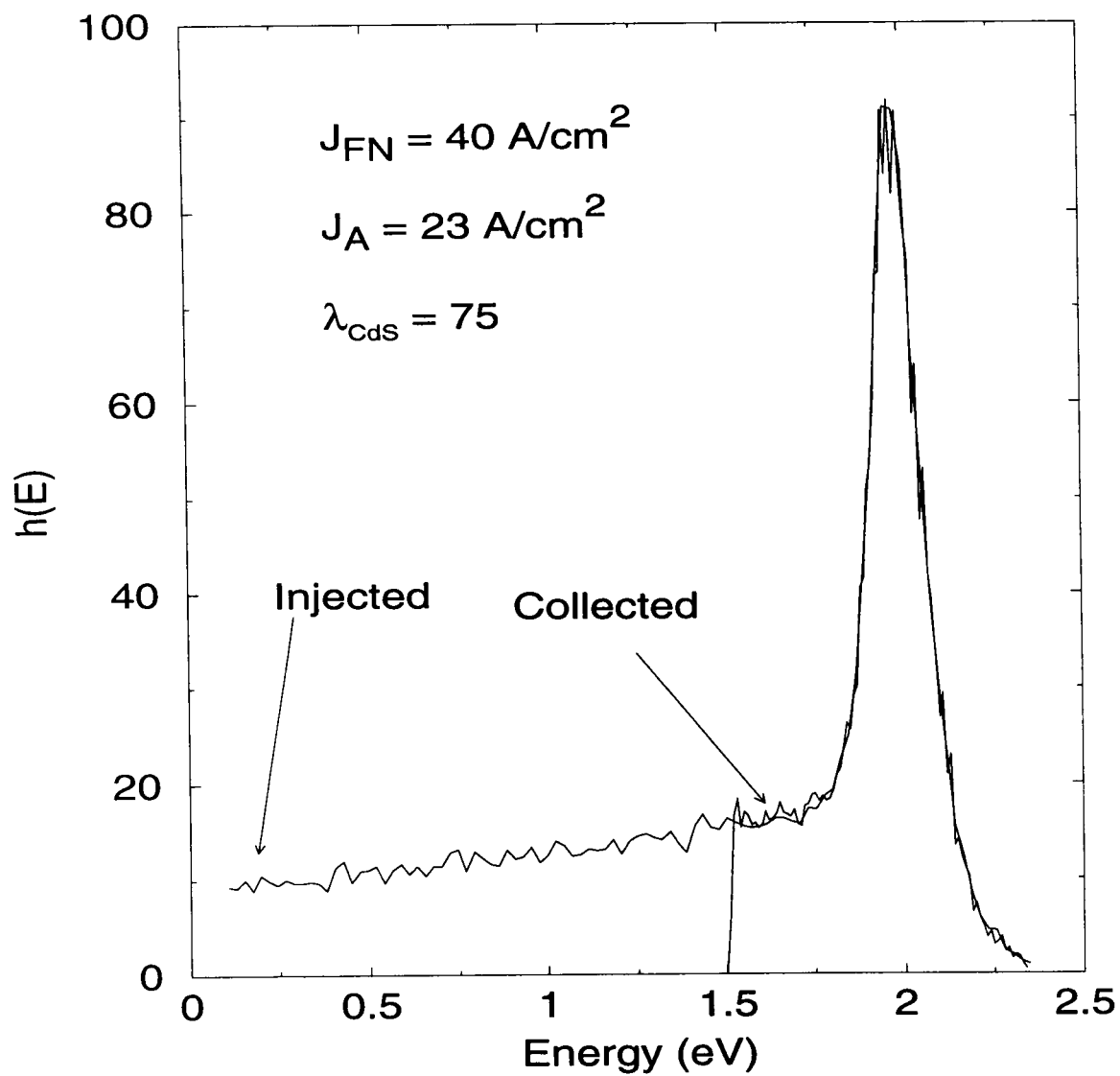


Figure 22: Plot of the Injected and Collected Energy Density Flux for  $J_{FN} = 40 \text{ A/cm}^2$



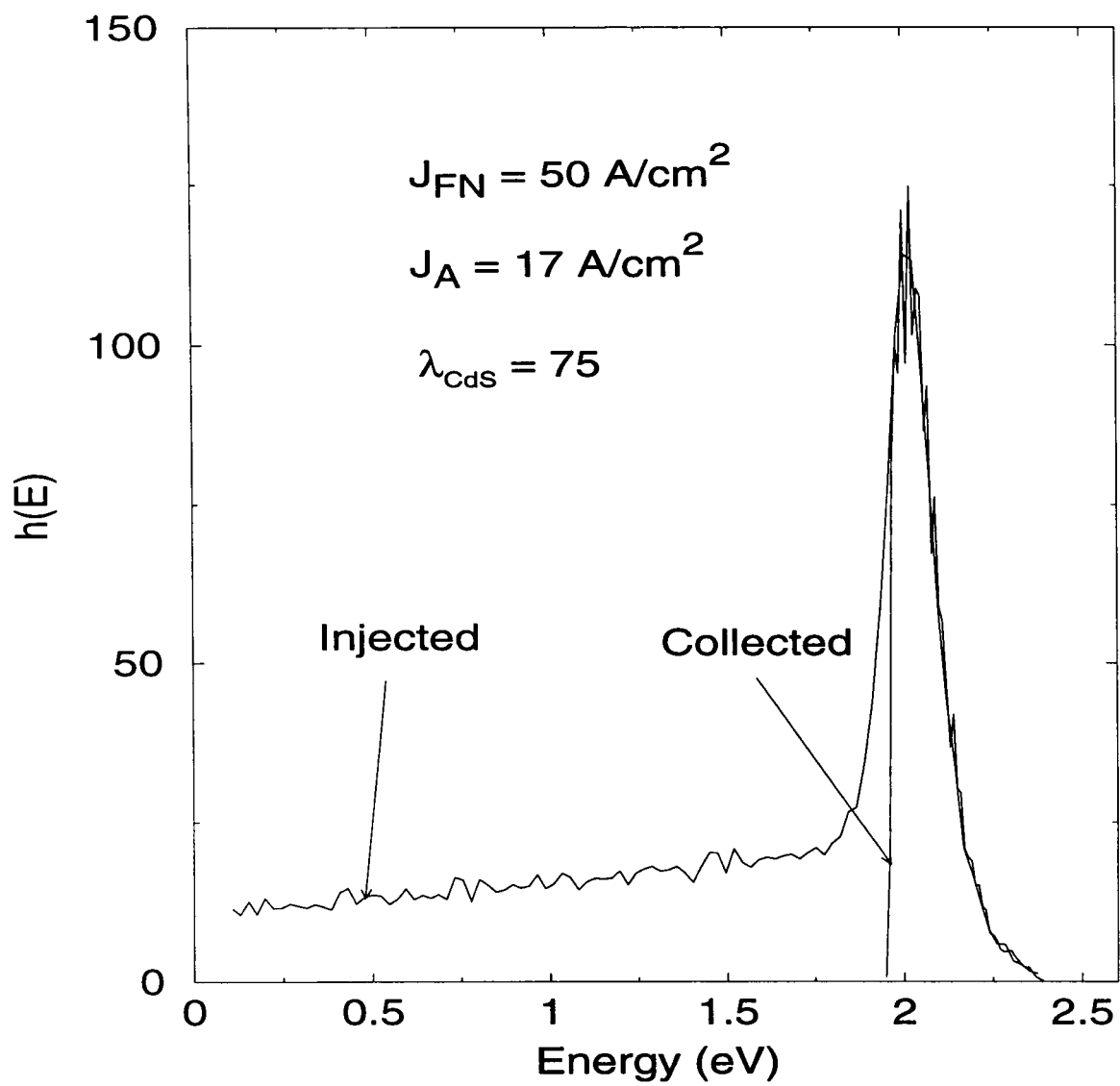


Figure 23: Plot of the Injected and Collected Energy Density Flux for  $J_{FN} = 90 \text{ A/cm}^2$ .

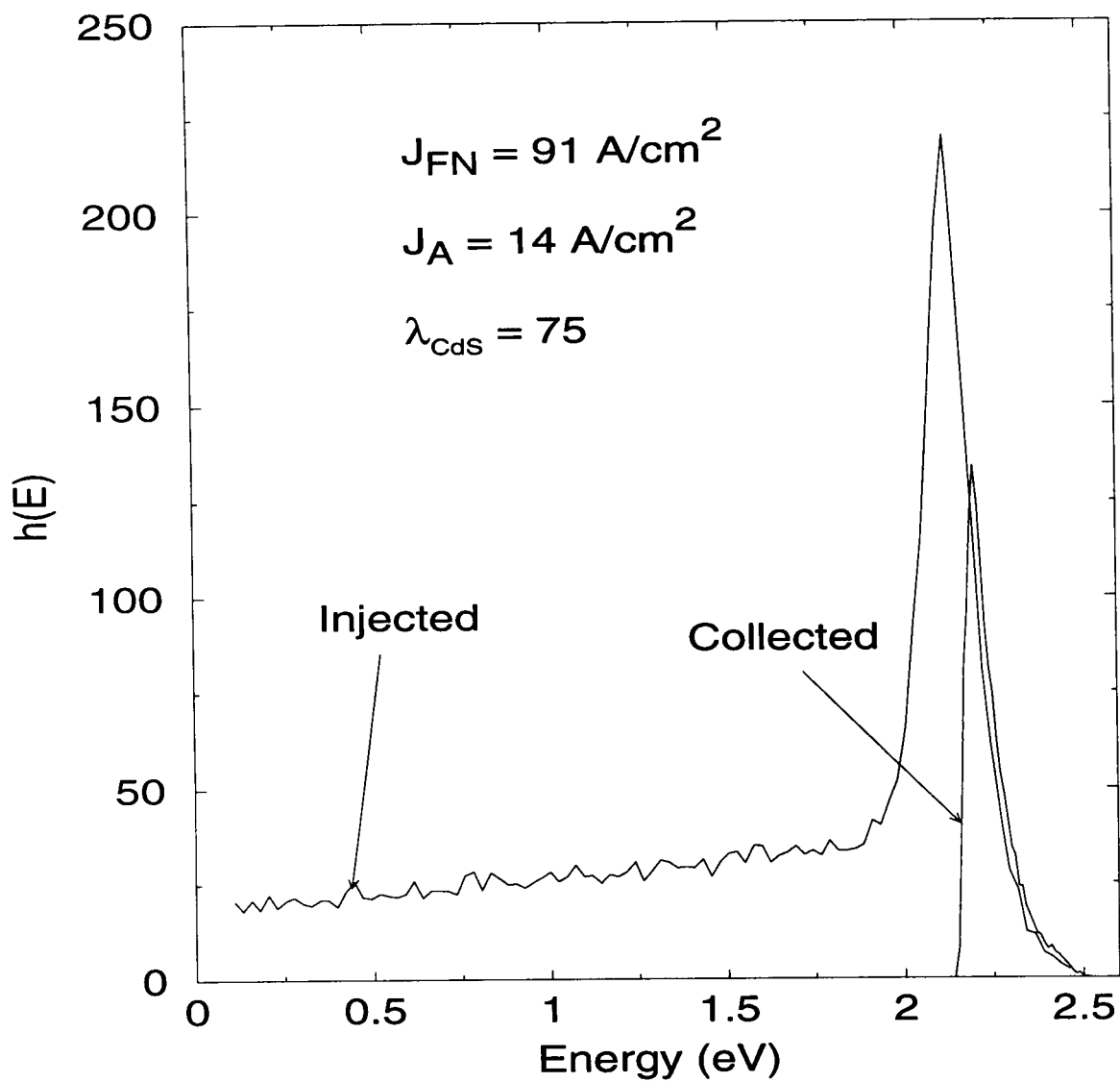


Figure 24: Plot of the Injected and Collected Energy Density Flux for  $J_{FN} = 50 \text{ A/cm}^2$ .

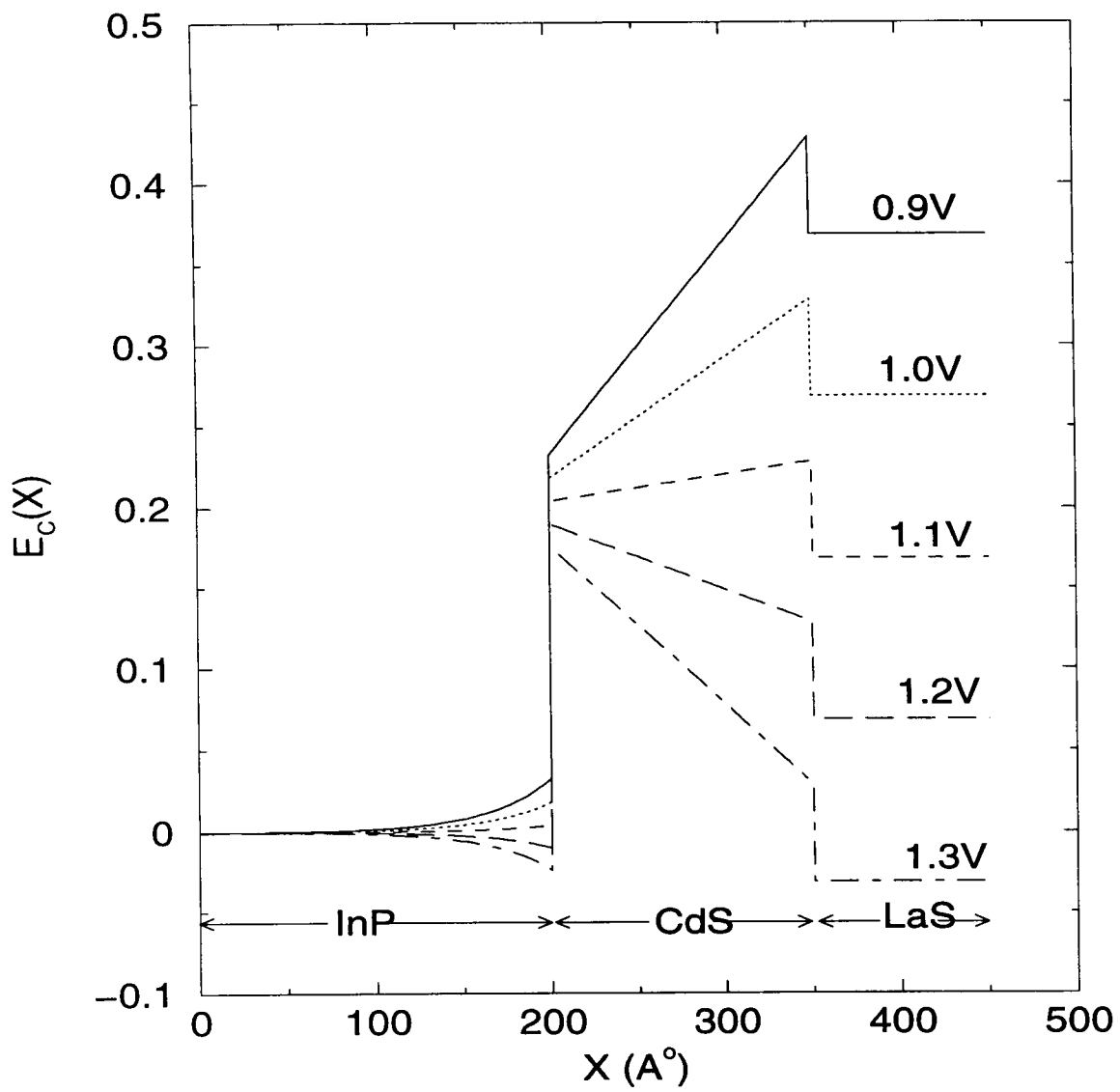


Figure 25: Bias Dependence of the Conduction Band Energy Profile Across the  $n^{++}$ -InP/CdS/LaS Heterostructure

Figure 25 illustrates the conduction band energy profile across the cathode as a function of the applied bias between the InP substrate and the LaS semimetallic thin film. The CdS layer is assumed to be intrinsic and the Fermi level in the LaS is halfway across the CdS bandgap (2.42 eV). The  $n^{++}$ -InP contact is assumed to be doped at  $5 \times 10^{18} \text{ cm}^{-3}$ . The thickness of the CdS is 150 Å. The height of the barrier at the InP/CdS interface is set to 0.2 eV. For zero bias, there is a depletion of the InP layer close to the InP/CdS interface despite the heavy doping of the substrate, as shown in Figure 25. The flat-band condition in the InP region is reached for a bias of 1.128 V. Beyond that value, there is accumulation of electrons in the triangular notch at the InP/CdS interface. For the range of biases shown in Figure 25 (0.9 to 1.3 V), the injection current density was calculated using the program **SEQUAL** and found to range from 25 to  $2.38 \times 10^5 \text{ A/cm}^2$ . Figure 26 shows the variation of the energy flux density  $h(E)$  for different values of the injection current. The latter were also obtained from **SEQUAL** by modeling the conduction band discontinuity at the CdS/LaS interface as a drop of 60 meV to simulate the NEA resulting from the CdS/LaS combination. In calculating  $h(E)$ , we neglected the kinetic energy ( $k_B T$ ) of the electrons in the plane parallel to the heterointerface. In this figure, energy is in reference to the vacuum level outside the LaS thin film. Figure 25 shows that the energy flux density  $h(E)$  has an average energy of about  $2k_B T$  above the vacuum level outside the cathode. In other words, the average energy of the injected carriers is fairly small. This is in contrast with the case of a metal/CdS/LaS cold cathode analyzed in Section 3.4.1 where we found the average velocity of the injected beam to be quite large. For the InP/CdS/LaS cathode, the value of anode current is therefore expected to be in fairly good agreement with the value predicted by the Child-Langmuir expression [9, 10].

We summarize the onset of current self-quenching in Figures 27 and 28 and for a bias between cathode and anode equal to 5 and 10 V, respectively. In these figures, the curves labeled "Ballistic" are the results of our EMC simulator. The bottom dashed line is the Child-Langmuir result. For  $V_{gap} = 5 \text{ V}$  and  $10 \text{ V}$ , Equation (57) gives  $J_{CL}$  equal to  $11.6 \text{ A/cm}^2$  and  $32.8 \text{ A/cm}^2$ , respectively. The curve labeled "Analytical" is the result of the Lagrangian integral formalism described in [12] based on the assumption of injection into vacuum at a finite velocity. In that case, we use the velocity corresponding to the maximum of the energy density flux  $h(E)$  of the electron beam injected into vacuum. This velocity varies with the bias across the CdS layer. The top dashed curves in Figures 27 and 28 are the extended Child-Langmuir results in the Lagrangian formalism.

As seen in Figures 27 and 28, the prediction for the threshold  $J_{CL}^{ext}$  to the current self-quenching regime (i.e., when  $J_A < J_{FN}$ ) is quite accurately predicted by Equation (58) in the assumption of ballistic transport through the CdS layer. Furthermore, the results of the EMC simulations for the anode current are about 25 percent larger than the results predicted by Equation (60).

### 3.5 Conclusions

We have used an EMC approach to theoretically analyze the magnitude of space-charge effects in the cathode to anode gap region of the proposed metal/CdS/LaS and  $n^{++}$ -InP/CdS/LaS cold cathodes. The influence of these effects on the energy distribution of the electrons collected at the anode was also analyzed. Our analysis was based on a mean-free path approach to include the effects of inelastic scattering in the CdS layer for the metal/CdS/LaS structure, following FN injection across the metal/CdS interface. We assumed ballistic transport in the CdS layer for the case of a  $n^{++}$ -InP/CdS/LaS structure.

For the case of a metal/CdS/LaS cold cathode, past the onset of current self-quenching, the energy spread of the electron beam collected at the anode is substantially narrower than for the beam injected from the cathode into vacuum due to the modulating of the beam by the oscillations of the electric potential in front of the cathode. Under the approximation of ballistic transport through the CdS layer, the value of the cathode injection current at which the onset of current self-quenching occurs is in very good agreement with the results obtained from a Lagrangian integral formalism under the assumption of electron injection from the cathode at a finite velocity. When the effects of inelastic scattering through the CdS layer are included, the transition to the regime of current self-quenching (i.e., drop in the anode current as a function of the injection current) is more gradual compared to the case of ballistic transport through the CdS layer. In the current self-quenching regime, our EMC simulations predict a larger anode

current than the Lagrangian formalism due to the energy spread of the injected energy distribution.

The discrepancy between the EMC and the analytical results for the anode current in the current self-quenching regime is less severe in the case of a  $n^{++}$ -InP/CdS/LaS than in the case of metal/CdS/LaS cold cathode because the average velocity of the injected beam is much smaller for the former. The results of this Section have been published in the reference [27].

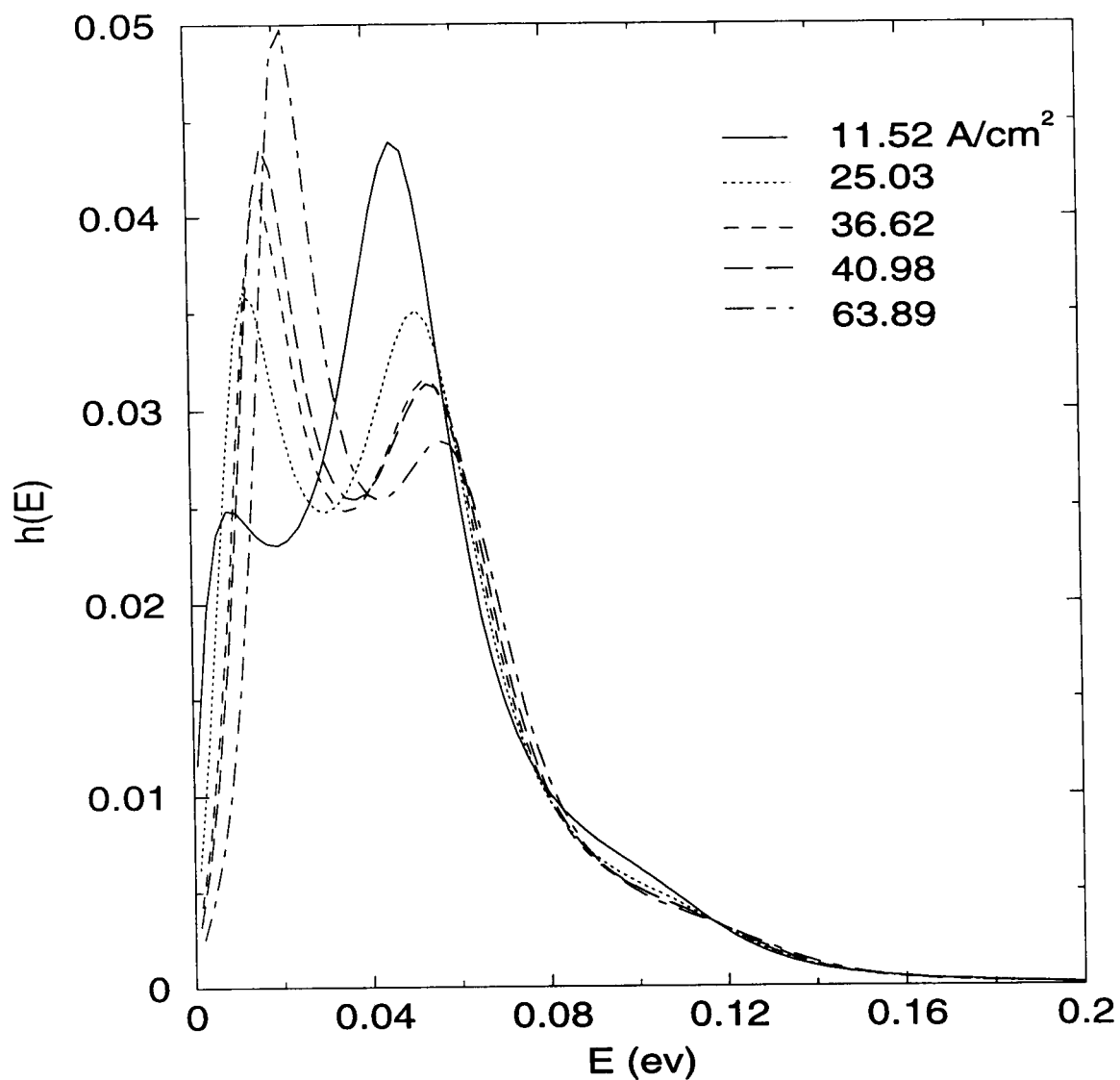


Figure 26: Plot of the Energy Density Flux of the Electron Beam Injected into Vacuum as a Function of the Injection Current Density

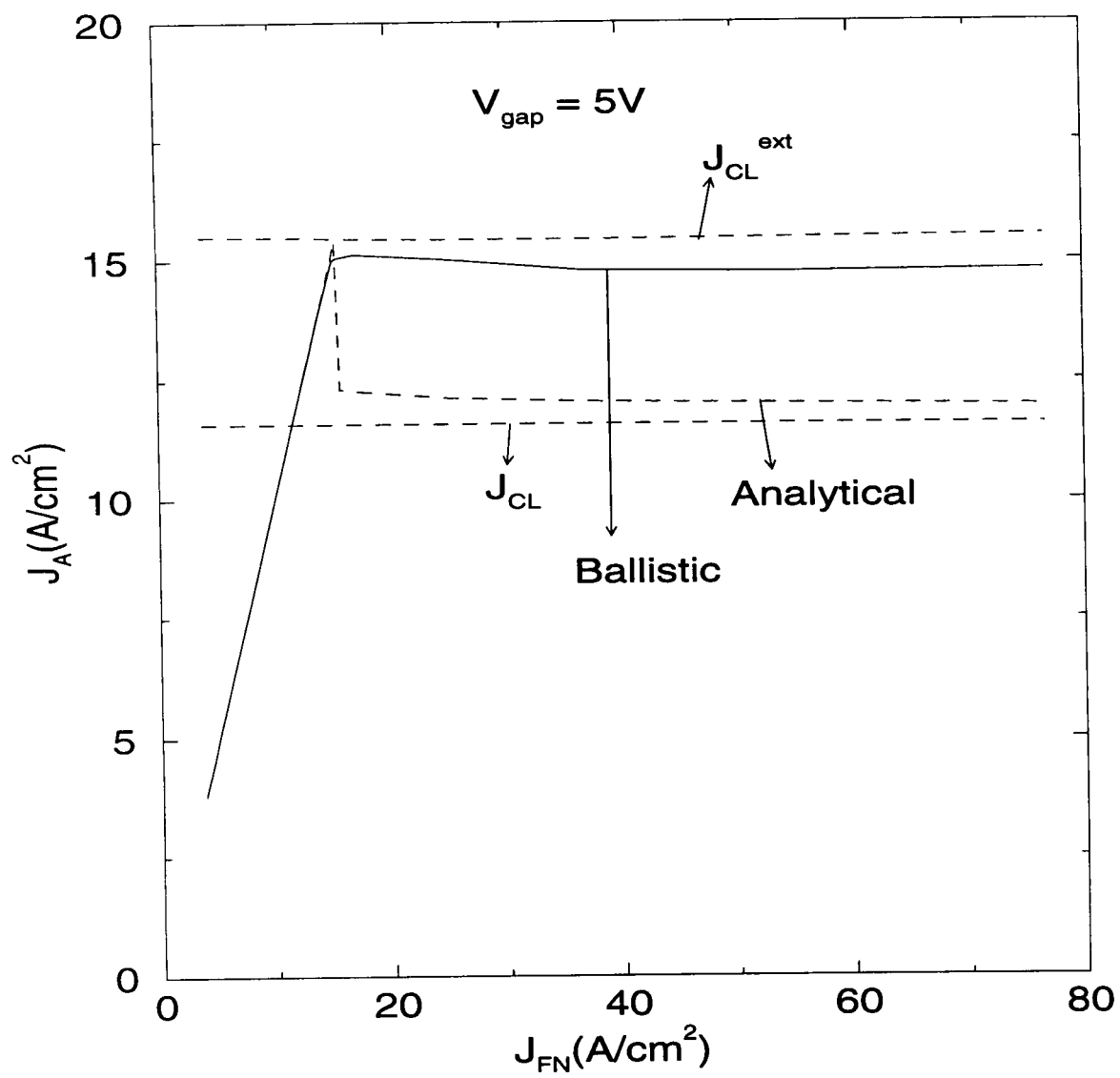


Figure 27: Time Average of the Conduction Current Density (5 V)

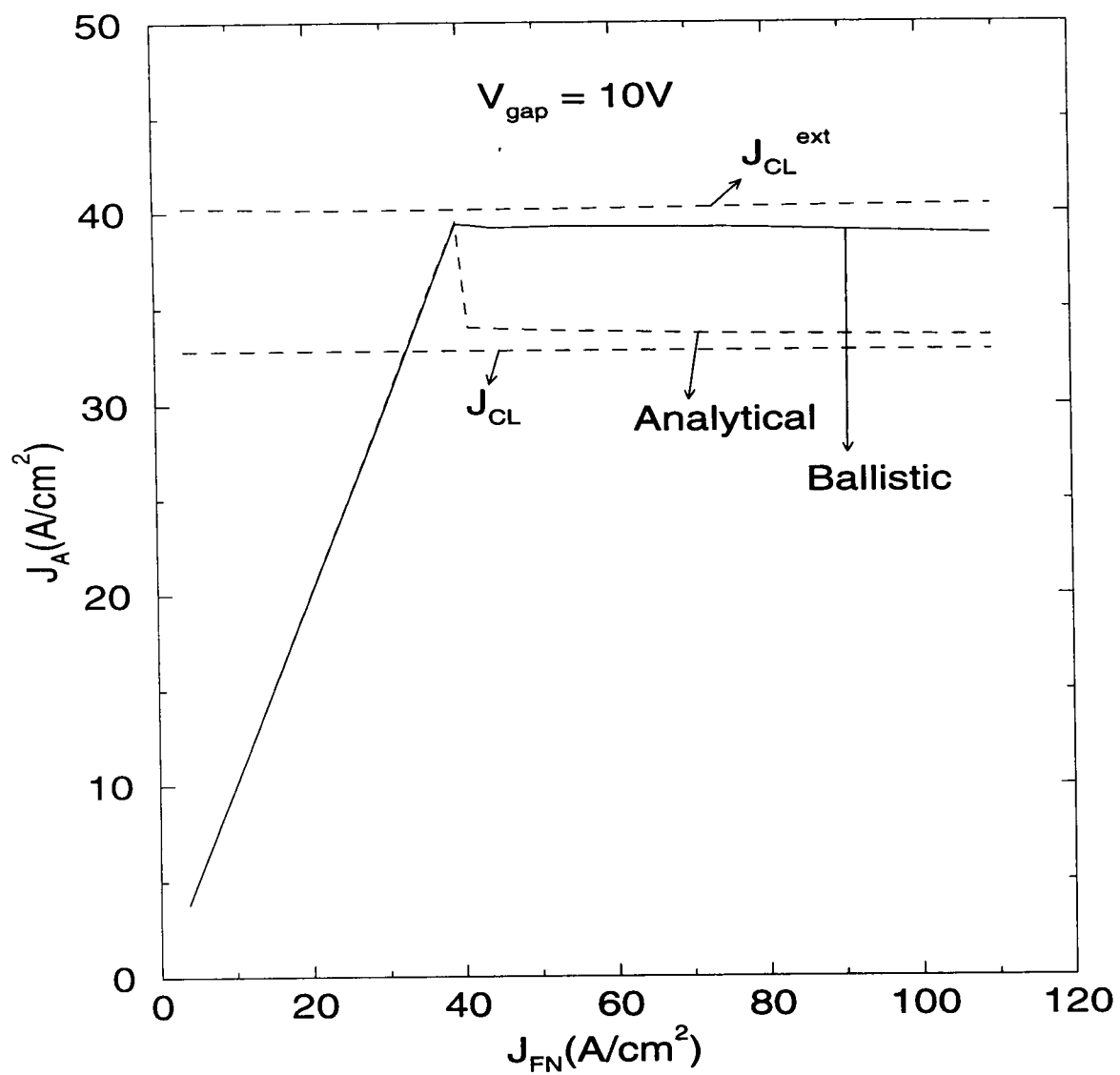


Figure 28: Time Average of the Conduction Current Density (10 V)

## 4. Interplay of Current Crowding And Current Self-Quenching Effects

### 4.1 Introduction

In Section 1, we briefly described the effects of current crowding between emitter fingers of metal(or  $n^{++}$ -InP/CdS/LaS cold cathodes. Due to the multiple electron reflections at the CdS/LaS and LaS/vacuum interfaces and due to the inelastic scattering in the LaS, a part of the FN emitted current at the metal/CdS is trapped in the LaS region (see Figures 2 and 4). This current travels to the Au contacts in the emission window, and due to the finite resistivity of LaS, a lateral potential drop will appear across the emission window between any two fingers of the contacts used to bias the cathode. This phenomenon is called DC current crowding and was originally studied by Mumford and Cahay [5]. They showed that DC current crowding leads to a symmetric and monotonic decrease in the emitted current from the emitter fingers toward the center of the window as illustrated in Figure 29. In Mumford and Cahay's analysis, space-charge effects in the vacuum region outside the cathode were neglected. As discussed Section 3, if the emission current is large enough, space-charge effects may become appreciable in the vacuum region between the cathode and the anode. This eventually leads to the formation of a potential energy hump in front of the cathode which reflects part of the emitted electron beam toward the cathode (Figure 29) and therefore increases the amount of charge collected in the surface film. In this way, the DC current crowding effect is disturbed. In this Section, we will show that the interplay between current crowding and current self-quenching effects can lead to a non monotonic profile for the anode current across the emission window.

For a metal/CdS/LaS cold cathode we have modeled the size of the energy potential hump due to self-quenching in Section 3 using an EMC description of space-charge effects which include the effects of inelastic scattering in the CdS and LaS layers on the energy distribution of the injected electron beam. It was shown that the anode current can be quite a small fraction of the emitted current above a certain threshold. We also showed that the transition to the regime of current self-quenching is fairly smooth when the combined effects of inelastic scattering in the CdS and LaS layers are taken into account.

A self-consistent analysis of current crowding and self-quenching together can lead to the following intriguing possibility. If the bias across the CdS layer is such that the current density at the edges of the emission window is above the threshold for current self-quenching, the anode current at the edges will be small because of the energy potential hump in front of the cathode close to the edges. However, if the emission window is quite large, there will be a reduction in the emitted current density toward the center of the emission window as a result of current crowding effects. Moving in towards the center of the emission window, the emitted current could drop below the threshold for current self-quenching, in which case the anode current closer to the center of the emission window could become larger than at the edges, i.e., the potential hump outside the cathode is expected to be larger toward the edges of the emission window and smaller toward the center. This interplay between current crowding and current self-quenching effects can therefore have an influence on the profile of the anode current density, which is a point of great concern if the cathode is to be used for flat panel display or high-power traveling wave tube applications.

### 4.2 Model

Current crowding effects are accompanied by a variation of the lateral electric potential across the LaS emission window. Figure 29(a-b) shows the energy band diagram at two different lateral locations within the window. As a result of current crowding, the bias across the CdS layer at a lateral location  $x$  becomes  $V(x)$  and consequently the bias across the gap at  $x$  becomes  $V_{gap} + V_{bias} - V(x)$ . Here  $V_{bias}$  and  $V_{gap}$  are the biases across the CdS layer and across the vacuum region at the edges of the emission window, respectively. If the potential across the CdS layer is reduced to  $V(x)$ , the thickness of the triangular barrier at the metal/CdS region is enhanced and the amount of FN tunneling current is also reduced. This will affect the amount of electrons captured in the LaS film at  $x$  and also the amount of emitted current in that cross section of the cathode. As a result, the amount of space-charge buildup in the vacuum region will also be affected, and so will the size of the energy potential hump in front of the cathode. In order to model this effect, we use the results of our recent EMC simulations of current self-quenching effects in a cathode similar to the one considered here. To simulate the effects of current self-quenching the following analytical



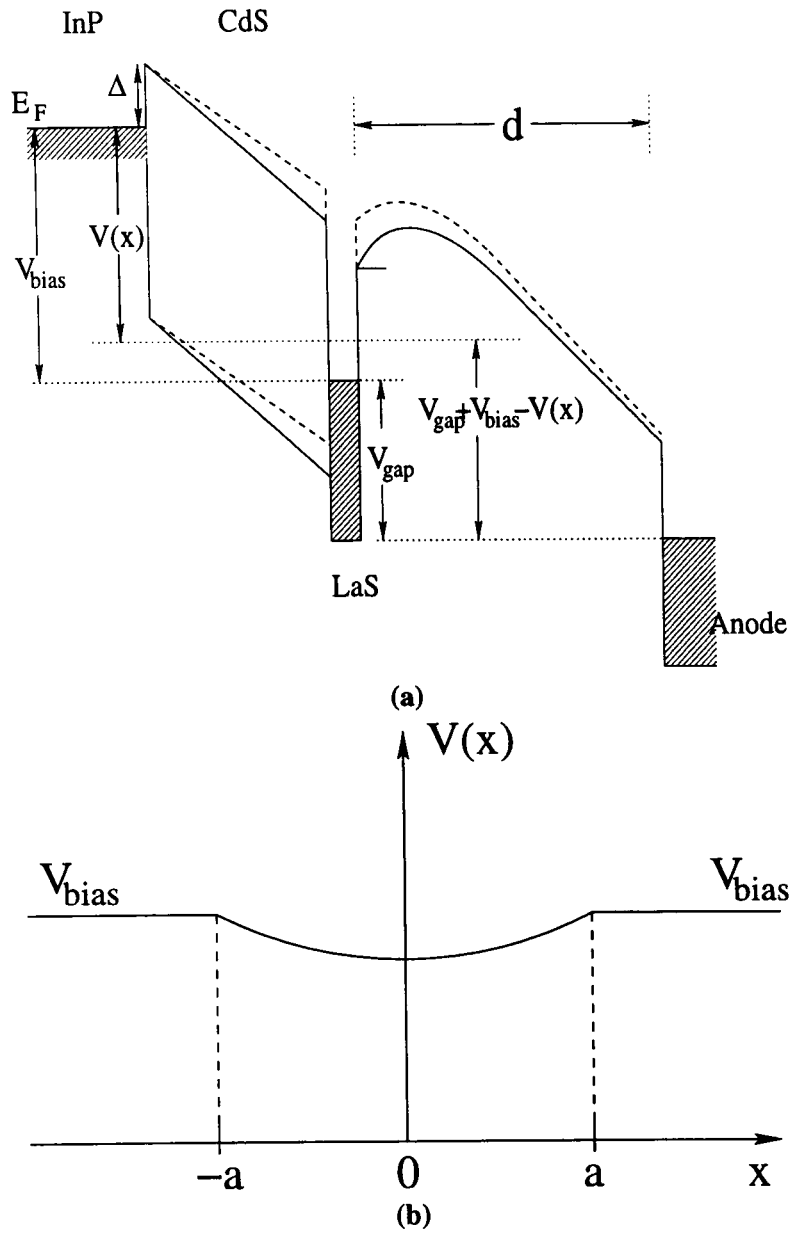


Figure 29: (a) Energy Band Diagram across the Metal/CdS/LaS Cold Cathode; (b) Lateral Potential Drop Between the two Metal Fingers used to Bias the Cathode

expression is used to model the ratio  $\eta$  between the anode current density ( $J_A$ ) and the current density emitted across the metal/CdS/LaS ( $J_{em}$ ):

$$\eta = \frac{J_A}{J_{em}} = \eta^* + \frac{1 - \eta^*}{1 + e^{(J_{em} - J_{th})/\sigma}}, \quad (75)$$

where  $\eta^*$  is the limiting value of the ratio for large values of the injected current density  $J_{em}$ ,  $J_{th}$  and  $\sigma$  are the parameters used to reproduce the transition region, and the sudden drop of the anode current when self-quenching occurs at large values of  $J_{em}$ . The parameter  $J_{th}$  is a threshold value above which current self-quenching is dominant. The parameter  $\sigma$  characterizes the extent of the transition region to the self-quenching regime. Equation (75) also leads to the correct limit,  $J_A = J_{em}$ , when  $J_{em}$  is far below threshold and no hump forms in front of the cathode. The parameters  $J_{th}$ ,  $\sigma$  and  $\eta^*$  depend on the amount of inelastic scattering in the CdS layer and also on the potential across the vacuum gap. The gap dependence is, however, rather smooth and, since the potential across the gap is kept at 1 V in all simulations, we neglect the dependence of  $J_{th}$ ,  $\sigma$  and  $\eta^*$  hereafter.

The numerical simulations then proceed as follows. For a given cathode configuration, the amount of current trapped in the LaS thin film is calculated as  $J_{capt} = J_{FN} - J_A$ , where the anode current  $J_A$  is given by Equation (75). above. The current density emitted from the metal/CdS/LaS cathode  $J_{em}$  is calculated using the results of Section 3, which takes into account inelastic scattering in the CdS and LaS layers and the multiple reflections at the CdS/LaS and LaS/vacuum interfaces. The emitted current  $J_{em}$  is a fraction of the FN current emitted across the metal/CdS interface, i.e.,  $J_{em} = \eta_1 J_{FN}$ . The function  $\eta_1$  also depends on the lateral potential and therefore on the lateral position. Thus the captured current can be written as  $J_{capt} = (1 - \eta_{tot})J_{FN}$ , where  $\eta_{tot} = \eta\eta_1$ . The quantity  $\eta_{tot}$  is given as  $\eta_{tot} = J_A/J_{FN}$ .

The calculation of the lateral variation of the anode current density is performed using an iterative procedure. First, the potential across the CdS layer is assumed independent of the lateral position. The effect of current crowding is then included using the technique outlined in reference [23], and the new lateral potential energy profile is used to calculate the new captured current density  $J_{capt}$ , which is now a function of the lateral position. The procedure is then iterated until convergence is obtained on a self-consistent solution for the anode current density.

### 4.3 Results

The metal/CdS/LaS cold cathode with the device parameters listed in Table 6 is considered. The interplay of current crowding and current self-quenching effects is studied for different emission window widths. The cathode to anode spacing is set to  $15 \mu m$  and  $V_{gap}$  is set to 1 V for all the simulations.

**Table 6: Physical Parameters of the Cold Cathode**

Thickness of CdS thin film	75 Å
Emission window width	(50,100,200,500 $\mu m$ )
Thickness of LaS thin film	24.6 Å
Electron mean-free path in CdS thin-film	300 Å
Electron mean-free path in LaS thin-film	300 Å
Barrier height at metal(Au)/CdS interface	0.78 eV
Anode to cathode spacing	15 $\mu m$

Figure 30 shows the ratio of  $\eta = J_A/J_{em}$  as a function of emitted current densities, as determined by Equation (25), with the values of the parameters  $J_{th} = 36 \text{ A/cm}^2$ ,  $\sigma = 4.57 \text{ A/cm}^2$  and  $\eta^* = 0.05$ . The points denoted by \* are the data points obtained by the EMC simulations. The dotted line is the fit of these points to Equation (75). The cathode is simulated for two bias points of  $V_{bias} = 3.15 \text{ V}$  and  $3.3 \text{ V}$ , where the injected electron current densities  $J_{em}$  at the edges of the emission window are equal to  $44.5 \text{ A/cm}^2$  and  $98.1 \text{ A/cm}^2$ , respectively.

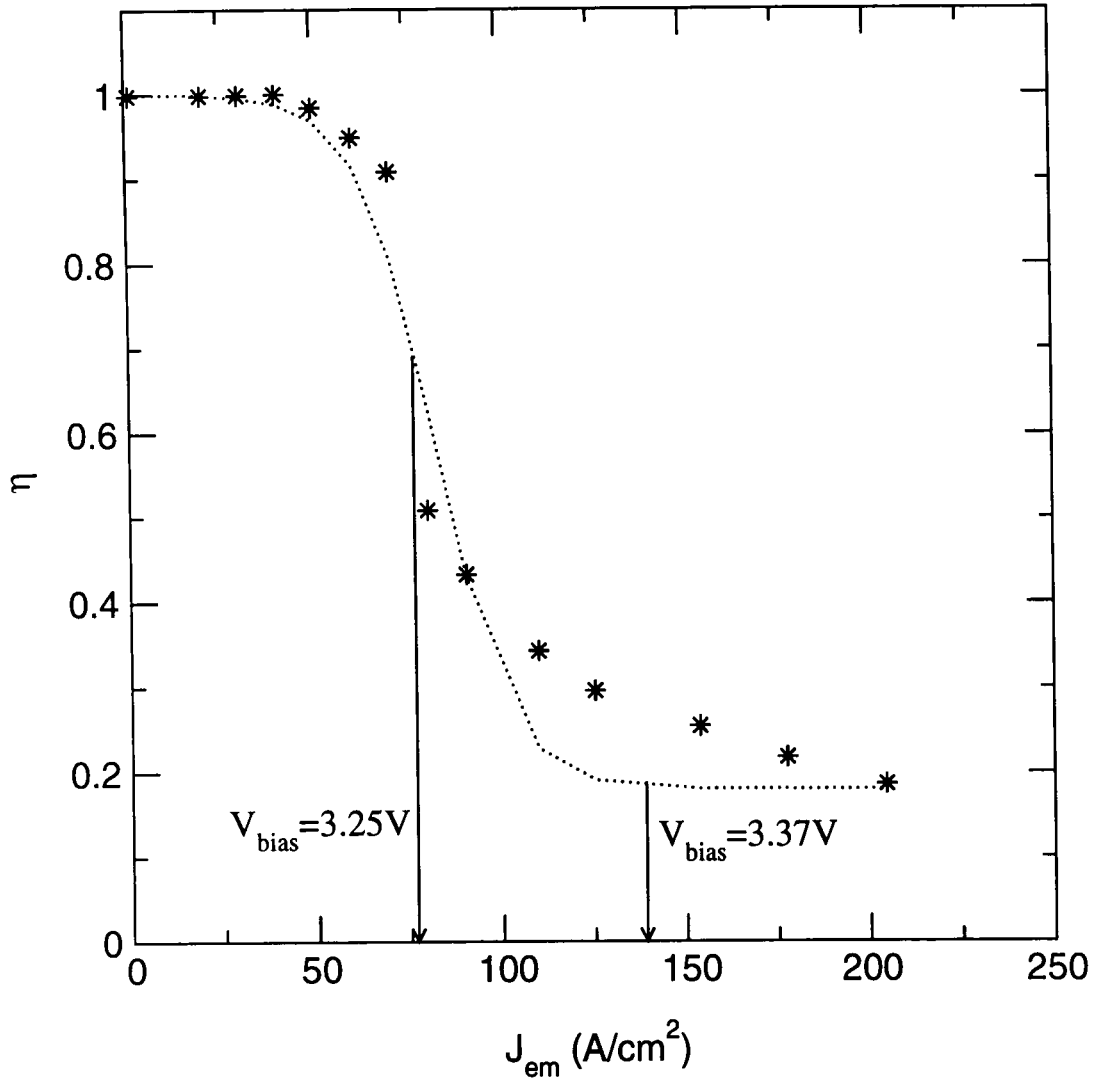


Figure 30: Ratio  $\eta$  of the Anode to Emission Current Densities Showing the Onset of Current Self-Quenching at Large Value of  $J_{em}$ .

In the first case, the injected current density is located within the transition region for the anode current toward the regime of current self-quenching. For the second case, the emitted current density is well within the regime of current self-quenching.

**4.3.1 The  $V_{bias} = 3.15$  V Case:** Figure 31 shows a plot of the lateral potential variation across the LaS window for different window widths. The width of the emission window is equal to  $2a$ , and the lateral dimension is normalized to half the window size. For the largest window, the potential in the middle of the window reaches a minimum of 2.95 V, which is roughly 6 percent below the bias at the edges of the emission window.

Figure 32 shows a plot of the lateral variation of the anode current density  $J_A$  for different emission window widths. For the full lines, from top to bottom at  $x = 0$ ,  $W$  is equal to 50, 100, 200, and 500  $\mu m$ , respectively. For the dashed lines, from bottom to top at  $x = 0$ , the  $W$  is set to 50, 100, 500, and 200  $\mu m$ , respectively (the dashed and full lines represent the  $J_A$  profiles when the effects of space-charge in the vacuum region are included and neglected, respectively). For the 50 micron window, the lateral potential drop at the center of the emission window is small, as shown in Figure 31. Hence, the FN current and associated  $J_{em}$  leaving the cathode at the center of the window is about the same as at its edges. Since this current density is within the self-quenching regime for the choice of  $V_{bias}$ , the anode current is fairly constant and roughly equal to  $2 A/cm^2$ . As the window size increases, the lateral potential drop is becoming more substantial.  $J_{em}$  is reduced more in the center and the factor  $\eta$ , which represents the importance of space-charge effects in the vacuum region increases. Since the larger  $\eta$  correlates with reduced space-charge effects, fewer electrons are being reflected due to a decreasing energy potential hump in front of the cathode as we move closer to the center of the emission window. Correspondingly, the anode current increases while approaching the center of the emission window. The larger the emission window, the more pronounced this effect will be. The deeper decrease of the lateral potential in the center allows  $J_{em}$  to sweep a broader portion of the transition region shown in Figure 30.

Figure 33 shows the lateral variation of  $\eta_{tot}$  which is the product of  $\eta_1$  and  $\eta$  for different window widths. In this Figure, from bottom to top, the  $W$  is set equal to 50, 100, 200, and 500  $\mu m$ , respectively.  $\eta_{tot}$  is above 0.75 over a larger fraction of the emission window with width of 500  $\mu m$ . This value corresponds to a regime where the effects of self-quenching of the anode current is rather weak. The sharp increase in  $\eta_{tot}$  in the center of the emission window is due to the strong variation of  $\eta$  with the lateral potential  $V$ , whereas the function  $\eta_1$  is found to be a rather weak function of  $V$ . This explains why  $J_A$  first increases from the edges of the emission window where self-quenching is dominant, i.e.,  $\eta_{tot}$  is small. Once  $\eta_{tot}$  is above 0.75, very few electrons are being reflected by the vanishing energy potential hump in front of the cathode. The electrons are being captured in the LaS well primarily because of the finite transmission coefficients at the CdS/LaS and LaS/vacuum interfaces and the effects of inelastic scattering in the CdS and LaS layers. As a result, current crowding effects occur between  $X_1$  and  $X_2$  in Figure 32, mostly without the feedback of the energy potential hump in front of the cathode.

**4.3.2 The  $V_{bias} = 3.3$  V Case:** Figures 34 and 35 show the lateral variation of  $\eta_{tot}$  and  $J_A$  respectively. In Figure 34, from bottom to top,  $W$  is equal to 50, 100, 200 and 500  $\mu m$ . On the scale used, the curves for  $W = 50$  and 100  $\mu m$  are not distinguishable. In Figure 35, for the full lines from top to bottom at  $x = 0$ ,  $W$  is equal to 50, 100, 200, and 500  $\mu m$  and for dashed lines, from bottom to top at  $x = 0$ ,  $W$  is equal to 100, 50, 200, and 500  $\mu m$ . Because the bias across the CdS layer is larger, the emitted current density is deeper into the regime of current self-quenching. As a result, for a given window width, it takes a larger distance from the edges before the lateral potential drop falls below a value necessary for the value of the emitted current to sweep the transition regime shown in Figure 30. Before this happens, the coefficient  $\eta$  defined by Equation (75) is nearly constant and so is  $\eta_{tot}$ . From Figures 33 and 34 we can see that  $\eta_{tot}$  stays constant over a larger fraction of the emission window close to the edges. In these regions, the amount of current captured is rather independent of position and the regular current crowding effects take place, i.e.,  $J_A$  falls below its value at the edges. Moving closer to the center of the emission window, the lateral potential drop will eventually make  $J_{em}(x)$  fall within the transition regime of Figure 30.

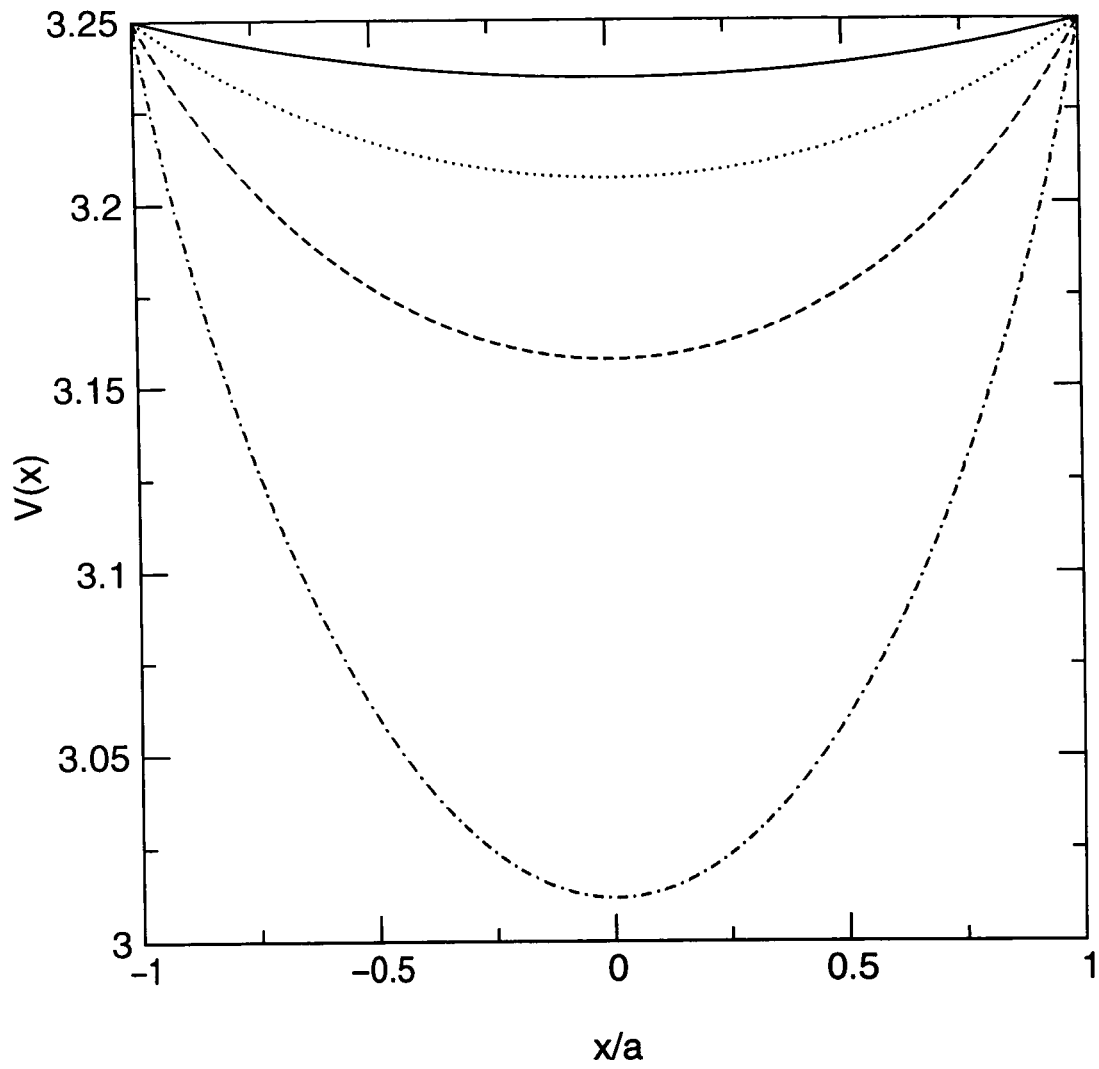


Figure 31: Lateral Potential Variation of the Potential Drop across the LaS Windows of Various Widths

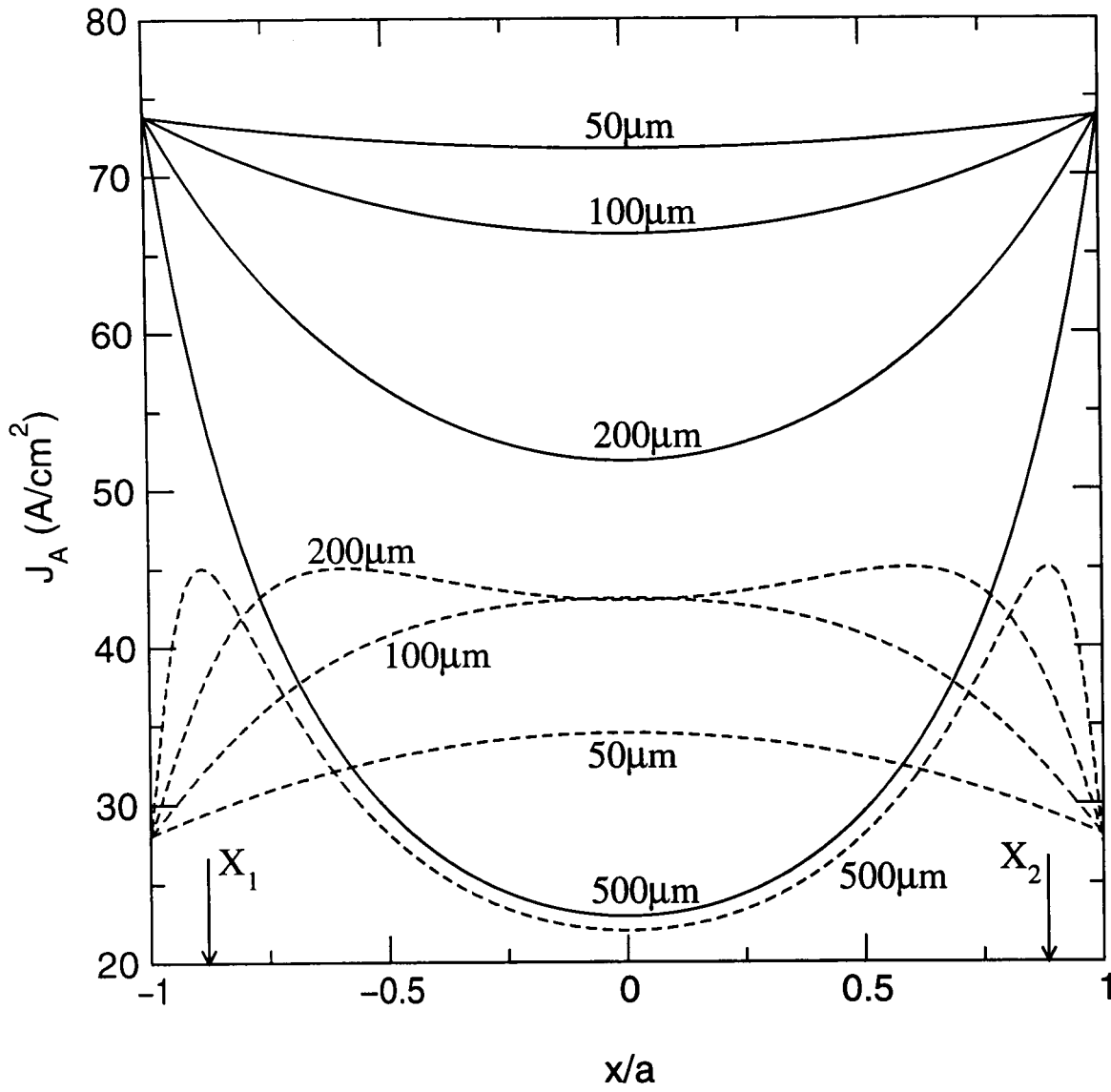


Figure 32: Lateral Variation of  $J_A$  for Different Window Widths

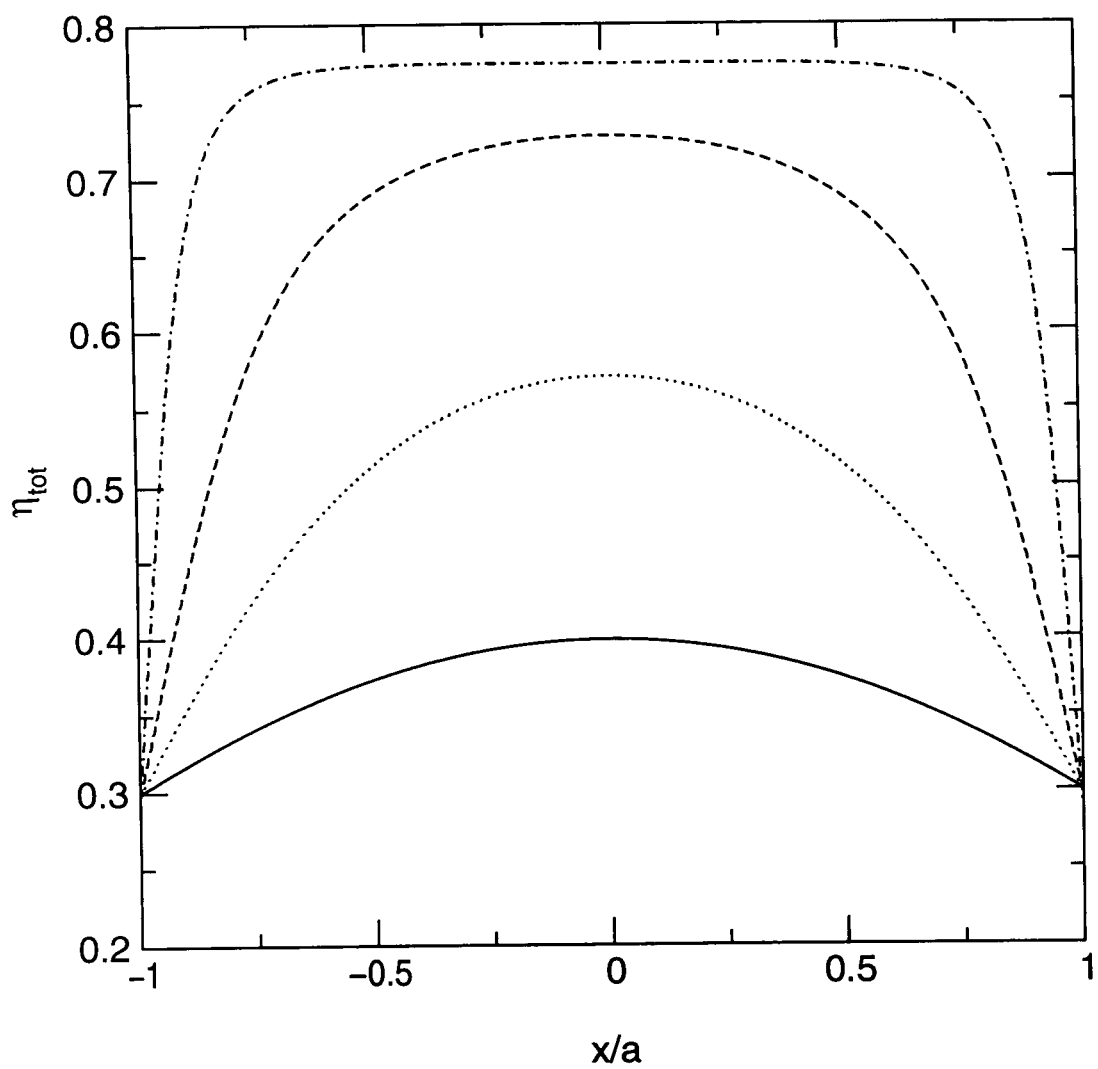


Figure 33: Lateral Variation of  $\eta_{tot}$  for Different Window Widths

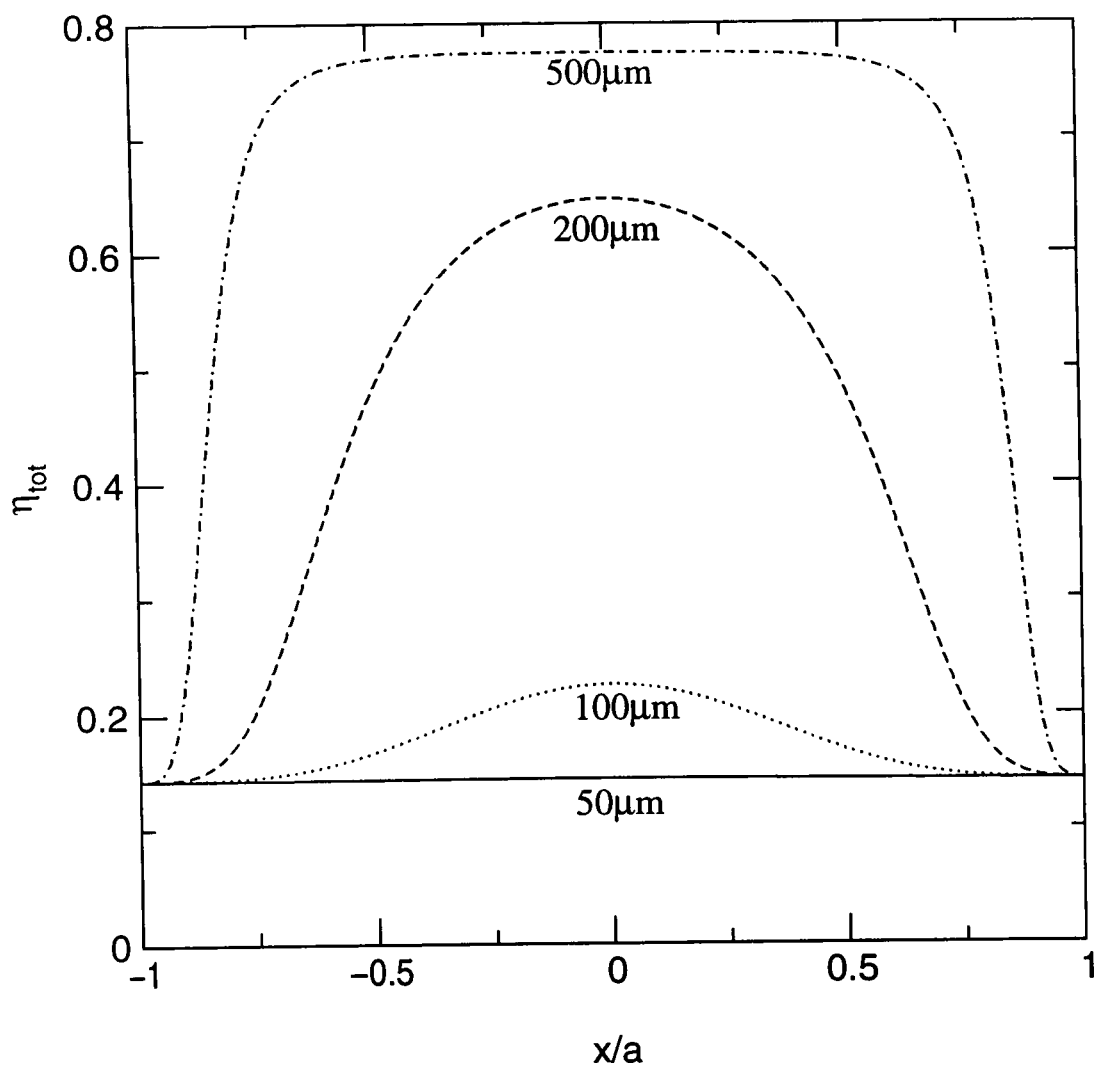


Figure 34:  $\eta_{tot}$  Variation across the Emission Window



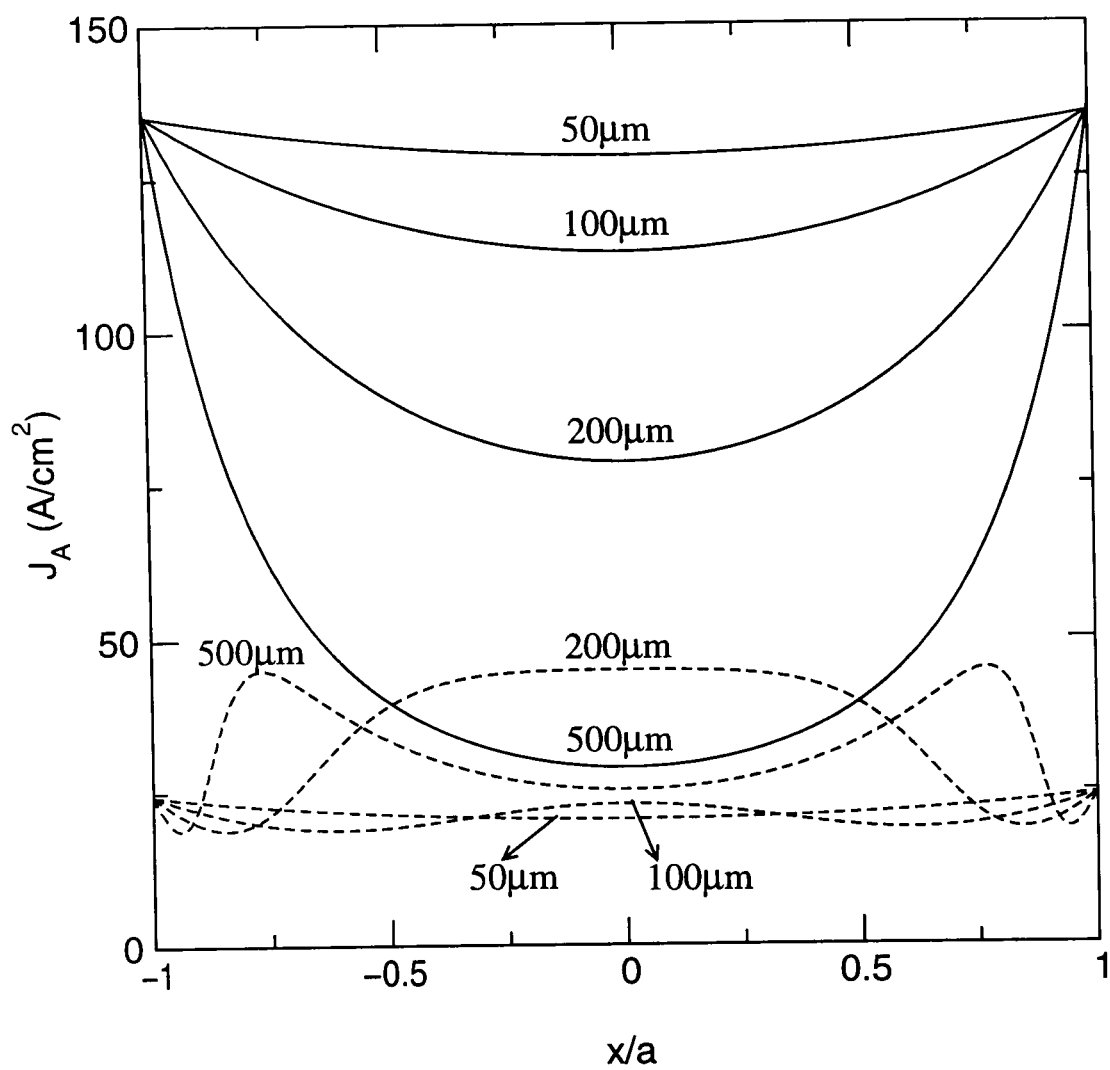
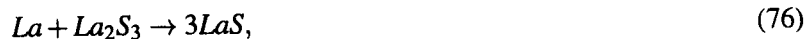


Figure 35:  $J_A$  variation for  $V_{bias} = 3.3 \text{ V}$

## 5. Growth and Characterization of Bulk LaS Samples

### 5.1 Introduction

The approach we pursued to build the InP/CdS/LaS cold cathode was to grow both CdS and LaS layers by RF magnetron sputtering. The deposition of CdS on InP substrates using this method was investigated by Hai Tang, a student under the supervision of Dr. Boolchand [13] and is described in Section 6. The LaS deposition is described in Section 7. In this Section, however, we first describe our efforts to synthesize enough LaS material to make a target for RF magnetron sputtering with the stoichiometry and purity needed. We describe two routes to synthesize pure LaS and the different methods used to characterize the materials. Because LaS is not available commercially, La and  $La_2S_3$  were taken to be the starting materials for the synthesis of LaS. These two materials, when heated appropriately, undergo the following reaction:



which we refer to as the sesquisulfide route. The starting materials were purchased from Cerac, Inc. in Wisconsin. The La powder was  $\sim 40$  mesh and the  $La_2S_3$  powder was  $\sim 200$  mesh (mesh is a common way to refer to the size of the grains). Both powders had a purity level of 99.9 percent. Pure LaS is quite difficult to prepare because La metal rapidly oxidizes in air. It reacts easily with trace amount of oxygen and water vapor to form oxides and hydroxides:



Hence, special handling of the starting materials is required. We handled the materials in a glove box which was maintained at an inert nitrogen ambient. Furthermore, La and S form several kinds of binary compounds like  $La_3S_4$  and  $La_2S_3$  besides  $LaS$  as shown on the phase diagram in Figure 36. Hence, the starting materials must be combined with the exact stoichiometry, otherwise other phases can be formed.

La can also react simultaneously with S and O to readily form a quite stable ternary oxysulfide compound  $La_2O_2S$ :



The formation of this oxysulfide phase in the preparation of rare-earth sulfides is a problem since it leads to an end product with increased WF. Under this effort, we have removed the oxysulfide phase in our bulk samples using a carbon reduction technique initially investigated by three students in our lab [13, 29, 30].

### 5.2 Techniques for Bulk LaS Synthesis

#### 5.2.1 The Arc Melting Process

**Step-1: Melting:** In this technique, stoichiometric quantities of La metal cubic pieces (about 1 cm on a side) and  $La_2S_3$  powder ( $\sim 200$  mesh) are placed at the bottom of a semispherical copper cup, which is cooled by running chilling water while passing an arc through the sample. The arc melting chamber is maintained at one-third atmospheric pressure of Ar. The temperature of the arc is estimated to be several thousand degrees celsius and well above the melting point of LaS. Since the melting point of La metal ( $918^\circ\text{C}$ ) is less than that of  $La_2S_3$  ( $1960^\circ\text{C}$ ), the arc leads to the melting of the elemental La, which then wets the  $La_2S_3$  powder. The materials are arced for a few seconds, after which a button of reacted material is formed. Once the chamber is cooled, the button is then turned over and again arced. This process is done about three times to ensure proper mixing of the sample. The button of the formed LaS sample is then sand blasted to remove the impurities which have moved to the surface during the arc melting process.

**Step-2: Purification by Carbon Reduction:** The X-ray scan of the arc melted sample after step-1 revealed the presence of the oxysulfide impurity phase ( $La_2O_2S$ ). This formation is due to the presence of trace amounts of

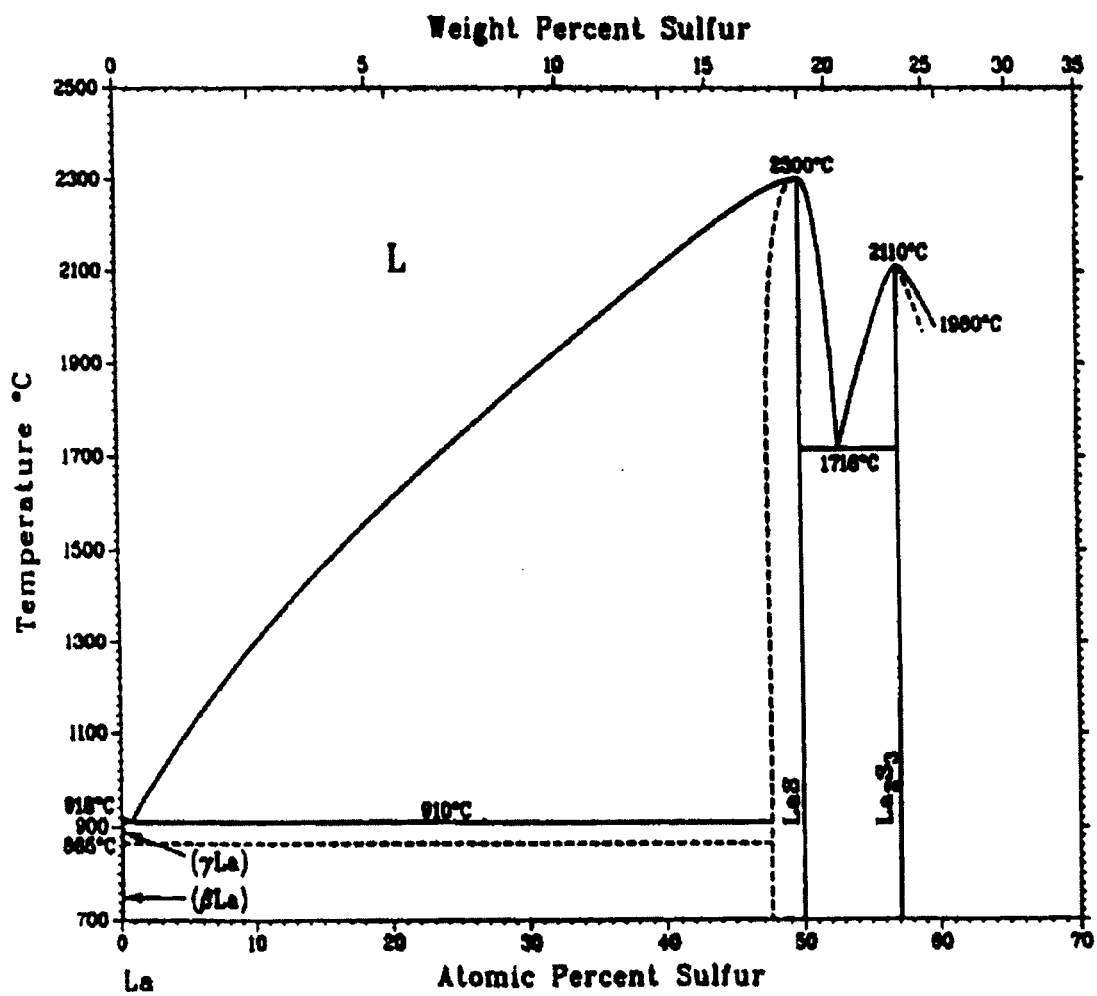
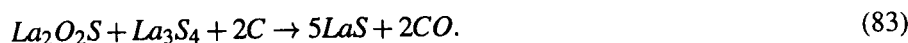
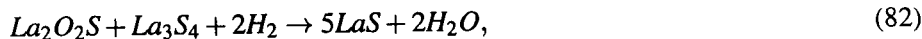
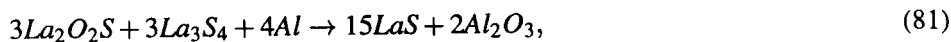


Figure 36: Phase Diagram of LaS

oxygen in the arc melting chamber, and also due to the exposure of the starting materials to atmosphere while being transferred from the glove box to the arc melting chamber. The presence of the oxysulfide phase in the sample may cause the work function of LaS to increase. Since the presence of oxygen cannot be eliminated completely in this process, it is important to find a method for removing the oxygen in the sample. There are several methods to reduce and eliminate  $La_2O_2S$  from the bulk sample, including the following:



We selected the carbon reduction process given by Equation (83) for purifying the arc melted sample. A predetermined amount of carbon powder is mixed thoroughly with the sample obtained after step-1, and pellets are formed. These pellets are then heated in a vacuum furnace (Brew furnace) at 1600° C for 4 hours. The precise amount of carbon was determined by trial and error until the presence of the oxysulfide peaks in the XRD scan was suppressed.

The method for making LaS bulk sample described above has also been applied successfully by other students in our lab to make NdS (neodymium sulfide) and ErS (erbium sulfide). A full account of the preparation of LaS and NdS bulk samples using the arc melting procedure has been published in reference [31]. In the latter stage of this contract effort, we acquired additional funding to purchase a high-temperature, high-vacuum furnace from Thermal Technologies, Inc.

### 5.2.2 The High-Temperature Vacuum Heating Process

The La and  $La_2S_3$  powders (40 and 200 mesh, respectively) from Cerac Inc., are first weighed in a stoichiometric ratio in a glove bag in a nitrogen ambient, mixed thoroughly, and then heated in our vacuum furnace in a tantalum crucible. The refractory metal furnace we acquired from Thermal Technologies has a mechanical pump and a diffusion pump with a liquid nitrogen trap so that it can reach a high vacuum of  $10^{-7}$  torr. The furnace has a programmable temperature control unit which helps us to set the heating time, and maximum heating temperature, as well as the ramp-up and ramp-down times. In all of the heating cycles, we use a trapezoidal heating cycle, as shown in Figure 37.

The starting material mixture is heated at 1800 °C for 2 hours. The ramp-up and ramp-down rates are set to 100 °C/min. Once the sample is cooled, the reacted mixture is crushed and remixed thoroughly and made into small compact pellets, and again heated to 1800 °C for 2 hours. At the end of this second heating cycle, the pellets appear golden-yellow in color. The XRD scans at the end of the second heating showed only LaS peaks, and had no  $La_2O_2S$  impurity phase in it. Hence, this method of synthesis is superior to that by arc melting, as in this process we do not need to add any carbon in order to purify the material. A pure sample was obtained at the end of the heating cycle. The temperature and duration of the heating cycle was very critical to the quality of the sample. Several trial runs were made at different temperatures and different times, and this set of temperature duration was found to yield the best sample. We used this method of growing LaS, as opposed to the arc melting process, to make a 2-inch-diameter and  $\frac{1}{8}$ -inch-thick target to be used for RF magnetron sputtering of LaS thin films. Figure 38 shows an optical micrograph of pure bulk LaS as seen using the microscope on the Raman spectrometer in Dr. Boolchand's lab. In this Figure, the smaller regions (blue in color) correspond to the  $La_3S_4$  phase [29].

## 5.3 Characterization of Bulk LaS

### 5.3.1 Powder XRD

XRD is an efficient and popular technique to identify and characterize unknown crystalline materials. Monochromatic X-rays are used to determine the interplanar spacings and hence the lattice constant of the unknown materials. In a powder XRD, the sample is analyzed in a powder form, with grains in random orientations to ensure that all the crystallographic directions are sampled by the X-ray beam, thereby providing a structural fingerprint of the unknown

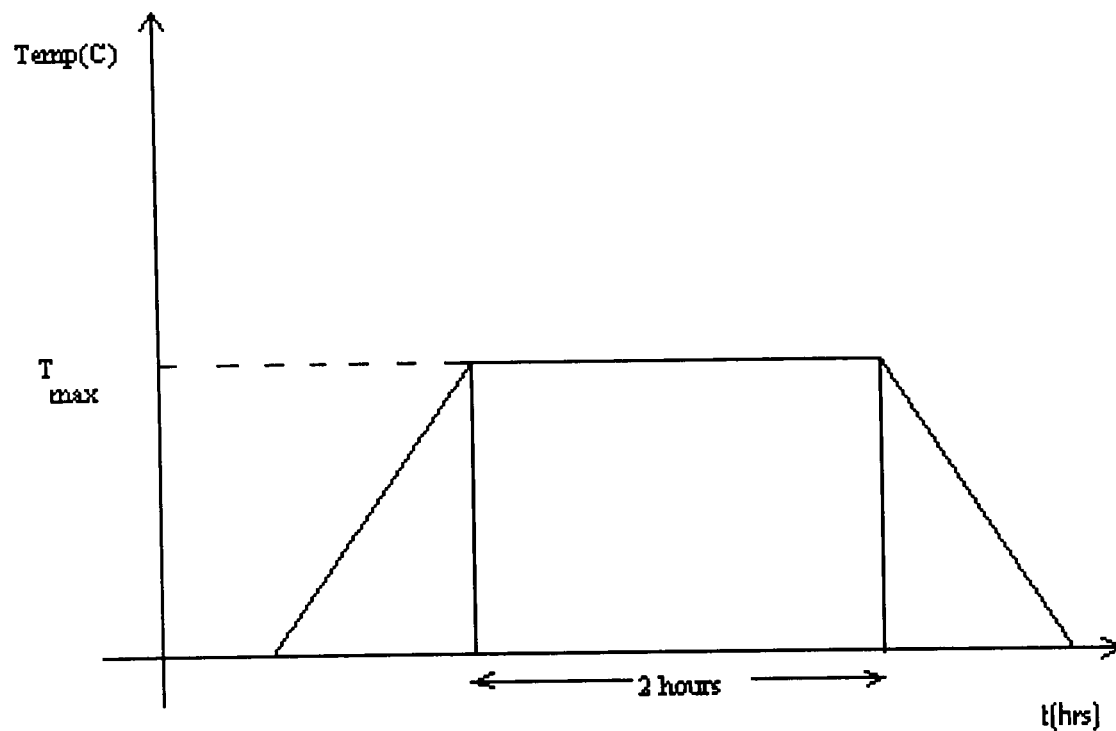


Figure 37: Typical Heating Cycle Used During Growth of Rare-Earth Samples Using the High-Temperature Furnace From Thermal Technologies, Inc.

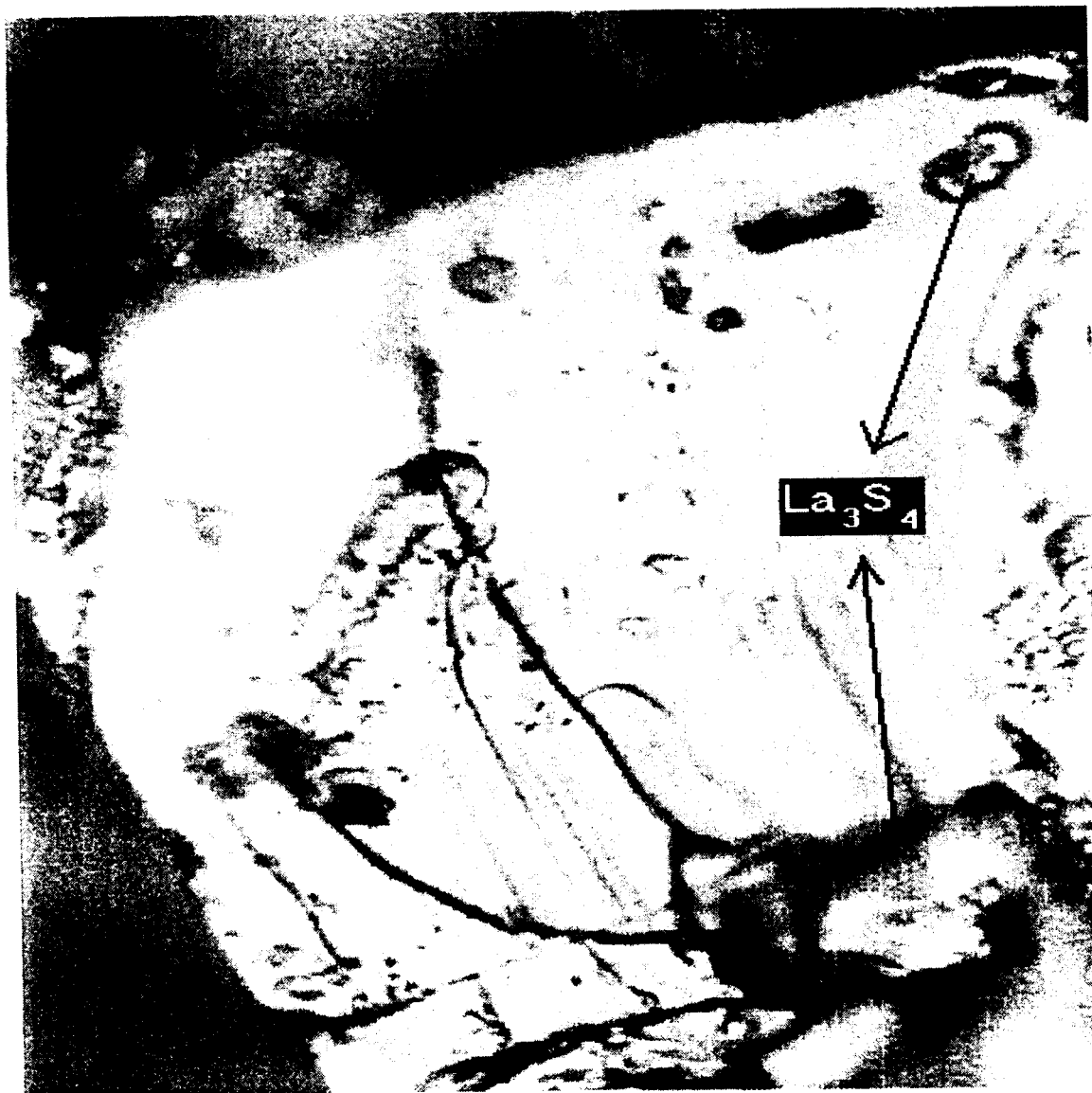


Figure 38: Optical Micrograph Showing a Large Crystallite (Gold Platelet) of the Cubic  $\text{LaS}$  With a Staircase-Like Growth Pattern

material. Mixtures of crystalline materials can also be analyzed and relative peak heights of multiple materials may be used to obtain semiquantitative estimates of the abundances. Changes in peak position that represent either compositional variation or structural-state information are readily detectable. Thus XRD is a versatile, nondestructive analytical technique for identification and quantitative determination of the various crystalline compounds or different phases present in crystalline materials. Identification of the unknown sample is done by comparing its XRD pattern with an internationally recognized database (JCPDS) containing the reference patterns for a large number of materials.

We used a RIGAKU D-200 model XRD machine. To make an XRD scan of bulk samples, a fine powder of the sample is spread onto a glass slide with the help of high quality stop cock grease, to ensure proper adhesion of the powder to the glass slide. The glass slide is then mounted on a circular rotating chuck using black clay in such a way to ensure that the reflection surface is exactly on the same plane as the mounting surface.

### Arc melted sample

Figure 39(a) shows the XRD pattern of the LaS sample after step-1 of the arc melting process described in Section 5.2.1. The LaS peaks are marked as **A** and the impurity peaks (of  $La_2O_2S$ ) are indicated as **B** in the figure. The (hkl) Miller indices of LaS are indicated next to each peak. The presence of oxysulfide peaks in the arc melted sample required the use of carbon reduction process as described in Section 5.2. Figure 39(b) shows the X-ray scan after carbon reduction. We note that all the oxysulfide peaks have disappeared and the only peaks in the scan are that corresponding to the cubic-rocksalt phase of LaS. Close examination of the Bragg reflections required a two-peak deconvolution. This is shown in Figure 40. As shown in the inset of this Figure, some of the Bragg reflection peaks are best approximated by a two-peak fit. This deconvolution suggests the presence of a majority LaS phase ( $a_0 = 5.857(2) \text{ \AA}$ ) and a minority LaS phase ( $a_0 = 5.875(2) \text{ \AA}$ ) in our samples. The two sets of reflections may come from a S-rich and a S-poor phase present in the samples, with the S-poor phase possessing a somewhat larger lattice constant. These results clearly suggest that the cubic phase can be stabilized over a range of La:S stoichiometry, as is known from the phase diagram. The typical full width at half maximum (FWHM) is found to be 0.14 degrees, suggesting that the samples obtained in the present synthesis are rather well crystallized.

For the extraction of the lattice constant, a peak fit profile is done on the X-ray data, and Table 7 shows the result of the analysis. The (h k l) indices are obtained by matching the X-ray spectrum with the JCPDS data files. The lattice constant is evaluated using the following formula:

$$a = d\sqrt{(h^2 + k^2 + l^2)}. \quad (84)$$

### High-Temperature Vacuum Heating Sample

Figure 41 shows the XRD spectrum of the LaS sample synthesized in the high-temperature vacuum furnace. Figure 41(a) is for the La and  $La_2S_3$  mixture heated at 1800 °C for 2 hours. The sample is then mixed, pelletized, and then heated again at 1800 °C for 2 hours, and the spectrum of this sample is shown in Figure 41(b). Comparing the two X-ray spectra, we note that in Figure 41(b) the number of counts of the peaks has increased, and there are no impurities in the sample. Hence, we have succeeded in synthesizing a pure LaS sample without the need for the carbon reduction process described earlier.

**Table 7: XRD Line Shape Analysis**

Peak(hkl)	2-Theta		d (Å)		a (Å)	
	Peak-1	Peak-2	Peak-1	Peak-2	Peak-1	Peak-2
111	26.3202		3.3833		5.8600	
200	30.4993		2.9285		5.8570	
220	43.6523		2.0718		5.8599	
311	51.7233		1.7659		5.8568	
222	54.1915		1.6911		5.8581	
400	63.5208	63.2364	1.4634	1.4693	5.8536	5.8772
331	69.9623	69.7300	1.3436	1.3475	5.8566	5.8736
420	72.0566		1.3096		5.8567	
$a_{av} =$					5.8573	5.8754

### 5.3.2 Raman Spectroscopy

Raman scattering is a powerful vibrational spectroscopic tool to study materials. The micro-Raman equipment that we used is a T64000 model triple monochromator system from Instruments SA Inc., equipped with a microscope and a CCD detector. The exciting laser beam is focused to one micron spot size on the sample (as opposed to the macro-Raman, where the laser beam is typically 1 mm in size and a sample is sampled over a larger area). We chose the 514.5 nm line, with 4 mW power from an Ar-ion laser to excite the sample.

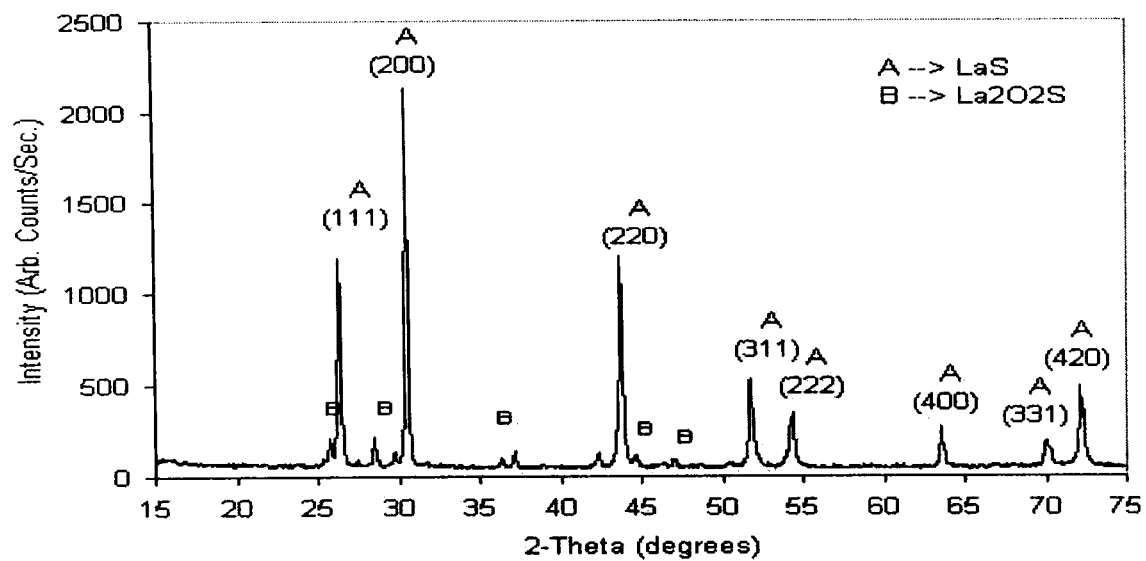
Cubic LaS in the rocksalt structure should display three zone-center optical modes which should be Raman silent because of inversion symmetry. The modes observed in Raman scattering (Figure 42) are either due to noncubic impurity phases or to defect-induced first order scattering which activates all vibrational modes in the Brillouin zone of the cubic phase to yield the full vibrational density of states (VDOS). The Raman scattering results on the samples complement the XRD results. In Raman scattering we observe changes in the VDOS due to a change in structure. In Figure 42, scans A, B, and C correspond to samples reduced in step-2 of the arc melting process with a C/LaS weight ratio of 0.3, 0.7, and 2.5 percent, respectively. The acoustic and optical phonon modes and some of their overtones are identified. Some of the impurity phases responsible for some of the sharp modes observed in the top two spectra are also identified. The peaks marked with asterisks correspond to the  $La_2O_2S$  phase and the arrows indicate the signature response of the  $La_3S_4$  phase. Since these impurity phases are non cubic, the Raman scattering from these phases is rather strong. In scan C, however, the sharp modes are absent, the scattering is extremely weak, and the vibrational modes are rather broad. These features of Raman scattering are characteristic of the VDOS of the cubic phase. These results are consistent with an improvement in sample quality due to carbon reduction.

The observed modes in scan C can be identified with specific phonons in the VDOS of the rocksalt phase. In LaS, the cation-anion mass ratio is close to 5:1. This permits the optic branch to be clearly separated from the acoustic one. We identify the  $261\text{ cm}^{-1}$  vibrational band with the longitudinal phonon (LO) phonon, the  $100\text{ cm}^{-1}$  band with the acoustic phonon (A), and the remaining vibrational bands as two-phonon modes (acoustic + optical) and 2LO mode. These results are in good agreement with an earlier report [32] where the LO mode and A modes were identified at  $268\text{ cm}^{-1}$  and  $96\text{ cm}^{-1}$ , respectively.

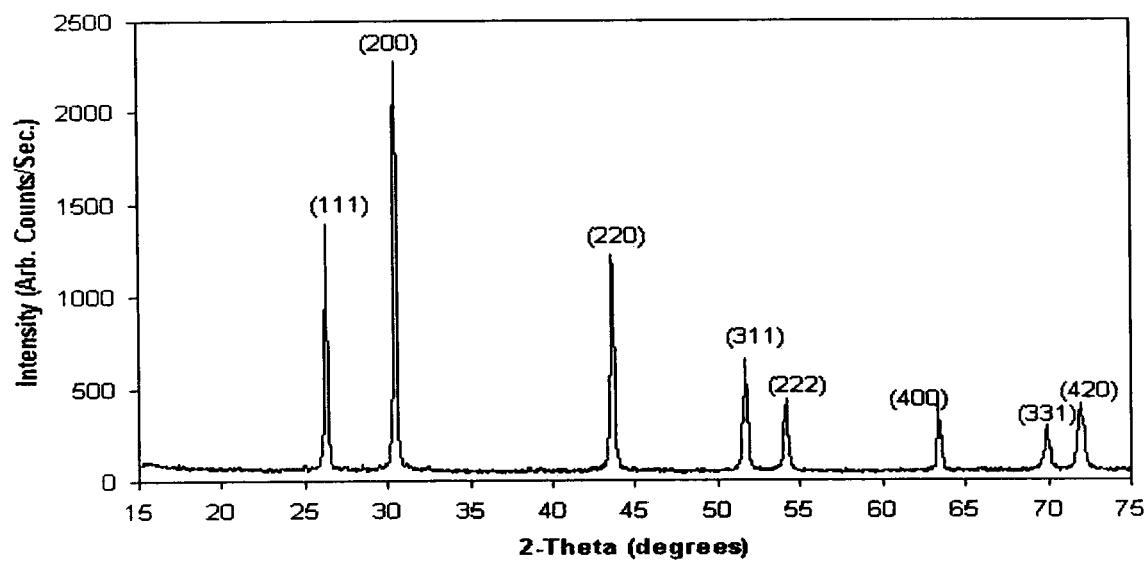
### 5.3.3 Work Function Measurements - Kelvin Probe Method

The WF of a metallic sample is the amount of energy required to move an electron from the Fermi level of a material to the vacuum level outside the sample with no kinetic energy. There are a large number of methods used





(a)



(b)

Figure 39: Comparison of XRD Scans of LaS Sample Produced (a) Right After the Arc Melting Process Step-1 and (b) After Step-2, Carbon Reduction (See Section 5.2)

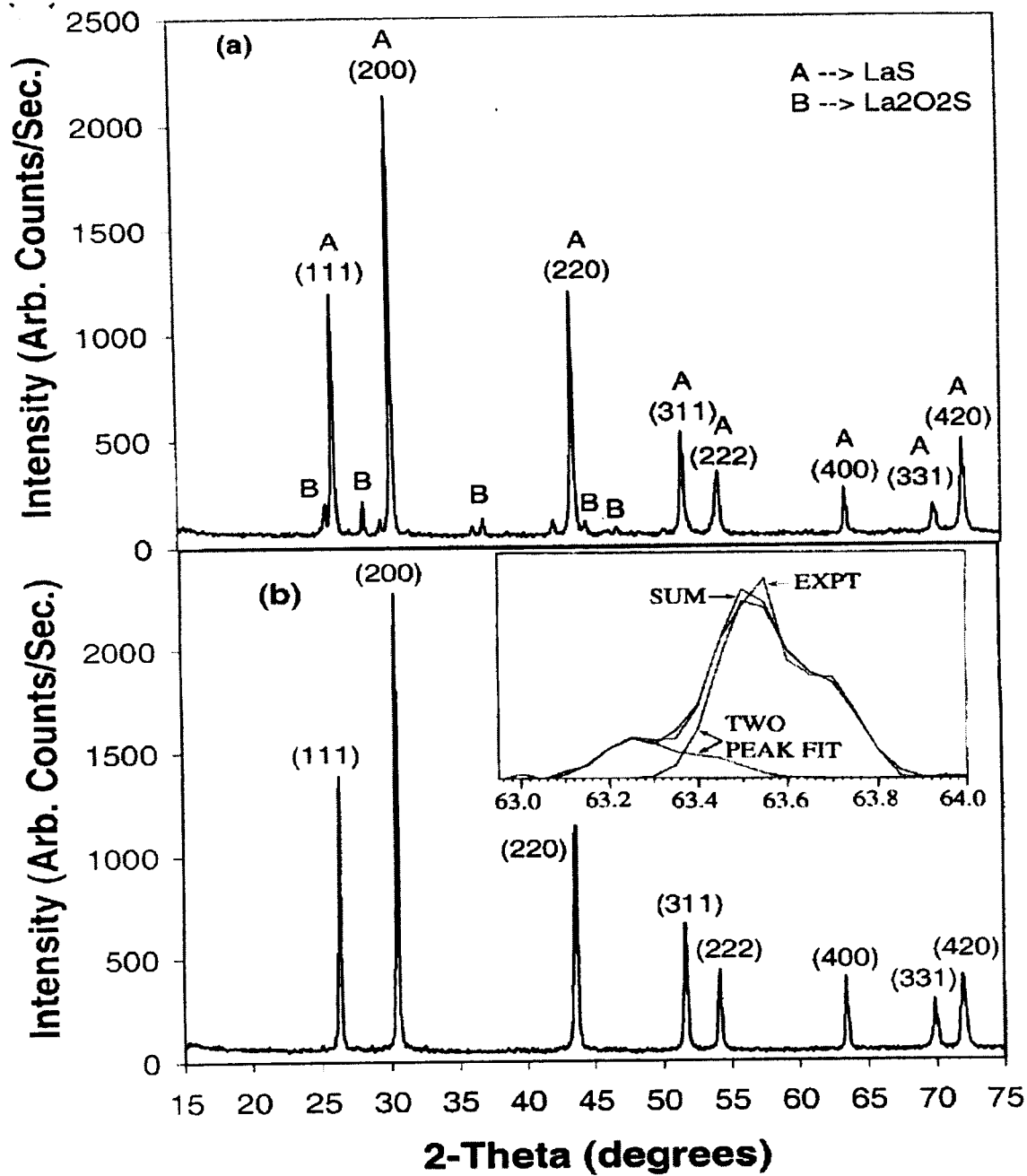


Figure 40: Comparison of XRD Scans of LaS Sample Produced (a) Right After the Arc Melting Process Step-1 and (b) After Step-2, Carbon Reduction (See Section 5.2)

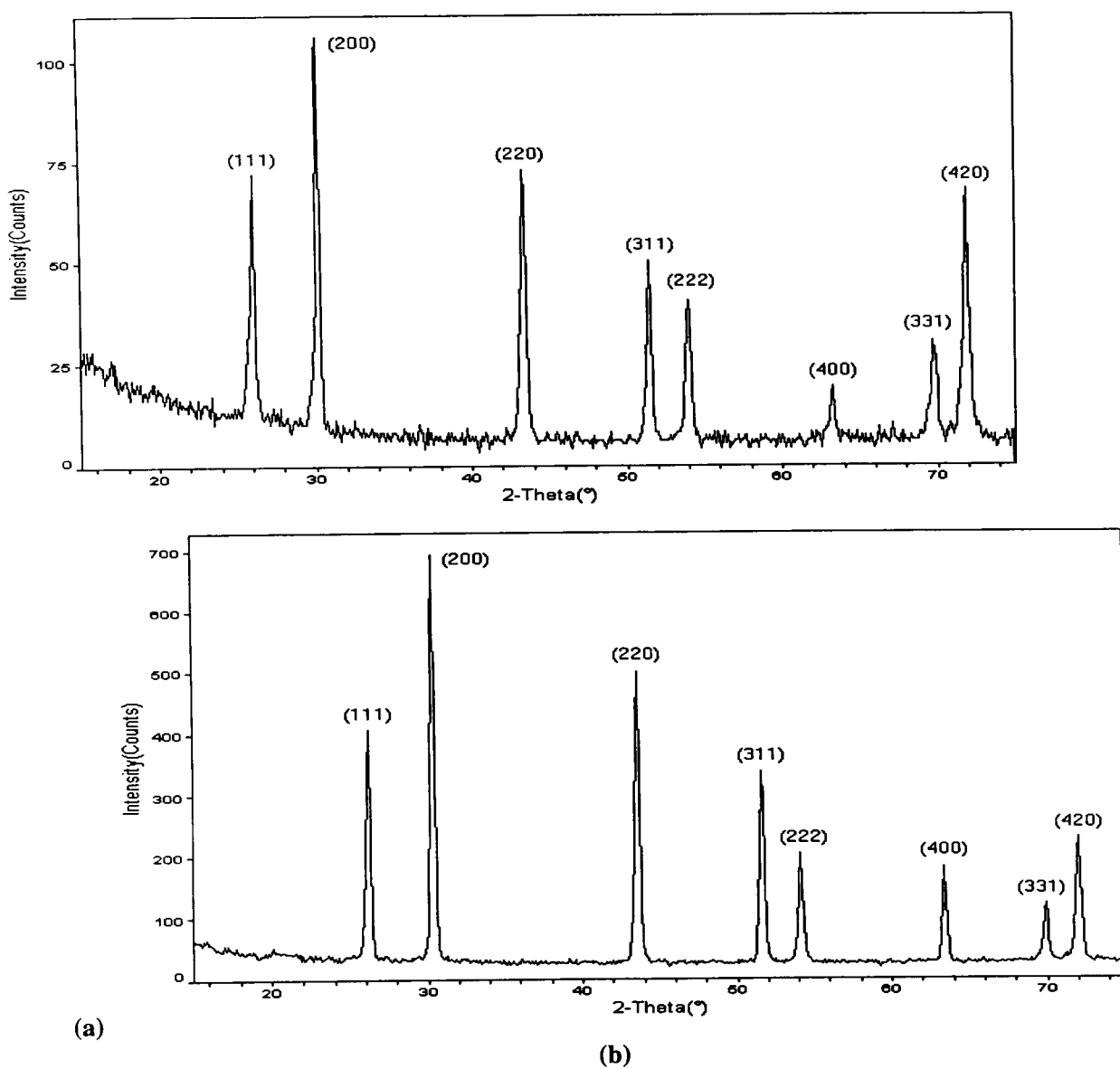


Figure 41: LaS Sample Synthesized in the Thermal Technologies, Inc. High-Temperature Furnace (a) Right After Heating at 1800 °C for 2 Hours (b) Mixing the Previous Sample, Pelletizing and then Heating again at 1800°C for 2 Hours

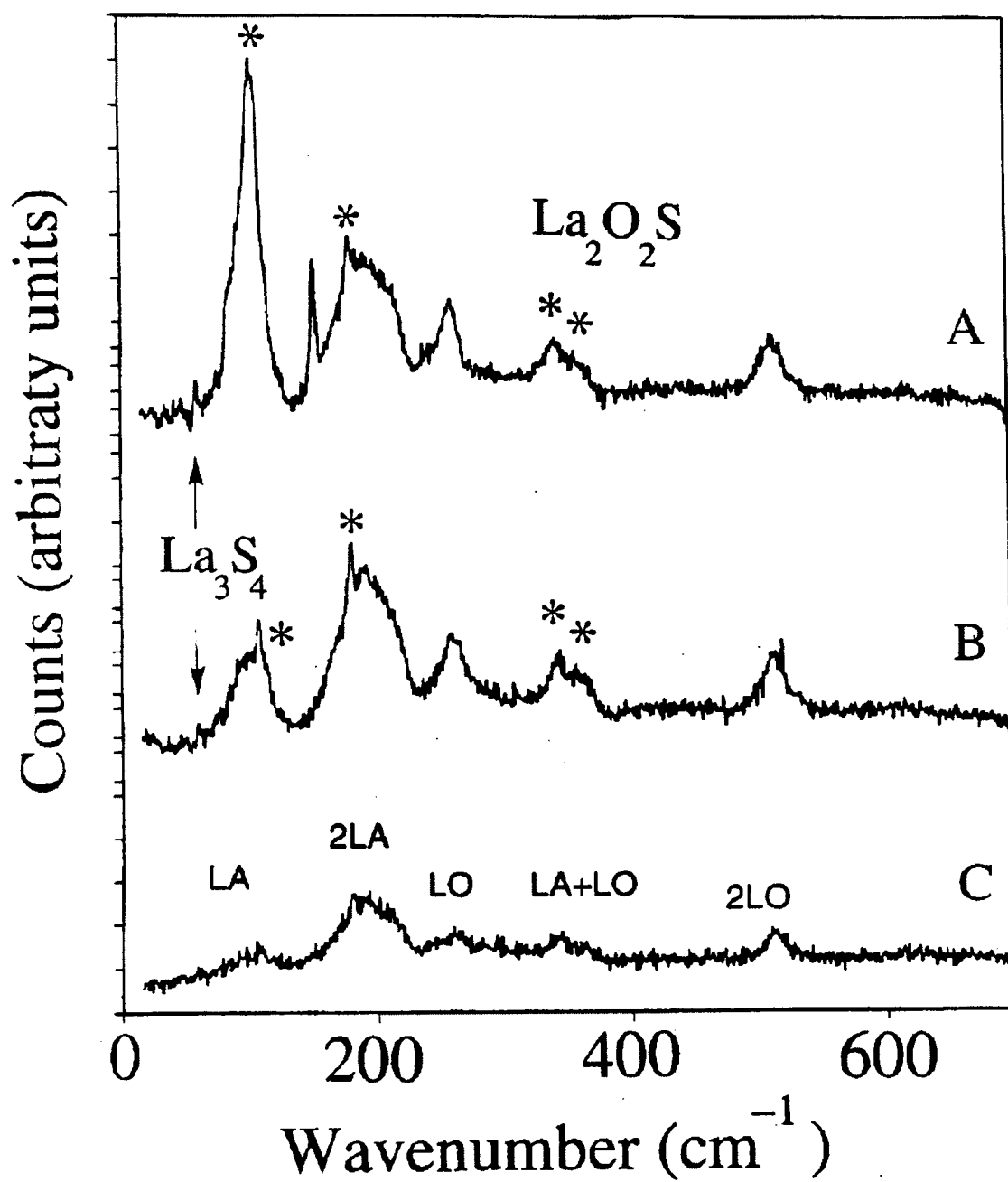


Figure 42: Raman Spectra of LaS Processed Using the two Step Arc-Melting Method

to measure the WF of metals and semiconductors including the thermionic emission method and the electron beam method [33]. We selected the Kelvin Probe method for our WF measurements. It is a non contact, non destructive vibrating capacitor device used for measuring the WF difference. The Kelvin Probe method was first postulated by the renowned Scottish scientist, W. Thompson (later known as Lord Kelvin) in 1861 [34].

The traditional Kelvin Probe method consists of a flat circular electrode (reference electrode) suspended above and parallel to a stationary electrode (the specimen), thus creating a simple capacitor. As shown in Figure 43, the two dissimilar metals are separated by a distance  $d$ . Before electrical contact is made, i.e., with SW1 open, the highest energy electrons in each metal occupy states at their respective Fermi level  $\epsilon_{f1}$  and  $\epsilon_{f2}$  located  $\phi_1$  and  $\phi_2$  electron volts below the vacuum level. Upon closing the SW1 switch, electrons flow from the metal having the lower WF to the higher one, i.e., from metal 2 to metal 1, resulting in a negative charge appearing on the inner face of metal 1 and a positive charge on metal 2. The contact potential  $V_c$  developed across the Kelvin capacitor  $C_k$  is given by  $V_c = 1/e(\phi_2 - \phi_1)$ , where  $e$  is the electronic charge, and the surface charge is given by  $Q_s = V_c C_k$ . The total surface charge is  $Q_s = (V_c + V_b)C_k$ , which is cancelled out at the value  $V_b = -V_c$ .

A schematic diagram of the actual Kelvin Probe setup in our lab is shown in Figure 44. The bottom plate of the Kelvin capacitor  $C_k$  represents the sample and is connected to the earth via the backing potential  $V_b$ . The upper vibrating reference electrode is connected to a low-noise operational amplifier acting as a current-to-voltage (I/V) converter, the output of which is amplified by a variable gain voltage preamplifier, then passed through a low pass filter (LPF) before being input to the analog-to-digital (AD) converter. The bottom Figure in Figure 44 shows the simplified circuit of the I/V converter where the operational amplifier has been replaced by its effective resistance  $R_{in}$ , which is  $\sim 20\Omega$ .

$R_{in}$  and the tip parasitic capacitor  $C_p$  are in parallel. The effective impedance is given by  $\frac{R_{in}}{1+j\omega R_{in}C_p}$ .  $C_p$  is on the order of pF, so for low driving frequencies ( $< 1$  KHz), the denominator is  $\sim 1$ , and  $i_2 \rightarrow 0$ , i.e., no signal is dropped across the parasitic capacitance. The total current,  $I_{tot}$ , produced by the vibrating capacitor is given by

$$I_{tot} = I_1 = (V_c + V_b)\delta C_k / \delta t \quad (85)$$

$$I_f = -V_1 / R_f. \quad (86)$$

Assuming a perfect operational amplifier, i.e., infinite input resistance,

$$\begin{aligned} I_1 &= I_f \\ \Rightarrow (V_c + V_b)\delta C_k / \delta t &= -V_1 / R_f \\ \Rightarrow V_1 &= -R_f(V_b + V_c)\delta C_k / \delta t, \end{aligned} \quad (87)$$

where  $V_1$  is the output voltage of the first stage amplifier and  $R_f$  is the feedback resistance. Assuming a periodic variation in spacing:  $d(t) = d_0(1 + \epsilon \cos \omega t)$ , where  $d_0$  is the mean spacing and  $\epsilon$  is the modulation index ( $\epsilon = d_1/d_0$ , where  $d_1$  is the amplitude of oscillation), the periodic Kelvin capacity becomes  $C_k(t) = C_0/(1 + \epsilon \cos \omega t)$ , where  $C_0 = \epsilon_0 A / d_0$ , ( $\epsilon_0$  is the permittivity of free space and  $A$  is the plate area). For small values of  $\epsilon$  ( $\epsilon < 0.3$ ), taking the derivative of  $C_k$  with respect to  $t$ , the output can be written as

$$\begin{aligned} V_{out} &= -(R_2/R_1)V_1 \\ \Rightarrow V_{out} &= -(R_2/R_1)[-R_f(V_b + V_c)\delta C_k / \delta t] \\ \Rightarrow V_{out} &= -(R_2/R_1)[-R_f(V_b + V_c)\delta(C_0/(1 + \epsilon \cos \omega t)) / \delta t] \\ \Rightarrow V_{out} &= -GR_f(V_b + V_c)C_0[\delta(1 - \epsilon \cos \omega t) / \delta t] \\ \Rightarrow V_{out} &= -GR_f(V_b + V_c)C_0[\epsilon \omega \sin(\omega t + \phi)] \\ \Rightarrow V_{out} &= -GR_f(V_b + V_c)C_0 \omega \epsilon \sin(\omega t + \phi), \end{aligned} \quad (88)$$

where  $G$  is the preamplifier gain ( $-R_2/R_1$ ) and  $\phi$  is a phase angle which depends on the initial conditions, i.e., on our choice of the time origin.

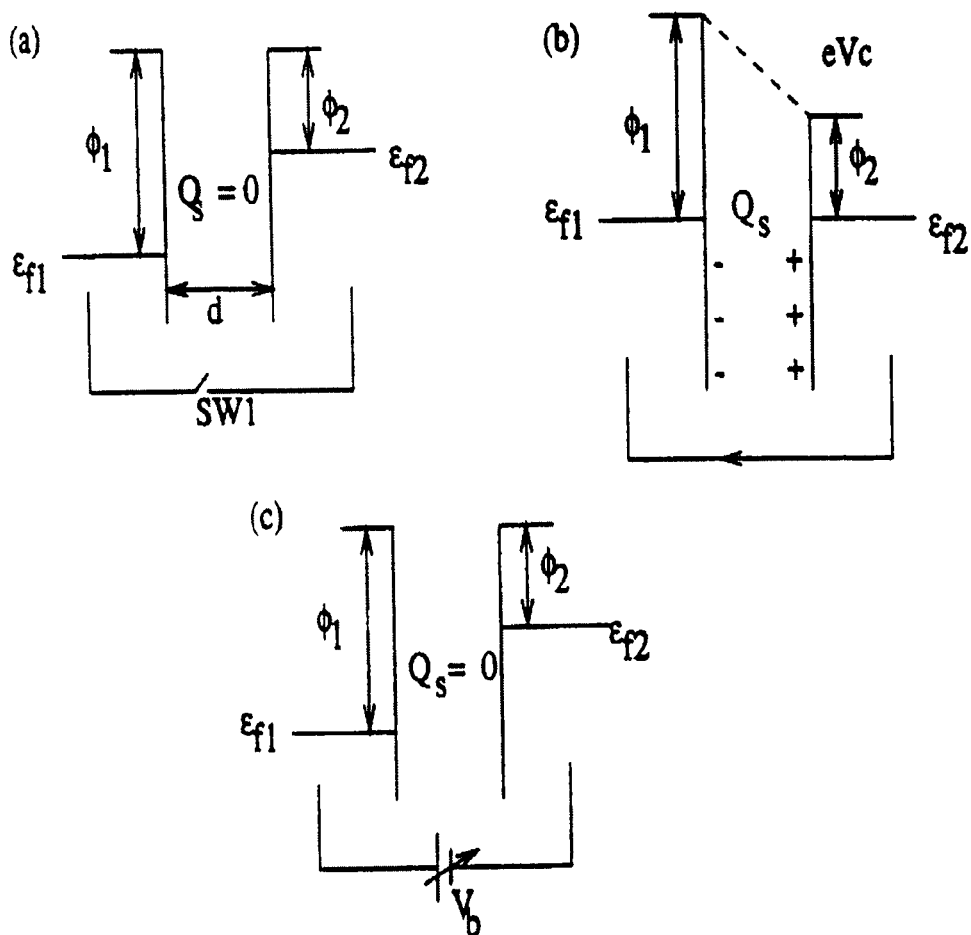


Figure 43: Electronic Energy Level Diagram for two Different Metals Separated by Distance  $d$  (a) Before Electrical Contact, (b) After Contact, and (c) After Inclusion of Backing Potential  $V_b$

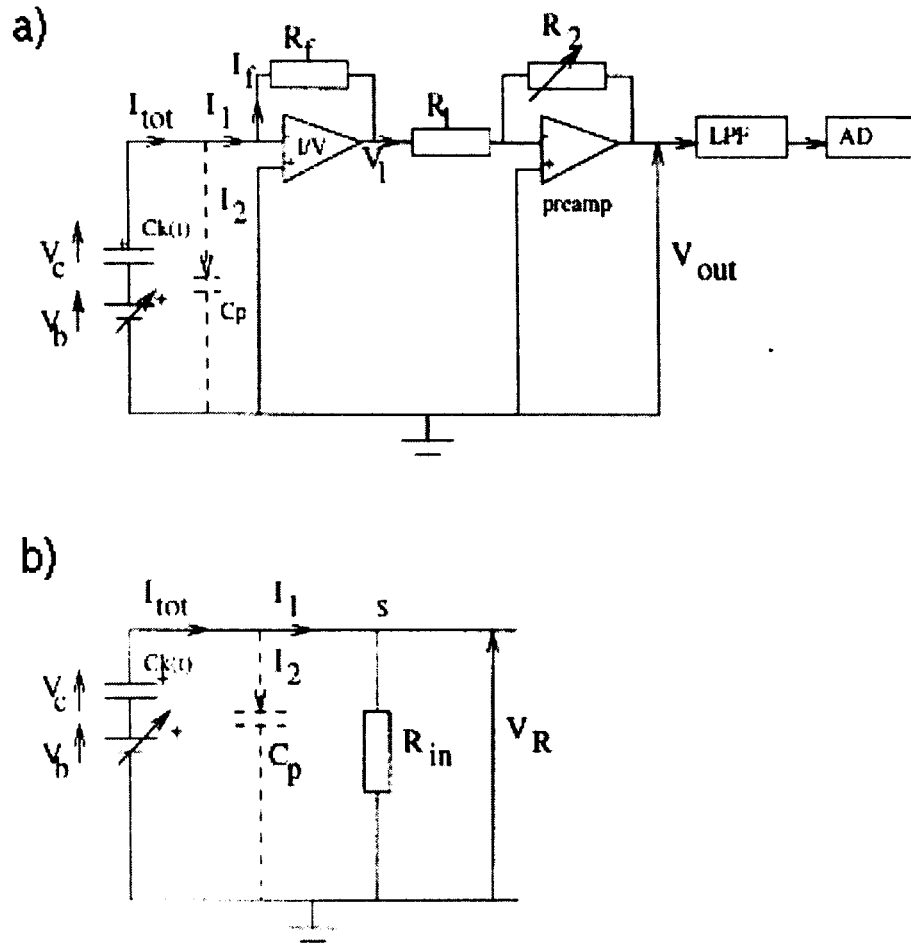


Figure 44: (a) Circuit Diagram of the Tip Amplifier, and (b) Simplified Diagram of the First Stage Amplifier Where the I/V Converter is Represented by its Input Resistance  $R_{in}$  [35]

In the Kelvin Probe method of determining the WF, we are in essence looking for the value of backing potential that would be equal and opposite to the contact potential setup between the sample and the reference electrode. It can be seen from Equation (89) that the peak-to-peak output signal,  $V_{ptp}$ , is linear with the backing potential  $V_b$ , i.e.,

$$V_{ptp} = 2(kV_b + kv_c). \quad (89)$$

This can be compared to the equation of a straight line in the form

$$V_{ptp} = mV_b + c, \quad (90)$$

where  $m = 2k$ , and  $c = 2kV_c$ . Using linear extrapolation,  $V_c$ , can be derived from the intersection of the best-fit line with the  $V_b$  axis. It can be seen from Figure 45 that this is the point corresponding to  $V_b = -V_c$ .

The WF measurements were done on LaS pellets after the second heating cycle, as described in Section 5.2.2. The sample whose WF is to be determined was made the bottom plate of the Kelvin capacitor  $C_k$ . To get an accurate WF measurement, the surface of the sample had to be as flat as possible and aligned in such a way that it is exactly parallel to the tip of the Kelvin Probe. The sample had to be eyeballed to make sure it was as close to the tip as possible for better accuracy. Care had to be taken not to crash the vibrating tip into the sample. This would have damaged the suspension mechanism of the vibrating tip. The details of the procedure to operate the Kelvin Probe, and its software is described in detail in Jugul Thachery's Master's thesis [30].

The measurements were performed in air directly after the arc-melting step followed by sand blasting. Prior to making the WF measurements, the surface of the samples was scratched gently with a razor blade to remove any contaminants on the surface due to exposure to air. The best value of WF in air for LaS we recorded in air was 2.6 eV. This value is comparable to the WF of Lanthanum Hexaboride ( $LaB_6$ ). The WF was then remeasured after a period of one month and the WF measured at the same location on the sample was found equal to 2.8 eV. The WF was also measured after crushing part of the samples and using the carbon reduction procedure to remove the oxysulfide phases. The lowest recorded WF in air after this step was found to be 3.7 eV. The low WF recorded from the samples directly after arc melting can be attributed to the lack of porosity. Once the sample is crushed and processed at 1600 °C in the Brew furnace for carbon reduction, the temperature is below the melting point and the samples are porous. In these measurements, the Kelvin Probe is actually measuring an average WF of the sample over the area of the Kelvin Probe tip ( $\sim 5$  mm in diameter). Micrographs of the samples shown in Figure 38 indicate that the samples are composed of crystallites with several tens of microns in size. Even though most of the sample is golden in color, there are also blue spots in the samples which were identified as being due to traces of  $La_3S_4$  phases still present in the samples [29]. The latter are known to have a larger WF.

## 5.4 Conclusions

We have described the successful growth of the fcc cubic phase of LaS bulk samples following the sesquisulfide route. We were able to remove the oxysulfide impurity phase ( $La_2O_2S$ ) present in the samples using a high-temperature carbon reduction process. The successful removal of the oxysulfide phase was supported by the absence of sharp phonon modes in Raman scattering experiments. Our refractory metal vacuum furnace with a tungsten heating element was used. We described a high-temperature growth technique where the carbon reduction step need not be done. This successful growth of extremely pure rare-earth monosulfides is the crucial step if thin films of these materials are to be used as more stable alternatives to Cs to reach NEA surfaces. The procedure described here could be used to grow other rare-earth monosulfides, but LaS has the advantage of a close lattice-match to the most widely used III-V semiconductors. The bulk samples were characterized by powder XRD and Raman spectroscopies. Powder XRD scans of the samples show the rocksalt phase with a lattice constant  $a_0 = 5.857(2)\text{\AA}$  for LaS. In Raman scattering, we observed the vibrational density of states and identified the longitudinal optical and transverse acousting phonons to occur at 261 and 100  $\text{cm}^{-1}$ . The lowest WF of LaS bulk samples we measured for samples prepared using the arc-melting procedure was 2.6 eV in air using the Kelvin Probe technique. The material presented in this section was published on reference [31].



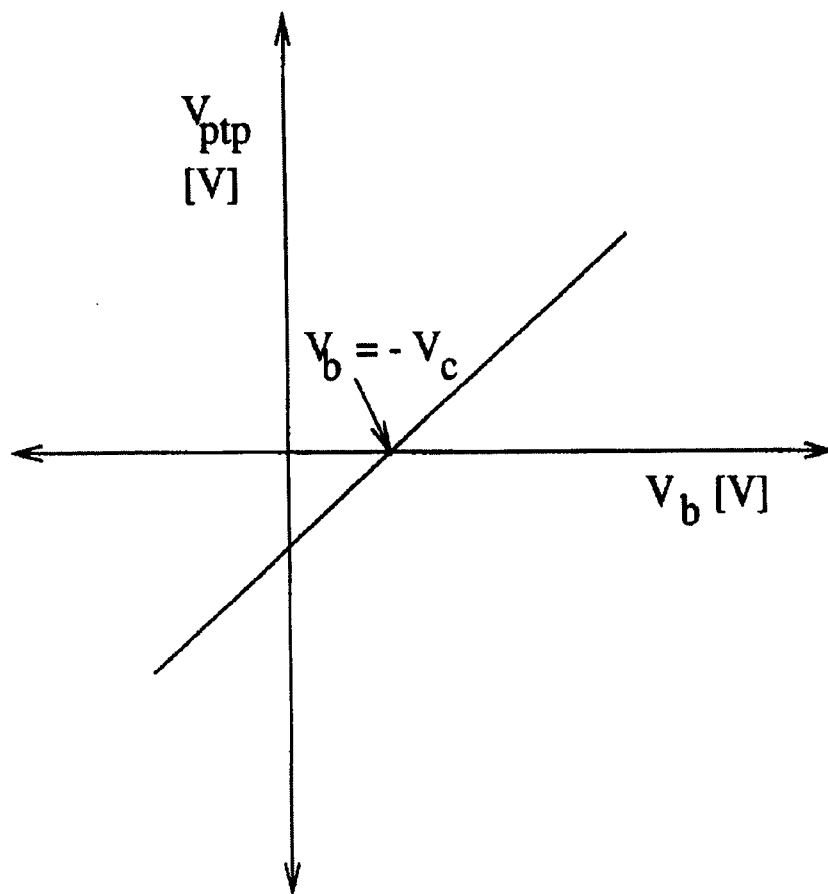


Figure 45: Schematic Diagram Showing the Variation of Peak-To-Peak Output Signal,  $V_{ptp}$  With the Backing Potential  $V_b$

## 6. RF Sputtering of CdS Thin Film

### 6.1 Introduction

As mentioned in Section 1, to minimize electron trapping due to surface states at the LaS/CdS and CdS/InP interfaces, and in the CdS film due to defect states, we need epitaxially grown, high quality CdS thin films.

Here, we report the successful deposition of CdS thin films on InP (100) wafers by RF magnetron sputtering using a CdS stoichiometric target. Deposition conditions, such as substrate surface preparation, substrate temperature, Ar pressure, and RF power, were optimized. The film quality was examined by means of XRD and photoluminescence. In this section, we describe the experiments, discuss the results, and compare them to the results on bulk hexagonal CdS crystallites and previous work in the field.

### 6.2 Background

CdS thin film growth and characterization has been studied for many years for applications in solar cell windows [36, 37, 38, 39, 40], piezoelectric transducers, and semiconductor laser diodes [41, 42]. CdS has a wide bandgap of 2.54 eV, which corresponds to the photon energy of visible green light. There exist two kinds of CdS phases: hexagonal wurtzite structure phase (referred to as the H-phase) and cubic zincblende structure phase (referred to as the C-phase). H-phase CdS film has been grown by means of CBD [36, 38, 39, 40, 43, 44], CVD [36], MOVPE [38], ALE [37] and MOCVD [38]. In many cases, the as-grown film has, to some extent, cubic modification [38, 39, 44]. After high-temperature annealing, the metastable cubic phase transforms into the more stable hexagonal modification characteristic of single crystalline CdS.

There are much fewer reports on C-phase CdS film than on H-phase CdS. C-phase CdS has a lattice constant of 5.818 Å which matches cubic InP (lattice constant 5.869 Å) quite well with only 0.9 percent lattice mismatch. However, the H-phase CdS is slightly more stable than C-phase CdS with an energy difference of 1.1 meV/atom. The tendency of CdS to become hexagonal structure makes the task of growing cubic CdS thin film difficult.

RF magnetron sputtering has the advantage of depositing CdS thin films at low temperature. This will avoid the cubic to hexagonal phase transition other people experience. Figure 46 is a schematic diagram of the magnetron sputtering process. Because the electric field and magnetic field are normal (at 90 degrees) to each other, electrons are trapped in the region between the center of the target and the edge of the target over the surface. The energetic electrons ionize the Ar atoms in this region. Ar<sup>+</sup> ions are then accelerated by the DC bias field toward the target and eject CdS from the target. Therefore, the plasma between target and substrate consists mostly of Ar atoms, electrons and Ar<sup>+</sup> ions, and some ions, atoms, and clusters from the CdS target. Some of the ions, atoms, and clusters from the CdS target diffuse toward the substrate and deposit on it.

The target sputtering rate depends on the DC bias between anode and cathode, RF power, and Ar pressure. When DC bias is high, the electric field intensity is high, and the bombardment effect will be enhanced. When the RF power and/or Ar pressure is increased, the electron and Ar<sup>+</sup> concentration increase too, resulting in more bombardment on the target. But when the Ar pressure is too high, the electron mean-free path is too short to accumulate enough energy to ionize Ar atoms. The same is true for Ar<sup>+</sup> to bombard the target.

During the deposition process, atoms and ions are first diffused onto the substrate surface and physically adsorbed on it. Then they move around (diffuse) on the surface and locate the lowest sites (steps and kinks) and chemically bound on the surface.

If the substrate is floating in the plasma, the fast moving electrons will quickly move toward the substrate surface, producing a sheath layer voltage between plasma body and the substrate. Positive ions in the plasma will be accelerated by this voltage and bombard the substrate surface. Because of this bombardment, some fresh surface bonds are broken open, providing more sites for chemical adsorption. The bombardment also gives the physisorbed species some more energy for surface diffusion. Thus, the deposition activation energy required for surface diffusion and site incorporation, which is usually provided by heating the substrate, is largely reduced. This bombardment has

some negative effects, too. It may cause surface resputtering and produce some bombardment related defects.

### 6.3 Deposition Experiments

Figure 47 shows a schematic diagram of the RF magnetron sputtering device. The magnetron sputtering gun (US Gun II) is housed in a stainless-steel bell jar. A hot pressed 2-inch high purity CdS target (99.999 percent pure) is mounted on top of the anode of the gun. Opposite to the target, a S-doped InP wafer is mounted with Ag paste onto a substrate heater about 5 cm above the gun in an on-axis position. A shutter that can be rotated manually is mounted between the gun and the substrate heater to shelter the substrate or target before sputtering begins. The substrate temperature is monitored using a S-type Platinum Vs Platinum 10 percent Rhodium thermal couple. High purity Ar gas is introduced into the chamber to produce the sputtering plasma, and the system is throttled by adjusting the gate valve to the CT-8 cryopump. The bell jar is typically pumped to a base pressure of  $10^{-7}$  torr using a CT-8 CTI cryopump. The substrate is maintained at a predetermined temperature.

There are several experimental parameters that can affect the quality of the CdS film. They are substrate surface preparation method, substrate temperature, RF power and Ar pressure. Our experiments cover the substrate temperature range from room temperature to 250 °C, RF power from 6 to 15 W, Ar pressure from 15 to 120 microns of mercury. The three methods of substrate surface preparation investigated are discussed later.

### 6.4 PL Characterization

The quality of the CdS thin film were examined using photoluminescence (PL). The 457.9 nm radiation from an Ar-ion laser was used to excite the PL in CdS film. A Joule-Thomson refrigerator is used to cool the sample to 77 K. Figure 48 is a typical PL spectrum of our sample. It consists of a main peak that is centered around 497 nm (2.49 eV) and, sometimes, weak features from 520 nm (2.38 eV) to 700 nm (1.77 eV) appear in the PL. The main peak comes from the overlap of band edge emission and sulfur vacancy related emission. The weak features at longer wavelength come from defect states in the material, for example, the small peak at around 590 nm (2.1 eV) is the yellow emission band which is related to the defect state of interstitial cadmium [45]. The small peak at around 690 nm (1.8 eV) is the red emission band which is related to the defect state of sulfur vacancies [37]. When a laser beam illuminates a perfect CdS crystal, ideally it will give an intensive narrow band edge emission peak at 488 nm (77 K)[46]. No other emission peak will be observed. However, if there are defects in the material, the PL peak from defect states will emerge, decreasing the 488 nm peak intensity. In a defect-prone material, the band edge emission will be quenched by defect states. Thus the location of the band-to-band emission peak and its FWHM can serve as a good criteria of film quality.

Our results suggested that the main PL peak can be deconvoluted into two peaks (see Figure 48). In most of the cases, the asymmetric PL peak cannot be well fit to a single peak. Fitting it to two peaks give a significantly better Chi-Squared. Figure 49 shows PL spectrum (77 K) of a high purity polycrystal CdS (Purdue University). It has a main peak at 501 nm (2.473 eV) with FWHM of 15 nm (0.07 eV). XRD scan shows it is a H-phase CdS crystal (as shown in Figure 50).

### 6.5 RF Sputtering Deposition Parameters

Experimental parameters such as substrate surface preparation methods, substrate temperature, Ar pressure and RF power have been optimized to obtain the best quality CdS thin film determined by PL. By comparing the main peak location and width, and the intensity of small features (that related to defect states) in the PL, we have obtained a set of deposition parameters that yield the best quality CdS film on InP.

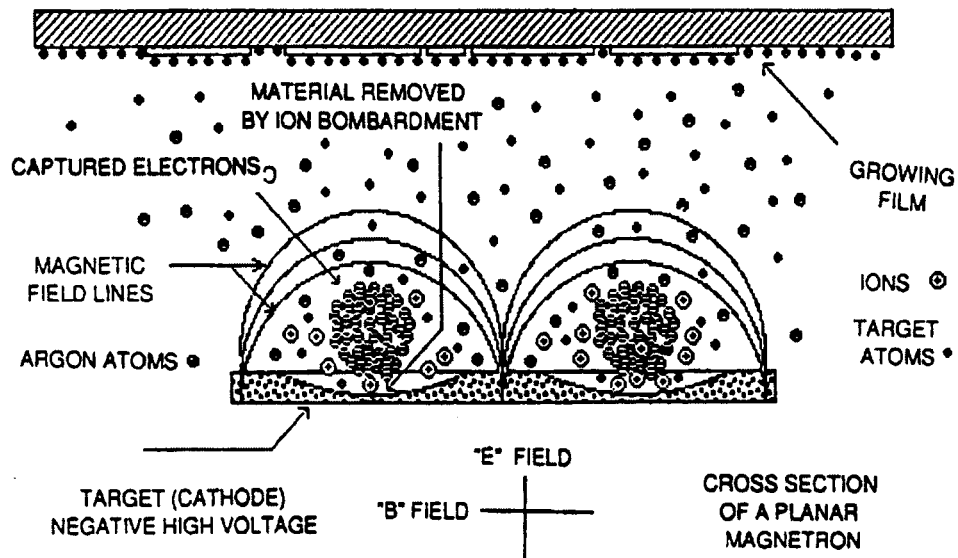


Figure 46: Planar Magnetron Sputtering

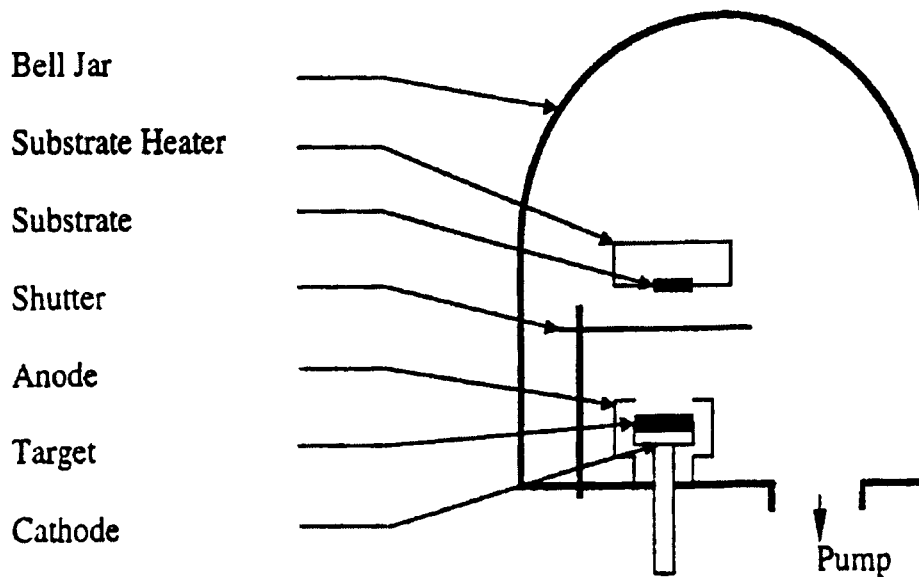


Figure 47: RF Sputtering Facility

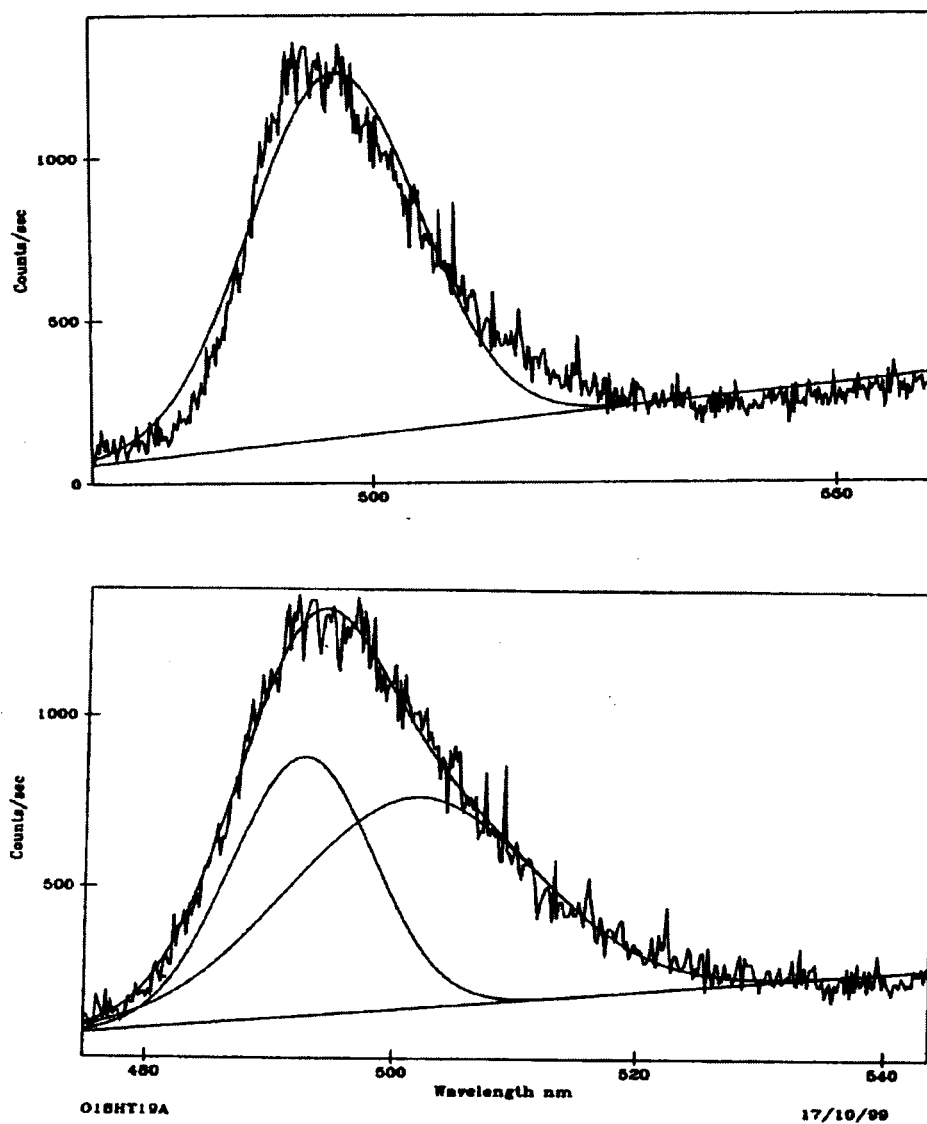


Figure 48: Typical PL Spectrum of CdS samples (Top) and Two-Peak Fit (Bottom)

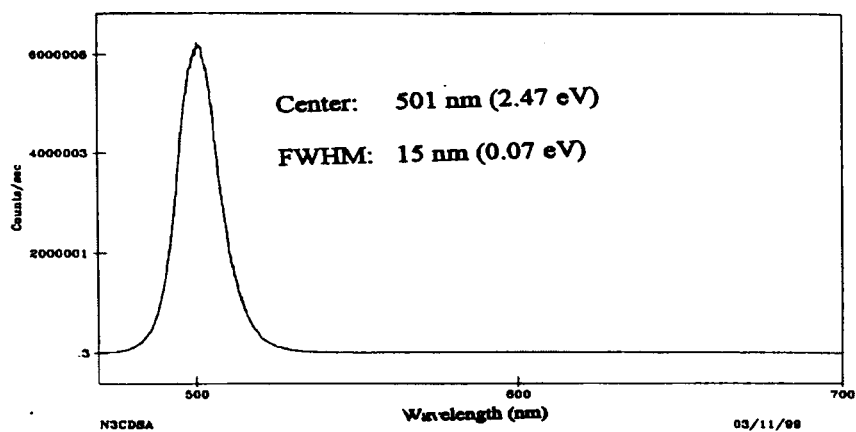


Figure 49: PL Spectrum Of High Purity CdS Crystallite

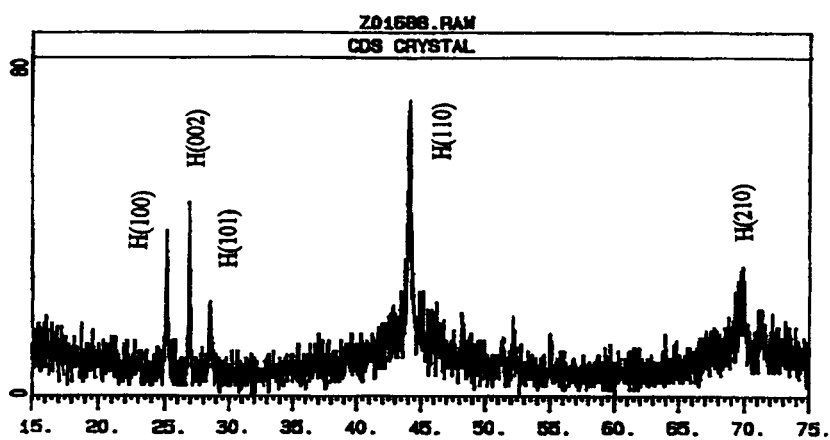


Figure 50: XRD Determining a H-phase crystal

### 6.5.1 Optimization of Substrate Preparation Method

Three substrate preparation methods are compared to determine which one gives the best PL result.

**Method 1: Etch Clean InP:** The InP (100) wafer is first immersed into two successive beakers of boiling trichloroethylene for 5 minutes each, and then immersed into a beaker of acetone kept in an ultrasonic cleaner for 5 minutes. The acetone is then replaced by methanol to repeat the ultrasonic cleaning process for 5 minutes. The InP wafer is then rinsed in DI water and blown dry with a nitrogen gun. In this step, the grease components (CH<sub>x</sub>)<sup>-</sup> of surface contamination are reduced by about 70 percent. Then the wafer is immersed into a beaker of etchant (5 H<sub>2</sub>SO<sub>4</sub>: 1 H<sub>2</sub>O: 1 H<sub>2</sub>O<sub>2</sub>), which is kept at 60 °C for 80 seconds. After this step, the most important contaminants on InP surface, (CH<sub>x</sub>)<sup>-</sup> and (PO<sub>4</sub>)<sup>-3</sup>, are reduced almost to zero. Method 1 is an effective procedure to clean the wafer surface. However, it brings a lot of damage to the wafer surface as shown in Figure 51.

**Method 2: Vacuum Heat InP:** The wafer is immersed into a beaker of acetone and cleaned in an ultrasonic cleaner for about 15 minutes. Then it is blow dried with N<sub>2</sub> gas. After it is attached to the substrate heater, pumped over night in a vacuum of  $2 \times 10^{-7}$  torr, the wafer is heated at 120 °C for 30 minutes. Then the temperature is raised to 550 °C, and the substrate cooled down slowly in about 1 1/2 hour.

**Method 3: Acetone Supersonic Clean InP:** This is the simplest method. The wafer is immersed into a beaker of acetone and cleaned in supersonic cleaner for 30 minutes. Then, it is blow dried with dry N<sub>2</sub> gas. Three samples prepared using the different cleaning procedures described above are loaded onto the substrate holder. After sputter deposition, PL spectra are taken to compare the effects of different cleaning methods.

Figure 52 shows the PL spectrum of three samples from run 16. This Figure that the best PL result is obtained by vacuum heating (method 2, middle). The peak is narrower and shifted toward higher energy. It is apparent that sample HT16bb has the narrowest and also highest photon energy peak for the PL. There is no doubt that method 2 is the best among the three. The reason is that chemical etching in method 1 causes too much damage to the wafer surface, while method 3 is not effective enough to remove the surface contamination. Figure 53 gives the peak analysis result. Method 1 includes degrease step and acid etching step. Method 2 is to clean the surface by heating the substrate in vacuum. Method 3 is just to clean the substrate in acetone in supersonic cleaner. Method 2 gives the best films.

### 6.5.2 Optimization of Substrate Temperature

A series of experiments were done to examine the role of substrate temperature. For all of these experiments, the Ar pressure is fixed at 25 microns and RF power fixed at 6 W. The substrate temperature is set sequentially at 50 °C, 100 °C, 150 °C, 200 °C and 250 °C, respectively. Figure 54 shows the PL spectrum taken from three samples. It is obvious that  $T_s = 150$  °C is the best of the three. Figure 55 is the analysis result. This Figure indicates that, at lower temperature, the particles may not have enough mobility on film surface. At higher temperature, we may lose some sulfur.

In the temperature range from 150 °C to 200 °C, samples have narrower peak and the PL peaks shift to higher energy. When the temperature is higher than 250 °C, the PL peak becomes wider. It is clear that the best substrate temperature is between 150 °C and 200 °C. Substrate heating is a means of providing extra energy for thin film formation. When  $T_s$  is low, there is not enough energy for surface species to move around and chemically bond to the surface, resulting in a lot of defects. When  $T_s$  is too high, some of the sulfur content will diffuse out of the surface, resulting in sulfur vacancies.

### 6.5.3 Optimization of Ar Pressure

Experiments were undertaken with different Ar pressure while keeping all other experimental parameters the same. Figure 56 shows the PL spectrum and Figure 57 is the analysis result. Figure 56 shows that samples with Ar pressure of 25 microns and 40 microns have narrow PL peaks at higher photon energy. Sample of 40 microns pressure gives a high peak below 1.9 eV, which is defect related. Although the PL for a sample prepared at 40  $\mu$ m Ar

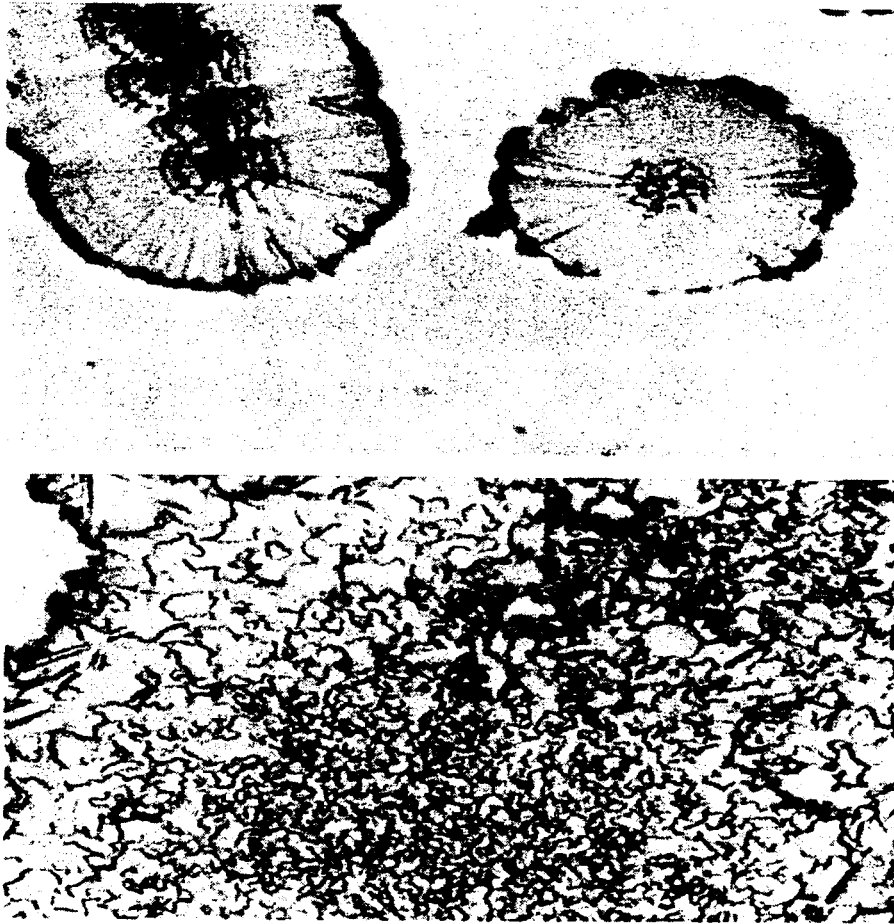


Figure 51: Surface of InP Wafer is Damaged After Chemical Etching Using the Method 1 of Cleaning Described in the Text



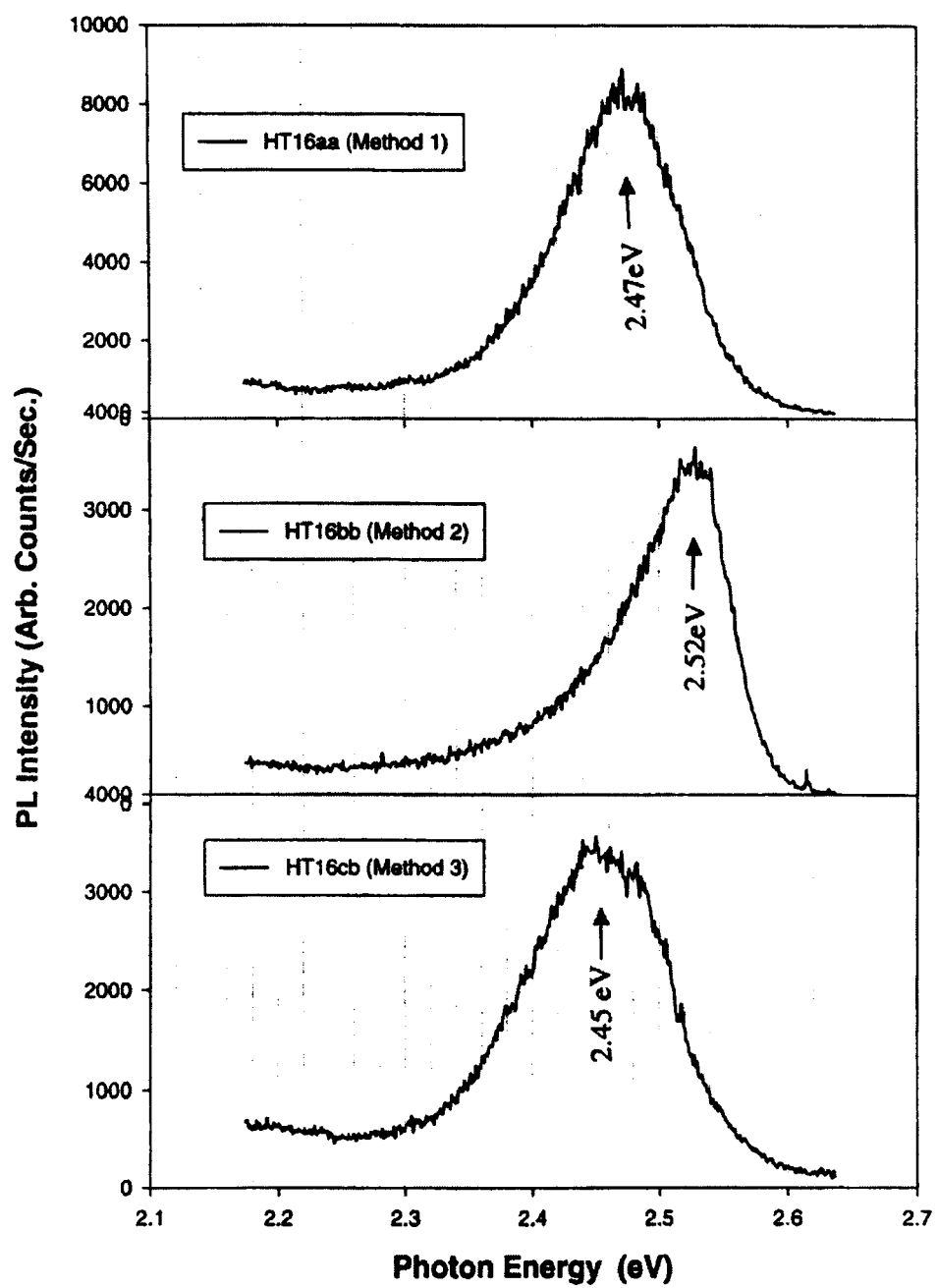


Figure 52: PL Spectrum for Samples Prepared by Three Different Substrate Preparation Methods

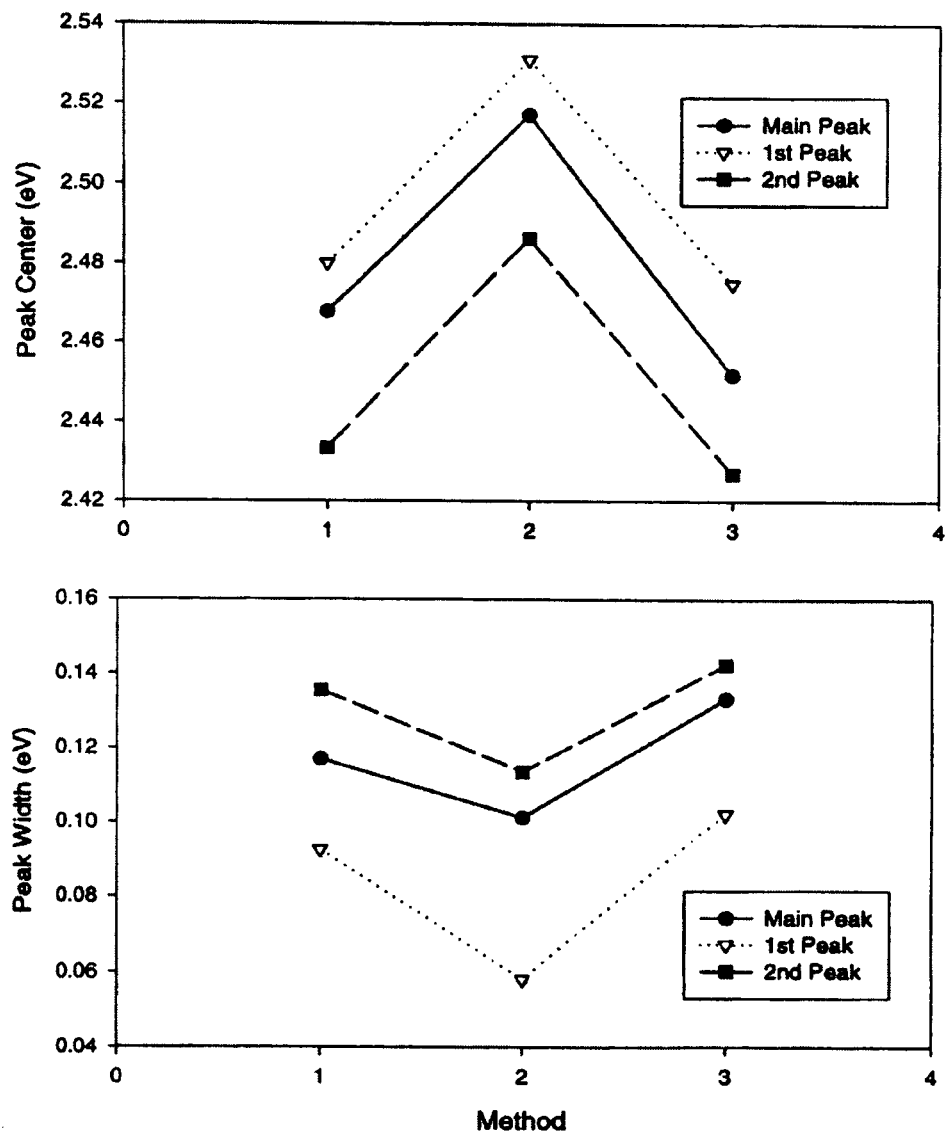


Figure 53: Three Kinds of Surface Preparation Methods are Compared

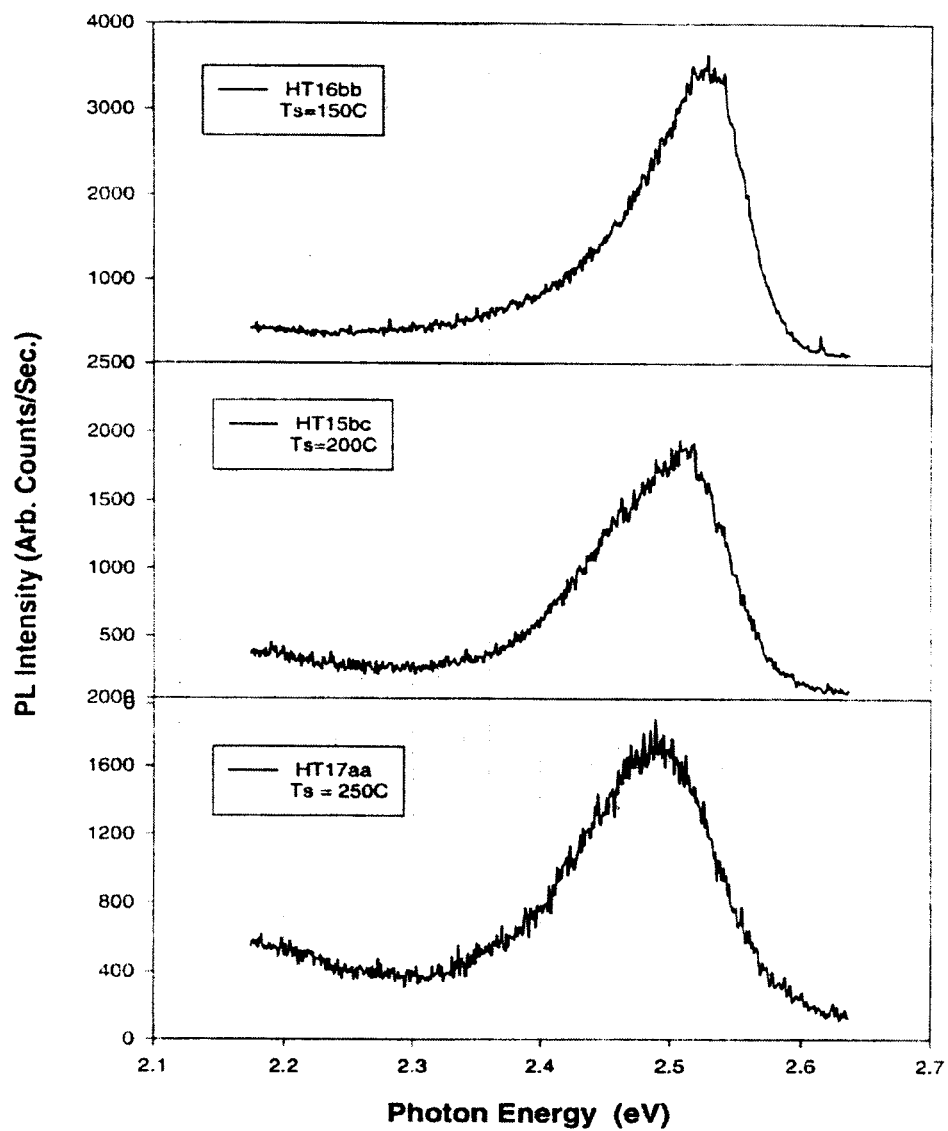


Figure 54: Comparison of the PL Spectrum for Samples With Different Substrate Temperatures

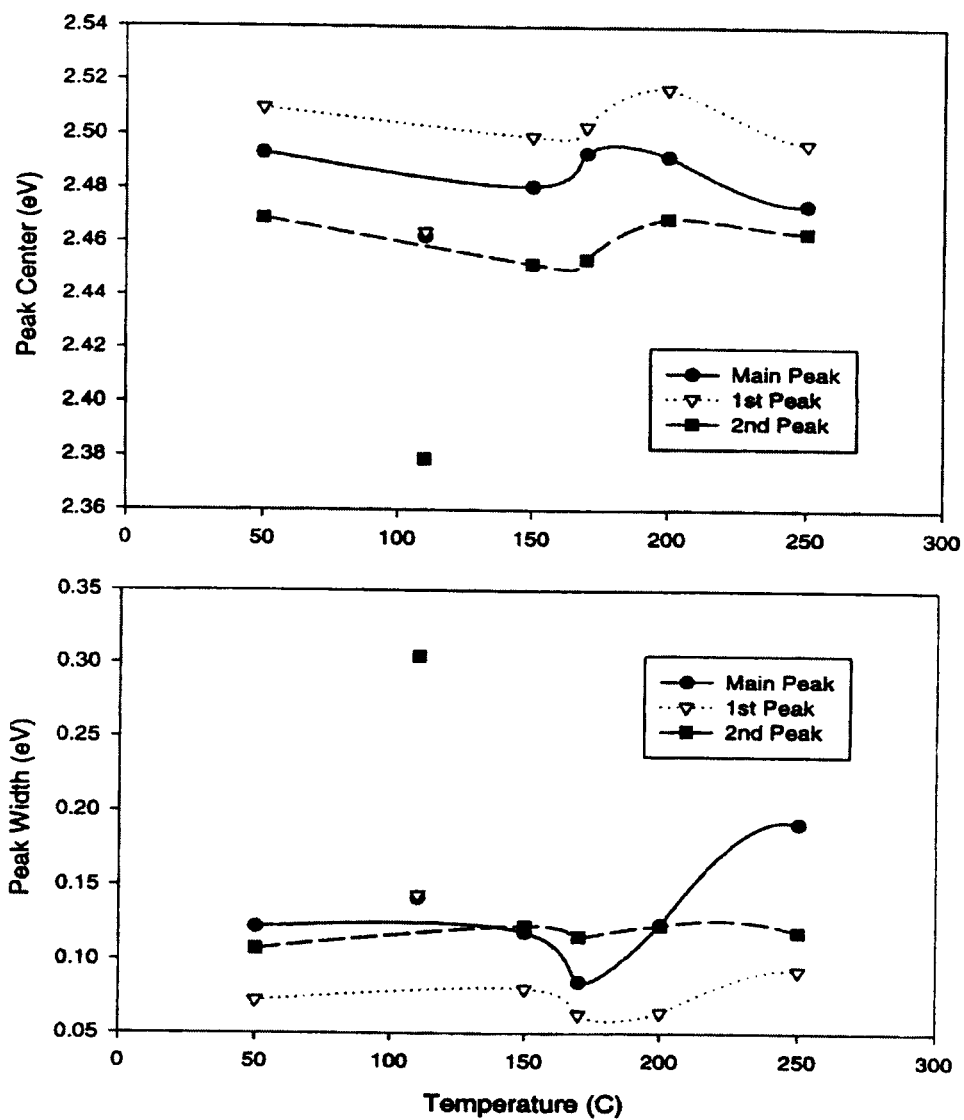


Figure 55: PL Spectrum Analysis Showing that the Samples With Substrate Temperature in the Range of 150 °C to 200 °C Have the Best Quality

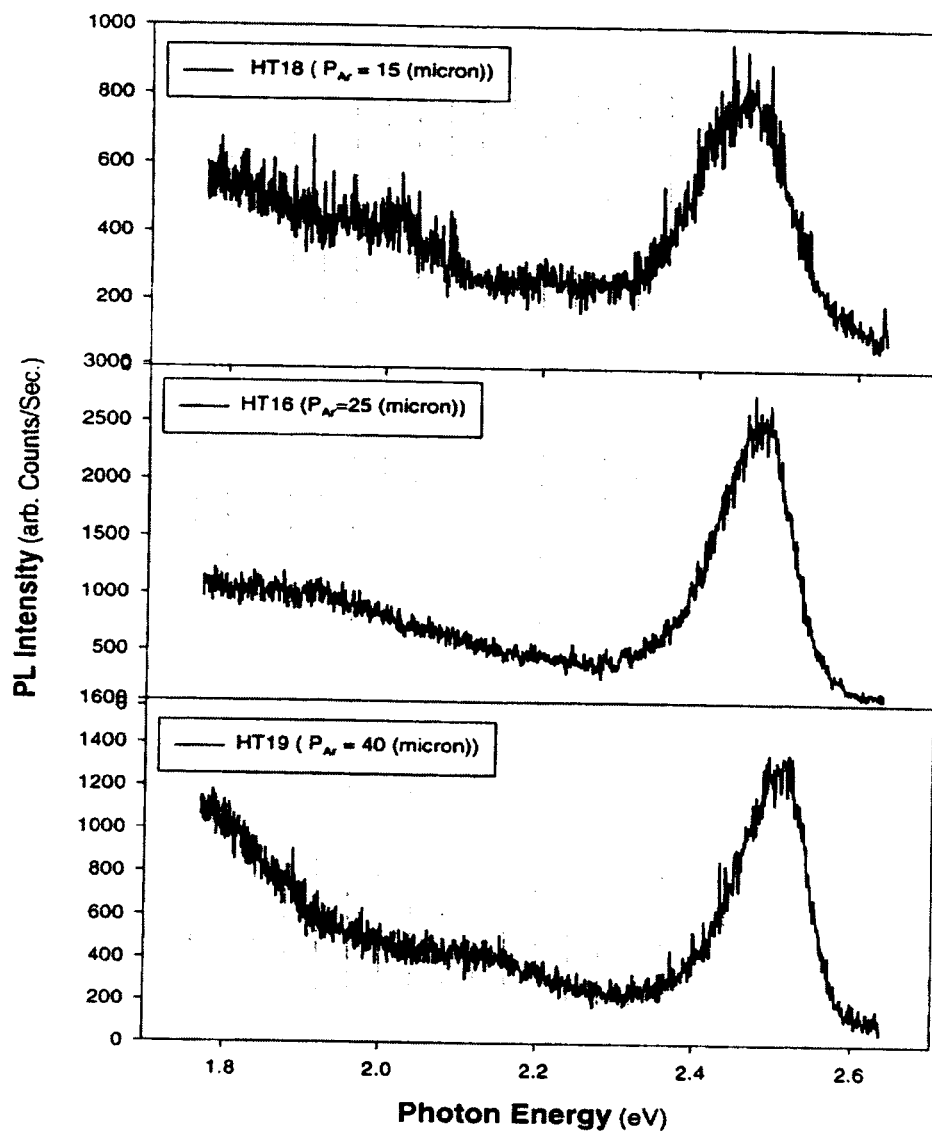


Figure 56: Illustration of the PL Peak Shift to Low Energy Side at Low Ar Pressure

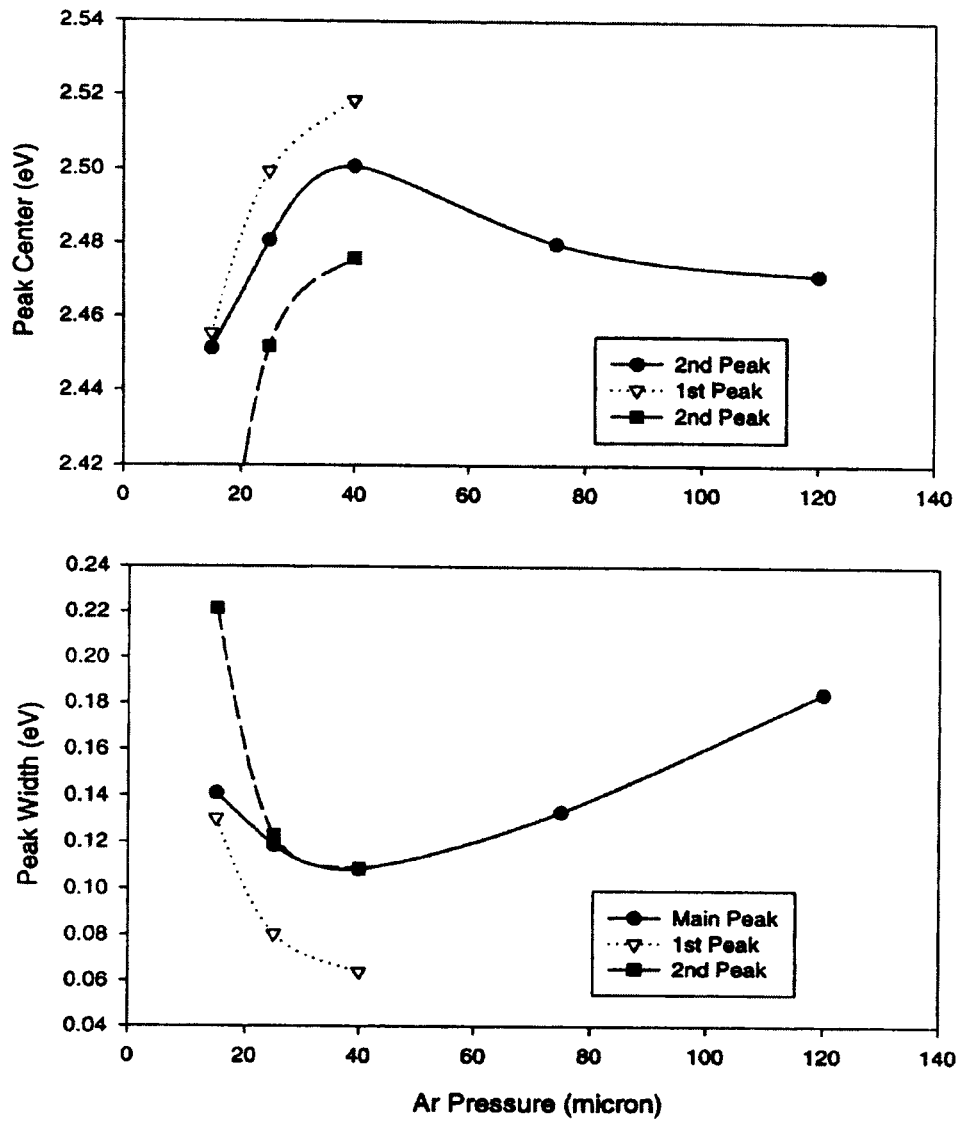


Figure 57: The Ar Pressure Plays an Important Role in Sputtering

pressure gives the highest photon energy peak, and the peak width is the narrowest; it also shows a high intensity red emission band that is related to sulfur vacancies. The best Ar pressure appears to be 25 microns. Figure 57 shows that, when the Ar pressure is low, there is too much bombardment of the substrate surface. When Ar pressure is high, the deposition rate is high. Particles on the surface may not have enough time to incorporate onto the surface of the film.

As we have already discussed above, bombardment of positive ions on substrate surface is one of the primary sources of energy required for thin film growth. When the Ar pressure is high, the mean-free path for ions is short. The energy provided by bombardment will be less, and the quality of the film will be poor.

#### 6.5.4 Optimization of RF Power

Figures 58 and 59 show the PL spectrum and analysis result for experiments on RF power. Generally speaking, changing the RF power does not change the PL result very much, including peak center and width. The latter is around 0.25 eV. The sample at 10 W gave the best PL result. According to previous discussion, higher power leads to higher  $\text{Ar}^+$  concentration in plasma, resulting in higher sputtering rate. Since the sputtering rate in our experiment is low, a little bit higher rate does not affect the quality of grown film very much. When RF power is 6 W, the red emission band intensity is lower, but the main peak is wider and at a lower photon energy position. When power is 10 W, the main peak is narrower, but red emission band intensity is higher.

In summary of the above experiments and analysis results, the best experiment parameter will be substrate temperature of 150 °C to 200 °C, Ar pressure 25 microns, RF power of 6 W and substrate surface preparation method 2. Under this set of experimental conditions, we obtained the best PL results for the CdS thin films.

#### 6.6 Comparison to the Previous Work in the Field

Single-crystal CdS gives a sharp PL peak at 488 nm (photon energy = 2.54 eV) at liquid nitrogen temperature [46]. It is believed to be the band edge emission. Sulfur vacancy first ionization ( $V_s^o/V_s^+$ ) and second ionization ( $V_s^+/V_s^{2+}$ ) levels are 0.05 eV and 0.15 eV below conduction band. Transitions between these levels and valence band give the PL bands at 502 nm (2.468 eV) and 522 nm (2.374 eV), respectively. If the amount of ( $V_s^o/V_s^+$ ) defect increases, the peak from band edge emission and the peak at 502 nm will overlap and become a broad main peak. The more ( $V_s^o/V_s^+$ ) defects, the more the main peak shifts to higher wavelength [46].

Now if we look back to the figures in which we fit the main PL peak into two peaks, these fits become meaningful. For example, in Figure 55, it is very clear now that we can see three emission bands. The first one is between 2.50 eV and 2.52 eV, which is from band edge emission, the second is one between 2.46 eV and 2.48 eV, which is from ( $V_s^o/V_s^+$ ) defects level to valence band emission, and the third is one at about 2.38 eV, which is from ( $V_s^+/V_s^{2+}$ ) defect level to valence band emission. Samples prepared at 110 °C substrate temperature have no band edge emission. Samples prepared in 150 °C to 200 °C region show more band edge emission than other temperature ranges.

If we look back at the PL of high purity CdS crystallite (Figure 49), we will see that its main peak is at 501 nm (2.47 eV), which is from ( $V_s^o/V_s^+$ ) defect level to valence band emission. Almost no band edge can be seen. Compared to other research results in the field, many people did not report any peak above 2.49 eV (shorter than 498 nm wavelength). The samples prepared in our group have relatively better quality.

#### 6.7 XRD Measurement Results And Discussion

Table 8 lists the 2-theta value in degree and Miller indices of cubic InP, cubic CdS and hexagonal CdS. The CdS (200) peak at 30.807 degrees and (400) peak at 64.029 degrees C are diagnostic for cubic structure CdS phase. However, it is difficult to discriminate them from cubic InP substrate (200) (at 30.431 degrees) and (400) (at 64.029 degrees) peaks because these peaks are very close to the InP peaks. If CdS thin film is epitaxially grown on InP, the CdS peaks are expected to shift even closer to InP peaks, making the judgement even harder to make. For hexagonal structure CdS, the diagnostic peak is at 47.839 degrees because it is unique for hexagonal CdS.

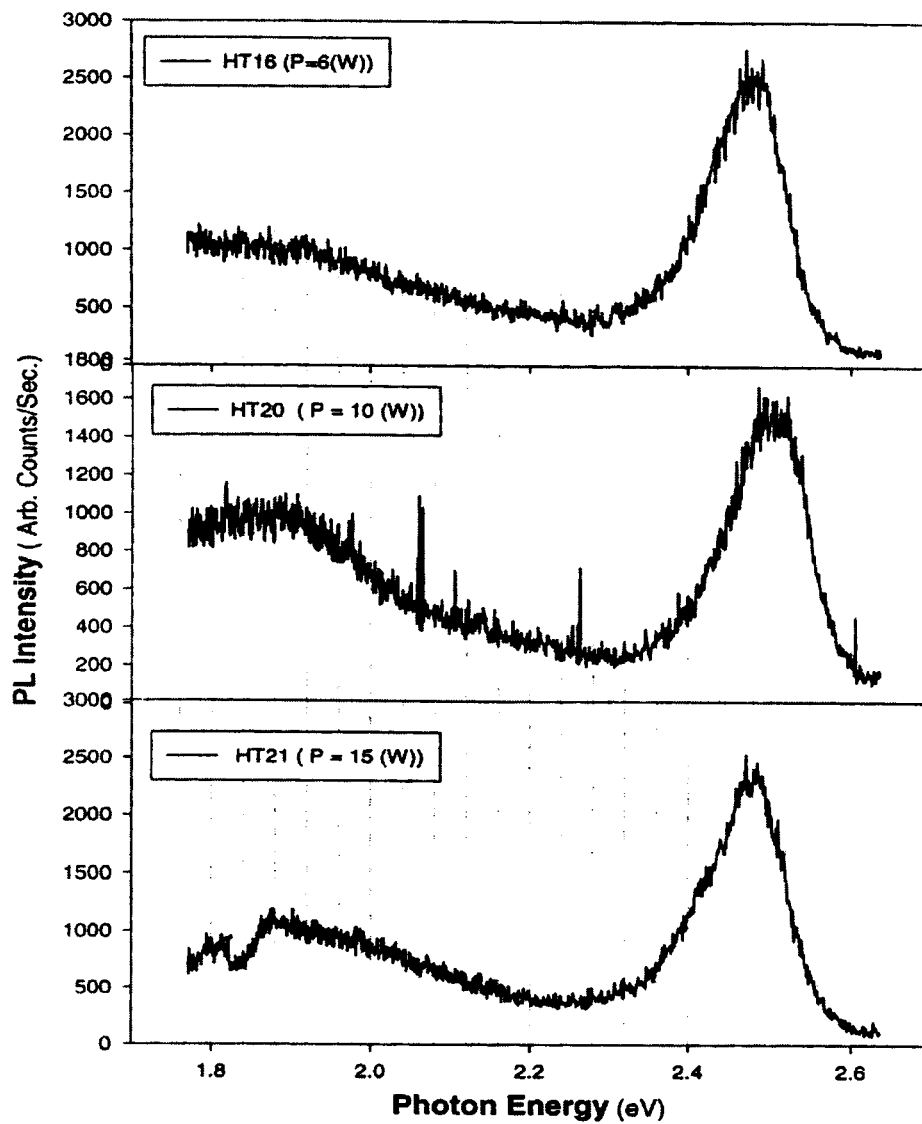


Figure 58: Similarity of PL Spectra for Samples Deposited at Different RF Power



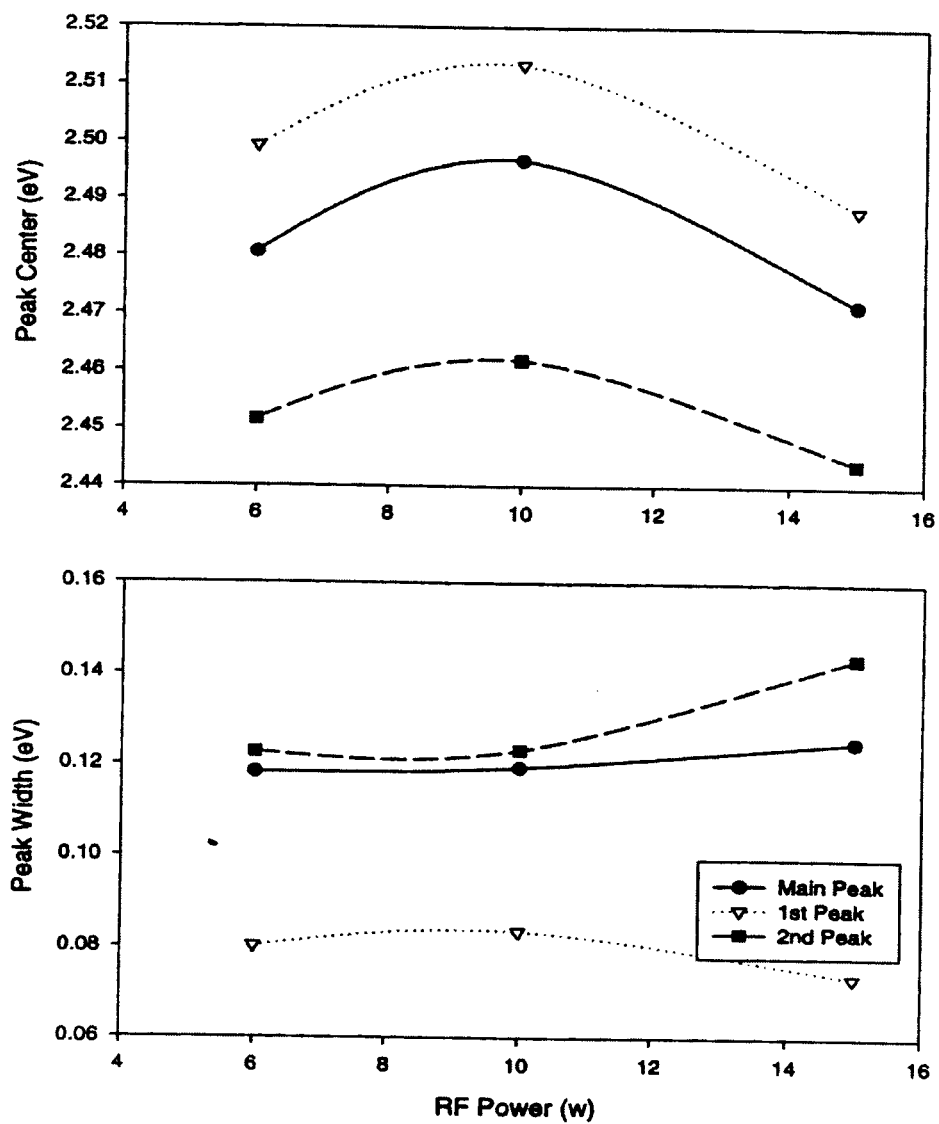


Figure 59: Effects on Peak Center and Width of Changing the RF Power From 6 W to 15 W

**Table 8: XRD Peaks And Corresponding Miller Indices From CdS And InP Bulk Samples**

2-theta	C-InP	C-CdS	H-CdS	2-theta	C-InP	C-CdS	H-CdS
24.807			100	69.802	331		
26.284	111			70.357		331	
26.506		111		70.862			211
26.507			002	71.893	420		
28.182			101	72.382			114
30.431	200			72.802		420	
30.807		200		75.478			105
36.620			102	77.855			204
43.605	220			80.038	422		
43.681			110	80.237			300
43.960		220		81.004		422	
47.839			103	83.252			213
50.882			200	86.007	333		
51.621	311			86.308			302
51.824			112	86.905		333	
52.132		311		91.459			205
52.796			201	95.907	440		
54.091	222			96.162			220
54.581		222		97.060		440	
54.584			004	101.856	531		
58.278			202	102.267			222
60.839			104	102.875			116
63.358	400			102.890		531	
64.029		400		103.884	600		
66.772			203	104.529			304
69.264			210	107.640			215

JCPD card 32-0452 Cubic InP  $a=5.869 \text{ \AA}$ , JCPD card 10-0454 Cubic CdS  $a=5.818 \text{ \AA}$ , and JCPD card 41-1049 Hexagonal InP  $a=4.1409 \text{ \AA}$ ,  $c=6.7198 \text{ \AA}$ .

Because of detector problems with our double-crystal X-ray system, we are unable to do the thin film XRD measurement on (200) and (400) peaks. The three samples deposited under the conditions listed in Table were shipped out for analysis. Sample CdS#19 was sent to AMIA Laboratories in Austin, Texas. The XRD experiment was set up to avoid bringing the single-crystal substrate (InP) peak into diffraction condition. Thus, the strong reflection from InP substrate is eliminated. Figure 60 is a whole range scan from 15 to 78 degrees. Vertical lines indicate the peak location and intensity of hexagonal CdS reflection (JCPD card 41-1049). All of the peaks detected can be identified with hexagonal CdS, with two major peaks at 26.5 and 47.8 degrees. The peak at 47.8 degrees is an indication that CdS hexagonal modification has been developed on InP (100) wafer at 150 °C substrate temperature (All XRD peaks match with the JCPD card 41-1049 hexagonal CdS (straight lines). The fact that the strongest peak appeared at 26.5 degrees and a weak peak appeared at 28.2 degrees (which is the highest in powder scan) indicates that the film is highly oriented with preferred  $\langle 002 \rangle$  orientation. Figure 61 is a higher resolution scan in 40 to 60 degree range. The peaks match exactly with JCPD card. No reflection from cubic phase can be identified.

**Table 9: Description Of Samples For XRD Measurement**

Sample ID	Base Pressure (torr)	Sputtering Pressure (micron)	RF Power (W)	Substrate Temperature (°C)	DC bias (V)	Deposition Time (hour)
CdS#19	$2 \times 10^{-7}$	40	6	150	-400	8
CdS#12	$2 \times 10^{-7}$	25	10	RT	-180	10
CdS#22	$2 \times 10^{-7}$	25	6	170	-300	9

Sample CdS #12 and CdS #22 were brought to University of Dayton for analysis. Figure 62 is the scan from the back side of the sample which is InP substrate. InP substrate gives a major peak at 79.9 degrees (InP(422)) and three small peaks at 38.0, 39.9, and 43.5 degrees. Figure 63 is the scan for sample CdS #22. Figure 64 is the scan for sample CdS #12. Spectrum from CdS #22 (Figure 63) is quite similar to the one provided by AMIA except the peaks from substrate. All other peaks are identified as hexagonal CdS peaks. Reflection at 47.8 degrees is strong which is diagnostic for hexagonal CdS phase.

Figure 64 is the XRD scan of CdS # 12. It is about the same as that from CdS # 22 except that the reflections are much stronger and the (103) reflection from H-CdS is very weak. Figure 64 also indicates the development of hexagonal CdS on InP, but with a little difference from Figure 63 in two aspects. First the intensity of the hexagonal CdS (002) peak at 26.4 degrees (which may also be cubic CdS (111) peak, or the overlap of the two) is five times stronger. Then the hexagonal (103) peak at 47.8 degrees is much weaker. Since the only major difference in experimental conditions is that the substrate temperature is room temperature, this may suggest that at lower substrate temperature, less hexagonal modification is developed.

As it is mentioned above, both the plasma sheath voltage and substrate heating help to provide the energy needed for surface mobility and energy for reaction activation. In our deposition experiment, it is possible that RF plasma has already provided enough energy for forming cubic CdS film. Extra energy provided by heating promotes the conversion of cubic phase to hexagonal phase. Therefore, it is worth trying to do some more experiments at room temperature to see if the cubic form of CdS film can be formed. Postdeposition annealing may be performed to improve the quality of the film.

In summary of the discussion on the XRD results on our CdS samples (taken at Austin and the University of

CdS thin film - Hexagonal P63mc (AMIA)

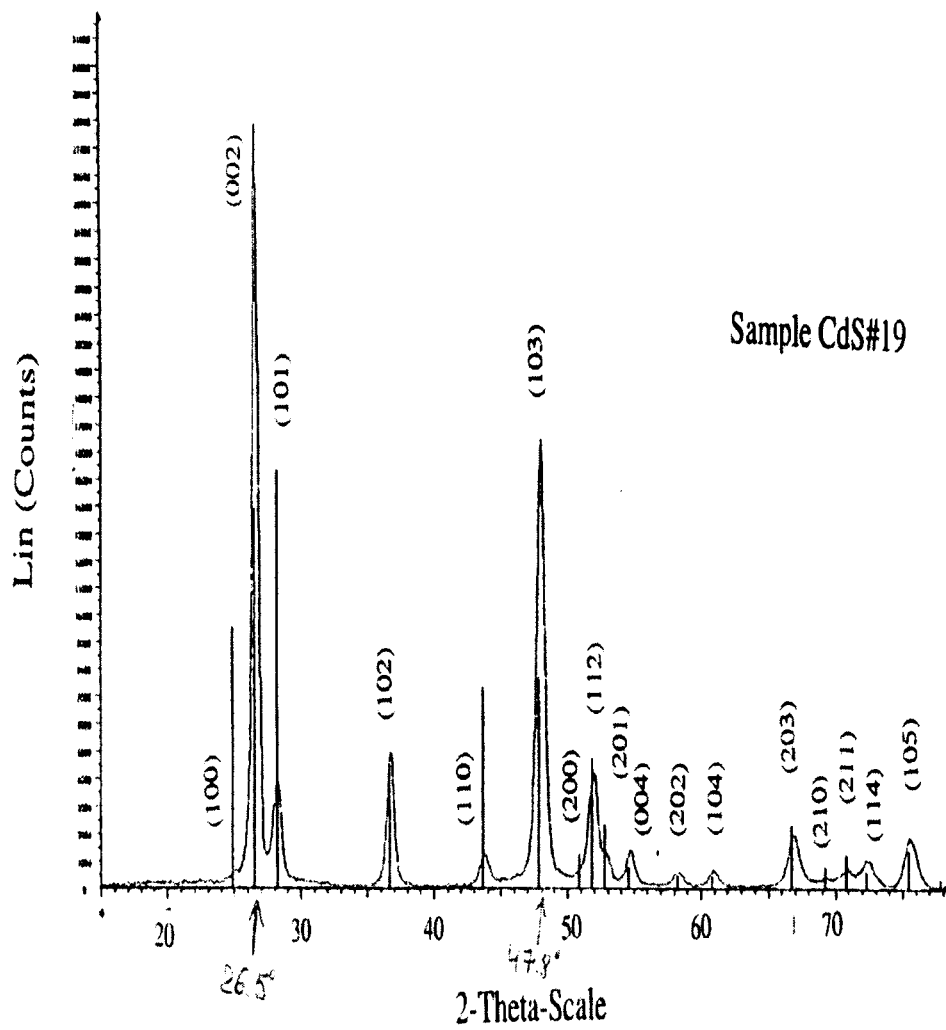


Figure 60: XRD Scan Showing Hexagonal CdS Modification

CdS thin film - Hexagonal P63mc

higher resolution scan (AMIA)

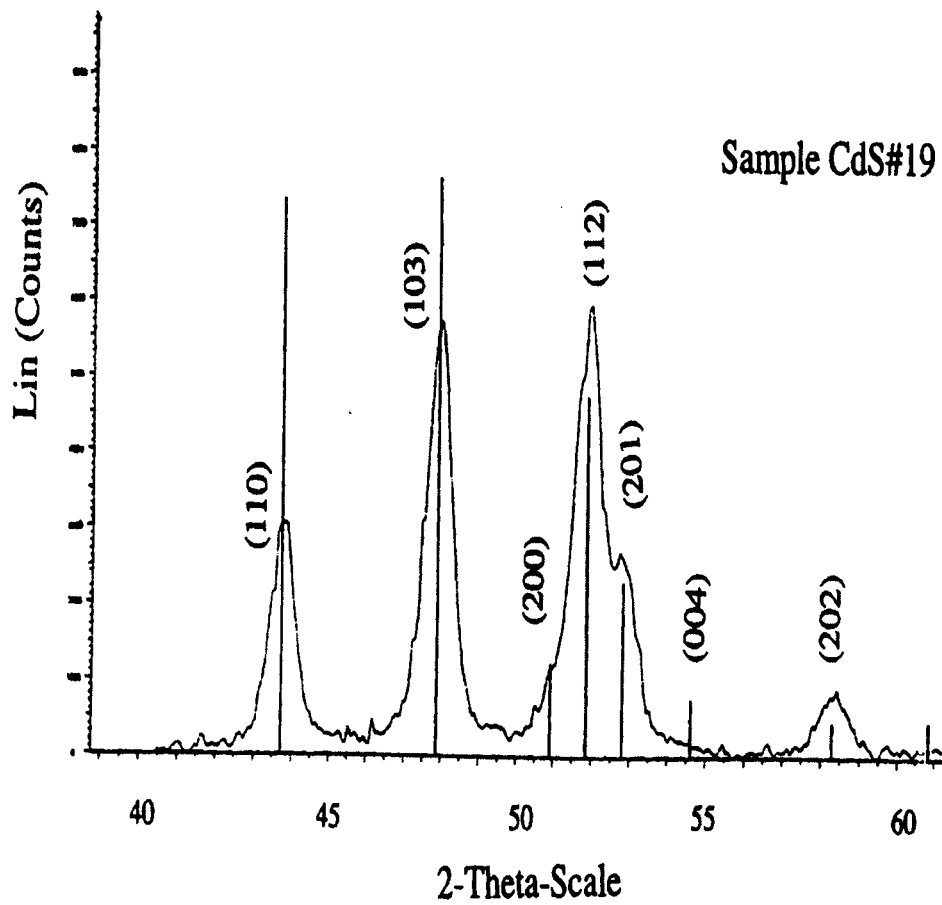


Figure 61: Higher Resolution Scan in 40 to 60 Degree Range

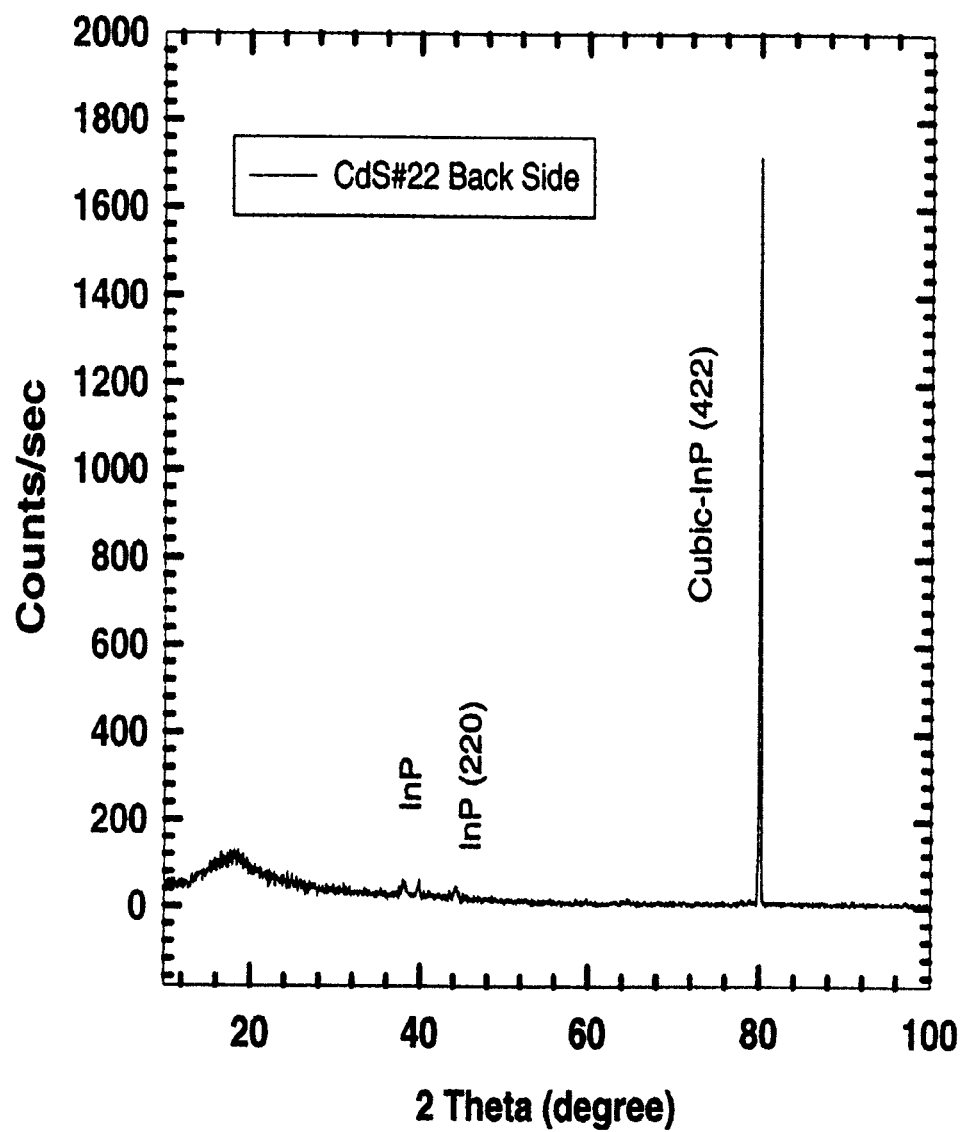


Figure 62: XRD Scan From the Back Side of CdS#22

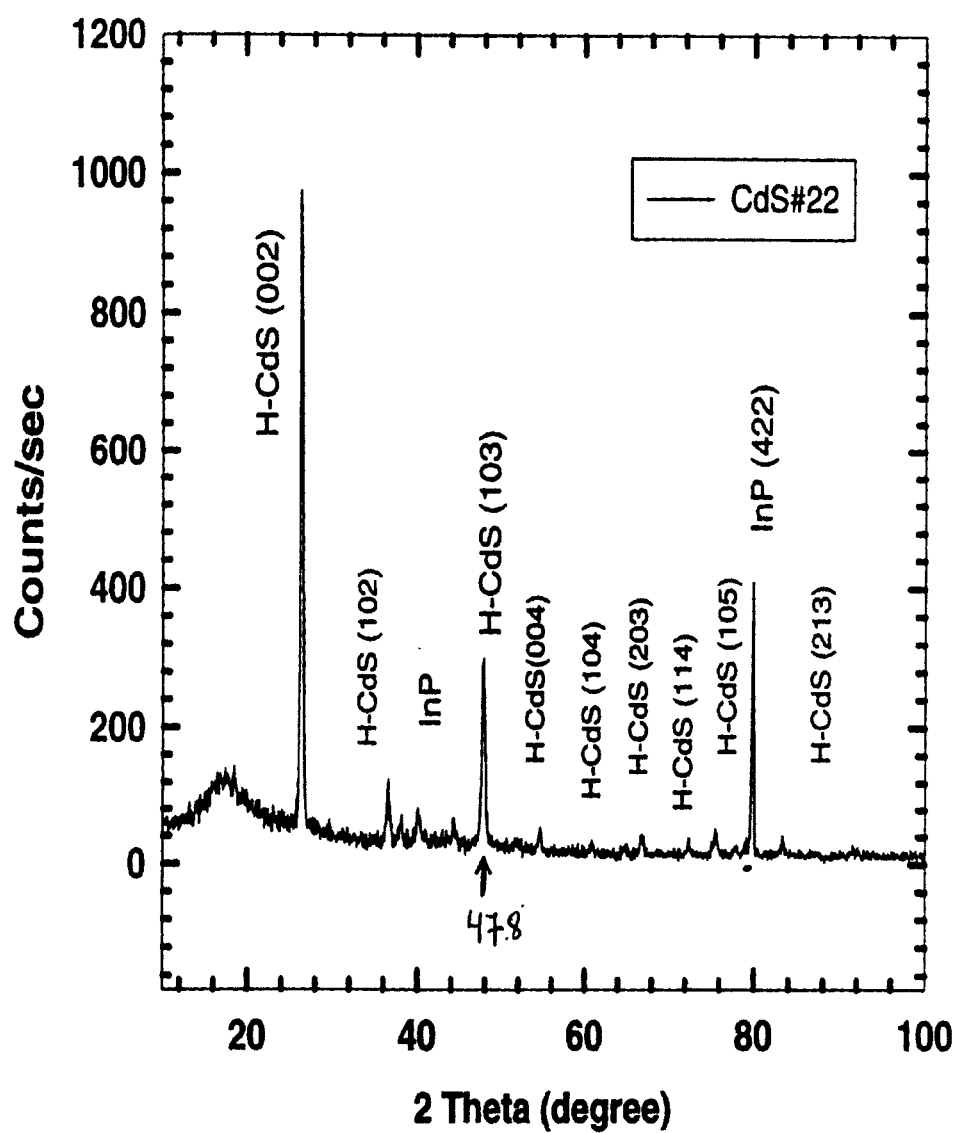


Figure 63: All Peaks From CdS #22 Are Identifiable as Either Due to the InP Substrate or Reflection From H-CdS

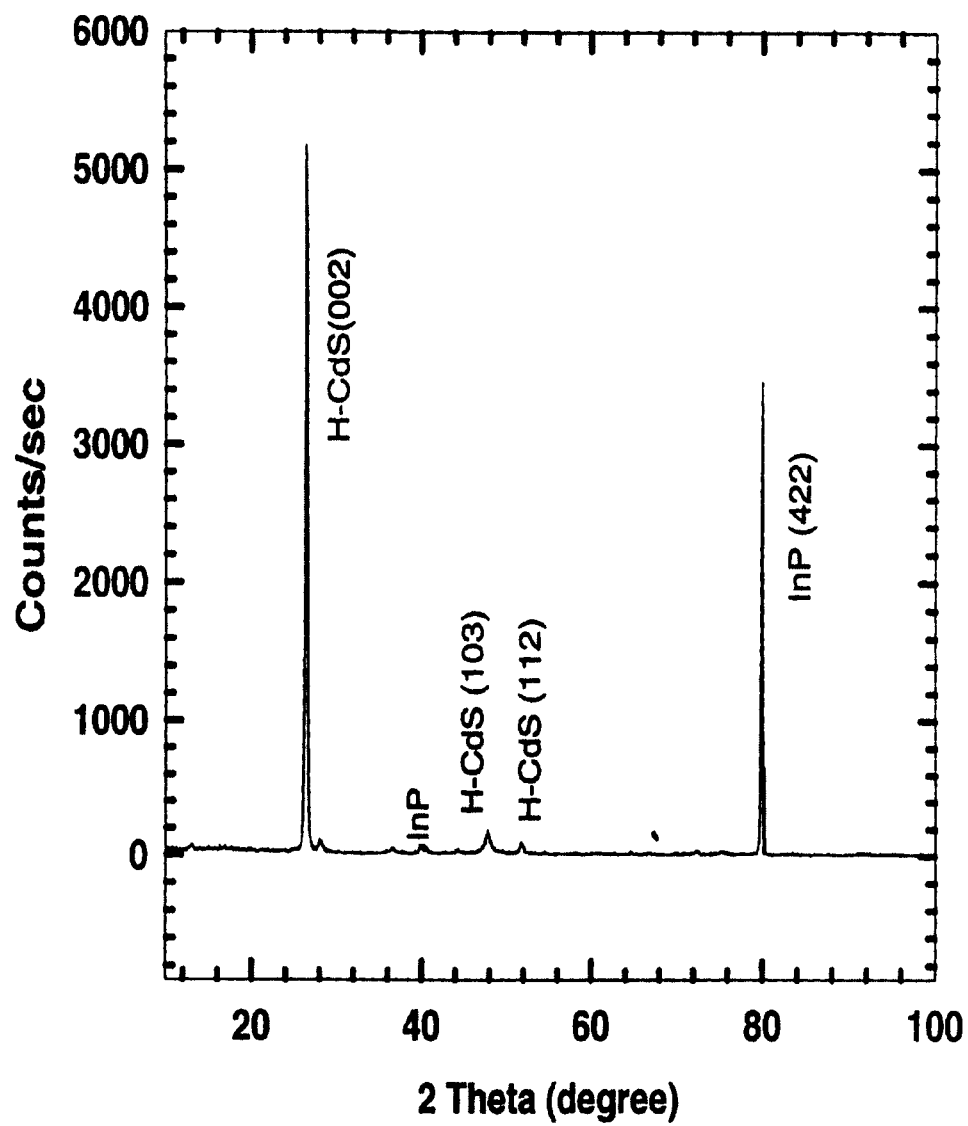


Figure 64: XRD Scan of CdS # 12



Dayton), it is clear that hexagonal structure CdS has been developed on InP (100) wafer under current experimental conditions. Further experiments on deposition conditions combined with thin film XRD and PL measurement are suggested in order to explore the conditions for high quality cubic CdS on InP.

## **6.8 Conclusion**

In conclusion of the above description and discussion, we have successfully deposited CdS thin films on InP (100) wafers by RF magnetron sputtering using a stoichiometric target. Best deposition conditions have been optimized using PL measurement as a diagnostic test. By preparing the substrate surface using vacuum heating and setting the substrate temperature in the 150 °C to 200 °C range during deposition, the Ar pressure to 25 to 40 microns and the RF power to 10 W, the CdS thin film deposited is of the best quality. XRD scan shows that the hexagonal CdS modification with preferred  $\langle 002 \rangle$  orientation is developed at 150° C. Photoluminescence shows that the film has band edge emission, though there are some sulfur-vacancy-related defect. The quality is relatively better than some of the results in the field.

## 7. Characterization of LaS Thin Films Grown on Si and InP Substrates by RF Magnetron Sputtering

### 7.1 Introduction

In Section 5, we described the successful growth of bulk LaS with a lattice constant of  $5.857(2)$  Å. Enough LaS was processed using the sesquisulfide route and the high-temperature furnace from Thermal Technologies, Inc. to press a 2-inch-diameter and 1/8-inch-thick target for use in RF magnetron sputtering experiments. In this Section, we describe the successful growth of LaS thin films by RF magnetron sputtering on Si and InP substrates with (100) orientation. RF magnetron sputtering is much less expensive than other epitaxial approaches such as Molecular Beam Epitaxy (MBE) or Metal Organic Chemical Vapor Deposition (MOCVD), and can also be scaled to large area wafers at relatively low costs.

### 7.2 Sputtering parameters

Our RF sputtering system was described in Section 6. As discussed in that section, the various parameters that are critical to the thin film deposition are Ar pressure, RF power, substrate temperature, and the substrate cleaning procedure. Higher RF power leads to higher  $\text{Ar}^+$  concentration in the plasma, resulting in higher sputtering rates. When the Ar pressure is high, the mean-free path for ions is short; therefore, the energy provided by bombardment will be less, and the quality of the film will be poor. Substrate heating is a means of providing extra energy for thin film formation. When  $T_s$  is low, there is not enough energy for surface species to move around and chemically bond to the surface, resulting in a lot of defects. When  $T_s$  is too high, some of the sulfur content will diffuse out of the surface, resulting in sulfur vacancies.

As an initial estimate of the optimum values of the four parameters listed above, we relied on prior experience with RF magnetron sputtering of CdS thin films on quartz and InP substrates described in detail in section 6. In this case, the optimum parameter values were determined to be an Ar pressure of  $25 \mu\text{m}$ , RF power of 6 W, substrate to target separation of 5 cm and the optimum temperature of the substrate in the range of  $150^\circ\text{C}$  to  $200^\circ\text{C}$ . In all experiments with LaS thin films, the RF parameters were tuned so that they would lead to a thin film of golden color, characteristic of successfully grown bulk samples in the cubic phase. We fixed the substrate to target separation to 5 cm in all depositions.

Careful preparation of the substrate is required for the growth of good epitaxial films. For Si wafer preparation, to remove the native oxide, the substrate is heated at about  $70^\circ$  in a mixture of five parts of water, one part of  $\text{H}_2\text{O}_2$  and one part of  $\text{NH}_4\text{OH}$  for a few minutes. Then the wafer is left in the mixture for another 15 minutes before taking it out and rinsing in DI water. For cleaning of the InP substrates, a mixture of 30 parts of DI water and 1 part of  $\text{H}_2\text{SO}_4$  is taken, and the wafer is dipped using teflon tweezers while gently moving the wafer around for one minute. It is important to move the wafer around in the mixture because the  $\text{H}_2\text{SO}_4/\text{H}_2\text{O}$  mixture tends to stratify. Teflon tweezers must be used as Fluoroware tweezers are attacked by  $\text{H}_2\text{SO}_4$ . The wafer is then taken out and blow dried with  $\text{N}_2$  gas and quickly mounted on to the substrate holder for making a sputtering run. The wafer is stuck to the substrate holder using silver paste for a good thermal contact.

### 7.3 Results

#### 7.3.1 RF Parameters for Growth of LaS Thin Films on Si and InP Substrates

Since InP substrates are rather expensive in relation to Si, we first deposited LaS on Si substrates despite the larger lattice mismatch between these materials (7.2 percent). In these experiments, the time of deposition was kept rather long (up to 24 hours) to be able to determine the thickness of the thin films, hence the growth rate, using a stylus profilometer. In our experiments, the RF power was set to either 10 or 15 W, the Ar pressure was set either to 30 or 50 microns and the InP substrate temperature was varied in the  $150^\circ\text{C} < T_s < 300^\circ\text{C}$  range. The  $T_s$  values are lower than the maximum temperature used for InP substrates in MBE growth of III-V heterostructures. These temperatures are lower than the congruent temperature of  $370^\circ\text{C}$  to avoid complications linked to the formation of

In droplets on the InP substrate. For the LaS/Si thin films, the Si substrate temperature was varied in the  $150^{\circ}\text{C} < T_s < 510^{\circ}\text{C}$  range. Several deposition times were tried ranging from 4 to 48 hours. The results of the Atomic Force Microscopy (AFM) and X-ray Photoelectron Spectroscopy (XPS) analysis of these samples are described below.

### 7.3.2 AFM scans

#### LaS/Si Thin Films

Figure 65 shows a  $1\mu\text{m} \times 1\mu\text{m}$  AFM scan of a LaS thin film deposited on a Si substrate (with 100 orientation) using the following RF parameters: Ar pressure = 30 microns, RF power = 10 watts, substrate temperature =  $510^{\circ}\text{C}$ , and deposition time = 13 hours. The RF magnetron sputtering conditions are indicated on the figure. The substrate to target separation was set equal to 5 cm. The RMS of the surface roughness is less than 5 nm. The scan was over a  $1\mu\text{m} \times 1\mu\text{m}$  area. The AFM scan indicates that the film is granular in nature. Using a profilometer, the film thickness was determined to be between 1500 and 2000 Å. The variation in film thickness is due to the fact that a shadow mask was used to cover part of the sample during deposition. The bulging of the film close to the shadow mask edge leads to variation in the recorded value of the film thickness. It is therefore estimated that the growth rate of the film for the RF parameters listed above is somewhere between 115 and 150 Å/hour. This is a fairly low deposition rate which could probably be improved by tuning the RF parameters. However, these low rates may not be of concern since our ultimate goal is to grow a few monolayers of the rare-earth sulfides to achieve NEA at the surface. For instance, to grow four monolayers on top of the CdS layer of the InP/CdS/LaS cathode proposed in references [4, 5], the deposition time needed would be between 5 and 10 minutes. In Figure 66, an AFM scan over a  $0.5\mu\text{m} \times 0.5\mu\text{m}$  area is the indicated inset. For that region, the root-mean-square (RMS) variation of surface roughness is measured to be 2.9 nm. This means that the film is rather smooth. The smoothness of the film was tested over the whole area of the  $0.5\mu\text{m} \times 0.5\mu\text{m}$  area of the substrate.

#### LaS/InP thin films

Figure 67 is an AFM scan over a  $10\mu\text{m} \times 10\mu\text{m}$  area of a LaS/InP thin film grown with the following deposition parameters: Ar pressure, 30  $\mu$ ; RF power, 10 watts; InP substrate temperature,  $300^{\circ}\text{C}$ ; and deposition time, 24 hours. The substrate to target separation was set equal to 5 cm. The distance between two vertical tick marks on the z-axis is 50 nm. This AFM plot shows the formation of parallel stripes in the film which were not due to an artifact in the AFM measurements, as confirmed in the next figure showing the presence of stripes at various locations in the samples. The film thickness was estimated to be between 1500 and 2000 Å using a profilometer. The film thickness was estimated using a profilometer to be in the 1500 to 2000 Å range. For a deposition time of 24 hours; this corresponds to a growth rate of 60 to 80 Å/hr.

Another AFM scan was taken over  $1\mu\text{m} \times 1\mu\text{m}$  area to resolve the surface roughness of the films in close proximity to some of the stripes shown in Figure 67. The distance between the tick marks along the z-axis equals 50 nm. The depth of the valleys shown in Figure 68 is estimated at  $22 \pm 3$  nm. The flat portions between valleys are found to be surprisingly smooth as shown in the AFM scan of Figure 69. This figure shows an AFM scan of a region of the sample between the two valleys appearing on the figure is shown in the next figure. This scan was performed over an area of  $0.25\mu\text{m} \times 0.25\mu\text{m}$ , and the RMS surface roughness variation was measured to be as small as 1.6 nm.

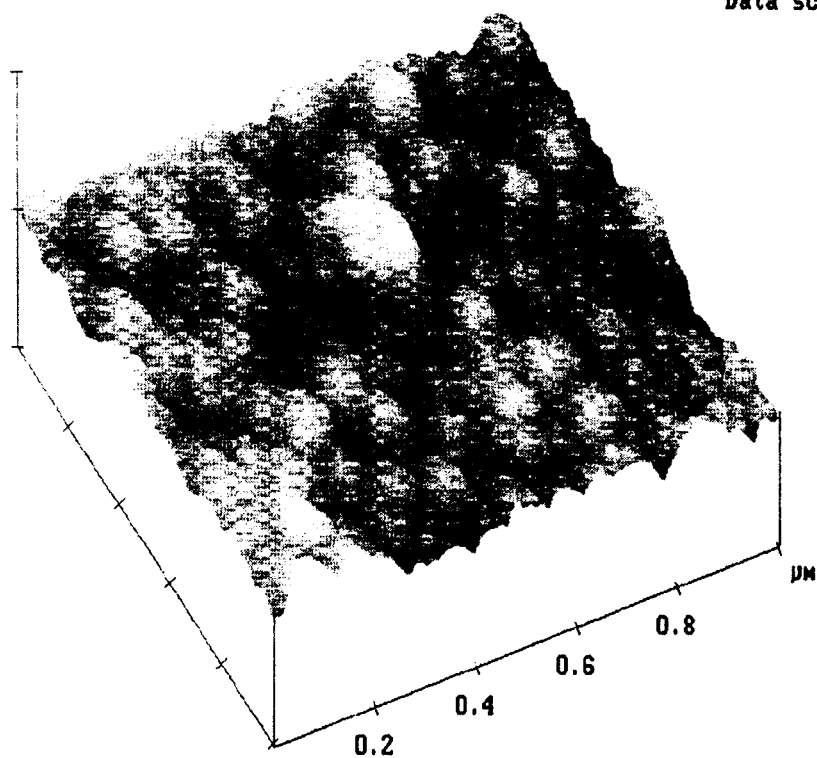
### 7.3.3 X-ray Photoelectron Spectroscopy (XPS) Results

XPS measurements were made using a Surface Science Instrument M-Probe on the as-received samples, i.e., without any preconditioning of the surface. No sputtering of the thin films was performed since it tends to damage the surface and change the composition of the films. The XPS analysis reveals the presence of carbon and oxygen in all thin films, probably due to surface contamination after prolonged exposition to air ambient during storage of the samples.

LaS/Si

30 microns, 510°C, 10 W, 13 hrs

Digital Instruments Nanoscope  
Scan size 1.000  $\mu\text{m}$   
Scan rate 1.001 Hz  
Number of samples 256  
Image Data Height  
Data scale 50.00 nm



X 0.200  $\mu\text{m}/\text{div}$   
Z 50.000 nm/div

Tue Feb 05 2002  
n0401.002

Figure 65: Example of AFM of LaS Samples Deposited on a Si Substrate

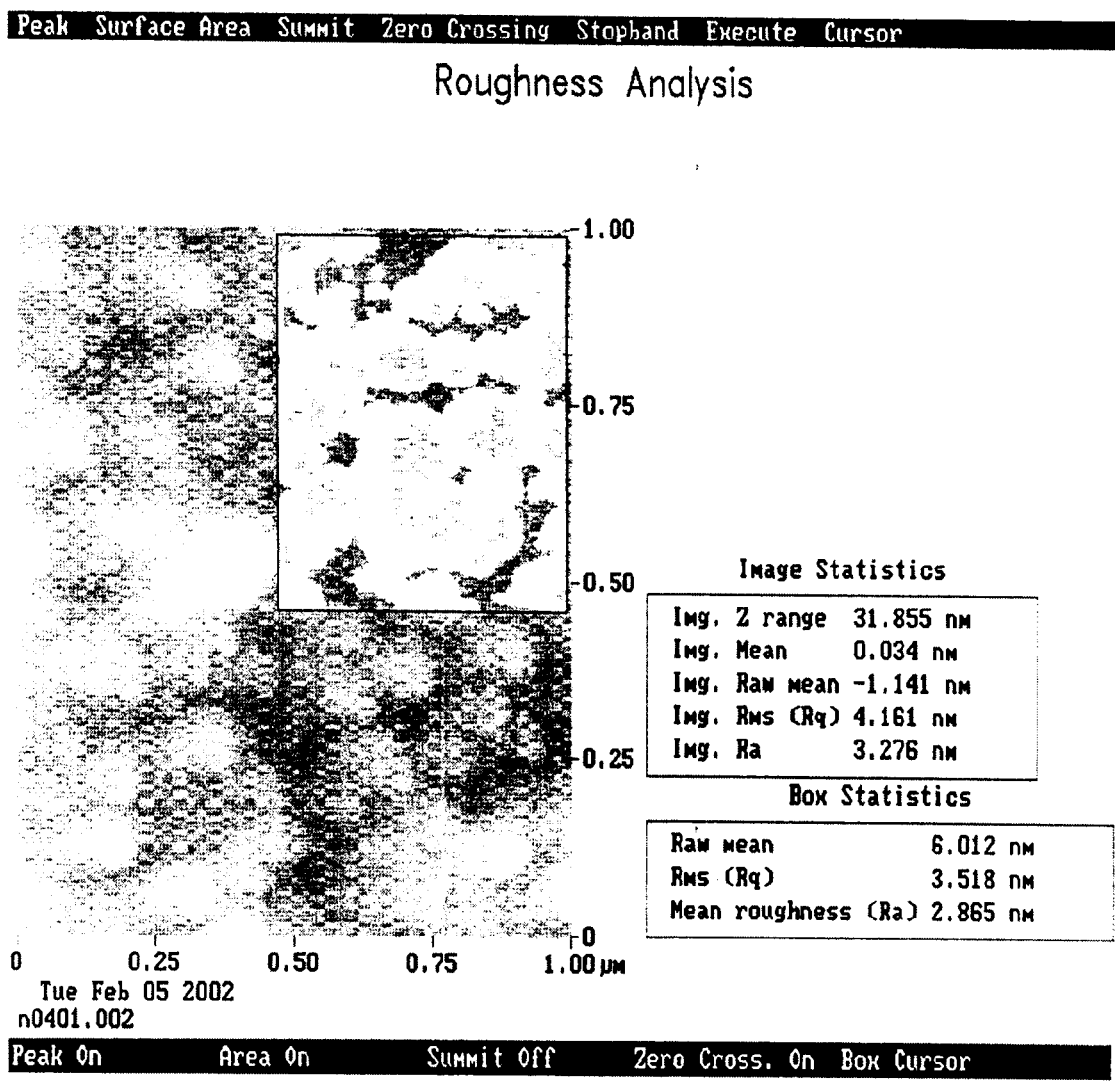


Figure 66: Example of AFM over a Smaller Region (Shown in the Inset) of a LaS Thin Film Deposited on a Si Substrate

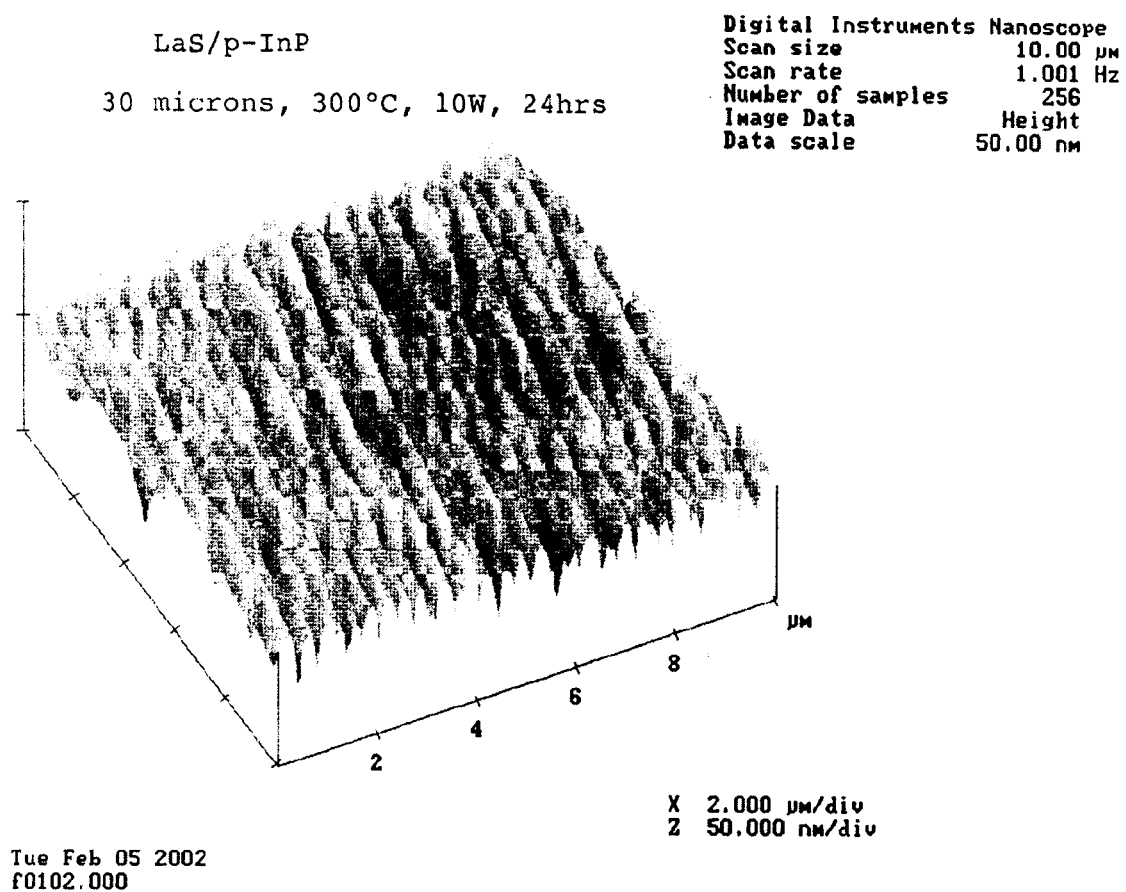
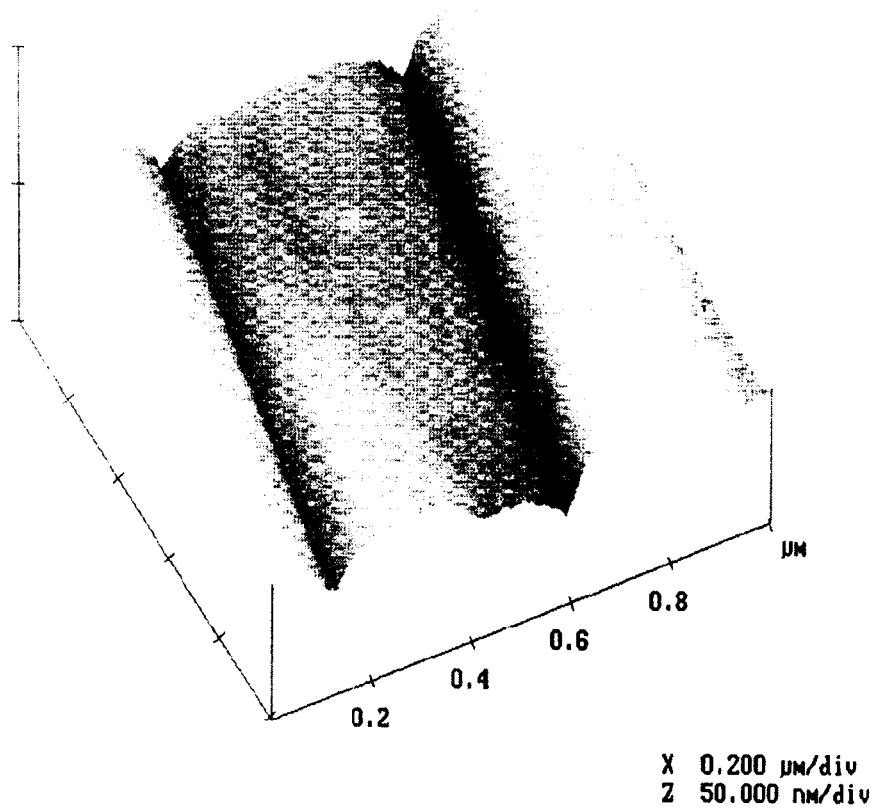


Figure 67: AFM Image of a LaS Thin Film Deposited on a InP

LaS/p-InP  
30 microns, 300°C, 10W, 24 hrs

Digital Instruments Nanoscope  
Scan size 1.000  $\mu\text{m}$   
Scan rate 1.001 Hz  
Number of samples 256  
Image Data Height  
Data scale 50.00 nm



f0102.001

Figure 68: Zoom on a  $1\mu\text{m} \times 1\mu\text{m}$  Region of a LaS/InP Film

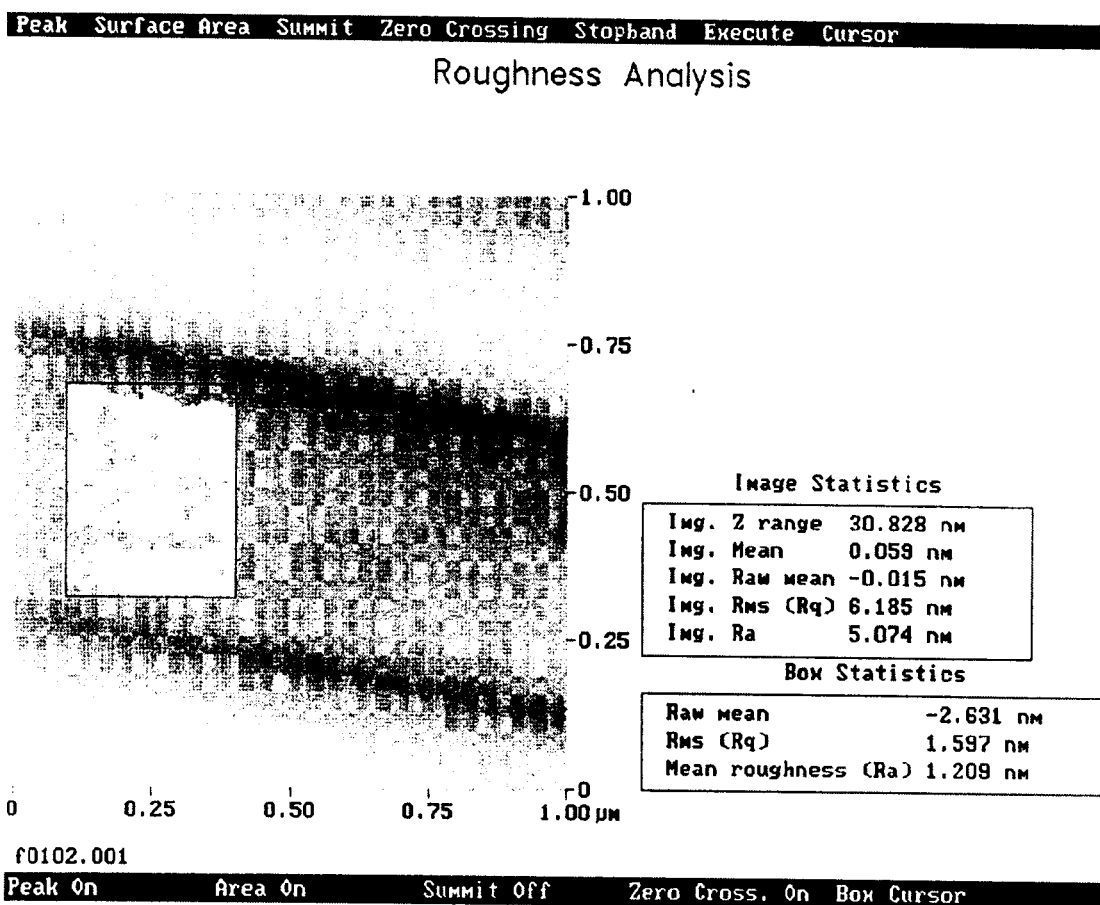


Figure 69: AFM Scan on a Portion Between two Stripes of the LaS/InP Thin Film Shown in Figure 67



**Table 10: InP/LaS XPS Measurements indicating the percentage of La and S in the grown thin films**

RF Parameters				La (%)	S (%)
RF Power (watts)	Pressure ( $\mu$ )	Substrate Temperature ( $^{\circ}$ C)	Time (h)		
10	30	300	23	44	56
10	30	160	24	44	56
15	30	160	24	45	55
15	30	160	48	65	35
10	30	300	4	51	49
10	50	160	24	51	49

The results of the stoichiometry analysis (relative percentage of La and S) of various LaS thin films grown under different RF sputtering conditions are shown in the two rightmost columns of Table 10. The lowest rows show that near perfect stoichiometry was reached for two different sets of values of the RF parameters. A typical XPS spectrum for the fifth LaS/InP sample of Table 10 is shown in Figure 70 for binding energy from 50 to 250 eV. The labeled peaks are the La 4d doublet and the  $4p_{3/2}$  transition, the S 2p and 2s transitions, and the Al 2p transition.

The Al 2s transition near 120 eV is superimposed on the La 4d loss structure. The La  $4p_{3/2}$  and the S 2p transitions were used for quantitative analysis since the kinetic energies of these electrons are very similar, and therefore eliminates any correction needed for a surface contaminant overlayer. The Al concentration was found to be somewhat higher than the La concentration. A substantial amount of aluminum was also detected in all samples. The only possible source of Al in our samples is the Al anode shield used on our RF gun. As the gun is fired, the RF sputtering of the 2-inch target mostly occurs on a ring located very close to the outer edge of the LaS target. For RF parameters selected in the experiments, the magnetic field line pattern around the RF gun could be such that there is substantial sputtering of the Al cap used as an anode shield. Some of the Al would then be deposited on the films. As an extension of this work, RF sputtering runs will be made with a new gun from US, Inc., which does not use the Al anode shield.

From Table 10, we can see that the last run with a RF power of 10 watts, an Ar pressure of 50  $\mu$ , and substrate temperature  $T_s$  of 160 $^{\circ}$  C, gave a good stoichiometry - 51 percent of La and 49 percent of S. This film was grown for 24 hours. The run with parameters RF power = 10 watts, Ar pressure = 30 microns,  $T_s$  = 300 $^{\circ}$  C, and 4 hours deposition also gives the same stoichiometry of La and S. These set of experiments therefore indicate that we have identified the RF parameters needed to successfully sputter thin films of LaS on InP substrates.

#### 7.3.4 XRD Results

When grazing angle XRD was performed on both bare InP wafer (with (100) orientation) and thin films of LaS sputtered on InP wafer, the major Bragg reflection peak observed was characterized by (311) Miller indices. This can be explained with the help of Figure 71. Referring to the figure and using the vector product, the angle  $\theta_1$  between the (100) and (311) crystallographic directions is found to be

$$\theta_1 = \cos^{-1}(3/\sqrt{11}) = 25.2394 \text{degrees.} \quad (91)$$

While the substrate is rotating around the (100) direction perpendicular to the substrate during the XRD scan, the plane defined by the two crystallographic directions will at some point be in the same plane as that of the incident X-ray beam. If we use the lattice constant of the substrate in the Bragg reflection condition

$$2d_{hkl}\sin\theta_2 = \lambda, \quad (92)$$

where  $\lambda=1.541 \text{ \AA}$  is the wavelength of the Cu -  $K_{\alpha}$  line and  $d_{hkl}=a / \sqrt{h^2 + k^2 + l^2}$ , we find that the Bragg condition is satisfied for  $\theta_2 = 26.816$  degrees.

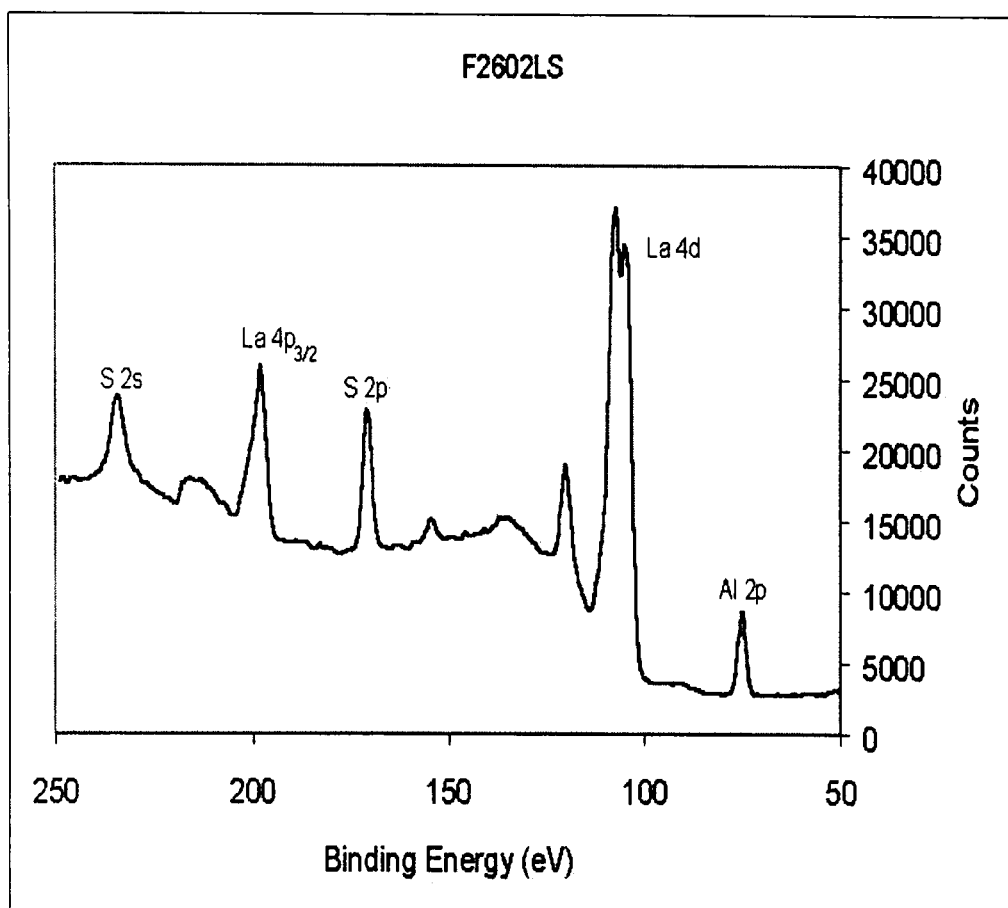


Figure 70: XPS Analysis of The Fifth LaS/InP Sample Shown in Table 10

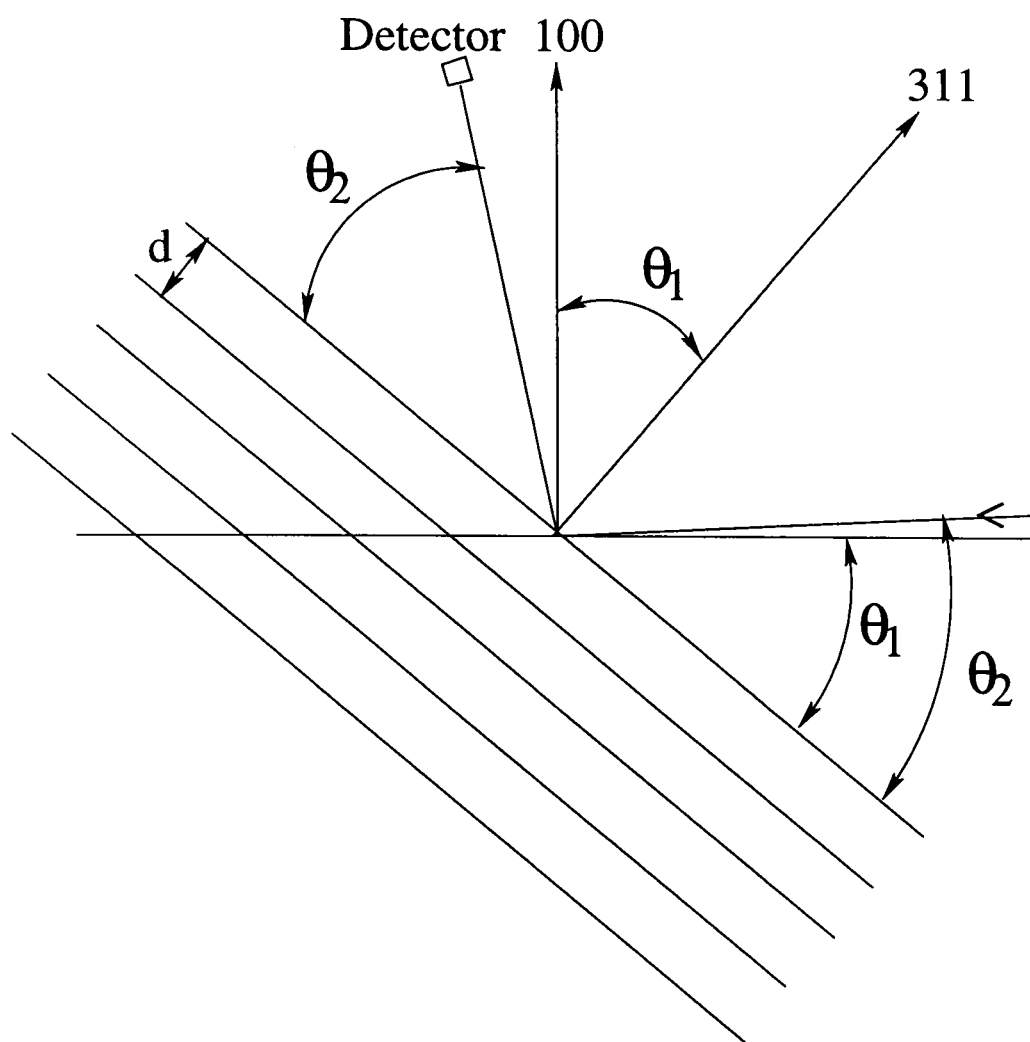


Figure 71: Schematic Representation of Occurrence of (311) Bragg Peak in the Thin Film XRD

This value of  $\theta_2$  is very close to the value of the angle  $\theta_1$  between the (100) and (311) crystallographic directions. This explains why the (311) Bragg reflections is the major peak in the thin film XRD done at small grazing angle around 1 degree.

The need for the grazing angle of the X-ray beam to be almost the difference between the values of  $\theta_1$  and  $\theta_2$  given above was observed during our thin film XRD scans where we noticed that if we set the grazing angle at a value below (0.5 degree) or above (2 degrees) the value  $\theta_2 - \theta_1$  obtained from Equations (91-92) above, the (311) Bragg peak amplitude was either substantially attenuated or nonexistent.

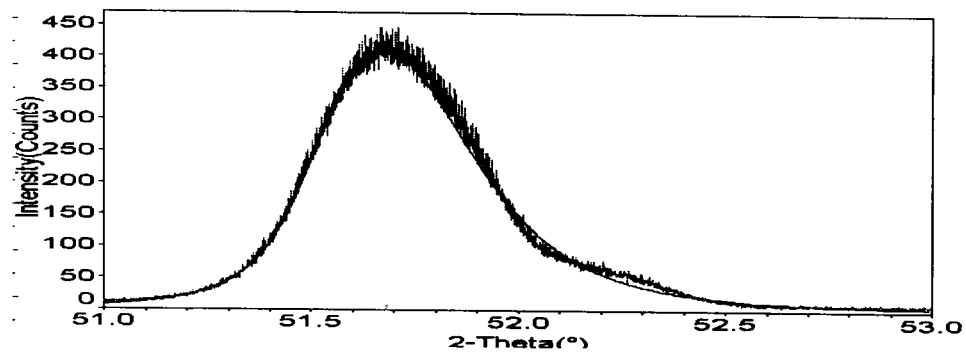
Table 11 shows the FWHM of various XRD runs done on a bare p-type InP wafer (doped at  $10^{-19} \text{ cm}^{-3}$ ). The XRD scans are shown in Figure 72. The grazing angle of the X-ray beam for all these three runs was 1.5 degree and the duration of the scan was 6 hours and 40 minutes. In the first run (INPWAFRD) XRD was done on a p-InP wafer, the FWHM and the angle of the (311) peak were 0.406 degree and 51.6081 degree, respectively. In the second run (INPWAFRE), the same wafer was taken and remounted on the substrate holder, to see if the way that the wafer is mounted would make any difference to the FWHM and the peak position. There was a major change in the FWHM from 0.4 degree to 0.21 degree, and a minor change in the angle from 51.6081 degree to 51.6441 degree. This wafer position was then left undisturbed, and another X-ray run was made (INPWAFRF), to see the change in the values from run to run without a change in the wafer mounting. As shown in the table, we see that FWHM and the peak position differ slightly from the previous run. This sensitivity of the XRD results to the placements of the InP substrates is rather puzzling, especially when comparing the results of second and third runs. The most intriguing result is the variation of the FWHM of the (311) Bragg reflection which is instrumental in determining the eventual presence of epitaxially grown thin films in the XRD experiments.

**Table 11: FWHM And The Angle At Which X-ray Peak Occurs For A p-InP Wafer Having (100) Orientation**

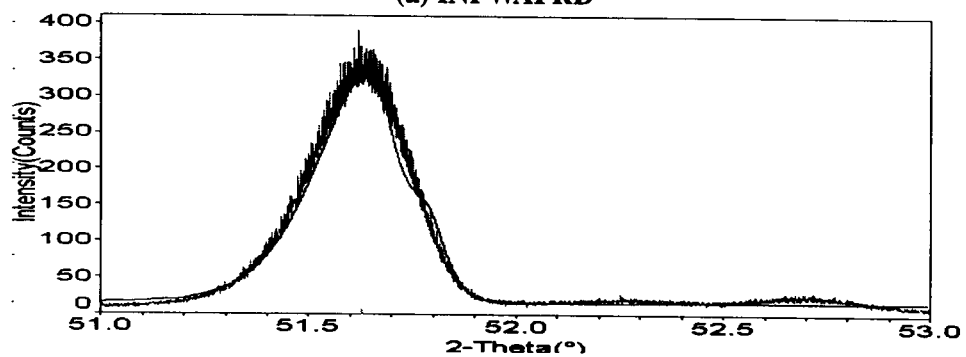
XRD run No.	X-ray description	FWHM	angle
INPWAFRD	Took a bare p-InP wafer	0.406	51.6081
INPWAFRE	Took INPWAFRD and remounted on the substrate holder	0.215	51.6441
INPWAFRF	Started one more run after INPWAFRE run without disturbing the substrate holder	0.278	51.5089

The X-ray results of LaS thin films on p-InP substrates also reveal a (311) peak. Table 12 shows the various LaS thin films, their growth parameters, and the FWHM and the (311) peaks. The X-ray runs have been made for two different grazing angles of 0.5 degree and 1.0 degree. As seen in the table, the FWHM and the peak positions depend slightly on the incident grazing angle of the X-ray beam. In spite of the different values of FWHM and peak positions obtained for bare p-InP wafer for different X-ray runs, and different mountings, we note from Table 11 that the (311) peak position is around 5.6 degree, and for the LaS thin films from Table 12 to be around 5.8 degree on an average. We infer from this peak shift that the (311) peak obtained in LaS/p-InP thin films is due to LaS. Figures 73 and 74 show the X-ray spectra for these different thin films for grazing angles of 0.5 degree and 1.0 degree, respectively. A possibility for the large variation of the FWHM values for bare InP substrates is that they are heavily doped ( $10^{19} \text{ cm}^{-3}$ ). The samples were grown for us by MBE at Oserin, Inc. (MN). XRD results should be compared with those performed on a Bede system before any conclusion can be reached about the crystallinity (mono or poly) of the films.

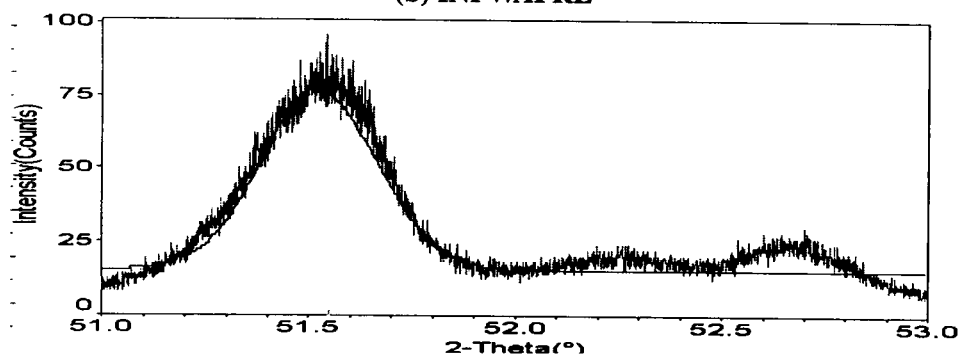
We have also grown thin films of LaS on silicon substrates with (100) orientation (Ar pressure = 20 to 30 microns, RF power = 10 to 15 watts,  $T_s = 300^\circ \text{ C} - 510^\circ \text{ C}$  and sputtering time of 7 to 24 hours). A typical X-ray spectrum of one of the films is shown in Figure 75 (for the growth conditions: Ar pressure = 30 microns,  $T_s = 510^\circ \text{ C}$ , RF power = 10 watts, and 13-hour run).



(a) INPWAFRD



(b) INPWAFRE



(c) INPWAFRF

Figure 72: Thin Film X-ray Spectra of Different Runs Made on Bare p-type InP Wafer

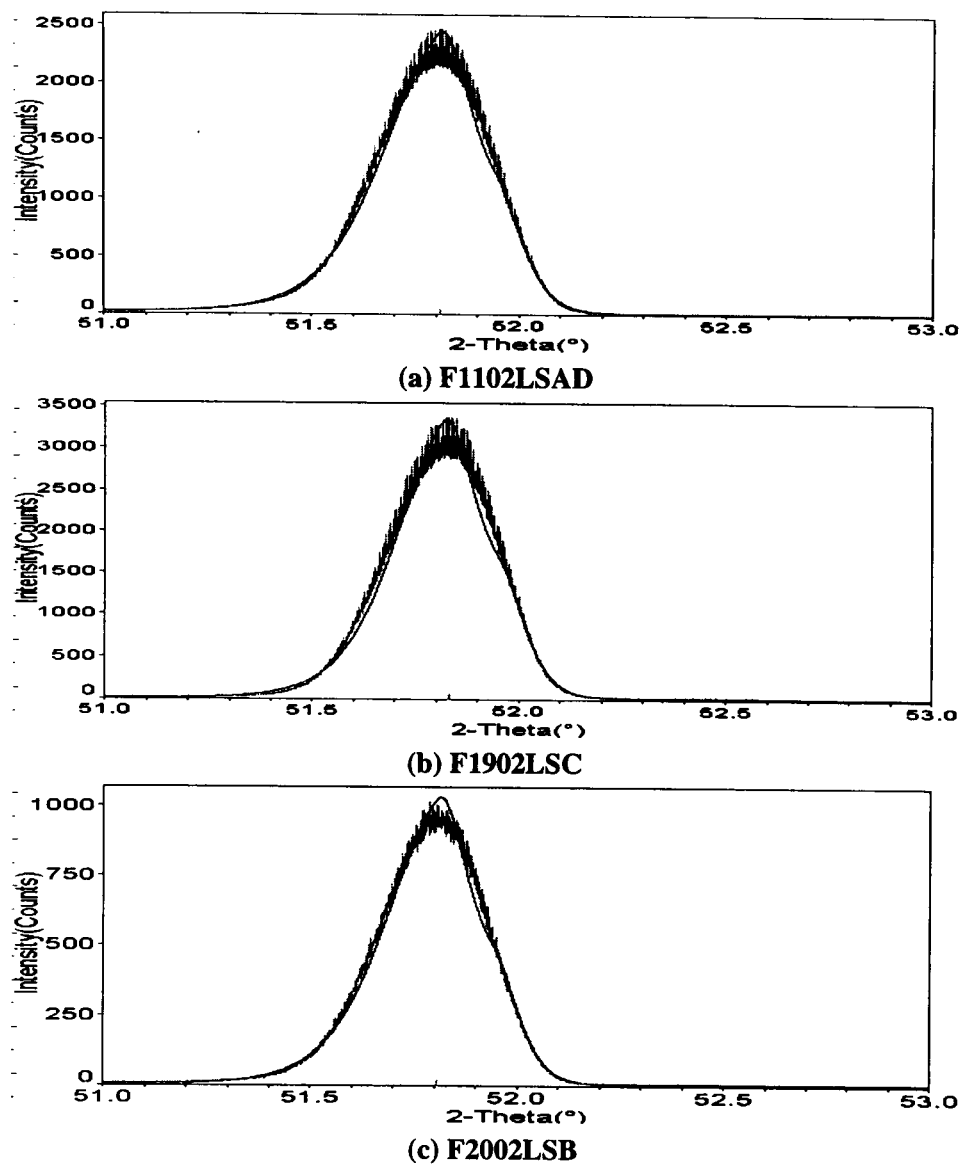
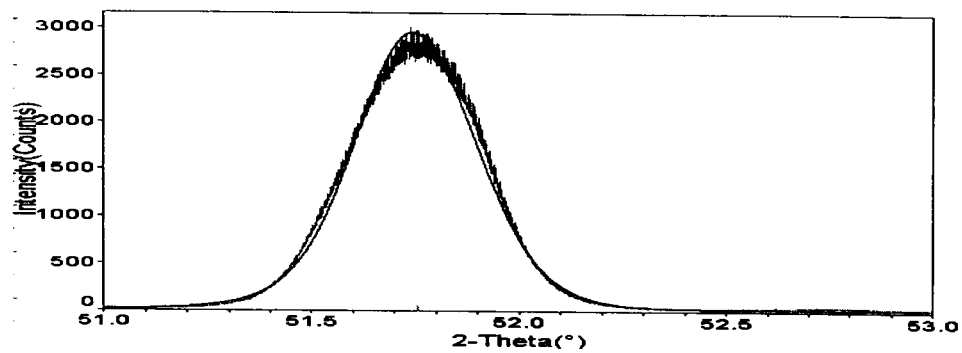
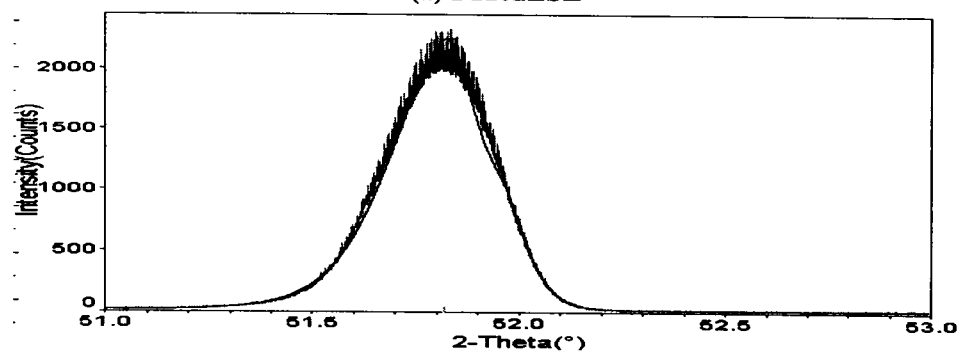


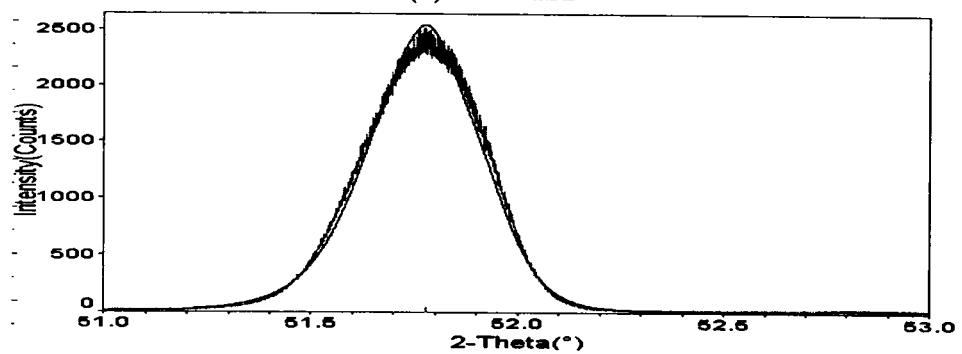
Figure 73: Thin-Film X-ray Spectra of LaS on p-InP at a Grazing Angle of 0.5 Degree



(a) F1102LSE



(b) F1902LSD



(c) F2002LSE

Figure 74: Thin-Film X-ray Spectra of LaS on p-InP at a Grazing Angle of 1.0 Degree

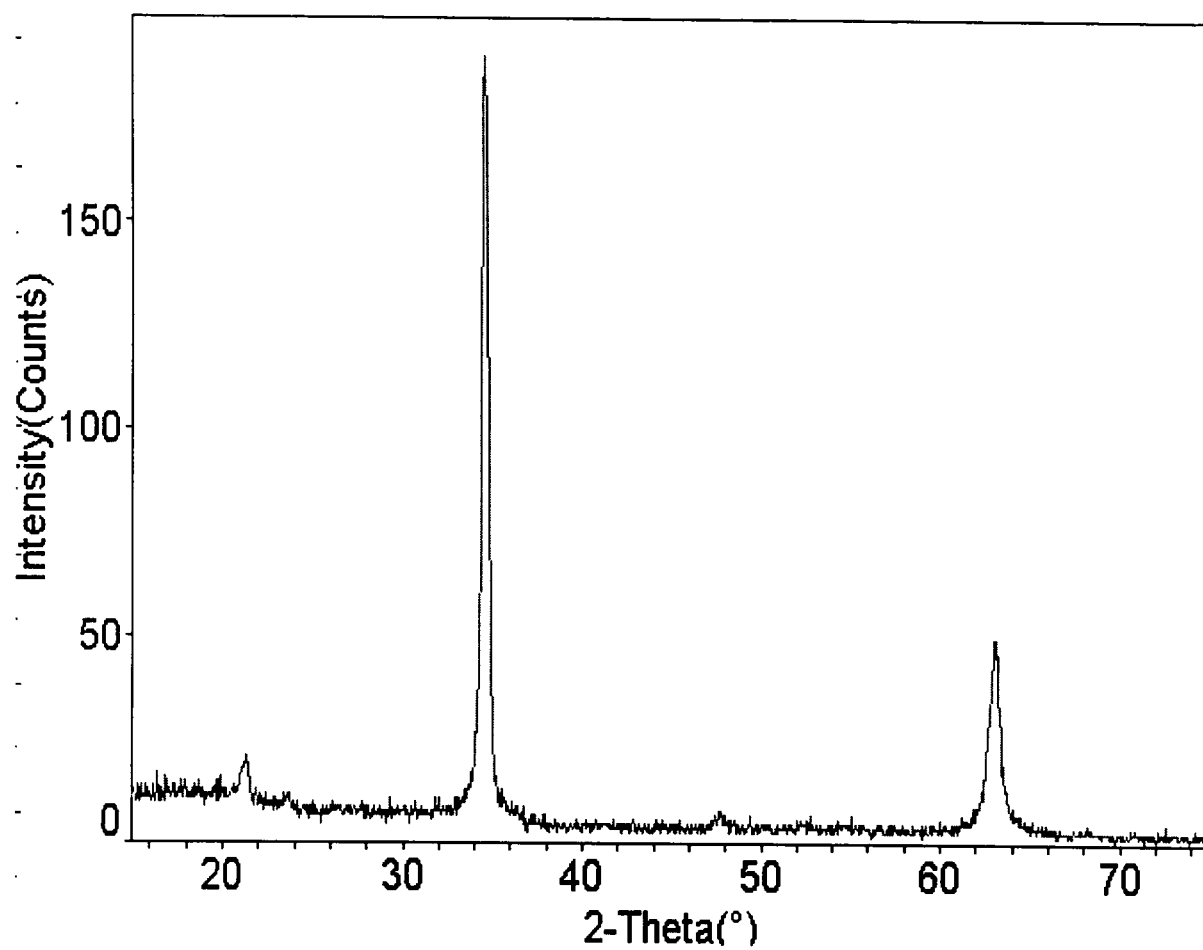


Figure 75: Thin Film X-ray Spectra of LaS on Si Wafer by RF Sputtering



**Table 12: FWHM And  $2\theta$  from the Thin Film X-ray Spectra of Different RF Sputtered LaS Samples on p-InP Substrates**

angle	Sample No.	RF parameters				FWHM	$2\theta$
		Pressure ( $\mu$ )	Temp. ( $^{\circ}C$ )	Power (W)	Time (hr)		
0.5 $^{\circ}$	F1102LSD	30	300	10	23	0.250	51.8090
	F1902LSC	30	160	10	24	0.222	51.8181
	F2002LSB	30	160	15	24	0.230	51.8108
1.0 $^{\circ}C$	F1102LSE	30	300	10	23	0.296	51.7157
	F1902LSD	30	160	10	24	0.237	51.8193
	F2002LSE	30	160	15	24	0.263	51.7618

In this case, we could not match the three peaks with any JCPDS data cards, not even to those of silicon. The difficulty is probably due to the large lattice mismatch (7.2 percent) between the two materials.

We also tried to grow LaS thin films on various substrates like glass and silicon by e-beam evaporation. These films were grown for us by Ron Flenniken using the e-beam evaporation system on the ninth floor clean room. Figure 76 shows the X-ray spectrum of such e-beam grown LaS thin film on silicon substrate. The different Bragg peaks could be matched to lanthanum oxide sulfide ( $La_2O_2S$ , JCPDS card # 27-0263). Some silicon peaks (JCPDS card # 27-1402) have also been identified. This thin film was obtained after using rapid thermal annealing (at 500 $^{\circ}C$  for 10 minutes) in air ambient immediately after the e-beam evaporation process. This explains the presence of large amounts of oxygen and the growth of the oxysulfide phase ( $La_2O_2S$ ). Also shown at the bottom of Figure 76 are the locations of the major Bragg reflection peaks expected for  $La_2O_2S$  and bulk Si. The Miller indices of the  $La_2O_2S$  are indicated next to each major Bragg reflection peak.

#### 7.4 Conclusions

In this section, we reported preliminary results on the deposition of LaS thin films by RF magnetron sputtering on Si and InP substrates. Using e-beam evaporation followed by RTA, we successfully formed a thin film with the XRD characteristics of the oxysulfide ( $La_2O_2S$ ) phase. The RF sputtering of LaS on Si leads to a thin film that is golden in color but with Bragg reflection peaks which could not be identified with any of the JCPDS data of LaS and Si or any mixture of these elements, even for a JCPDS search including oxygen content. The difficulty in interpreting the XRD results may be linked to the large lattice mismatch (7.2 percent) between LaS and Si in their cubic phase.

The parameters (RF power, Ar pressure, substrate temperature, and substrate to target separation) which lead to growth of stoichiometric LaS thin films on InP substrates are identified (see Table 10). Most of the thin films (between 1500 and 2000  $\text{\AA}$  thick) appear golden in color, as do their bulk counterparts. Using a stylus profilometer, the growth rate of the films is found to be quite low (50 to 100  $\text{\AA}/\text{hr}$ ). This rate could probably be increased by varying the parameters of the RF sputtering unit, but low rates are not a major concern since cold cathode applications would require just a few monolayers of the rare-earth sulfides to achieve NEA at the surface of LaS/p-InP cold cathodes.

AFM analysis reveals that all thin films are very smooth with a RMS variation of surface roughness of just a few nanometers. However, all thin films are found to contain aluminum comparable to the amount of rare-earth sulfide in the samples. The presence of Al was identified as originating from the cathode shield cap of the RF gun used. New films of rare-earth sulfides are now being deposited using a new US gun design which does not require the use of an Al cathode shield cap. The results of this Section were published in reference [47].

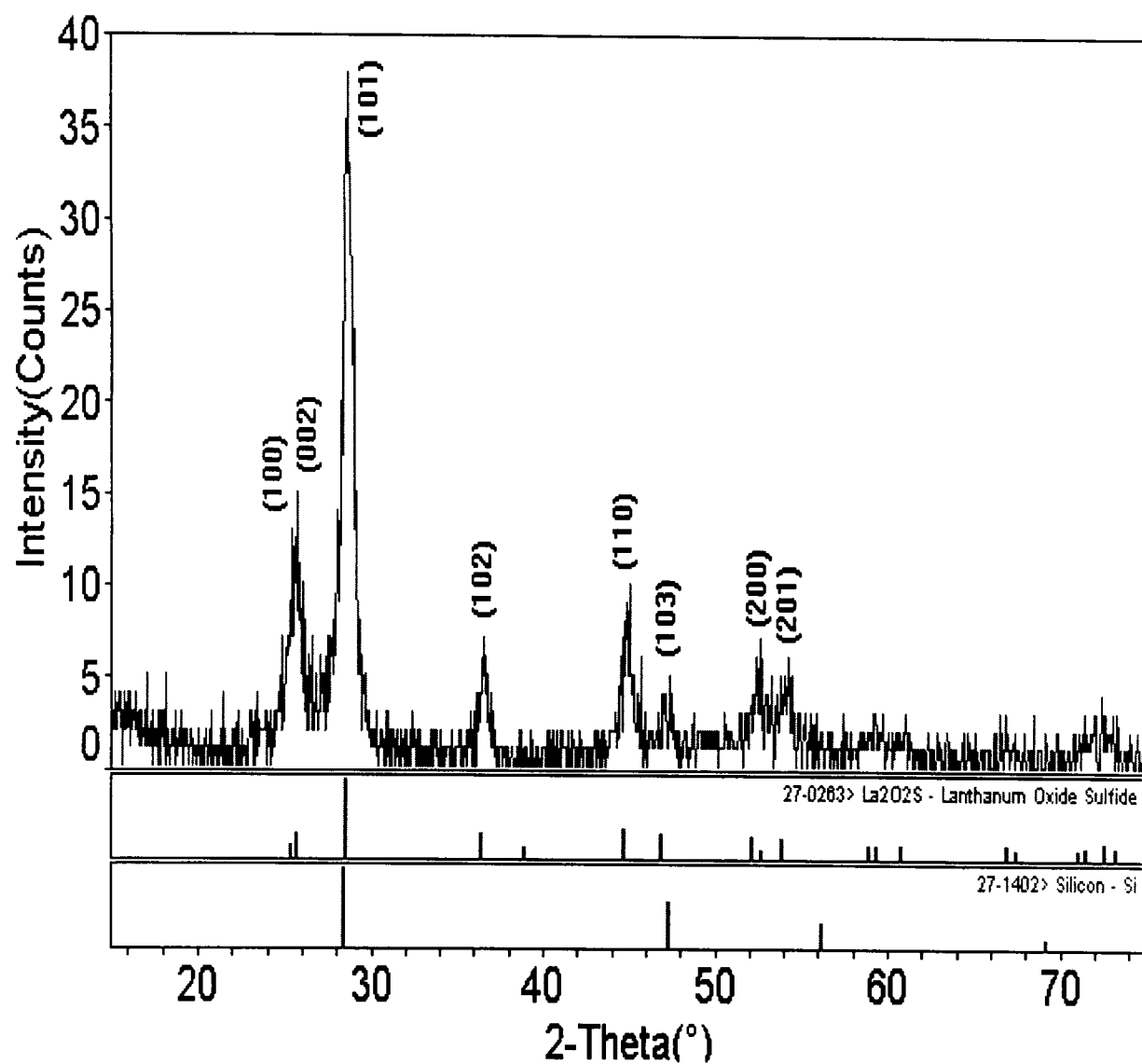


Figure 76: Thin Film X-ray Spectra of LaS on Si Wafer by E-Beam Evaporation

## 8. Conclusions and Future Work

### 8.1 Conclusions

In this research effort, we have investigated theoretically the metal/CdS/LaS and  $n^{++}$ -InP/CdS/LaS cold cathodes proposed by Mumford and Cahay [4, 5, 6], to include self-heating effects, the importance of space-charge effects on the regime of current self-quenching, and finally the interplay between current crowding and current self-quenching effects. In Section 2, we described the various power dissipation mechanisms and their influence on the operating temperature of a InP/CdS/LaS cold cathode shown schematically in Figure 5. For the cold cathodes analyzed here, the effects of current crowding were found to occur at a lesser bias than the one at which self-heating effects can no longer be neglected. At the maximum bias at which current crowding effects can be tolerated, the emission current density is found to reach several  $10^2 \text{ A/cm}^2$ . However, the ballistic fraction of the beam emitted into vacuum is found to be dominant only if the width of the CdS layer is kept under  $150 \text{ \AA}$ . In order of decreasing importance, the leading contributions to power dissipation in the cathode were found to be (1) the power dissipation due to the shadowing effect of the emitter fingers used to bias the device, (2) the power dissipation due to the trapping of electrons by the LaS thin film, and (3) the power released as a result of inelastic scattering in the CdS layer. For the cathode analyzed here, the overall power efficiency of the cathode was around 20 percent and decreased with applied bias as a result of current crowding and self-heating effects. Larger power efficiency is possible by reducing the width of the biasing emitter fingers. However, the height of the metal fingers would have to be increased simultaneously to avoid a substantial voltage drop along the emitter fingers.

Anode current self-quenching due to space-charge effects is described in Section 3. We have used an ensemble Monte-Carlo approach to analyze these effects in InP/CdS/LaS and metal/CdS/LaS cold cathodes. Inelastic scattering in the CdS layer was considered in the case of metal/CdS/LaS structure, and ballistic transport in the case of InP/CdS/LaS structure. In both cases, the energy spread of the electron beam collected at the anode was shown to be substantially narrower than for the beam injected from the cathode into vacuum due to the modulation of the beam by the oscillations of the electric potential in front of the cathode. When the effects of inelastic scattering through the CdS layer are included, the transition to the regime of current self-quenching is more gradual compared to that of ballistic transport through the CdS layer.

The interplay between current crowding and current self-quenching was described in Section 4. When space-charge effects are neglected, the anode current decreases monotonically from the edges of the emission window towards the center as a result of the finite conductivity of the LaS thin films. This is the *regular* current crowding effect described by Mumford and Cahay [5]. When a self-consistent solution between current self-quenching and current crowding effects is used, the anode current density profile across the emission window can be non-monotonic. We saw that the anode current density profile can increase above its value at the edges of the emission window followed by a maximum before dropping again upon approaching the center of the emission window for a metal/CdS/LaS cold cathode.

In this work, we also have initiated the experimental steps needed to realize prototypes of the cold cathodes. First, we needed to grow the bulk LaS material. We have described the successful growth and characterization of the bulk material in Section 5 using a sesquisulfide route. The lattice constant of the end product was determined to be  $5.8679 \text{ \AA}$ , in good agreement with earlier results published in reference [45]. The work function of bulk LaS has been measured by the Kelvin probe method and its lowest value was found to be  $2.6 \text{ eV}$  in air. We have also identified the RF parameters (RF power, Ar pressure, substrate temperature, and substrate to source separation) needed for RF magnetron sputtering of CdS thin films starting from a CdS target (99.99 percent pure bought from Cerac, Inc.). The details of this investigation are given in Section 6. In Section 7, we report our successful fabrication of 2-inch-diameter and 1/8-inch-thick sputtering target of LaS, which we used to grow thin films of LaS by RF magnetron sputtering on both Si and InP substrate. We have identified the RF parameters (RF power, Ar pressure, substrate temperature, and substrate to source separation) which lead to thin films with a close to stoichiometric ratio (La:S = 51:49). RF Magnetron sputtering was performed on various substrates like Si, glass, and InP. The parameters leading to samples with stoichiometric amounts of La and S atoms are identified. Thin film samples are characterized by XPS, AFM, and XRD.

## 8.2 Suggestions for Future Work

More work needs to be done to fine tune the parameters so that the LaS thin film growth is uniform, and to a few monolayers. We have grown thin films on InP substrate. To realize the cold cathode emitter, we need a metal( $n^{++}$ -InP)/CdS/LaS structure. So an in situ growth of a few hundreds of angstroms of CdS first needs to be sputtered on to InP, and immediately a few monolayers of LaS needs to be grown. The work function of LaS thin film also needs to be measured in situ immediately after the deposition, so that the film is not exposed to air.

In the last few months of this research effort, we were able to acquire a Revap-3000 (thermal evaporation unit) from Thermal Technologies, Inc. and have been experimenting with the deposition of very thin films of LaS (a few monolayers) by thermal evaporation. In the near future, we will deposit the CdS and LaS layers in situ (i.e., without breaking the vacuum), and the resulting cathodes will be tested for field emission.

All along, we have been reporting the results of both the theoretical and experimental efforts described in this report in the form of journal publications, proceeding papers, and conference presentations. A complete list of these reports is given in Section 8.3.

## 8.3 List of Journal Publications, Conference Proceedings Papers, and Conference Presentations

- Y. Modukuru, M. Cahay, P. Boolchand, and J. T. Grant, "RF Magnetron Sputtering of LaS Thin Films on InP Substrates," Joint Meeting of the 15th *International Vacuum Microelectronics (IVMC)* and 48th *International Field Emission Symposium (IEFS)* 2002, Lyon (France), July 7-11, 2002.
- Y. Modukuru and M. Cahay, "Interplay of Current Crowding and Current Self-Quenching Effects in Planar Cold Cathodes," *Journal of Vacuum Science and Technology B* **19**, p. 2149 (2001).
- Y. Modukuru, J. Thachery, H. Tang, A. Malhotra, M. Cahay, and P. Boolchand, "Growth and Characterization of Rare-Earth Monosulfides for Cold Cathode Applications," *Journal of Vacuum Science and Technology B* **19**, p. 1958 (2001).
- Y. Modukuru, M. Cahay, H. Kolinsky, and P. D. Mumford, "Onset of Current Self-Quenching in a Metal/CdS/LaS Cold Cathode in the Presence of Inelastic Scattering in the CdS Layer," *Journal of Applied Physics* **87**, p. 3386 (2000).
- A. Malhotra, Y. Modukuru, and M. Cahay, "Self-Heating Effects in a *InP/CdS/LaS* Cold Cathode," *Journal of Vacuum Science and Technology B* **16**, p. 3086 (1998).
- Y. Modukuru and M. Cahay, "Non Uniformity of The Anode Current Distribution In Cold Cathodes Based on Thin Films of Rare-Earth Chalcogenides," *Proceedings of the Sixth International Symposium on Quantum Confinement*, 200th Meeting of the Electrochemical Society, San Francisco, CA, September 2001.
- M. Cahay, Y. Modukuru, J. Thachery, H. Tang, A. Malhotra, and P. Boolchand, "The use of Rare-Earth Monosulfides to realize low or Negative Electron Affinity Cold Cathodes," 2001 Advanced Research Workshop on "Future Trends in Microelectronics: The Nano Millennium," Ile de Bendor, France, June 25-29, 2001.
- Y. Modukuru and M. Cahay, "Onset of Current Self-quenching in an  $n^{++}$ -*InP/CdS/LaS* Cold Cathode," *Proceedings of the First International Symposium on Cold Cathodes*, 198th Meeting of the Electrochemical Society, Phoenix, AZ, October 2000.
- Y. Modukuru, J. Thachery, H. Tang, M. Cahay, and P. Boolchand, "Synthesis and Work Function Measurement of *LaS* and *NdS* bulk samples," *Proceedings of the First International Symposium on Cold Cathodes*, 198th Meeting of the Electrochemical Society, Phoenix, AZ, October 2000.
- Y. Modukuru, A. Malhotra, H. Tang, M. Cahay, and P. Boolchand, "Design and Fabrication of an *InP/CdS/LaS* Cold Cathode," Poster presented at the First Symposium on Nano-, Micro-, and Mesoscale Technologies in Science and Engineering, Engineering Research Center, University of Cincinnati, May 13, 1999.

- M. Cahay, A. Malhotra, Y. Modukuru, H. Tang, W. Bresser, P. Boolchand, P. D. Mumford, and W. Friz, "Towards the Realization of a InP/CdS/LaS cold cathode," *Proceedings of the Symposium on Vacuum Micro-electronics*, MRS meeting, Spring 1999.
- M. Cahay, A. Malhotra, Y. Modukuru, H. Tang, W. Bresser, P. Boolchand, P. D. Mumford, and W. Friz, "Design and Fabrication of an *InP/CdS/LaS* Cold Cathode," MRS meeting, Spring 1999, April 5-9, San Francisco, CA.
- Y. Modukuru, M. Cahay, and P. Mumford, "Space-Charge Effects in a InP/CdS/LaS Cold Cathodes," American Physical Society Meeting, Atlanta, GA, March 1999.

Three students were supported under this contract. Two already defended their Masters Thesis, and one student should be graduating early in 2003. The titles of their theses are given in Section 8.4, below.

#### **8.4 Theses Supported By This Research Effort**

- H. Tang, "Synthesis and Characterization of Pure LaS and Growth of CdS Thin-Film by RF Sputtering," Advisor: P. Boolchand, Masters Thesis, University of Cincinnati, January 2000.
- A. Malhotra, "Growth and Characterization of Rare-Earth Sulfides for Use in Negative Electron Affinity Cathodes," Advisor: M. Cahay, Masters Thesis, University of Cincinnati, June 1999.
- Y. Modukuru, "Theoretical and Experimental Investigation of Low and Negative Electron Affinity Cold Cathodes Based on Rare-Earth Monosulfides," Advisor: M. Cahay, Ph.D. Thesis, University of Cincinnati, Summer 2002.

## 9. References

- [1] S. Iannazzo, "A Survey of the Present Status of Vacuum Microelectronics," *Solid-State Electronics*, Vol. 36, pp. 301-320 (1993).
- [2] I. Brodie and C.A. Spindt, "Vacuum Electronics," Advances in Electronics and Electron Physics, Vol. 83, New York: Academic Press, Inc., pp.1-106, 1992).
- [3] P.R. Bell, Negative Electron Affinity Devices, Oxford: Clarendon Press, 1973.
- [4] P.D. Mumford and M. Cahay, "Dynamic Workfunction Shift in Cold Cathode Emitters Using Current Carrying Thin Films," *J. Appl. Phys.*, Vol. 79, pp.2176-2179, 1996.
- [5] P.D. Mumford and M. Cahay, "Current Crowding Effects in a CdS/LaS Cold Cathode," *J. Appl. Phys.*, Vol. 81, pp.3707-3715, 1997.
- [6] P.D. Mumford and M. Cahay, "Space-Charge Effects and Current Self-Quenching in a Metal/CdS/LaS Cold Cathode," *J. Appl. Phys.* Vol. 84, pp.2754-2767, 1998.
- [7] G.V. Samsonov, High Temperature Compounds of Rare-Earth Metals with Nonmetals, New York: Consultants Bureau, 1965.
- [8] V.S. Fomenko, Handbook of Thermionic Properties, New York: Plenum Press Data Division, 1966.
- [9] C.D. Child, "Discharge from CaO," *Phys. Rev.*, Vol. 32, pp.492-511, 1911.
- [10] I. Langmuir, "The Effect of Space-Charge and Initial Velocities on the Potential Distribution and Thermionic Current between Parallel Plate Electrodes," *Phys. Rev.*, Vol. 21, pp. 419-435, 1923.
- [11] H. Kolinsky and H. Schamel, "Arbitrary Potential Drops between Collector and Emitter in Pure Electron Diodes," *J. Plasma Phys.*, Vol. 57, pp. 403-423, 1997.
- [12] H. Kolinsky, "Das Stabilitätsverhalten von Plasmadioden" (On the Stability Conditions in Plasma Diodes), Ph.D. thesis, Universität Bayreuth, Germany, 1998.
- [13] H. Tang, "Synthesis and Characterization of Pure LaS and Growth of CdS Thin-Film by RF Sputtering," Masters Thesis, University of Cincinnati, January 2000.
- [14] R.H. Good, Jr. and E. Muller, "Field Emission," in Handbuch der Physik, Vol. 21, pp.176-231, Berlin:Springer-Verlag, 1956.
- [15] S. Wang, Fundamentals of Semiconductor Theory and Device Physics, p. 252, Prentice Hall (1989).
- [16] O. Madelung (ed.), Semiconductors. Other than Group IV Elements and III-V Compounds, New York: Springer-Verlag, 1992.
- [17] K.L. Jensen, "Improved Fowler-Nordheim Equation for Field Emission from Semiconductors," *J. Vac. Sci. Technol.*, Vol. 13, pp. 516-521, 1995.
- [18] K.L. Jensen and A.K. Ganguly, "Numerical Simulation of Field Emission and Tunneling: A Comparison of Wigner Function and Transmission Coefficient Approaches," *J. Appl. Phys.*, Vol. 73, pp. 4409-4427, 1993.
- [19] J.M. Ziman, Theory of Solids, Cambridge, UK: Cambridge University Press, 1972.
- [20] C. Cohen-Tannoudji, B. Diu, and F. Laloë, Quantum Mechanics, Vol.1 (translation of Mécanique Quantique), Chap.1, New York: Wiley-Interscience, 1977.

- [21] J. A. Edminister, Schaum's Outline of Theory and Problems of Electromagnetics, New York: McGraw-Hill, 1979.
- [22] J.J. Liou, L.L. Liou, C.I. Huang, and B. Bayraktaroglu, "A Physics-Based, Analytical Heterojunction Bipolar Transistor Model, Including Thermal and High Current Effects," *IEEE Trans. Electron Devices*, Vol. 40, pp. 1570-1577, Sep. 1993.
- [23] A. Malhotra, Y. Modukuru, and M. Cahay, "Self-Heating Effects in InP/CdS/LaS Cold Cathodes," *J. Vac. Sci. Technol. B*, Vol. 16, pp.3086-3096, 1998.
- [24] M.S. Chung, P.H. Cutler, N.M. Miskovsky, and T.E. Sullivan, "Energy Exchange Processes in Electron Emission at High Fields and Temperatures," *J. Vac. Sci. Technol. B*, Vol. 12, pp. 727-736, 1994.
- [25] L.G. Il'chenko and V.M. Ogenko, "Imafe forces near the surface of a semiconductor with a space-charge region", *Surf. Sci. Lett.*, Vol.262, L147, 1992.
- [26] S. M. Sze, Physics of Semiconductor Devices, 2nd ed. New York: Wiley, 1981, (p. 219).
- [27] Y. Modukuru, M. Cahay, H. Kolinsky, and P.D. Mumford, "Onset of Current Self-Quenching in a Metal/CdS/LaS Cold Cathode in the Presence of Inelastic Scattering in the CdS Layer," *J. Appl. Phys.*, Vol. 87, pp. 3386-3393, 2000.
- [28] Y. Modukuru and M. Cahay, "Interplay of Current Crowding and Current Self-Quenching Effects in Planar Cold Cathodes," *J. Vac. Sci. Technol. B*, Vol. 19, pp.2149-2154, 2001.
- [29] A. Malhotra, "Growth and Characterization of Rare-Earth Sulfides for Use in Negative Electron Affinity Cathodes," Masters Thesis, University of Cincinnati, June 1999.
- [30] Jugul Thachery, "Synthesis and Characterization of Neodymium Sulfide Bulk Samples and Thin Films," M.S. Thesis, University of Cincinnati, January 2002.
- [31] Y. Modukuru, J. Thachery, H. Tang, A. Malhotra, M. Cahay, and P. Boolchand, "Growth and Characterization of Rare-Earth Monosulfides for Cold Cathode Applications," *J. Vac. Sci. Technol. B*, Vol 19, pp.1958-1962, 2001.
- [32] I. Frankowski and P. Watcher, "Point Contact Spectroscopy on LaS, GdS, and TmSe," *Solid State Communications*, Vol. 40, pp.885-888, 1981.
- [33] L.W. Swanson and P.R. Davis, "Work Function Measurements", in *Solid State Physics: Surfaces* (R.L. Park and M.G. Lagally, eds., *Methods of Experimental Physics Series*, Vol.22), Orlando, FL: Academic Press, 1985, (pp. 1-22).
- [34] For a review of the Kelvin probe technique, see I.D. Baikie, S. Mackenzie, P.J.Z. Estrup, and J.A. Mayer, "Noise and the Kelvin method," *Review of Scientific Instruments*, Vol. 62, pp. 1326-1332, May 1991.
- [35] I.D. Baikie, P.J.S. Smith, D.M. Porterfield, and P.J. Estrup, "Multitip Scanning Bio-Kelvin Probe," *Review of Scientific Instruments*, Vol. 70, pp. 1842-1850, Mar. 1999.
- [36] M.R. Lozada Morales and A.O. Zelaya Angel, "Photoluminescence Analysis of CdS Thin Films under Phase Transition," *Thin Solid Films*, Vol. 281-282, pp. 386-389, 1996.
- [37] C. Mejia-Garcia, A. Escamilla-Esquivel, G. Contreras-Puente, M. Tufino-Velazquez, M.L. Albor-Aguilera, O. Vigil, and L. Vaillant, "Photoluminescence Studies of CdS films grown by close-spaced vapor transport hot walls," *J. Appl. Phys.*, Vol. 86, pp. 3171-3174, 1999.
- [38] T. Yodo and S. Tanaka, "Growth of CdS by Atmospheric Pressure Metalorganic Vapor-Phase Epitaxy at Low Temperature," *J. Appl. Phys.*, Vol. 72, pp. 2781-2790, 1992.

- [39] O. Zelaya-Angel, L. Hernandez, O. de Melo, J.J. Alvarado-Gil, R. Lozada-Morales, C. Falcony, H. Vargas, and R. Ramirezbon, "Band-Gap Shift in CdS: Phase Transition from Cubic to Hexagonal on Thermal Annealing," *Vacuum*, Vol. 46, pp. 1083-1085, 1995.
- [40] H. Ariza-Calderon, R. Lozada-Morales, O. Zelaya-Angel, J.G. Mendoza-Alvarez, and L. Banos, ""Photoluminescence Measurements in the Phase Transition Region for CdS Thin Films," *J. Vac. Sci. Technol. A-Vacuum Surfaces and films*, Vol. 14, pp. 2480-2482, 1996.
- [41] W.P. Shen and H.S. Kwok, "Doped P-type and N-type ZnS, ZnSe, CdS, and CdSe Thin Films Growth by Pulsed Laser Deposition", Materials Research Society Symposium Proceedings, Vol. 340, pp.457-459, 1994.
- [42] T. Miyasato and M. Tonouchi, "Preparation of Compound Semiconductor Films by Means of Hydrogem Plasma Sputtering," *Materials Science and Engineering B- Solid State Materials for Advanced Technology*, Vol. 9, pp. 195-199, 1991.
- [43] R. Ramirez-Bon, N.C. Sandoval-Inda, F.J. Espinoza-Beltran, M. Sotelo-Lerma, O. Zelaya-Angel, and C. Falcony, "Structural Transition of Chemically Deposited CdS Films on Thermal Annealing," *J. Phys.-Condensed Matter*, Vol. 9, p. 10051-10058, 1997.
- [44] D. Lincot, B. Mokili, M. Froment, R. Cortes, M.C. Bernard, C. Witz, and J. Lafait, "Phase Transition and Related Phenomena in Chemically Deposited Polycrystalline Cadmium Sulfide Thin Films," *J. Physical Chemistry B*, Vol. 101, pp. 2174-2181, 1997.
- [45] V.P. Zhuze, M.G. Krin, D.P. Lukirskii, V.M. Sergura, and A. I. Shelykh, "Optical Properties and Electronic Structure of La and Gd monochalcogenides," *Sov. Phys. Sol. State*, Vol. 22, p.1558, 1981.
- [46] C.T. Tsai, D.S. Chuu, G.L. Chen, and S.L. Yang, "Studies of Grain Sizes Effects in RF Sputtered CdS Thin Films," *J. Appl. Phys.*, Vol. 79, pp.9105-9109, 1996.
- [47] Y. Modukuru, J. Thachery, M. Cahay, and P. Boolchand, "Growth and Characterization of LaS and NdS Thin Films on Various Substrates," *Proceedings of the Second International Symposium on Cold Cathodes*, 201<sup>st</sup> Meeting of The Electrochemical Society, Vol. 2002-18, pp.365-384, Philadelphia, May 12-17, 2002.



## LIST OF ACRONYMS

AFM ... Atomic Force Microscopy  
CdS ... Cadmium Sulfide  
CL ... Child-Langmuir  
EMC ... Ensemble Monte Carlo  
FN ... Fowler-Nordheim  
FWHM ... Full Width at Half Maximum  
InP ... Indium Phosphide  
KP ... Kelvin Probe  
 $La_2O_2S$  ... Lanthanum Oxysulfide  
LaS ... Lanthanum Sulfide  
NEA ... Negative Electron Affinity  
PL ... Photoluminescence  
RF ... Radiofrequency  
RMS ... Root Mean Square  
UHV ... Ultra High Vacuum  
WF ... Work Function  
WKB ... Wentzel-Kramers-Brillouin  
XPS ... X-Ray Photoelectron Spectroscopy  
XRD ... X-Ray Diffraction